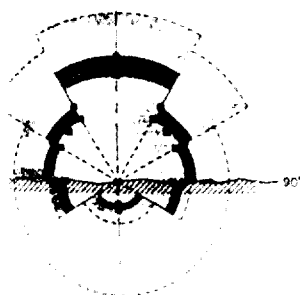




US Army Corps
of Engineers

AD-A225 622



TECHNICAL REPORT SL-90-10

2

SHALLOW UNDERGROUND TUNNEL/CHAMBER EXPLOSION TEST PROGRAM SUMMARY REPORT

DTIC FILE COPY

by

Charles E. Joachim

Structures Laboratory

DEPARTMENT OF THE ARMY

Waterways Experiment Station, Corps of Engineers
3909 Halls Ferry Road, Vicksburg, Mississippi 39180-6199

DTIC
ELECTE
AUG 23 1990
S B D



August 1990

Final Report

**BEST
AVAILABLE COPY**

Approved For Public Release; Distribution Unlimited

Prepared for US DOD Explosives Safety Board and KLOTZ Club
Alexandria, Virginia 22331-0600

90 08 21 066

Unclassified
SECURITY CLASSIFICATION OF THIS PAGE

REPORT DOCUMENTATION PAGE				Form Approved OMB No. 0704-0188	
1a REPORT SECURITY CLASSIFICATION Unclassified			1b RESTRICTIVE MARKINGS		
2a SECURITY CLASSIFICATION AUTHORITY			3 DISTRIBUTION/AVAILABILITY OF REPORT Approved for public release Distribution unlimited		
2b DECLASSIFICATION/DOWNGRADING SCHEDULE					
4 PERFORMING ORGANIZATION REPORT NUMBER(S) Technical Report SL-90-10			5 MONITORING ORGANIZATION REPORT NUMBER(S)		
6a NAME OF PERFORMING ORGANIZATION USAEWES Structures Laboratory		6b OFFICE SYMBOL (If applicable) CEWES-SE-R	7a NAME OF MONITORING ORGANIZATION		
6c ADDRESS (City, State, and ZIP Code) 3909 Mills Ferry Road Vicksburg, MS 39180-6199			7b ADDRESS (City, State, and ZIP Code)		
8a NAME OF FUNDING/SPONSORING ORGANIZATION US DOD Explosives Safety Board and KLOTZ Club		8b OFFICE SYMBOL (If applicable)	9 PROCUREMENT INSTRUMENT IDENTIFICATION NUMBER		
8c ADDRESS (City, State, and ZIP Code) Hoffman Building 1 2461 Eisenhower Avenue Alexandria, VA 22331-0600			10 SOURCE OF FUNDING NUMBERS		
			PROGRAM ELEMENT NO.	PROJECT NO.	TASK NO.
			WORK UNIT ACCESSION NO.		
11 TITLE (Include Security Classification) Shallow Underground Tunnel/Chamber Explosion Test Program, Summary Report					
12 PERSONAL AUTHOR(S) Joachim, Charles E.					
13a TYPE OF REPORT Final Report		13b TIME COVERED FROM TO		14. DATE OF REPORT (Year, Month, Day) August 1990	
				15 PAGE COUNT 207	
16 SUPPLEMENTARY NOTATION Available from National Technical Information Service, 5285 Port Royal Road, Springfield, VA 22161					
17 COSATI CODES			18 SUBJECT TERMS (Continue on reverse if necessary and identify by block number)		
FIELD	GROUP	SUB-GROUP			
			Ammunition storage Underground magazines		
			Explosives safety		
			Explosives storage		
19 ABSTRACT (Continue on reverse if necessary and identify by block number) The Shallow Underground Tunnel/Chamber Explosion Test Program was a large-scale test simulating an accidental explosion in a shallow underground magazine. The purpose of the test was to record the nature and extent of hazardous effects produced by the explosion. The program was divided into four study areas; tunnel/chamber pressure, external airblast, external ground motion, and ejecta/debris. The tunnel/chamber pressure measurements provided data on the internal explosion environment and the exit pressure at the access tunnel portal. The external airblast measurements established the airblast hazard ranges from the tunnel portal. Ground motion and artificial debris measurements furnished data on hazard ranges for ejecta produced by rupture of the chamber overburden, and for debris blown from the tunnel portal. An analysis of the data was presented comparing the results to current hazard range criteria specified in the DOD and NATO manuals for ammunition and explosives safety. <i>Key words:</i>					
20 DISTRIBUTION/AVAILABILITY OF ABSTRACT <input type="checkbox"/> UNCLASSIFIED/UNLIMITED <input checked="" type="checkbox"/> SAME AS RPT <input type="checkbox"/> DTIC USERS			21 ABSTRACT SECURITY CLASSIFICATION Unclassified		
22a NAME OF RESPONSIBLE INDIVIDUAL Charles E. Joachim			22b TELEPHONE (Include Area Code) (601) 634-2245		22c OFFICE SYMBOL CEWES-SE-R

Mr. William Martin (Mine Development Engineering Co./Valley Engineers, Bakersfield, CA (tunnel/chamber cross section and volume data and artificial debris and fragment recovery measurements)

Dr. Khosrow Bakhtar, Earth Technology Corporation, Long Beach, CA (rock mass characterization data and analysis)

Airblast and ground motion measurements were made by Mr. John Stout, assisted by Messrs. Sherman Price, Greg Phillips, and Dwayne Fuller, EED, and by Messrs. Robert Dinan, J. Wayne Beard, and Albert Elmore, WES Instrumentation Services Division. Messrs. Ronald Wood and Benard Barnes, WES Construction Services Division, also assisted in the field operations. Mr. James Ingram, EED, served as technical advisor for the instrumentation work and assisted in coordinating the technical field operations. Ms. Donna Richey and Elizabeth Felts, EED, prepared the draft and final copies of this report.

This work was performed under the overall supervision of Mr. L. K. Davis, Chief, EED. During the period of this work, Mr. Bryant Mather was Chief, SL.

COL Larry B. Fulton, EN, was Commander and Director of WES, and Dr. Robert W. Whalin was Technical Director.

Accession For	
NTIS GRA&I	<input checked="checked" type="checkbox"/>
DTIC TAB	<input type="checkbox"/>
Unannounced	<input type="checkbox"/>
Justification	
By _____	
Distribution/	
Availability Codes	
Dist	Avail and/or Special
A-1	

PREFACE

The Shallow Underground Tunnel/Chamber Explosion Test Program was sponsored by the US DOD Explosives Safety Board and the KLOTZ Club, an organization consisting of defense representatives from seven countries: France, Germany, Norway, Sweden, Switzerland, the United Kingdom, and the United States. The purpose of the club is a cooperative exchange of technical information and support research efforts designed to improve the safety of underground ammunition storage.

Mr. Arnfinn Jenssen, Norwegian Defence Construction Service, was leader of the International Steering Group which designed and directed the Shallow Underground Tunnel/Chamber Test Program. The Steering Group was comprised of Mr. Jenssen, Dr. N. J. M. Rees, Safety Services Organisation, Ministry of Defence, United Kingdom, and Dr. Jerry M. Ward, US DOD Explosives Safety Board. Dr. Ward served as the in-country coordinator for the test program.

The test was conducted at the Naval Weapons Center (NWC) test range at China Lake, CA. Mr. Carl C. Halsey of NWC coordinated the project activities at the test site. The coordination of technical data acquisition and analysis of technical data was performed by the Explosion Effects Division (EED) of the Structures Laboratory (SL), US Army Engineer Waterways Experiment Station (WES). Mr. Charles E. Joachim, EED, was the Technical Project Officer.

This report was prepared by Mr. Joachim. Contributors included:

Mr. Halsey, Mr. W. F. Durbin, and Ms. Sharon Berry, NWC
(information regarding test preparations, construction, technical photography, and post shot ejecta/debris collection)

Mr. Ron C. Edgar, Ballistech Systems Incorporated, Quebec, Canada
(airblast overpressure and overdensity data)

Mr. Noel H. Ethridge, Aberdeen Research Center, Aberdeen, MD
(blast cube results)

Dr. John M. Dewey and Mr. Douglas J. McMillin, Dewey McMillin & Associates, Victoria, British Columbia, Canada (wire drag gage and smoke puff data)

CONTENTS

	Page
PREFACE.....	i
LIST OF FIGURES.....	vi
LIST OF TABLES.....	xi
TABLE OF SYMBOLS.....	xiii
CONVERSION FACTORS, SI (METRIC) TO NON-SI UNITS OF MEASUREMENT.....	xv
SECTION 1 INTRODUCTION.....	1
1.1 BACKGROUND.....	1
1.2 OBJECTIVES.....	1
SECTION 2 PROCEDURE.....	3
2.1 DESCRIPTION OF TEST.....	3
2.2 EXPERIMENTAL PLAN.....	3
2.2.1 Tunnel and Chamber.....	4
2.2.2 Explosive Charge.....	4
2.3 INSTRUMENTATION.....	5
2.3.1 Tunnel and Chamber Pressure Measurements.....	6
2.3.1.1 Internal Pressure Predictions.....	7
2.3.2 External (Free-Field) Airblast Measurements.....	8
2.3.2.1 Free-Field Airblast Pressure Predictions.....	9
2.3.2.2 Total Pressure Prediction.....	10
2.3.3 Sound Pressure Level Measurements.....	11
2.3.4 Dynamic Blast Stations.....	11
2.3.5 Ground Motion Measurements.....	11
2.3.6 Ground Motion Predictions.....	12
2.4 PASSIVE MEASUREMENTS.....	12
2.4.1 Wire Drag Gages.....	13
2.4.2 Smoke Puffs.....	13
2.4.3 Blast Cubes.....	13
2.5 EJECTA AND ARTIFICIAL DEBRIS.....	14
2.5.1 Ejecta Measurements.....	14
2.5.2 Artificial Debris.....	15
2.6 DOCUMENTARY PHOTOGRAPHY.....	16

CONTENTS (Continued)

SECTION 3 INSTRUMENTATION--RESULTS AND DISCUSSION.....	17
3.1 INSTRUMENT PERFORMANCE.....	17
3.2 ARRIVAL TIME.....	17
3.3 AIRBLAST MEASUREMENTS.....	20
3.3.1 Tunnel/Chamber Airblast Measurements.....	20
3.3.2 Free-Field Airblast Measurements.....	21
3.4 PASSIVE BLAST MEASUREMENTS.....	23
3.4.1 Blast Cubes.....	24
3.4.2 Wire Drag Gages.....	25
3.4.3 Smoke Puffs.....	27
3.5 AIRBLAST CALCULATIONS WITH HYDRODYNAMIC COMPUTER MODELS.....	29
3.6 GROUND MOTION MEASUREMENTS.....	29
SECTION 4 CRATER AND EJECTA/ARTIFICIAL DEBRIS--RESULTS AND DISCUSSION..	33
4.1 CRATER.....	32
4.2 EJECTA.....	33
4.3 INERT ARTILLERY ROUNDS.....	34
4.4 ARTIFICIAL MISSILES.....	35
4.5 PHOTO INTERPRETATION.....	36
SECTION 5 HAZARD ANALYSIS.....	39
5.1 CURRENT DEFINITIONS OF AIRBLAST HAZARD RANGE.....	39
5.1.1 Significance of Magazine Cover Depth.....	39
5.1.2 Directional Variation of Airblast.....	40
5.2 COMPARISON OF AIRBLAST TEST RESULTS WITH CURRENT PREDICTION METHOD..	41
5.2.1 Shallow Underground Tunnel/Chamber Test.....	41
5.2.2 Alvdalen (Sweden) Test.....	42
5.2.3 Validity of Small-Scale Tests.....	43
5.3 GROUND MOTION HAZARD RANGE.....	43
5.3.1 Current Prediction Method.....	43
5.3.2 Shallow Underground Tunnel/Chamber Test Results.....	44
5.4 DEBRIS HAZARD RANGE.....	47
SECTION 6 SUMMARY, CONCLUSIONS, AND RECOMMENDATIONS.....	50
6.1 SUMMARY OF FINDINGS.....	50
6.2 CONCLUSIONS.....	52

CONTENTS (Concluded)

6.3 RECOMMENDATIONS.....	53
REFERENCES.....	55

LIST OF FIGURES

	Page
1. Site contour map.....	57
2. Site contour map for Shallow Underground Tunnel/Chamber Explosion Test Program.....	58
3. Tunnel/Chamber longitudinal cross-sections (plan and profile)..	59
4. Location of 20,000-kg Composition B explosive charge for Shallow Underground Tunnel/Chamber Explosion Test Program (plan and profile).....	60
5. Interior pressure transducer locations for Shallow underground Tunnel/Chamber Test Program.....	61
6. Cable protection schematic for interior airblast gage signal lines on Shallow Underground Tunnel/Chamber Test Program.....	62
7. Charge and Chamber configuration for BLASTIN calculation.....	63
8. Predicted airblast overpressure record (gas plus shock at station C.5, at tunnel/chamber interface as calculated by WES's BLASTIN code.....	64
9. Chamber reflected airblast (gas plus shock) at stations C.1 and C.2.....	65
10. Reflected airblast (gas plus shock) at stations C.3 and C.4...	66
11. Free-field close-in airblast gage locations for Shallow Underground Tunnel/Chamber Explosion Test Program.....	67
12. Free-field airblast gage locations for Shallow Underground Tunnel/Chamber Explosion Test Program.....	68
13. Free-field overpressure scaled to Shallow Underground Tunnel/Chamber Explosion Test parameters.....	69
14. Peak incident pressure versus peak dynamic pressure, TM 5-855-1.....	70
15. Free-field ground motion gage locations for Shallow Underground Tunnel/Chamber Explosion Test Program.....	71
16. Scaled radial particle acceleration in rock, from HARD HAT (nuclear) and MINERAL LODGE (high explosive) detonations.....	72
17. Coupling factor versus loading density.....	73
18. Airblast-induced acceleration in granite versus free-field airblast pressure, from the 100-ton MINERAL ROCK surface detonation	74
19. Peak airblast-induced particle velocity in rock versus free-field airblast pressure, from the MINERAL ROCK event.....	75
20. Wire drag gage locations for Shallow Underground Tunnel/Chamber Explosion Test.....	76
21. Smoke mortar locations for Shallow Underground Tunnel/Chamber Test.....	77
22. Contour map of test area showing pretest locations of blast cubes.....	78
23. Ejecta collection pad locations.....	79
24. Pre-test locations of artificial missiles on overburden surface above tunnel/chamber centerline.....	80

LIST OF FIGURES (Continued)

25.	Pre-test locations of inert 155-mm artillery rounds for Shallow Underground Tunnel/Chamber Test Program.....	81
26.	Camera, photo pole and photo target locations for Shallow Underground Tunnel/Chamber Explosion Test.....	82
27.	Shock wave arrival time in and just outside the access tunnel.	83
28.	Free-field airblast shock wave arrival time versus distance from tunnel portal along the extended tunnel/chamber centerline.....	84
29.	Free-field airblast shock wave arrival time versus distance from tunnel portal.....	85
30.	Free-field ground shock arrival time versus distance from center of chamber.....	86
31.	Peak side-on overpressure versus distance from the initiation end of the explosive charge.....	87
32.	Comparison of predictions with measured free-field airblast data (0-degree azimuth).....	88
33.	Comparison of measured full-scale and calculated free-field airblast data, 0° azimuth.....	89
34.	Comparison of measured full-scale and calculated free-field airblast data, 30° azimuth.....	90
35.	Comparison of measured full-scale and calculated free-field airblast data, 45° azimuth.....	91
36.	Comparison of measured full-scale and calculated free-field airblast data, 60° azimuth.....	92
37.	Comparison of measured full-scale and calculated free-field airblast data, 90° azimuth.....	93
38.	Comparison of measured full-scale and calculated free-field airblast data, 180° azimuth.....	94
39.	Peak overpressure versus azimuth, Shallow Underground Tunnel/Chamber Explosion Test.....	95
40.	Peak impulse versus distance from the center of the charge, Shallow Underground Tunnel/Chamber Explosion Test.....	96
41.	Peak impulse versus azimuth, Shallow Underground Tunnel/Chamber Explosion Test.....	97
42.	Peak stagnation pressure versus distance from tunnel portal, Shallow Underground Tunnel/Chamber Explosion Test.....	98
43.	A comparison of peak stagnation, side-on and dynamic pressure at the 75-m range.....	99
44.	A comparison of peak stagnation, side-on and dynamic impulse at the 75-m range.....	100
45.	Overdensity versus azimuth on the 75-m range.....	101
46.	Density ratio versus pressure ratio.....	102
47.	Total blast cube displacement versus azimuth along the 75-m range.....	103
48.	Blast cube dynamic pressure impulse versus azimuth along the 75-m range.....	104

LIST OF FIGURES (Continued)

49.	Steel blast cube total displacement versus azimuth.....	105
50.	Inferred dynamic pressure impulse versus distance along the tunnel/chamber extended centerline.....	106
51.	Free-field airblast flow direction as indicated by wire drag gages.....	107
52.	Comparison of dynamic pressure impulse measured by BSI and data inferred by blast cubes and wire drag gages.....	108
53.	Smoke puff location-time contours.....	109
54.	Particle trajectories measured from positions of Smoke Trail #1 (15 m), Dewey (1989).....	110
55.	Particle trajectories measured from positions of Smoke Trail #2 (90 m), Dewey (1989).....	111
56.	Measured smoke trail particle flow velocities along Smoke Trail #1, Dewey (1989).....	112
57.	Initial smoke trail particle velocities along trail #1 as a function of height above ground surface.....	113
58.	Blast wave reconstruction from smoke puff trails compared to wave fronts measured by WES and calculated by S-CUBED, Inc....	114
59.	Comparison of WES measured and smoke puff calculated-time history at the 75 m radial.....	115
60.	Comparison of overpressure-time histories from experimental record and two calculations (rigid and sand models) inside access tunnel 4 m from portal (C-10, 4.7 m).....	116
61.	Comparison of overpressure-time histories from experimental record and two calculations (rigid and sand models) inside access tunnel 2.5 m from portal (C-12, 2.2 m).....	117
62.	Peak direct-induced vertical particle velocity versus slant distance from center of the charge.....	118
63.	Peak direct-induced horizontal particle velocity versus slant distance from center of the charge.....	119
64.	Peak airblast-induced vertical particle velocity versus slant distance from center of the charge.....	120
65.	Comparison of predicted and measured peak airblast induced, vertical particle velocity versus slant distance to the center of the explosive charge.....	121
66.	Peak airblast-induced, horizontal particle velocity versus slant distance from the center of the charge.....	122
67.	Scaled crater dimensions versus scaled depth of burst in rock; comparison of crater from Shallow Underground Tunnel/Chamber Explosion Test with data bands from previous, fully-coupled detonations in rock.....	123
68.	Impact density for ejecta missiles found on collection pads, as a function of distance from the tunnel portal.....	124
69.	Large fragment impact as a function of distance from the tunnel portal.....	125
70.	Ejecta/debris missile impact density versus distance from the portal.....	126

LIST OF FIGURES (Continued)

71.	Areal density and number of strikes of natural material versus distance from tunnel portal.....	127
72.	Comparison of number of strikes versus scaled distance from charge for large-yield surface chemical weapons simulation tests and Shallow Underground Tunnel/Chamber Explosion Test (decoupled buried explosive charge).....	128
73.	Number of inert 155-mm round impacts as a function of distance from the tunnel portal.....	129
74.	Artificial missile post-test versus pretest slant distance....	130
75.	Launch velocity of cover rock ejected from Shallow Underground Tunnel/Chamber Explosion Test, compared to ejecta velocities from other sources on previous tests.....	131
76.	Growth rates of fireball clouds from tunnel portal and ejecta cloud from breach of cover rock over magazine.....	132
77.	Ejecta missile paths recorded by Camera Station 6. Center of field of view is 55 m from portal along 0-degree bearing.....	133
78.	Ejecta missile paths recorded by Camera Station 7. Center of field of view is 138 m from portal along 0-degree bearing.....	134
79.	Ejecta missile paths recorded by Camera Station 8. Center of field of view is 190 m from portal along 0-degree bearing.....	135
80.	Ejecta missile paths recorded by Camera Station 10. Center of field of view is 294 m from portal along 0-degree bearing.....	136
81.	Ejecta missile paths recorded by Camera Station 11. Center of field of view is 375 m from portal along 0-degree bearing.....	137
82.	Ejecta missile paths recorded by Camera Station 12. Center of field of view is 454 m from portal along 0-degree bearing.....	138
83.	Ejecta missile paths recorded by Camera Station 13. Center of field of view is 494 m from portal along 0-degree bearing.....	139
84.	Ejecta missile velocity versus ballistic trajectory angle, as recorded by Camera Station 6.....	140
85.	Ejecta missile velocity versus ballistic trajectory angle, as recorded by Camera Station 7.....	141
86.	Ejecta missile velocity versus ballistic trajectory angle, as recorded by Camera Station 8.....	142
87.	Ejecta missile velocity versus ballistic trajectory angle, as recorded by Camera Station 10.....	143
88.	Ejecta missile velocity versus ballistic trajectory angle, as recorded by Camera Station 11.....	144
89.	Ejecta missile velocity versus ballistic trajectory angle, as recorded by Camera Station 12.....	145
90.	Ejecta missile velocity versus ballistic trajectory angle, as recorded by Camera Station 13.....	146
91.	Ejecta missile velocity versus maximum particle dimension, as recorded by Camera Station 6.....	147
92.	Ejecta missile velocity versus maximum particle dimension, as recorded by Camera Station 7.....	148
93.	Ejecta missile velocity versus maximum particle dimension, as recorded by Camera Station 8.....	149

LIST OF FIGURES (Concluded)

94.	Ejecta missile velocity versus maximum particle dimension, as recorded by Camera Station 10.....	150
95.	Ejecta missile velocity versus maximum particle dimension, as recorded by Camera Station 11.....	151
96.	Ejecta missile velocity versus maximum particle dimension, as recorded by Camera Station 12.....	152
97.	Ejecta missile velocity versus maximum particle dimension, as recorded by Camera Station 13.....	153
98.	Geometry of Inhabited Building Distances for airblast from explosions in underground magazines; Ammunition and Explosives Safety Standards (DOD 6055.9-STD).....	154
99.	Airblast Inhabited Building Distances specified by Explosives Safety Standards (DOD 6055.9-STD) for open and underground munitions storage, compared to 5.0 and 6.2 kPa distances measured on Shallow Underground Tunnel/Chamber Explosion Test.	155
100.	Airblast Inhabited Building Distances specified by Standards (DOD 6055.9-STD) compared to measured distances to 5.0 and 6.2 kPa pressure levels for the Shallow Underground Tunnel/Chamber Explosion Test.....	156
101.	Airblast Inhabited Building Distances specified by Standards (DOD 6055.9-STD) for open and underground munitions storage, compared to 5.0 and 6.2 kPa distances measured in 1987 KLOTZ Club Test 8 at Alvdalen, Sweden.....	157
102.	Airblast Inhabited Building Distances specified by Explosives Safety Standards for underground munitions storage, compared to measured distances to 5.0 and 6.2 kPa pressure levels, for 1987 KLOTZ Club Test 8 at Alvdalen, Sweden.....	158
103.	Airblast Inhabited Building Distance along the 0-degree azimuth (extended tunnel axis) as a function of loading density, as indicated by full-scale and model test data.....	159
104.	Maximum velocity vector versus slant distance from center of the charge; comparison of prediction curves with data from 0, 90, and 180-degree azimuths on Tunnel/Chamber Test.....	160
105.	Earth cover function, f_c , for ejecta/debris versus scaled chamber earth cover depth, Ammunition and Explosives Safety Standards (A&ESS).....	161
106.	Inhabited Building Distances from debris hazards specified in the Explosives Safety Standards and NATO AC/258 for a 20,000-kg detonation, compared to ranges indicated by data collection on the Shallow Underground Tunnel/Chamber Explosion Test.....	162

LIST OF TABLES

	Page
1. Calculated Chamber Gas Pressures for a Range of Net Explosive Weights and Candidate Explosive Sources.....	163
2. Locations and Peak Pressure Predictions for Internal Airblast Measurements.....	164
3. Locations and Predicted Peak Pressures for Free-Field Airblast Measurements.....	165
4. Sound Pressure Level Dosimeter Locations.....	166
5. Location and Predicted Peak Values for Surface Ground Motion Measurements.....	167
6. Wire Drag Gage Locations (Dewey, 1989).....	168
7. Smoke Puff Launcher Locations.....	169
8. Blast Cube Pre-test Locations (Ethridge, 1989).....	170
9. Ejecta and Debris Collection Pad Locations.....	172
10. Artificial Missile Location Data.....	173
11. Shallow Underground Tunnel/Chamber Explosion Test: Tunnel/Chamber Airblast Measurements.....	174
12. Shallow Underground Tunnel/Chamber Explosion Test: External Airblast Measurements.....	175
13. Shallow Underground Tunnel/Chamber Explosion Test: Ground Motion Measurements.....	176
14. Shallow Underground Tunnel/Chamber Explosion Test: Sound Pressure Level Measurements.....	177
15. Shallow Underground Tunnel/Chamber Explosion Test: Dynamic Pressure Measurements.....	178
16. Blast Cube Post-Test Measurements and Calculated Data, 75-m Arc (Ethridge, 1989).....	179
17. Blast Cubes: Post-Test Measurements and Calculated Data for 5-m Arc (Ethridge, 1989).....	183
18. Blast Cubes: Post-Test Measurements and Calculated Data for 10-m Arc (Ethridge, 1989).....	184
19. Blast Cubes: Post-Test Measurements and Calculated Data for cubes in Tunnel (Ethridge, 1989).....	185
20. Wire Drag Gage Results.....	186
21. Calculated Values for Minimum Lethal Ejecta Missile Impact Velocities.....	187

LIST OF TABLES (Concluded)

22. Comparison of Airblast Inhabited Building Distances for
22,000-kg NEW; Current Standards versus Measured Distances
(in metres)..... 188

TABLE OF SYMBOLS

A	front surface area of blast cube, m^2
A_c	cross-sectional area of a storage chamber, m^2
A_f	overpressure azimuth function
A_j	cross-sectional area of a tunnel, m^2
a	ambient sound velocity in air, m/s
C_c	minimum overburden thickness over an underground magazine, m
C_D	ballistic air drag coefficient
C_p	the stress wave velocity of a material, m/s
C_v	minimum overburden thickness for airblast suppression, m
D	equivalent hydraulic diameter of a tunnel exit, m
D_c	explosive energy coupling factor (ground motion prediction)
D_e	distance from wire drag gage to source, m
D_{id}	debris hazard range, m
D_{ig}	ground shock hazard range, m
D_{20}	equivalent distance from a 20-ton surface burst to produce a similar effect, m
f_c	a function relating scaled overburden depth and ejecta hazard range, $kg^{-0.41}$
f_d	a function of chamber loading density
f_g	decoupling factor (ground shock hazard range)
k	a constant associated with storage chamber geometry relative to the tunnel ($k = 1$ for the "shotgun" magazine design)
k_{hc}	ratio of heat capacities
M	Mach number
M_e	charge mass of an equivalent surface burst, metric ton
m	mass
n	constant related to the number of tunnel entrances
P	peak free-field airblast overpressure, kPa
P_a	peak ambient overpressure, Pa
P_c	peak chamber pressure, bar
P_e	peak tunnel exit pressure, kPa
P_o	peak stagnation pressure, kPa

TABLE OF SYMBOLS (Concluded)

Q	net explosive weight (TNT equivalent) stored in the chamber, kg
Q_r	effective explosive weight, kg
R	the gas constant, per-unit-mass
R_a	distance from a detonation or from a tunnel portal to a point of interest, m
T	absolute temperature, °K
u	the shock wave velocity, m/s
v	peak particle velocity from fully coupled charge, m/s
V_c	explosive chamber volume, m ³
v_d	peak particle velocity from a decoupled charge, m/s
v_h	horizontal component of particle velocity, m/s
v_o	calculated initial blast cube velocity, m/s
V_t	total volume (chamber plus tunnel), m ³
v_t	ejecta missile terminal velocity, m/s
v_v	vertical component of particle velocity, m/s
θ	horizontal angle (or azimuth) from the extended centerline of a tunnel exit, degrees
ρ	density of a material, kg/m ³

CONVERSION FACTORS, METRIC (SI) TO NON-SI
UNITS OF MEASUREMENT

SI (Metric) units of measurement used in this report can be converted to Non-SI units as follows:

<u>Divide</u>	<u>BY</u>	<u>To Obtain</u>
kilopascals	99.9739765	bars
cubic metres	0.02831685	cubic feet
radians	0.1745329	degrees (angle)
degrees Celsius*	1.8 C + 32	degrees Fahrenheit
metres	0.3048	feet
metres per kilogram ^{1/3}	0.3955977	feet per pound ^{1/3}
kilograms	0.45359237	pound (mass)
megapascals	0.006894757	pounds (force) per square inch**
kilograms per cubic metre	16.01846	pounds (mass) per cubic foot
square metres	0.09290304	square feet

* To obtain Fahrenheit (F) temperature readings from Celsius (C) readings, use the following formula: $F = 1.8 C + 32$. To obtain kelvin (K) readings, use: $K = C + 273.15$.

** For pressure, 14.7 psi = 1.0 atmosphere = 1.014 bar = 101.4 kPa

SHALLOW UNDERGROUND TUNNEL/CHAMBER
EXPLOSION TEST PROGRAM
SUMMARY REPORT

SECTION 1

INTRODUCTION

1.1 BACKGROUND

A considerable amount of research has been performed in the last two decades to develop a technical data base and methods to predict the airblast and ejecta/debris hazards from accidental explosions in underground magazines. Much of this work was concerned with detonations in magazines so deep that venting of the detonation through the magazine cover rock does not occur. The effect of cover venting on the reduction of external airblast from the entrance portal has been demonstrated in small-scale tests performed in the United Kingdom (Millington, 1985). The Shallow Underground Tunnel/Chamber Test Program was designed to provide large-scale airblast and ejecta/debris effects from a detonation of 20,000-kg¹ (net explosive weight) in a shallow underground magazine.

The test program was primarily funded on an equal share basis by three organizations: the U.S. Department of Defense Explosives Safety Board (DDESB); the Safety Services Organisation (SSO) of the Ministry of Defense, United Kingdom; and the Norwegian Defence Construction Service (NDCS). Additional funds were provided by the Pyrotechnie Saint Nicolas (PSN), France; the Royal Swedish Fortifications Administration (FORTF), Sweden; and the Amt fur Bundesbauten (AB), Switzerland, to expand the scope of blast instrumentation and debris measurements.

This report summarizes the technical data acquired during the test program and presents a comprehensive analysis of the results.

¹ A table of factors for converting SI (metric) units of measurement to Non-SI units is presented on page xv.

1.2 OBJECTIVES

The overall objective of the test program was to determine the hazardous effects (debris, airblast, and ground motion) produced by a (simulated) accidental detonation of explosive stores which ruptures the overhead cover of the underground chamber. The results will be used to evaluate and validate current quantity-distance (Q-D) safety standards for underground storage of munitions.

SECTION 2

PROCEDURE

2.1 DESCRIPTION OF TEST

The Shallow Underground Tunnel/Chamber Explosion Test Program involved the detonation of a 20,000-kg charge of Composition B explosive, simulating an accidental explosion of ammunition stored inside an underground magazine in granitic rock. A large-scale storage chamber and access tunnel were constructed for this test at a selected site on the Naval Weapons Center test range at China Lake, CA. For the TNT-equivalent (1.1 equivalence factor) 20,000-kg net explosive weight (N.E.W), the chamber loading density was 66.4 kg/m^3 . A site contour map showing the approximate tunnel/chamber location is presented in Figure 1. An enlarged contour map showing the tunnel portal, access tunnel, and chamber locations is shown in Figure 2. Active measurements included: (1) internal chamber and access tunnel airblast pressures; (2) free-field overpressure along the 0, 30, 45, 60, 90, and 180-degree azimuths, measured from the tunnel portal; (3) beta densitometer/general purpose blast (GPB) stations at the 75-m range along the 15, 30, and 60-degree azimuths; and (4) ground motion measurements along the 0, 90, and 180-degree azimuths. Passive airblast and ejecta/debris measurement devices consisted of blast cubes, wire drag gages, smoke puffs, and artificial missiles. In addition, an ejecta collection study was performed and motion picture film was analyzed to quantify the ejecta missile ranges.

2.2 EXPERIMENTAL PLAN

The Shallow Underground Tunnel/Chamber Explosion Test Program was divided into four study areas; tunnel/chamber blast pressure, free-field airblast, free-field ground motion, and ejecta/debris. The tunnel/chamber pressure measurements provided data on the internal explosion environment and the exit pressure at the access tunnel portal. The free-field airblast measurements established the airblast hazard range from the tunnel portal. Ground motion measurements provided data on overburden movement and ground shock hazard range. The ejecta and

artificial debris measurements furnished data on hazard ranges for overburden ejecta, unexploded munitions, and other debris.

2.2.1 Tunnel and Chamber

The chamber and access tunnel were excavated from weathered and highly jointed granitic rock. The chamber was 18 m long, 4 m wide, and 5 m high with a volume of 322.3 m³ and an average cross-section of 17.4 m². The interior chamber surfaces were rock-bolted and covered with wire mesh embedded in shotcrete to stabilize the wall rock and, in some instances, to replace rock removed as a result of overbreak during the excavation. The access tunnel was 25 m long, 2.4 m wide, and 2.4 m high with a minimum cross-section of 5.3 m². The total volume was 465.3 m³ (access tunnel plus chamber). The tunnel support system consisted of rock bolts used in conjunction with a reinforced concrete liner, wire mesh and shotcrete. The concrete liner extended a distance of 10 m from the portal. During the initial excavation, the overburden collapsed along the first 3.7 m of the access tunnel. This material was replaced with shotcrete and rubble fill. Tunnel and chamber cross-sections are shown in plan and profile in Figure 3. Site, geologic, and construction data are contained in the "KLOTZ Underground Magazine Trial, Data Report" (Halsey, et al, 1989).

2.2.2 Explosive Charge

Operational and safety considerations prevented the use of actual artillery (155-mm) munitions as the explosive source for this test program. The 155-mm round contains either TNT or Composition B as the basic charge. After evaluating costs and availability of these and other explosives, two were selected for further consideration--ANFO and Composition B. Chamber gas pressures were calculated for 1,000 and 20,000 kg TNT charges using WES's BLASTIN computer code. Additional calculations were made for ANFO and Composition B to determine the quantities of these materials which produced chamber gas pressures equivalent to those from the TNT charges. The results of these calculations are presented in Table 1. Based on the calculations, 20,000 kg of Composition B was selected as the explosive source for this

test.

A calibration experiment, planned as a 1,000-kg internal detonation, was deleted from the test program. The highly jointed and fractured rock encountered throughout the tunnel/chamber excavation raised concern that the calibration event would produce excessive damage to the chamber. To check out the instrumentation electronics, a full-power test was conducted with all recording systems operating, during which four electric blasting caps were initiated.

The Composition B explosive was placed on a plywood platform 1 m above the floor of the chamber. Overall explosive charge dimensions were 1.82 m wide by 1.52 m high by 12.2 m long. The charge was equi-distant from the chamber side walls and 1.26 m from the back wall. The charge position in the chamber is shown in Figure 4 (plan and profile). The chamber loading density (TNT-equivalent) was 66.4 kg/m^2 and the total (access tunnel plus chamber) loading density was 47.4 kg/m^3 .

The results of model tests conducted by the Norwegian Defence Construction Service indicated significant differences in pressures measured from charges initiated by detonators on the front of the charge versus other detonator locations. Therefore, it was decided to initiate the 20,000-kg charge for this experiment at four points on the front vertical face, in order to develop a planar detonation front within the charge as soon as possible. These four points were located at the centers of the four quarter sections of the front surface area. The initiation system used electric blasting caps and C-4 booster charges.

2.3 INSTRUMENTATION

The instrumentation program was subdivided into four study areas; internal airblast (tunnel and chamber), free-field airblast, dynamic blast stations, and ground motion. The interior airblast and dynamic blast station measurements provide useful data for developing blast prediction theories for accidental detonations in underground magazines. The free-field airblast and ground motion measurements also provide quantitative data on hazard ranges.

2.3.1 Tunnel and Chamber Pressure Measurements

Reflected pressure measurements were made at points 3 m from each end of the chamber (at mid-height on the east chamber wall). Two additional reflected pressure gages were placed in the chamber adjacent to the primary gages to provide redundant measurements at these high-risk measurement locations.

The original test plan called for five side-on and three stagnation pressure measurements from gages installed in the access tunnel floor. Later predictions of pressures inside the access tunnel indicated that stagnation pressures might exceed the capability of available transducers. Therefore, these three gages were replaced by additional side-on pressure gages located in the tunnel floor 1.0 m from existing side-on pressure gages. The differences in shock wave arrival times over this separation distance allowed the calculation of shock front Mach numbers and airblast stagnation pressures.

Two shock-mounted, self-recording, "Test Instrumentation Development" (TID) gage packages, measuring side-on pressure, were installed in the tunnel floor at 1.7 m inside and 0.3 m outside the portal to evaluate the performance of these gages, which are under development by WES. The locations of the chamber, access tunnel and TID interior pressure gages are shown in plan and profile in Figure 5, and tabulated in Table 2.

Kulite Model HKS-375 transducers were used for all interior tunnel and chamber airblast pressure measurements. All interior airblast transducers were installed in shock-isolation mounts for increased survivability from direct shock effects. Cables from gages inside the tunnel were protected by 9.5-mm diameter stainless steel tubing, installed in the concrete tunnel floor from each shock mount to a point outside the tunnel. The cable protection schematic for the tunnel floor is shown in Figure 6. Cables from gages in the chamber walls were routed directly through holes drilled from the side of the chamber to the surface of the overburden.

2.3.1.1 Internal Pressure Predictions. An empirical method developed by Weibull (1968) for predicting pressures in a partially closed chamber uses the following equation:

$$P_c = 22.5 [(Q / V)^{0.63} - 0.013] \quad (1)$$

where P_c is the chamber pressure, bars

Q is the TNT equivalent explosive weight, kg

and V is the chamber volume, m^3 .

Using this equation, the calculated chamber pressure was 29.8 MPa.

Propagating this chamber pressure through the access tunnel using the gas law gave an exit pressure of 21.3 MPa.

Kingery (1989) recommends an empirical relation developed by the Norwegian Defence Construction Service to calculate exit pressure from an underground tunnel/chamber system:

$$P_e = 1.21 \times 10^6 [Q / V_t]^{0.607} [A_j / A_c]^{0.19} \quad (2)$$

where P_e is the exit pressure, Pa

Q is the TNT equivalent explosive weight, kg

V_t is total volume (chamber plus tunnel), m^3

A_j is the cross-sectional area of the tunnel, m^2

and A_c is the cross-sectional area of the chamber, m^2

The exit pressure calculated by this relation is 9.4 MPa. Using the gas law, the estimated chamber pressure required to produce this exit pressure is 13.2 MPa.

The WES BLASTIN computer code was also used to calculate a chamber pressure (shock plus gas pressure). The 20,000-kg explosive charge was divided into four 5,000-kg charges (Figure 7) in order for this calculation to approximate the actual linear shape of the charge inside the chamber. In the calculation, the charge was initiated at the front end (end nearest the tunnel/chamber interface) and the detonation propagated at the shock front velocity through the explosive. The calculated chamber pressure at the tunnel/chamber interface (gage position C.5) is shown in Figure 8. The peak calculated overpressure at this point was 165 MPa. This pressure was then propagated through the

access tunnel (using the gas law) to obtain an exit pressure of 118 MPa.

The peak reflected pressure-time histories calculated by BLASTIN for gage locations C.1/C.2, and C.3/C.4 are shown in Figures 9 and 10, respectively. The calculated peak chamber pressure was 303 MPa at these gage stations. In 1986, BLASTIN calculations were made for a 24,000-kg NEW detonation in a standard U.S. Air Force igloo structure conducted at China Lake, CA. The calculated values were approximately four times greater than the measured data. Assuming that the same error margin applies for the tunnel/chamber test, the overpressure predicted by BLASTIN was reduced by 75 percent, giving a predicted peak overpressure of 41.2 MPa. Thus, the three methods used to predict peak chamber overpressure data, as discussed in this section, produced estimated peak values of 41.2, 29.8, and 13.2 MPa, with a factor of three difference between the upper and lower limits. The predicted peak interior pressures given in Table 2 are derived from the highest prediction; i.e., the 25-percent BLASTIN calculation.

2.3.2 External (Free-field) Airblast Measurements

A total of 32 free-field airblast gages were installed along the extended tunnel/chamber centerline (0-degree azimuth) and along the 30, 45, 60, 90, and 180-degree azimuths in the clockwise direction. Both side-on and stagnation pressure measurements were made at a range of 5 m outside the tunnel entrance to establish mass flow and dynamic pressure levels along the extended tunnel centerline. The stagnation gage was mounted on a steel mount 75 cm above the ground surface, with the side-on pressure gage flush-mounted immediately below. All other WES free-field gages were flush-mounted on the ground surface for side-on measurements. Gage distances were measured from the tunnel portal, and extended out to the predicted 50-Mbar pressure level. The close-in airblast gage locations are shown in Figure 11. The free-field airblast gage locations are shown in Figure 12 and are tabulated, along with the predicted peak pressures, in Table 3.

Kulite Model HKS-375 pressure gages were used in all locations where the predicted peak pressures exceeded 1.5 MPa. Kulite Model XT-190

gages were used for lower pressures. The stagnation pressure measurement was made with a low-impedance, quartz, PCB Model 109A High-Pressure Transducer with a rated range of 689 MPa.

2.3.2.1 Free-field Airblast Pressure Predictions. Estimates of the free-field airblast pressures were developed by examining data from previous large-scale, near-surface bursts, small-scale model tests, and empirical calculations. A data plot developed by Jenssen (1988) included results extrapolated from 1:24.8-scale tests and from calculations of a model with an expansion chamber. The extrapolated Norwegian model data are plotted in Figure 13. The general assessment of the test planning group was that these free-field overpressures were lower than expected, based on the predicted chamber pressure (Table 1).

Skjeltnorp, Hegdahl, and Jenssen (1975) developed an empirical relation for predicting free-field overpressure with distance from an underground magazine. The peak overpressure equation is:

$$P = \frac{1.24 P_e (R/D)^{-1.35}}{1 + (\theta/56)^2} \quad (3)$$

where P is the peak free-field overpressure, Pa

P_e is the exit pressure at the tunnel portal, Pa

R is the distance from the portal, m

θ is the angle referenced to the extended tunnel centerline, (in degrees).

and D for this case, is the equivalent circular diameter of the tunnel exit, m, where

$$D = 2 (A_j / \pi)^{1/2} \quad (4)$$

The exit pressure derived from BLASTIN was used for P_e in this equation. Figure 13 shows the free-field airblast overpressure curve from the above relation (Skjeltnorp, et al, 1975) and from a curve based on 25 percent of

the BLASTIN prediction.

Tancreto (NCEL) provided data from a 1:15-scale model test conducted in a 30-cm diameter gun tube. The 5.4-kg charge was centered 1.2 m from the back end of the 4.9-m long gun barrel. These data are also plotted in Figure 13. The straight tube (without the choke-down effect provided by the smaller cross-section of the access tunnel) should produce higher pressures than those calculated by Equation 3. However, note that these data are asymptotic to the empirical equation of Skjeltpor, et al, (1975) close-in, decreasing to 1/3 the empirical relation at greater distances.

Scaled airblast pressures from the MINE ORE event (a 100-ton TNT sphere detonated at 0.9 charge radii above the ground surface) and a Speicher-Brode calculation (surface burst) are included in Figure 13 for comparison. As expected, these data indicate peak overpressures that are less than those predicted by Equation 3, but greater than the Norwegian model data. This fact would indicate that peak overpressure predictions for the full-scale tunnel/chamber test should not be less than those predicted by Equation 3. The peak overpressure prediction given in Table 3 was calculated using Equation 3 and the exit pressure derived from the 25-percent BLASTIN chamber pressure (29.5 MPa).

The prediction curves shown in Figure 13 were used to range the free-field airblast pressure transducers. Because of the wide variation in these predicted values (a factor of 20) it was impossible to cover the entire range. The airblast gages were therefore adjusted to measure the higher range of estimated values, with the lower range falling within the noise band.

2.3.2.2 Total Pressure Prediction. The total (or stagnation) airblast pressure is equal to the dynamic pressure plus the side-on overpressure. The peak side-on overpressure at Station A.1 was estimated to be 15 MPa. The curves of Figure 14 (adapted from TM 5-855-1) relate peak dynamic pressures to side-on overpressures. Entering Figure 14 with the side-on overpressure value gives a peak dynamic pressure of 48 MPa. By summing the side-on and dynamic pressures at this location, we get an

estimated total pressure of 63 MPa.

2.3.3 Sound Pressure Level Measurements

Sound pressure level (SPL) measurements were made with Larson-Davis Model 700 dosimeters. The Model 700 is a hand-held, self-recording system measuring sound pressures in decibels. SPL units were placed along the main road from the chamber test site to U.S. Highway 395, a distance of some six miles. The SPL measurement locations are listed in Table 4.

2.3.4 Dynamic Blast Stations

Ballistech Systems, Incorporated (BSI) fielded three general purpose blast (GPB) stations for the Shallow Underground Tunnel/Chamber Explosion Test. The GPB stations were installed at the 75-m range at 15, 30, and 60 degrees from the extended tunnel/chamber centerline. Additional side-on pressure gages were placed at the 75-m range on the 7.5-degree azimuth and at the 100-m range on the 30-degree azimuth. Each GPB station contained four transducers, measuring airblast overdensity, side-on overpressure, dynamic pressure, and stagnation pressure. Kulite Model XT-190 Series pressure gages were used to measure side-on and stagnation pressures. A custom-designed Beta densitometer, developed by BSI, measured overdensity. These gages were connected to digital data recorders installed in plywood boxes and buried in the ground immediately behind the GPB stations.

2.3.5 Ground Motion Measurements

Fourteen ground motion canisters were installed by WES to measure the overburden rise and free-field ground motion produced by the explosion. Accelerometers were used to measure the strong, close-in motions, and velocity-sensing seismometers were employed further out, where predicted accelerations were less than 1.0 g. One canister with a vertical sensing accelerometer was placed 2.5 m above the center of the chamber roof in a hole drilled from the ground surface. Another canister, with horizontal and vertical accelerometers, was placed on the ground surface above this location.

A TID self-recording package (G.14V), containing a vertically-oriented accelerometer, was placed on the overburden surface directly

above the tunnel/chamber interface. This package was emplaced in a bucket partially filled with concrete (to provide additional mass), and was intended to measure the spall velocity of the overburden surface and provide an artificial ejecta datum point. All horizontal sensing transducers were aligned along the azimuth towards the center of the chamber. Ground motion instrument locations are shown in Figure 15 and listed in Table 5.

2.3.6 Ground Motion Predictions

Ground motion predictions were derived from two previous high explosive tests in granite; MINERAL ROCK, a 100-ton spherical TNT charge detonated at 0.9 charge radii above the surface, and MINERAL LODE, a 16-ton (11-ton TNT equivalent) ammonium nitrate slurry charge, detonated 30.5 m below the surface. The MINERAL LODE data curve for radial acceleration-versus scaled distance (Figure 16) was used to predict close-in accelerations for the tunnel/chamber test. A coupling factor of 20 percent was assumed, based on Figure 17 (Project Cowboy test and WES 1:75-scale model data (Smith, et al, 1989)).

The direct-induced accelerations are known to attenuate rapidly with distance. Surface accelerations at greater distances from detonations on or near the ground surface are primarily induced by airblast. Therefore the MINERAL ROCK near-surface acceleration data were used to predict these motions. A peak airblast pressure-versus-acceleration curve (Figure 18), developed from the MINERAL ROCK data, was the basis of these predicted values. Peak accelerations less than 1.0 g were predicted at several long-range stations. These levels are too small for measurement with the accelerometers normally used by WES. Consequently, ground motion measurements at these locations were made with velocity gages. A peak airblast pressure-versus-particle velocity curve (Figure 19), developed from the MINERAL ROCK data, was used for these estimates. A summary of the peak ground motion predictions is given in Table 5.

2.4 PASSIVE MEASUREMENTS

Three types of passive diagnostic measurements were installed to provide supplemental data on external airblast for the Shallow Underground Tunnel/Chamber Explosion Test. These were wire drag gages,

smoke puffs, and blast cubes.

2.4.1 Wire Drag Gages

Twenty-one wire drag gages were installed outside the tunnel portal to measure blast flow direction and total dynamic pressure and impulse, and to determine blast wave symmetry in a plane near the ground surface. Installation, operation, and data interpretation for the wire drag gages were provided by Dewey McMillin & Associates, Inc. The gages were placed symmetrically about the extended tunnel centerline (0 degrees) on azimuths ranging from 300 to 60 degrees. The wire drag gage locations are shown in Figure 20 and tabulated in Table 6.

2.4.2 Smoke Puffs

Twenty-one smoke puff launchers were installed on the ground surface along the extended tunnel/chamber centerline. Fifteen of these launchers were placed in front of the tunnel portal (0-degree azimuth). Five launchers were located on top of the overburden directly behind the portal (180-degree azimuth). One launcher was positioned over the tunnel portal and tilted at 45 degrees from the vertical, in the direction of the 0-degree azimuth. The smoke puff launchers were intended to be fired just before charge initiation to create near vertical smoke trails. Subsequent motion of the smoke trail was to be recorded using high-speed motion picture photography to provide accurate, time-resolved flow velocities at several heights above the ground surface, and to define the shape of the shock front. The smoke puff launcher locations are shown in Figure 21 and listed in Table 7.

2.4.3 Blast Cubes

A total of 136 blast cubes (Ethridge, et al, 1989) were used for the Shallow Underground Tunnel/Chamber Explosion Test to estimate total pressure impulse levels of the airblast exiting the tunnel portal. Cubes were placed in the access tunnel, and on arcs at 5, 10, 70, and 75 m from the tunnel portal. Four steel cubes (152 mm) were placed in the access tunnel, one each on either side of center near the wall at 2 and 12 m from the portal. Steel cubes were also placed along the 5 and 10-m arcs at azimuths ranging from 320 to 50 degrees, and 335 to 35 degrees, respectively.

One hundred and nine blast cubes were placed along the 75-m arc at azimuths ranging from 355.7 to 61.85 degrees. Because of the large uncertainties in the predicted airblast environment, several different materials were used for the cubes, providing a range of area-to-mass ratios. Three types of wood (152-mm) cubes were used; oak (29), poplar (29), and balsa wood (29). Twenty aluminum (51-mm) and two steel (152-mm) cubes were also used along the 75-m arc. Mean cube masses were 0.613 kg (balsa wood), 1.896 kg (poplar), 2.561 kg (oak), 0.351 kg (aluminum), and 27.7 kg (steel). The blast cube locations are shown in Figure 22, and listed in Table 8. Blast cube placement, recovery, and data interpretation were performed by Aberdeen Research Center.

Calibration tests were conducted at the test site to relate displacement to initial velocity for all cubes (except steel). The tests were made on a -3.5 degree slope, corresponding to the surface slope at the 75-m radius in front of the tunnel portal. The cubes were suspended approximately 60 mm above the ground in a quick release apparatus attached to a vehicle. Cubes were released as the vehicle, moving at constant velocity, rode over a switch. A second switch located a known distance away established the initial cube velocities. The results of the calibration tests were used to estimate dynamic pressure and impulse levels from measured cube displacements, assuming that the total impulse imparted to the cubes was due to the dynamic pressure of the blast wave.

2.5 EJECTA AND ARTIFICIAL DEBRIS

2.5.1 Ejecta Measurements

The objectives of the ejecta portion of the test program were to measure and characterize the ejecta and debris produced by the chamber charge detonation. Two different sources of ejecta and debris are of interest; debris blown out the tunnel entrance by the escaping blast pressures, and ejecta resulting from breakup of the overburden (chamber and tunnel cover). The former consists of undetonated munitions, casing fragments (not present in this test), and rock or concrete debris from the tunnel walls, while the latter includes rock fragments from the chamber and tunnel cover material and artificial ejecta placed upon the

cover.

An array of 27 collection pads was established posttest to permit representative sampling of debris thrown out through the access tunnel by the 20,000-kg detonation. These collection pads covered a sector extending 10 degrees either side of the extended tunnel/chamber centerline. An additional ten collection pads were established on the site access road (five each side of the projected tunnel/chamber centerline) to determine ejecta/debris distribution as a function of azimuth. Two pads were located at 300 m from the center of the explosive chamber, along radials 45 degrees to each side of the extended tunnel/chamber centerline, to assess the distribution of the overburden breakup. Large pieces of rock and concrete which did not fall within the collection area were individually recorded and categorized. Ejecta/debris collection pad locations are shown in Figure 23 and listed in Table 9.

2.5.2 Artificial Debris

Artificial debris missiles were placed on top of the chamber overburden for the 20,000-kg detonation to provide coded "tracers" of the source and impact locations of the rock debris from the cover breakup. These missiles were constructed of aluminum stock, and were 152 mm in diameter by 152 mm long. Alternating black and yellow bands were painted on the missiles and cloth streamers were attached to aid in their recovery after the tests. The aluminum missiles were placed above the tunnel/chamber centerline at pretest locations shown in Figure 24. Additional aluminum cylinders, 102 mm in diameter by 102 mm long, were placed on the surface above the chamber along a line perpendicular to the vertical plane of the chamber/tunnel centerline. These missiles were located 5, 10 and 15 m from the plane of the centerline. All missiles were marked to identify pre-detonation positions.

Six 15-cm steel blast cubes (borrowed from the blast cube study) were placed on the overburden at locations lying 15 m either side of the tunnel/chamber centerline, two were placed even with the tunnel/chamber interface, two were even with the center of the chamber, and two were

even with the rear of the chamber. Six selected rock blocks painted, numbered, and wrapped with yellow duct tape were placed behind (uphill from) the steel cubes. Cube and rock block location data are given in Table 10.

Inert 155-mm artillery rounds were placed inside the explosive storage chamber and in the access tunnel to simulate unexploded munitions. Four inert 155-mm rounds were placed in a standing position behind the explosive charge. Sixteen inert rounds (eight lying and eight standing) were placed in the chamber in front of the charge. Pairs of rounds were also placed along the wall opposite three pressure gage locations in the access tunnel. The inert artillery round locations are shown in Figure 25.

2.6 DOCUMENTARY PHOTOGRAPHY

Motion picture cameras were positioned around the test area to record blast effects, including the smoke puff trails, fire ball and cloud development, initial overburden rise, and ejecta/debris movement (trajectories and velocities). Photo poles and targets provided reference points for determining spacial relations within the field of view. Photo poles are wood posts painted with alternating, 30-cm long, white and black bands. Photo targets are 1.2-m square plywood sheets, attached to posts for support. The surface area of each target was divided into quarters, painted alternately white or black. Camera and photo pole/target locations are shown in Figure 26.

SECTION 3

INSTRUMENTATION--RESULTS AND DISCUSSION

3.1 INSTRUMENT PERFORMANCE

A total of 91 transducers were installed (79 by WES and 12 by BSI) to define the airblast and ground motion effects from the Shallow Underground Tunnel/Chamber Explosion Test. Eighty-four instruments were operational at shot time. Six free-field airblast pressure sensors (WES) and one accelerometer (WES) failed preshot, due to an electrical storm during the night before shot day. Of the 72 channels recorded from this event, 3 accelerometers (WES) produced very noisy records with no discernable data. The upper bound predictions for these gages were just above the minimum gage capabilities, and the recorded data fell well below this level. One gage (WES G.14V) failed during the test, and two chamber airblast gages failed upon shock arrival, producing no useful data. The active instrumentation results (transducer time histories and peak data) are reported in "KLOTZ Underground Magazine Trial, Data Report" (Halsey, et al, 1989).

3.2 ARRIVAL TIME

Shock arrival time and peak pressure data for gages in the chamber and tunnel are given in Table 11. Three distinct peaks (an initial peak and two reflections) are discernable before cable and/or transducer failure. The TID airblast recorder package at station C.13 shut off when the recorder memory filled, and consequently did not record the third peak. The TID package at Station C.14 captured the first peak of the airblast at the portal, but failed a few milliseconds later due to penetration of the metal case by the detonation gas flow.

Airblast shock wave arrival time in and just outside the access tunnel is plotted versus distance from the tunnel portal in Figure 27. The data indicates a nearly uniform shock wave velocity in the access tunnel of 2,400 m/sec. The calculated shock velocity at Gage A.2 (Table 12), 5 m outside the tunnel, is 1,770 m/s. This value was calculated using the measured stagnation pressure, and the assumed

ambient air temperature and pressure. First, the Mach number was calculated from the relation (Kinney, 1985):

$$P_0/P = [1 + (M / 5)]^{7/2} \quad (5)$$

where P_0 is the stagnation pressure, kPa

P is the ambient pressure, kPa

and M is the Mach number

Atmospheric pressure and temperature data were not recorded at the site but were obtained from Rawindsonde recordings made within an hour of the test on the NWC range near Range Tower 8, at an elevation of 665.4 m msl. Assuming similar conditions at comparable elevations, the atmospheric pressure and temperature at 1,101.9 m (tunnel elevation) msl were 895.64 mb and 28 degrees C, respectively. Solving Equation 5 for Mach number we get

$$M = 5.087$$

The Mach number is the ratio of the shock velocity to the speed of sound in the ambient air:

$$M = u / a \quad (6)$$

where u is the shock wave velocity, m/s

and a is ambient sound velocity in air, m/s.

Ambient sound speed can be calculated from the relation:

$$a = (k R T)^{1/2} \quad (7)$$

where a is the ambient sound speed, m/s

k is the ratio of heat capacities (1.4 for air)

R is the gas constant per-unit-mass

and T is absolute temperature, °K

Solving Equation 7 for ambient sound speed, we get

$$a = 347.8 \text{ m/s.}$$

Solving Equation 6 for shock wave velocity yields

$$u = 1,770 \text{ m/s.}$$

A graph of free-field airblast arrival time versus distance from the tunnel portal (Table 12) along the extended tunnel/chamber centerline is shown in Figure 28. The far-field shock velocity (300 to 600-m radial distance) is 357.1 m/s, or approximately 10 m/s faster than the ambient acoustic velocity calculated from Equation 7, which indicates that the assumed (from Range Tower 8) ambient temperature was low. Substituting the shock wave velocity into Equation 7 and solving for the Celsius temperature, we get 44.6 degrees C for the ambient temperature at the site, which is 16.5 degrees C warmer than the temperature assumed from the Range Tower 8 data.

Shock front arrival time at all the free-field airblast gages (Table 12) is plotted versus horizontal distance from the tunnel portal in Figure 29. The slope of the time/distance plot approaches a constant velocity at radial distances greater than 300 m. The data scatter can be attributed to elevation differences not considered when plotting horizontal distances, and local conditions around the gage (vegetation and surface irregularities). Elevation effects are particularly evident along the 180-degree measurement line, where the slant distances were much greater than the horizontal distances (especially close to the portal) due to the surface slope.

Free-field ground shock arrival time at the near-surface ground motion gages (Table 13) is plotted versus horizontal distance from the center of the chamber in Figure 30. The curve fit to the long-range airblast arrival data from Figure 29 (referenced to the center of the chamber) is included for comparison. The arrival time data for the ground motion gages indicate a constant shock velocity (2,166 m/s) out to 400 m from the center of the chamber. This value exceeds the seismic velocities reported for the tunnel/chamber site, which ranged from 944 to

1,626 m/s (Halsey, et al, 1989).

3.3 AIRBLAST MEASUREMENTS

3.3.1 Tunnel/Chamber Airblast Measurements

The peak side-on overpressures measured in the chamber and tunnel are listed in Table 11 and plotted versus distance (from the initiation end of the explosive charge) in Figure 31. These data include two anomalous values--Gages A.13 (TID self-recording gage) and C.11. The remaining data indicate a consistent trend of decreasing pressure with distance along the tunnel. The equation of the least squares fit to the remaining peak pressures in the access tunnel is shown in Figure 31. The correlation coefficient of this data fit is -0.9951 (a high degree of correlation), with a 0.08815 standard error of estimate. The peak side-on overpressure at the tunnel portal computed from this relation is 5.2 MPa. Gage C.14 (TID self-recording gage), located 0.3 m outside the tunnel portal, recorded an initial peak of 5.3 MPa before gage failure, which is very close to the exit pressure indicated by the least squares fit to the tunnel data. The 5.2 MPa exit pressure was used as an input parameter for later free-field overpressure calculations.

Stagnation pressure is related to the ambient pressure and the shock front's Mach number by Equation 5 (Kinney, et al, 1985), given in Section 3.2. The Mach number, as computed from Equation 6 using the acoustic velocity calculated from the Range Tower 8 weather data ($a = 347.7$ m/s) and the shock wave velocity from Figure 27 ($u = 2400$ m/s), was

$$M = 6.90$$

The ambient pressure and temperature at the portal were assumed to be equal to those measured at Range Tower 8, which were 89.54 kPa and 28 degrees C, respectively. Substituting these values into Equation 5, the stagnation pressure in the access tunnel was computed to be

$$P_o = 338.3 \text{ Mpa}$$

Since the data indicated that the shock wave velocity in the access tunnel was constant (Figure 27), the stagnation pressure was also constant. In other words, the blast pressure jet moved at a constant velocity through the access tunnel, with a uniform stagnation or total pressure.

3.3.2 Free-Field Airblast Measurements

Free-field airblast pressure data are presented in Table 12 (airblast pressure gages) and Table 14 (sound pressure level meters). A comparison of the predicted and measured peak overpressures along the extended tunnel/chamber centerline (0-degree azimuth) is presented in Figure 32.

The measured peak free-field overpressures (Table 12) are plotted against normalized radial distance (R/D) from the tunnel portal in Figure 33. The peak sound pressure (Table 14) measured six miles away at the Coso Rest Area is included in this figure. The range (R) is normalized by the equivalent circular diameter (D) of the tunnel, which is the diameter of a circle having an area equivalent to that of the tunnel cross-section.

These data are compared with airblast prediction curves computed using the Skjeltorp, Hegdahl, and Jenssen (1975) empirical relation (Equation 3, Section 2.3.2.1), which predicts external airblast peak pressure as a function of the tunnel exit pressure. The two curves are based on different exit pressures; one derived from the least squares fit of the access tunnel peak overpressure data (Figure 31), and the other computed from the equation shown at the top of Figure 33 (Helseth, 1985). As shown in Figure 33, these curves bound all data except for two points. The upper curve, derived from the computed exit pressure (Helseth, 1985), gives better results from a safety point of view in that it provides a conservative estimate of the measured data. Similar comparisons between measured data (Tables 12 and 15) and predicted peak pressures for the 30, 45, 60, 90 and 180-degree azimuths are given in Figures 34 - 38, respectively. As seen in Figures 33 - 38, conservative agreement exists between the measured data and the prediction curves developed using

Equation 3 with the experimentally determined exit pressure.

The effect of azimuth on peak external overpressure is shown in Figure 39. Data from Tables 12 (WES) and 13 (BSI) are presented in this figure. The overpressure at 50 m on the extended tunnel/chamber centerline (Figure 33) was approximately 50 kPa. To determine the off-axis overpressure according to equation 3, the centerline (0-degree azimuth) overpressure is divided by an azimuth function, A_f , which is the denominator of the right hand side of Equation 3:

$$A_f = [1 + (\theta / 56)^2] \quad (8)$$

where θ is the angle (degrees) from the tunnel centerline axis. As seen in Figure 39, dividing the centerline overpressure by the azimuth function gives a reasonably good approximation of the off-axis peak overpressures as measured on this test.

The peak impulse values (Table 12) recorded along the extended tunnel/chamber centerline (0-degree azimuth) are presented in Figure 40. These peak data are plotted versus the distance from the gage to the center of the charge, so that a comparison can be made to the Naval Ordnance Laboratory's (NOL) curve for airblast from spherical, surface-burst charges (Swizdak, 1975). As shown here, the data closely match the NOL curve, except for the gage station closest to the tunnel exit, where the airblast jetting effect from the tunnel is expected to be greatest.

The effect of azimuth on peak impulse is shown in Figure 41. Data from Tables 12 (WES) and 14 (BSI) are shown in this figure. The estimated impulse at 140.1 m (100 m from the tunnel portal) on the 0-degree azimuth (Figure 40) is 1.5 kPa-sec. Dividing this impulse value by the azimuth function (Equation 8), gives the $R = 100$ m curve (Skjeltorp, Hegdahl and Jenssen (1975)) shown in Figure 41. As seen in Figure 41, this relation provides a good approximation of the effect of azimuth on peak impulse.

Peak stagnation pressure (Tables 12 and 15) is plotted versus distance from the tunnel portal in Figure 42. Stagnation pressure is the

sum of the side-on and dynamic pressures. Stagnation pressures inside the tunnel (negative distances from the portal) were calculated from the shock arrival times recorded by the airblast gages in the tunnel. The 0-degree gage at 5 m outside the tunnel was located in a probe-type mount 75 cm above the surface of the ground.

BSI pressure measurement stations were located at the 15, 30 and 60-degree azimuths along an arc 75 m from the portal. Gages at these stations recorded side-on pressure, stagnation pressure, dynamic pressure, and overdensity (Table 14). The BSI pitot tube stagnation pressure data from gages at the 75-m radius are also given in Figure 42. Compared to the calculated stagnation pressure in the tunnel and the value measured at 5 m, these data indicate that exterior stagnation pressures drop rapidly with distance from the tunnel portal. The relation of peak stagnation, side-on, and dynamic pressures are shown in Figure 43. A similar graph of peak impulse is presented in Figure 44.

Peak overdensity is plotted versus azimuth on the 75-m radius in Figure 45. Overdensity is the increase in air density above the ambient at the gage location during passage of the shock wave. The air density ratio (ρ_2 / ρ_1) versus the overpressure ratio (P_2 / P_1) along the 75-m radius is presented in Figure 46. Subscripts 1 and 2 denote the ambient values and peak shock values of density and pressure, respectively. The calculated ambient air density was 1.037 kg/m³. The ambient pressure was 89.5 kPa, as extrapolated from Range Tower 8 weather data. The equation of the dashed line drawn through the data in Figure 46 is

$$(\rho_2 / \rho_1) = (P_2 / P_1)^{1/1.4} \quad (9)$$

This is the density ratio equation for isentropic compression or expansion of an ideal gas (Kinney, et al, 1985).

3.4 PASSIVE BLAST MEASUREMENTS

Passive diagnostic devices provide an inexpensive method of augmenting active measurement systems for evaluating blast wave symmetry, jetting, and other effects. Passive measurements for the Shallow

Underground Tunnel/Chamber Explosion Test included blast cubes (steel, aluminum, and wood), wire drag gages, and smoke puffs.

3.4.1 Blast Cubes

The primary blast cube installation was along the 75-m arc. Blast cube measurements and calculated data for the 75-m arc are presented in Table 16 (Ethridge, et al, 1989). The pre- and posttest cube positions were surveyed and the data were used to calculate the total displacement of the cubes by the blast wave, and the deviation angles (the difference between the azimuths to the posttest position and the pretest location). The relation between a cube's initial velocity and the distance it travels (displacement) was determined by a set of calibration tests (see Section 2.4.3). From the cube displacement distances measured after the detonation, the initial velocity of each cube (induced by the blast wave) was calculated using an equation developed from a least squares fit to the calibration data. These velocities are given in Table 16. The dynamic impulse values shown in Table 16 were calculated using the relation (from Ethridge, et al, 1989):

$$I = m v_o / C_D A \quad (10)$$

where m is the mass of the cube, kg

v_o is the calculated initial cube velocity, m/s

C_D is the drag coefficient, assumed to be 1.2

and A is the cube's front surface area, m^2 .

Figure 47 is a plot of total cube displacement versus azimuth along the 75-m arc. The total displacements of cubes of different materials and sizes are in proportion to the area-to-mass ratios (AMR) of the cubes. Therefore, the balsa wood cubes, with the largest AMR (5 times that of the aluminum cubes) were displaced the greatest distance. The AMR for the poplar and oak cubes were 1.9 and 1.2, respectively, times that of the aluminum cubes, and the wood cubes moved correspondingly greater distances. As shown in Figure 47, much greater displacements were found within 15 degrees of the extended tunnel/chamber centerline, indicating the presence of airblast jetting within this region.

The equivalent value of dynamic impulse calculated for each cube location is given in Table 16 and plotted versus azimuth in Figure 48. These data are derived from the total cube displacements, with corrections for the cube AMR's. As shown here, equivalent dynamic impulse is inversely related to the cube AMR. Values of dynamic impulse obtained by integration of the BSI (Edgar, 1988) stagnation pressure-time histories are included in Figure 48 for comparison. As shown here, the dynamic impulse values obtained from integrations of the gage records compare well with the balsa cube data.

Total displacements of the steel cubes (Tables 17, 18 and 19) are plotted versus azimuth in Figure 49. The cubes in the tunnel and on the 5 and 10-m arcs were displaced by the airblast beyond the level ground immediately outside the portal, and most became airborne. Therefore, it is not possible to infer values of impulse from the displacements of these steel cubes. However, they do show that a solid object can be thrown up to 2,400 m from an original position within the access tunnel, about 1,700 m from a position along the 5-m arc (measured from the portal), 200 m from the 10-m arc, and a metre or less from the 75-m arc.

Inferred values of dynamic pressure impulse along the extended tunnel/chamber centerline are shown in Figure 50. The dynamic impulse inside the access tunnel was calculated using Equation 10, and the shock front velocity taken from Figure 27 (2,400 ms). This calculation yields an upper bound for the dynamic impulse in the access tunnel. The measured data was obtained by integrating the WES stagnation pressure-time history at the 5-m station. The blast cube data point was derived from the dynamic impulse calculations (shown in Figure 48) for the balsa cube at the 75-m range. The terrain elevation drops approximately 9 m between the 10 and 75-m stations, thus reducing the dynamic impulse by some unknown amount. The inferred data shown in Figure 50 provide the best estimate to date of dynamic impulse in the jet flow exiting the tunnel from an accidental detonation in an ammunition storage chamber.

3.4.2 Wire Drag Gages

The breaching failure of the chamber overburden by the detonation

produced a large quantity of debris, which damaged a majority of the wire drag gages. Only four wire drag gages produced information about flow symmetry which is believed to be valid (Dewey, et al, 1989). These gages (Nos. 3, 8, 9, and 11) indicate a generally non-symmetric flow pattern to the right (as seen from the tunnel portal), with deflection angles ranging from 2 to 18 degrees. Gage No. 11 (0-degree azimuth, 75-m arc) indicates that the mean flow is 15 degrees to the right, at this location. Flow directions at each gage location are depicted in Figure 51 and mean values are listed in Table 20.

A sufficient number of undamaged wires were found on Gages 3 and 9 to permit a valid determination of bending angle (Dewey, et al, 1989). These gages showed bending angles of 44 and 60 degrees, respectively. The distances from a 20-ton surface burst at which the airblast impulse will bend a 1-mm diameter solder wire to these angles are 132 m and 125 m, respectively. Since 3-mm solder wire was used in the wire drag gages employed on this experiment, laboratory tests were conducted to develop an adjustment factor for the effect of wire diameter. The tests showed that approximately 24 times as much force was required to produce a specific bending angle in 3-mm solder as in 1-mm wire. Since the cross-sectional area of the 3-mm wire is 3 times greater, the drag force is approximately 8 times greater than that needed to produce the same angle of bending in the 1-mm wire. The equivalent explosive charge weight that produces a measured angle of bend at the range of the measurement can be determined from the equation (Dewey, et al, 1989):

$$M_e = 20 [D_e / D_{20}]^{1/0.37} \quad (11)$$

where M_e is the equivalent surface burst charge mass (in metric tons) which produces the measured wire bend angle at the wire drag gage distance,

D_e is the distance of a wire drag gage (in metres) from the explosion source in question,

and D_{20} is the distance (in metres) from a 20-ton surface burst at which the airblast will produce the same angle of bending.

Wire drag Gage 3, located on the 60-degree azimuth at a range of 75 m from the tunnel portal, sustained a residual bending angle of 44 degrees. This bending angle would be produced in a 1-mm wire gage at a range of 132 m from a 20-ton TNT surface burst. Using Equation 11, the same bending angle would have been predicted at 75 m from a 4.34-ton charge.

The dynamic airblast impulse at 75-m from a 4.34-ton charge is 0.100 kPa-sec. Correcting for wire diameter gives a dynamic impulse of 0.800 kPa-sec, which would occur at a range of 75 m from a 25-ton surface burst. Similarly, the Gage 9 wire experienced 60-degree bending, which would occur at a range of 125 m from a 20-ton surface burst. Gage 9 was 100 m from the tunnel portal. The calculated equivalent charge (to produce the same bending) is 56 tons, with a predicted dynamic impulse of 1.144 kPa-sec. Wire drag gage locations, bend angles and inferred data for the tunnel/chamber test are presented in Table 20.

The dynamic pressure/impulse levels inferred from the wire drag gage data are plotted in Figure 52. These data are compared with the impulse and integrated total pressure-time histories inferred from the blast cube data. As shown in Figure 52, both methods of inferring dynamic pressure/impulse from wire drag gage data produce results that are approximately an order of magnitude higher than other data. Dewey, et al, (1989) recommends using these data qualitatively; i.e., a general comparison of wire drag gage data can be used as an indicator of trends and patterns of blast phenomena.

3.4.3 Smoke Puffs

A severe rainstorm during the night before the tunnel/chamber test damaged several of the launchers for the smoke puff system. As a result, only two launchers functioned when initiated. The smoke trails from launchers at ranges of 15 m (Trail 1) and 90 m (Trail 2) from the tunnel portal were successfully photographed. Smoke trail positions are shown as a function of time after detonation, in Figure 53 (Dewey, et al, 1989). These traces comprise the principal results of the smoke puff experiment.

Figure 54 shows smoke trail profiles recorded from the launcher located 15 m from the portal. Note that the trail's position between -5 and 10 degrees plot almost on top of each other, indicating a near-constant velocity from the airblast shock front, suggesting flow similar to that produced by a shock tube (Dewey, et al, 1989). Figure 55 shows similar data for the smoke trail at the 90-m range. The shock front arrival time at the initial position of Trail 1 (at 15 m) and Trail 2 (at 90 m) are clearly shown in Figures 54 and 55. Shock wave arrival times were 12.9 msec at 15 m and 133 msec at 90 m.

Flow velocities computed from the traced particle trajectories of Smoke Trail 1 are plotted versus time in Lagrangian coordinates in Figure 56. As shown here, flow velocities are near constant for the 0-degree and lower radials, and decrease drastically below the a height of 5 m. This is dramatically shown in Figure 57, where initial flow velocities are plotted versus height above the ground surface. The peak flow velocities range from 1.5 m/s on the 0-degree radial to 0.15 m/s on the 45-degree radial. Neglecting real gas effects, these peak velocities correspond to peak overpressures of 3.05 MPa and 70 kPa (Dewey, et al, 1989), respectively.

Dewey, et al, (1989) used the measured particle trajectory of Smoke Trail 1 to define the path of a hypothetical piston. A hydrodynamic computer code was used to calculate the flow ahead of this piston, which was assumed to be the same as the actual air flow produced by the test. The resulting reconstructed blast wave is shown in Figure 58. The data recorded by WES and blast waves calculated by S-Cubed, Inc. (Kennedy, et al, 1989) are included for comparison. As shown in Figure 58, the smoke puff-calculated blast wave is in good agreement with the S-Cubed results. The WES data shows a constant time offset of approximately 15 msec. The reason for this discrepancy is not known but is probably related to the way zero time was determined. The WES zero time was taken from a relay closed by the NWC firing pulse. Therefore, a relay closure time of 4.9 msec was subtracted from the WES recorded time-histories to account for relay closure time.

An overpressure time-history was computed from the smoke puff shock

calculations for the 75-m radial (Figure 59). Smoke Trail 1 was overtaken by the fireball at 55 msec, limiting the trajectory of the piston in the calculation. As shown in Figure 59, the calculated time-history is slightly lower than the measured data.

3.5 AIRBLAST CALCULATIONS WITH HYDRODYNAMIC COMPUTER MODELS

Two calculations of airblast propagation in the Shallow Underground Tunnel/Chamber Explosion Test were performed by S-CUBED, Inc., using the SHARC hydrocode. The first calculation assumed the chamber and tunnel surfaces to be perfect reflecting boundaries; thus, the calculation was for a "non-responding" model, in which the overburden was not allowed to rupture or displace. In the second calculation, the granitic rock surrounding the chamber and tunnel was replaced by a loose sand, using a Tillotson Sand material model to define the material properties. Since this model allowed venting and rupture to occur, it represented a "responding" chamber model. These airblast calculations were expected to provide upper and lower bounds of the actual internal pressures (Kennedy, et al, 1989). The calculations were not extended to the point that the airblast front passed outside the tunnel portal.

Comparisons of the calculated and measured overpressure-time histories (Kennedy, et al, 1989) are presented in Figures 60 and 61. As shown in these figures, the non-responding model produced calculated peak overpressures four times greater than the measured peak data. According to Kennedy, et al, (1989), the response of the chamber walls has a significant effect on the exit pressure and the overpressure-time history at the portal. Significant improvement in both the waveform and exit pressure predictions could probably be obtained by selection of a material model for the calculation which better represents jointed and fractured granite.

3.6 GROUND MOTION MEASUREMENTS

A plot of direct-induced peak vertical particle velocity versus slant distance is presented in Figure 62. A comparison is shown between the measured data and two curves; one a relation developed by Vretblad (1988) for decoupled detonations in competent granite, and the other an

empirical equation given in Table 7-III of NATO AC/258 publication "Manual on NATO Principles for the Storage of Ammunition and Explosives, Part III". The relation developed by Vretblad consists of three equations,

$$v = 12.7 (R / Q^{1/3})^{-1.17} \quad (12)$$

$$v_d = D v \quad (13)$$

and $D = 0.024 (Q / V_c)^{0.51} \quad (14)$

where v is peak particle velocity from a fully-coupled charge, m/s

R is distance from the detonation to the point of interest, m

Q is charge weight, kg

v_d is the peak particle velocity from a decoupled charge, m/s

D is the coupling factor

and V_c is the chamber volume, m^3

The NATO AC/258 empirical equation for direct-induced vertical (v_v) and horizontal (v_h) peak particle velocity is

$$v_v = v_h = 0.95 (R / Q^{1/3})^{-1.5} \quad (15)$$

The close-in gage on the 180-degree radial was located on the overburden directly above the center of the storage chamber. Thus, this gage measured the peak overburden spall velocity. The close-in gage on the 0-degree radial was located 9 m (horizontal distance) downslope on the overburden directly above the tunnel/chamber interface. Although the overburden containing this gage also spalled, the trajectory was more horizontal. The Vretblad (1988) curve provides a reasonably good upper bound to the measured data.

Peak, direct-induced, horizontal particle velocity is plotted versus slant distance in Figure 63. A comparison is shown to the Vretblad (1988) and NATO AC/258 (1977) curves discussed in the previous paragraph. Here again, the Vretblad curve provides a reasonably good

upper bound to the data.

Peak, airblast-induced, vertical particle velocity data are plotted versus slant distance in Figure 64. Comparison is made between the measured peak data and the NATO AC/258 empirical equation

$$v_v = P_o / (\rho c_p) \quad (16)$$

where v_v is the airblast-induced vertical particle velocity, m/s

P_o is the peak overpressure, Pa

ρ is the earth material density, kg/m³

and c_p is the earth material compressional wave velocity, m/s.

Two curves are shown; one for soil and one for rock. Generic values of density and compressional wave velocity used for soil and rock were taken from the NATO AC/258 manual (densities equal to 1,520 and 2,560 kg/m³ and compressional wave velocities equal to 460 and 4,000 m/s for soil and rock, respectively). Although the particle velocity data shown in Figure 64 are limited, motions along the 90-degree azimuth tend to fall below the NATO soil curve, while the peak particle velocity at the 400-m range along the 0 and 180-degree azimuths plot above the soil curve. The gages along the 180-degree azimuth were attached to the rock surface upslope from the tunnel portal. The peak velocity at the 400-m range along this azimuth is an order of magnitude greater than indicated by the NATO curve for rock.

Hadala (1973), in a study of outrunning ground motion, determined that peak airblast-induced particle velocities are a function of the material's stress wave velocity, rather than the compressional wave velocity. He proposed a one-dimensional relation of the form given in Equation 16, substituting stress wave velocity (c_L) for the compressional wave velocity (c_p). A typical stress wave velocity for desert alluvium (Nevada Test Site soils) is 146 m/sec. Using this value for the stress wave velocity, the peak vertical particle velocity curves were calculated for soil ($\rho = 1,520$ kg/m³). As shown in Figure 65, the curves tend to provide an upper bound to the measured data. An exception is the velocity measured at the 400-m station on the 180 degree azimuth, which

is a factor of four greater than the airblast predicted motion. This may be due to the fact that the properties of the weathered rock at the tunnel/chamber site differ drastically from the assumed "typical" values for rock.

Peak, airblast-induced, horizontal particle velocity data are plotted versus slant distance in Figure 66. The NATO AC/258 curves for soil (based on the peak airblast overpressure data along the 0 and 90-degree azimuths) are shown for comparison. The horizontal motions were computed from the relation

$$v_h = v_v \tan [\sin^{-1} (c_p / U)] \quad (17)$$

where U is the airblast shock front velocity, m/s. As shown in Figure 66, the NATO curves for soil provide a reasonable upper bound to the peak horizontal airblast-induced particle velocity data. The velocities of horizontal motions in a horizontally-layered system are normally independent of the layers.

SECTION 4

CRATER AND EJECTA/ARTIFICIAL DEBRIS--RESULTS AND DISCUSSION

4.1 CRATER

The apparent crater formed by the Shallow Underground Tunnel/Chamber Explosion Test was oval-shaped in plan, with the long dimension along the tunnel/chamber centerline. The apparent crater was 57.9 m long (parallel to the overburden slope), 36.6 m wide (perpendicular to the original tunnel/chamber centerline), and 7.8 m deep. The scaled apparent crater dimensions are compared to a band of prediction curves for craters in rock in Figure 67. The referenced crater data (Davis, et al, 1981) are from fully-coupled detonations (with both stemmed and unstemmed emplacement holes), while the Shallow Underground Tunnel/Chamber Explosion Test was a decoupled explosion. As shown in Figure 57, the measured crater parameters plot within the expected limits for rock.

4.2 EJECTA

Two types of ejecta data were collected from the Shallow Underground Tunnel/Chamber Explosion Test--material deposited inside prescribed sample areas (ejecta collector pads), and large, discrete pieces found outside these established collection areas (large fragments). The locations of the ejecta collection pads are shown in Figure 23 and listed in Table 9. The raw ejecta data are published in "KLOTZ Underground Magazine Trial, Data Report" (Halsey, et al, 1989).

In Figure 68, the number of ejecta impacts per 56 m² are plotted versus distance from the tunnel portal. One impact per 56 m² is the current safety criterion for ejecta quantity-distance (Q-D). The data are grouped according to azimuth (from the tunnel centerline) and range from the portal. Ejecta collection pads centered on the 0, 5, and 355-degree azimuths are combined and plotted as the +/- 5-degree sector. Similarly, the pads located on the 10 and 350-degree azimuths are combined in the +/- 10-degree sector.

To describe the locations of the discrete large fragments, the sectors were subdivided at distances of 50, 100, 250, 500, 1,000, 1,250, 1,500, 1,750, 2,000, 2,250 and 2,500 m. Impact data points are plotted at the mid-distance of each sector subdivision. As shown in Figure 68, the number of impacts (and hence the impact probability) decreases with both distance and azimuth (from the tunnel centerline).

The large fragment data are plotted versus distance from the tunnel portal in Figure 69. Although these data exhibit considerable scatter, there is an indication that the greatest ejection distances for large fragments occurred close to the extended tunnel/chamber centerline. While large fragments represent a hazard, the numbers of large fragments in a given area are well below the Q-D criteria of one per 56 m². The ejecta pad and large fragment data are combined in Figure 70 to show the total number of impacts per 56 m².

The combined ejecta and large fragment data are presented in Figure 71, where number of strikes and areal density are displayed on the right and left ordinates, respectively. A dashed horizontal line indicates the Q-D safety criterion for ejecta (one strike per 56 m²), which occurs at a range of 656 m. The areal density at this range is 0.053 kg/m².

In Figure 72, the Shallow Underground Tunnel/Chamber Explosion Test data is compared to previous data from large-yield surface detonations. As shown here, the scaled distance to the Q-D hazard criterion (one strike per 56 m²) is approximately four times greater for previous, surface-burst explosive tests than for the buried, decoupled detonation of the tunnel/chamber test.

4.3 INERT ARTILLERY ROUNDS

Inert 155-mm artillery rounds were placed in the explosives chamber and access tunnel at the locations shown in Figure 25. Figure 73 shows the angular sectors within which the 155-mm rounds came to rest after being ejected from the tunnel. Symbols identify pre-test round locations as (1) back of chamber (behind explosive charge), (2) front of chamber (in front of explosive charge), (3) unlined tunnel (rear portion of

access tunnel closest to chamber), and (4) lined tunnel (front 10 m of access tunnel). None of the rounds placed behind the explosive charge were found posttest. The rounds initially placed in the access tunnel were thrown over a kilometer from the portal by the blast. This pretest placement represents an unrealistic condition, however, since munitions are not ordinarily stored in the access tunnel. Considering only the rounds originating from the chamber, the maximum range traveled is 1.0 km. This distance is well beyond the measured range for one impact per 56 m².

4.4 ARTIFICIAL MISSILES

The pre- and posttest locations of the artificial missiles are given in "KLOTZ Underground Magazine Trial, Data Report," (Halsey, et al, 1989). The ejection ranges of the artificial missiles are plotted versus their pretest locations in Figure 74. In this figure, "slant distance" is the distance from the center of the 20,000 kg Comp B charge to the missile pre- and posttest position, as calculated from surface coordinates and elevation data. Symbols identify the missile pretest locations with respect to the surface ground zero (SGZ), a point on the overburden directly above the center of the explosive charge. FRONT denotes pretest missile locations down-slope from the SGZ. As shown in Figure 74, artificial missiles from pretest locations down-slope from the SGZ (FRONT) moved the greatest distance and those up-slope (BACK) the least. All missiles were found down-slope from their original positions. The differences in displacement of missiles on the east side compared to those on the west side of the magazine are attributed to slope effects. The surface elevation dropped gradually to the east and rapidly to the west.

Launch velocities were computed for three artificial missiles-- 6"-5, 6"-7 and 6"-8 (Table 10)--using the known missile displacement and assuming a launch angle of 45 degrees. The calculated launch velocities are plotted in Figure 75, where a comparison is shown with data presented by Helseth (1982). Helseth's data are from previous tests, and include data from storage wall debris tests, aircraft shelter detonations, and large-scale buried detonations, both tamped and untamped. The artificial

missile launch data from the tunnel/chamber test are in good agreement with the other data shown in Figure 75.

4.5 PHOTO INTERPRETATION

Motion picture film from eight cameras was projected frame-by-frame for analysis of ejecta phenomena. Camera No. 1 provided data on ground rise and cloud formation, and Cameras 6-13 (excluding No. 9) provided information on ejecta parameters (trajectory angle, relative arrival time, velocity, and maximum dimension). Cameras 6-13 were 35-mm cameras equipped with 75-mm objective lenses, and were run at 120 frames per second. No provision was made for recording zero-time (time of initiation of the explosive charge) on any of the cameras, so all times are relative either to first visible light of the detonation fireball (Camera Station 1), or to arrival of the first ejecta particle in the camera's field of view. During the analysis, a single-frame advance projector was positioned a fixed distance from a white cardboard sheet, upon which the data was traced. Distances in the projected image were scaled from landmarks whose positions or separation distances were known, such as photo poles and photo target boards. The lens aperture used for this experiment provided a large depth of field, which made determination of the ejecta distance from the camera difficult. However, an attempt was made to include only those ejecta particles falling near the extended tunnel/chamber centerline.

The positions of the detonation shock front, ground surface rise, the fireball emerging from the tunnel portal, and the growth of the chamber venting/ejecta cloud at selected times were traced from a projection of the film from Camera No. 1. The resulting time plot is shown in Figure 76. Times are referenced to first light from the fireball, as reflected by objects just outside the access tunnel portal. As shown here, the detonation products emerge from the access tunnel long before significant movement of the overburden surface occurs over the chamber itself. The overburden above the chamber moves approximately 2.8 m in the first 150 ms after first light. Thus, the initial ground rise velocity is approximately 19 m/s. This value compares favorably with 19.4 m/s obtained by integrating the acceleration-time history at

Gage Station G.9V, which was located on the ground surface directly above the center of the chamber.

Tracings of ejecta missile paths recorded by Cameras 6, 7, 8, 10, 11, 12, and 13 are shown in Figures 77 through 83, respectively. Actual ejecta missile paths are displayed in vertical panels in each figure. Lines are used in other areas of the figure to show the ejecta trajectories through the camera field of view. Numeric labels give apparent impact velocities of the ejecta missiles, followed (in parentheses) by the relative time of arrival of the missile at the edge of the camera field of view. All times are referenced to arrival of the first ejecta missile observed by each camera, which was assigned an arrival time of 0 seconds. As a general trend, it was noted that the first-arriving ejecta missiles had low-angle impact trajectories, with the impact angle becoming progressively steeper for later-arriving missiles.

Ejecta impact velocity is plotted versus ballistic impact trajectory angle in Figures 84 through 90. These data are derived from the motion picture film analysis for Camera Stations 6, 7, 8, 10, 11, 12, and 13, respectively. The data indicate that a significant portion of the ejecta missiles have low-angle impact trajectories (nearly horizontal). Similar plots of ejecta impact velocity versus maximum missile dimension are presented in Figures 91 through 97.

A lethal ejecta missile fragment is defined in the DOD Ammunition and Explosives Safety Standards as one possessing kinetic energy greater than 79 Joules (58 ft-lb). Kinetic energy can be calculated using the following relation:

$$K.E. = 1/2 m v^2 = 79 \text{ Joules minimum (lethal fragment)} \quad (18)$$

where m is the mass of the fragment, kg
and v is it's terminal velocity, m/s.

Assuming that an ejecta missile can be approximated as a rectangular parallelepiped with a maximum dimension along one side being

4 times the other two sides, the minimum lethal fragment impact velocity can be calculated. Maximum missile dimensions and corresponding minimum lethal impact velocities (calculated using Equation 18) are tabulated in Table 21. A similar exercise can be performed using ejecta found on the collector pads. The smallest ejecta missile found on collector pads at the 600-m range had a mass of 0.156 kg. Solving Equation 18 for impact velocity using this fragment mass, we get a minimum impact velocity for a lethal fragment of 31.8 m/s. The largest missile found on the collector pads at 600 m had a mass of 3.9 kg, giving a minimum lethal impact velocity of 6.4 m/s. Thus, all the ejecta missiles seen in the film records and recovered on the collection pads were judged to be lethal hazards.

SECTION 5
HAZARD ANALYSES

5.1 CURRENT DEFINITIONS OF AIRBLAST HAZARD RANGE

5.1.1 Significance of Magazine Cover Depth

The distances required for protection of inhabited areas from airblast and debris depends, to a large degree, on the depth of overburden over the storage chamber. The chamber cover depth for the Shallow Underground Tunnel/Chamber Explosion Test ranged from 9.4 to 13.7 m. The minimum cover depth required to ensure containment of the explosion (except for gas venting through the access tunnel), and to ensure that no significant surface disruption occurs, is calculated in the current DOD Explosives Safety Standards (DOD 6055.9-STD) from

$$C_c = 1.4 Q^{1/3} \quad (19)$$

where C_c is the minimum overburden depth, m

and Q is the TNT equivalent explosive weight, kg.

For overburden depths less than this, the Standards require consideration of both airblast and debris hazard effects. When the actual overburden depth is less than

$$C_v = 0.2 Q^{1/3} \quad (20)$$

where C_v is the minimum overburden depth for airblast suppression, the Standards state that airblast at large distances may not be appreciably reduced from that of a surface burst. Values of C_c and C_v calculated for the explosive loading used in the Shallow Underground Tunnel/Chamber Explosion Test are 39 and 5.6 m, respectively. Thus, the actual chamber cover depth for this test falls between these limits, and the Standards require that airblast and debris projection must be considered in the Q-D hazard analysis.

5.1.2 Directional Variation of Airblast

If the depth of overburden C equals or exceeds the value of C_v calculated from Equation 20 above, the Standards require consideration of the effects of airblast issuing from the access tunnel. In the absence of data and analysis of far-field airblast propagation for the site being evaluated, the Standards divide the area outside the access tunnel into five sectors, as shown in Figure 98. The distance required for protection of inhabited areas against airblast is taken to be proportional to the cube root of a reduced net explosive quantity, Q_r , with Q_r being defined as:

$$Q_r = Q / n k \quad (21)$$

where Q is the TNT equivalent NEW, kg

n is a constant related to the number of entrances from the ground surface ($n = 1$ for this test)

and k is a constant associated with the storage chamber geometry

relative to the tunnel ($k = 1$ for the "shotgun magazine" design).

Thus, Q_r is equal to Q for the Shallow Underground Tunnel/Chamber Explosion Test experiment geometry.

The distances required for protection of inhabited areas against airblast pressure in the sectors defined in Figure 98 are calculated in the Standards as follows:

$$D_{11} = 7.6 Q_r^{1/3}, \quad 180 > \theta > 120 \text{ degrees} \quad (22)$$

$$D_{12} = 13 Q_r^{1/3}, \quad 120 > \theta > 90 \text{ degrees} \quad (23)$$

$$D_{13} = 20 Q_r^{1/3}, \quad 90 > \theta > 60 \text{ degrees} \quad (24)$$

$$D_{14} = 27 Q_r^{1/3}, \quad 60 > \theta > 30 \text{ degrees} \quad (25)$$

$$D_{15} = 30 Q_r^{1/3}, \quad 30 > \theta > 0 \text{ degrees} \quad (26)$$

where θ is the horizontal angle measured from the extended centerline of

the access tunnel.

5.2 COMPARISON OF AIRBLAST TEST RESULTS WITH CURRENT PREDICTION METHOD

5.2.1 Shallow Underground Tunnel/Chamber Test

The present Standards use two different airblast pressure criteria to define Inhabited Building Distances: 5 kPa (0.73 psi) for underground storage, and 6.2 kPa (0.9 psi) for open or other aboveground storage. For the 20,000 kg NEW detonated in the Shallow Underground Tunnel/Chamber Explosion Test, the distances to these two pressure contours as calculated by equations 22-26 (from the present Standards) are shown as dashed lines in plan view in Figure 99. For comparison, Figure 99 also shows the actual distances to the 5 and 6.2 kPa pressure contours that were defined by measured pressures on the Tunnel/Chamber Test. Since overpressures were not measured along the 120-degree radial on the test, the distance to the 5 and 6.2 kPa contours along the 120-degree azimuth were assumed to be the same as on the 180-degree azimuth.

Figure 100 compares the Inhabited Building Distances, derived from the Standards and from the test data, as a function of azimuth. The measured distance to the 5-kPa peak pressure on the Tunnel/Chamber Test falls well within the airblast Inhabited Building Distance specified in the Standards. The measured distance to the 5 kPa pressure level was 75 percent of the distance the Standards call for along the 0 degree azimuth, 58 percent at 30 degrees, 71 percent at 60 degrees, 88 percent at 90 degrees and 68 percent at 180 degrees. Thus, except over an arc that extends from 120 degrees to approximately 150 degrees, the present airblast Inhabited Building Distance can be seen to be generally conservative, for underground magazines with geometries and loading densities similar to the Shallow Underground Tunnel/Chamber Explosion Test.

As also shown in Figure 99, the distance along the extended tunnel axis to the 6.2-kPa overpressure level indicated by the test data is close to the airblast Inhabited Building Distance specified by the present Standards for above-ground storage ($20 Q^{1/3}$). The off-axis distance to the measured 6.2 kPa level were approximately two-thirds of

the distance specified by the Standards for above-ground storage at 30 degrees, 61 percent at 60 degrees, 50 percent at 90 degrees, and 20 percent at 180 degrees.

5.2.2 Alvdalen (Sweden) Test

In 1987, a 4,540-kg ANFO charge (3,815-kg TNT-equivalent NEW) was detonated in a KLOTZ Club test in an underground tunnel/chamber test facility at Alvdalen, Sweden (Vretblad, 1988). Figure 101 shows the measured distances to the 5 and 6.2 kPa overpressure contours for this test. Also shown are the 5 kPa contour specified by the present Standards (DOD 6055.9-STD) for underground storage of the 3,815-kg NEW tested at Alvdalen, and the 6.2 kPa contour specified by the Standards for above-ground storage of the same NEW.

Along the extended tunnel axis, the measured distance to the 5.0 kPa pressure was 85 percent of the distance specific by the Standards. Off-axis (see Figure 102), the measured distance was 80 percent of the current Standard at 45 degrees from the tunnel axis, 41 percent at 75 degrees, 13 percent at 110 degrees, and 11 percent at 180 degrees. The comparison in Figure 101 also shows that the measured distance to the 6.2 kPa overpressure for the Alvdalen test is far less than that specified by the current Standards for Inhabited Building Distance from above-ground explosions.

In Figure 103, the Inhabited Building Distance (distance to the 5-kPa overpressure level) derived from the Shallow Underground Tunnel/Chamber test data is plotted versus loading density, where loading density is the NEW in the chamber divided by the total volume (chamber plus access tunnel). The Alvdalen test in Sweden was conducted in an underground complex containing two chambers, as depicted in Figure 101. The overburden depths were sufficient to prevent rupture of the detonation chamber. Total volume for this tunnel/chamber system was taken as the volume of the loaded chamber, plus the volume of the access tunnel through which the airblast exited to the portal (disregarding the volume of the second, empty chamber).

Table 22 compares the Inhabited Building Distances for airblast specified by the current Standards with those indicated by the

tunnel/chamber test and the Alvdaalen tests. Note that, as a maximum, the hazard areas indicated by the test data are less than half that required by the Standards.

5.2.3 Validity of Small-Scale Tests

Figure 103 also compares airblast Inhabited Building Distances indicated by small-scale tests with those from full-scale tests. The Norwegian model test (1:24.8 scale) was conducted using a geometric replica of the Shallow Underground Tunnel/Chamber Explosion Test. This model did not simulate the prototype material properties of the full-scale test, or any gravity effects. Therefore, the overburden mass and inertia were not scaled in the model. This apparently resulted in much earlier overburden rupture and chamber venting, which greatly reduced the scaled free-field airblast overpressures that exited from the tunnel portal in the model test. As a result, the Inhabited Building Distance implied by the Norwegian model is less than half that indicated by the results of the Shallow Underground Tunnel/Chamber Test.

The WES model (Smith, et al, 1989) consisted of a small-scale (1:75 scale) tunnel and magazine cast into a large concrete block. Since there was no rupture of the concrete block (simulating the magazine overburden) over the range of loading densities tested (shown in Figure 103), no venting through the chamber cover occurred. This resulted in higher free-field airblast overpressures from the tunnel entrance, which gave significantly greater Inhabited Building Distances than implied by either the Norwegian model or the full-scale Tunnel/Chamber Test, both of which vented through the cover.

5.3 GROUND MOTION HAZARD RANGE

5.3.1 Current Prediction Method

In the current Standards (DOD 6055.9-STD), the Inhabited Building Distance for ground shock is related to site geologic conditions. The criteria states that the maximum particle velocity at the building site may not exceed 6.1 cm/s in sand, gravel, and moist clay (compressional wave velocities from 900 to 1,500 m/s); 11 cm/s in soft rock (compressional wave velocities from 1,800 to 3,000 m/s); and 23 cm/s in

hard rock (compressional wave velocities from 4,600 to 6,100 m/s). The Standards further state that, unless ground shock attenuation data specific to a given site are available, the required Inhabited Building Distance will be calculated from one of the following expressions:

$$D_{ig} = 0.91 f_g Q_r^{4/9} \text{ (sand, gravel, and moist clay)} \quad (27)$$

$$D_{ig} = 4.8 f_g Q_r^{4/9} \text{ (soft rock)} \quad (28)$$

$$D_{ig} = 5.4 f_g Q_r^{4/9} \text{ (hard rock)} \quad (29)$$

where D_{ig} is the ground shock hazard range, m

Q_r the effective explosive weight, kg

and f_g is a dimensionless term called the decoupling factor, such that:

$$f_g = 0.116 (Q_r / V)^{0.3} \quad (30)$$

where V is the explosive storage chamber volume, m^3

The computed decoupling factor, f_g , for the Shallow Underground Tunnel/Chamber Explosion Test is 0.408.

5.3.2 Shallow Underground Tunnel/Chamber Test Results

The measured compressional wave velocity of the rock mass in the region of the explosive storage chamber ranged from 944 to 1,626 m/sec, with an average value of 1,309 m/sec (Halsey, et al, 1989). These values are more typical of compressional wave velocities in soil, rather than in solid rock, and indicate that the rock at the Shallow Underground Tunnel/Chamber site was heavily jointed and weathered. The plot of the ground motion arrival time recorded on the test (Figure 30) indicates a higher compressional wave velocity (2,166 m/sec), implying the existence of less weathered, more competent rock at depth. This value is within the compressional wave velocity range for material described in the Standards as soft rock.

Data points for the maximum particle velocity vectors measured on the Shallow Underground Tunnel/Chamber Test are plotted in Figure 104 as

a function of slant distance from the center of the chamber. The velocity curve given by Vretblad (1988) falls slightly below the measured data along the 0-degree azimuth (i.e., the extended tunnel axis), but closely matches the far-field data in other directions.

The gages beyond the 100-m range along the 0-degree azimuth in the Tunnel/Chamber Test were emplaced in desert alluvium soil in the valley floor in front of the tunnel, while the gages in other directions were emplaced in the rock surface. Using the criterion of 6.1 cm/sec and the equation (equation 28) given in the Standards for soft rock, the calculated Inhabited Building Distance for ground shock should be 160 m. Based on an interpolation of the data, the Tunnel/Chamber Test results indicate that the 6.1 cm/sec level occurred at a distance of 580 m. For the 90 and 180-degree azimuths, the test measurements indicate a range of 155 m.

The NATO (AC/258) Inhabited Building Distances for ground shock are also displayed in Figure 104. The NATO criteria specifies levels of damage that occur at certain peak particle velocity thresholds; 5 cm/s (threshold for no damage), 14 cm/s (minor damage), and 19 cm/s (major damage). These values are independent of velocity direction or earth media. The NATO Inhabited Building Distances for major damage from a detonation corresponding to the Shallow Underground Tunnel/Chamber Explosion Test are 300 m in soil (0-degree azimuth) and 120 m in rock.

There are two dominant factors associated with the Tunnel/Chamber Test that may explain the discrepancies between the predicted and the measured ranges to the 6.1 cm/s level of ground shock along the 0-degree azimuth. The first is the fact that the gages along the 0-degree azimuth were emplaced in soil, rather than rock. Since the detonation chamber was surrounded by rock, the use of Equation 27 (for soil) in the Standards is obviously inappropriate. On the other hand, the use of Equation 28 (for soft rock) does not take into account the affect of the soil layer overlying the bedrock along 0-degree radial, in front of the tunnel opening.

The second factor is the apparent fact that the ground motions recorded by the gages on the 0-degree azimuth were predominantly induced by the airblast issuing from the tunnel portal. This is indicated by the

arrival times of the ground motions at the gage locations, which match the arrival times recorded by the airblast gages along the 0-degree azimuth. Thus, it is obvious that the direct-induced motions transmitted to the gages in front of the tunnel, through the bedrock initially and then through the overlying soil, were completely obscured by the strong airblast-induced motions.

Figure 104 also shows a prediction curve from NATO AC/258 that does account for airblast induced motions. This curve is based on the equation

$$v_v = \frac{P}{\rho C_p} \quad (31)$$

where v_v = the vertical velocity of motion

P = the airblast overpressure at the location of interest

ρ = the density of the material

and C_p = the wave velocity of the material

In NATO AC/258, C_p is defined as the seismic velocity of the material. However, Hadala (1973) found that the stress wave velocity is actually the controlling parameter in regions where the airblast-induced motions outrun the direct-induced ground shock. Using a typical stress wave velocity for desert alluvium and the overpressures measured on the Tunnel/Chamber Test, a prediction curve for airblast-induced ground motion velocity based on Equation 31 is shown in Figure 104. While the curve obviously overpredicts the close-in motions directly in front of the tunnel portal, it comes within 50 percent or so of matching the measured velocities on the 0-degree azimuth at the distances of interest for ground shock hazard definition.

A final comparison made in Figure 104 is with the curve established for ground shock velocity by Vretblad (1988), based on the results of the Alvdalen test in Sweden (see Equation 12, Section 3.6). Vretblad's equation provides a better fit to the off-axis ground shock data at the ranges of interest for the Tunnel/Chamber Test, but still underpredicts the motions measured at the most distant gages.

In summary, the NATO AC/258 equation for airblast-induced motions provides the best fit to data along the 0-degree azimuth for the

Tunnel/Chamber Test, at the ranges of interest for defining the Inhabited Building Distance. For the other "off-axis" directions, the NATO AC/258 equation for direct-induced motions and Vretblad's equation both closely predict the motions measured in the Tunnel/Chamber Test at the ranges of interest. In all cases, however, the values predicted by these methods should be increased by a factor of two to provide a safe upper bound of the motions measured on the test.

5.4 DEBRIS HAZARD RANGE

The Explosives Safety Standards and the NATO AC/258 debris hazard criteria consider two sources of hazardous debris: material blown through the access tunnel portal and rock thrown by the overburden rupture. The Explosives Safety Standards require a debris Inhabited Building Distance of 610 m along and 15 degrees either side of the extended access tunnel centerline. The NATO AC/258 debris Inhabited Building Distance is 600 m over the same 30 degree arc.

For debris originating from rupture of the magazine cover, the Standards give a hazard range of

$$D_{id} = f_d f_c Q^{0.41} \quad (32)$$

where D_{id} is the hazard range, m

f_c is a constant related to the scaled overburden depth, m

Q is the explosive quantity (NEW) stored in the chamber, kg

and f_d is a function of chamber loading density, given by the relation

$$f_d = 0.364 Q^{0.18} \quad (33)$$

The function f_c is given graphically in Figure 105 for hard rock (granite or limestone) and for soft rock (sandstone).

The minimum overburden depth above the chamber at the Tunnel/Chamber Test site was 9.4 m, giving a scaled (TNT-equivalent) overburden depth $0.34 \text{ m/kg}^{1/3}$. The earth cover function, f_c , for this scaled overburden depth is $5.09 \text{ m/kg}^{0.41}$ from the "soft rock" curve of Figure 105. The loading density function (Equation 33) calculates to be

0.77. Substituting these values in Equation 32, the Inhabited Building Distance for protection from debris is 236 m.

The NATO AC/258 debris hazard criteria for a scaled cover depth of $0.34 \text{ m/kg}^{1/3}$ is given as

$$D4 = 5.10 Q^{0.41}, \text{ for hard rock} \quad (34)$$

and $D5 = 5.00 Q^{0.41}, \text{ for soft rock} \quad (35)$

These criteria were developed for a loading density of 270 kg/m^3 . A reduction is allowed for smaller loading densities. For a TNT-equivalent loading density of 66.4 kg/m^3 , the correction factor for the NATO AC/258 "soft rock" is 0.80. For hard rock, the Inhabited Building Distance for debris is 308 m before correction for loading density, and 246 m with the correction. The NATO AC/258 document also states, "If the terrain (cover) is sloping in such a way as to favour debris throw at an angle near 45 degrees above the horizontal, the distances should be increased by 50 percent in the sloping direction". Thus, for the Shallow Underground Tunnel/Chamber Explosion Test underground magazine with a 30-degree overburden slope, the NATO AC/258 criteria predict an Inhabited Building Distance for debris of 369 m (1.5 times 246 m) to the front and 246 m to the sides of the magazine.

The current Explosives Safety Standards (DOD 6055.9-STD) criterion for debris hazard range is the distance to a fragment or debris density of one hazardous particle per 56 m^2 . Analysis of the debris on the motion picture records of the Tunnel/Chamber Test indicates that almost all debris seen on the film is potentially lethal (kinetic energy greater than 79 J), and thus considered hazardous. As shown in Figure 70, a debris density of one missile impact per 56 m^2 occurred at a distance of 656 m. This distance is 1.08 times the hazard range calculated by the Standards, and is 1.09 times the NATO (AC/258) Inhabited Building Distance for debris range along the access tunnel axis.

The debris and ejecta collection on the Tunnel/Chamber Test was concentrated within a sector extending 45 degrees each side of the

extended tunnel/axis; therefore the effect of azimuth on debris range can only be based on data within this sector. These data are shown in Figure 70, where curves are drawn to approximate the debris limits at 0, 20, and 40 degrees. As shown here, the distance to a debris density of one strike per 56 m² is 656 m, 447 m, and 287 m along the 0, 20, and 40-degree azimuths, respectively. For the Tunnel/Chamber Test configuration, Figure 106 compares debris hazard ranges, as a function of azimuth, based on criteria given in the Explosives Safety Standards and NATO AC/258, with ranges derived from the actual debris data collected on the test. As shown in the comparison, both sources slightly underpredict the hazard ranges in front of this tunnel/chamber geometry and loading density.

Neither source (Explosives Safety Standards or NATO AC/258) addresses the hazard of possible secondary explosions of unexploded ordnance thrown from the underground storage chamber by an accidental explosion within the chamber. Inert 155-mm rounds placed around the explosive charge in the storage chamber for the Tunnel/Chamber Test were found well beyond the one-strike-per 56 m² debris hazard range. Had these munitions been live rounds, there is some possibility that they would have detonated upon impact, with associated hazards to personnel or property in the vicinity. If such secondary detonations are determined to be a serious potential hazard, this phenomenon should be addressed in a separate study.

SECTION 6

SUMMARY, CONCLUSIONS, AND RECOMMENDATIONS

6.1 SUMMARY OF FINDINGS

The active and passive airblast instrumentation used to assess the blast hazard from the Shallow Underground Tunnel/Chamber Explosion Test provided extensive and consistent data. A single total-pressure measurement on the extended tunnel axis indicated that flow pressures on the order of 7 times the peak overpressure exist at 5 m outside the tunnel portal. Total pressure measurements at the 75-m range indicate that the strong flow or "jetting" of pressure beyond the portal is confined to a narrow region extending 15 degrees either side of the extended tunnel axis at this range. This jet region was further defined by wire drag gages and blast cube displacements.

Empirical relations developed by Skjeltnorp, Hegdahl and Jenssen (1975) provided reasonable predictions of external airblast overpressures. Their empirically-based method for computing tunnel exit pressure yields a value (9.8 MPa) which is a factor of 1.9 greater than the measured pressure (5.2 MPa), derived from a least squares fit to the side-on overpressure data recorded in the access tunnel. However, the exit pressure calculated by this method provides a reasonable (but conservative) basis for developing the free-field airblast prediction. The Skjeltnorp, Hegdahl and Jenssen (1975) free-field relation provides a good prediction if the tunnel exit pressure is known (note: As long as the exit pressure is known, the external pressures will be independent of the internal geometry of the underground munition storage complex). In addition, the peak airblast pressures measured on the test, along with the computed impulse values, are in good agreement with the azimuth decay parameter used in this relation.

Two hydrocode calculations (performed by S-CUBED, Inc., with their SHARC code) produced results which bound the possible airblast response spectrum of the tunnel/chamber system. A "non-responding" model calculation gave an upper bound of the access tunnel overpressure-time

histories, with peak values several times the measured data. The lower bound was established by using an equation of state for sand to simulate the poor quality rock in a "responding" model, and gave overpressure-time histories about 50 percent lower than the measured data. These results suggest that selection of a more realistic material model for the calculation would yield results closely approximating the measured data. The "responding" computer model could thus serve as an excellent tool for parametric studies, once the hydrocode has been validated for a particular underground storage system design.

The Inhabited Building Distances for airblast given in the U.S. DOD Explosives Safety Standards are very conservative for the area in front of the access tunnel portal (azimuths from 0 to 90 degrees and 270 to 0 degrees), as shown in Figure 99. Over an arc from 90 degrees to 270 degrees (Figure 100), the distance specified by the manual provides a reasonable upper bound of the data measured on the Shallow Underground Tunnel/Chamber Test. Analysis of the overpressure-time histories along the 180-degree azimuth from the Tunnel/Chamber test (Halsey, et al, 1989) shows that overburden venting is a low-pressure, late-time phenomenon which does not contribute to the airblast Inhabited Building Distance. When compared to the pressures measured between the 90 and 270-degree azimuths on the KLOTZ Club's Alvdalen, Sweden test, which did not vent through the cover, the Standards overpredict for this area just as they do for the 0 to 90-degree azimuth area. The greater overprediction for this test is attributed to the lower loading density (5 kg/m^3) of the Alvdalen underground storage site.

The Standards set a damage criterion for airblast pressure against inhabited buildings of 5 kPa (50 mb). As shown in Figure 99, the 5-kPa overpressure level measured during the Shallow Underground Tunnel/Chamber Explosion Test occurred at approximately the same distance that the Standards specify as the airblast Inhabited Building Distance for open storage of a 20,000-kg Composition B charge. The airblast Inhabited Building Distances specified in the Standards for underground storage are even more conservative when compared to the results of tests at Alvdalen, Sweden, as shown in Figure 101. The airblast Inhabited Building Distance

is strongly dependent on the explosive loading density of the chamber (charge weight divided by volume of access tunnel plus storage chamber), as shown in Figure 103.

The Inhabited Building Distances for ground shock given by the Explosives Safety Standards and NATO AC/258 yield reasonable results for shock transmitted through rock. For the case of a soil layer over bedrock, however, such as existed at the Tunnel/Chamber Test site, the Standards and NATO AC/258 both severely underestimate distances to the particle velocity levels used as criteria for Inhabited Building Distance to protect against ground shock.

The results of the Shallow Underground Tunnel/Chamber Explosion Test indicate that the Inhabited Building Distance for ejecta/debris along the extended tunnel axis (0-degree azimuth) is underestimated by the NATO AC/258 guidance. The data indicates (Figure 70) that the inhabited building hazard range decreases with angle from the 0-degree azimuth, and approaches the distance specified by the Standards and NATO AC/258 at an azimuth of 45 degrees.

6.2 CONCLUSIONS

- Using a peak pressure criterion of 5 kPa (0.73 psi) for airblast Inhabited Building Distance, the test data indicated that the actual Quantity-Distance ($Q-D_{ib}$) is 25 percent less, and the $Q-D_{ib}$ area some 50 percent less, than the values specified by the current Ammunition and Explosive Safety Standards (DOD 6055.9-STD) for underground storage.
- If the same damage criterion for inhabited buildings (6.2 kPa or 0.9 psi) used for above-ground storage is applied to underground storage, the test results indicate that the actual $Q-D_{ib}$ for underground storage is approximately equal to the $Q-D_{ib}$ specified in the Standards for above-ground storage, but the $Q-D_{ib}$ area is only one-third that specified for above-ground storage.
- A strong airblast jet produced by the detonation was confined to a narrow sector extending 15 degrees each side of the extended tunnel axis.

- The empirically-based equation developed by Skjeltnor, Hegdahl, and Jenssen provides good predictions of external airblast, given an accurate estimate of the tunnel portal exit pressure.
- The results of this test alone were insufficient to determine the extent to which shallow magazine cover depths reduce external blast pressures by relieving chamber pressures through rupture of the cover.
- The existing Standards and NATO AC/258 prediction methods for ground shock hazards appear to provide reasonably accurate estimates of the hazard ranges in homogeneous geologies, but may underestimate the ranges in layered geologies.
- Both the Standards and the NATO AC/258 guidance underpredict the hazard range for ejecta/debris along the extended tunnel axis, by about ten percent.

6.3 RECOMMENDATIONS

Additional data are needed to evaluate the effect of storage loading density and cover depth on the Inhabited Building Distance for airblast. Previous data from WES model tests, shown in Figure 103, indicate that a non-linear relation exists, but the model and full-scale data follow separate curves. Also, the effect of cover venting on the Inhabited Building Distance for airblast cannot be adequately defined based on the results of the Shallow Underground Tunnel/Chamber Explosion Test and other existing data. Additional tests, where the extent of venting is varied and other factors held constant, are needed to isolate this effect.

Computer model studies can also help define the effect of venting on external blast hazards, after a reliable material model is established that simulates the response of the rock surrounding the magazine chamber.

The Shallow Underground Tunnel/Chamber Explosion Test demonstrated that current Inhabited Building Distance criteria for ground shock in a layered geology (with soil over rock) is inadequate. Improved methods must be developed to better predict these distances in complex geologies.

The Inhabited Building Distance that is currently specified in the Standards for debris expelled from the access tunnel should be

re-evaluated and corrected. Recent work in Sweden indicates that the large distances to which debris was thrown out the access tunnel on the Tunnel/Chamber test could be reduced by a barrier outside the tunnel portal. Additional study is needed to evaluate such methods, and their most effective design, to reduce the external debris hazard.

REFERENCES

- Bakhtar, Khosrow, 1988, "Rock Mass Characterization at Tunnel Explosion Test Site, U.S. Naval Weapons Center," The Earth Technology Corporation, Long Beach CA.
- Davis, Landon K.; McAneny, Colin C., and Joachim, Charles E., 1981, "PROJECT SPERRE, Report 3, Phase II: Field Tests--Explosive Cratering Experiments in Granite and Sandstone," Technical Report SL-81-5, U.S. Army Engineer Waterways Experiment Station, Vicksburg, MS.
- Department of the Army, 1986, "Fundamentals of Protective Design (Non-Nuclear)," TM 5-855-1, Headquarters, Department of the Army, Washington, D.C.
- Department of Defense, 1984, "Ammunition and Explosives Safety Standards," DoD 6055.9-STD, Assistant Secretary of Defense (Manpower, Installations, and Logistics), Washington, D.C.
- Dewey, J. M. and McMillin, D. J., 1989, "Wire Drag Gauge Measurements, China Lake Tunnel Test, 24 August 1988," Dewey McMillin & Associates, Victoria, B.C., Canada.
- Dewey, J. M. and McMillin, D. J., 1989, "Smoke Puff Photogrammetry, China Lake Tunnel Test," Dewey McMillin & Associates, Victoria, B.C., Canada.
- Edgar, Ron C., 1989, "Graphical Presentation of Overpressure and Overdensity Data, Shallow Underground Tunnel Test, China Lake, California," Ballistech Systems Incorporated, St. Hubert, Quebec, Canada
- Ethridge, Noel H.; Dixon-Hiester, Lisa A.; and Peterson, Robin S., 1989, "Blast Cube Experiment, KLOTZ Underground Magazine Trial," Applied Research Associates, Inc., Aberdeen Research Center, Aberdeen, MD.
- Hadala, Paul F., 1973, "Effect of Constitutive Properties of Earth Media on Outrunning Ground Shock from Large Explosions," Technical Report S-73-6, U.S. Army Engineer Waterways Experiment Station, Vicksburg, MS.
- Halsey, Carl C.; Durbin, William F.; and Berry, Sharon L., 1989, "KLOTZ Underground Magazine Trial, Data Report," NWC TM-6562, Naval Weapons Center, China Lake, CA.
- Helseth, Einar S., 1982, "Underground Ammunition Storage, Model Test In Scale 1:100 in Sand," Fortifikatorisk Notat NR 160/82, Progress Report to KLOTZ Club Meeting, Norfolk, VA.
- Helseth, Einar S., 1985, "Blast Effects From Accidental Explosions," Report NR 174/85, Norwegian Defence Construction Service, Oslo, Norway.

Kennedy, Lynn W. and Schneider, Kenneth D., 1989, "Hydrodynamic Code Calculations Of Airblast For An Explosive Test In A Shallow Underground Storage Magazine," S-CUBED, Albuquerque, NM.

Kinney, Gilbert F. and Graham, Kenneth J., 1985, "Explosive Shocks in Air," Springer-Verlag, New York, NY.

Kingery, Charles N., 1989, "Survey of Airblast Data Related to Underground Munition Storage Sites," Technical Report BRL-TR-3023, U.S. Army Laboratory Command, Ballistic Research Laboratory, Aberdeen Proving Ground, MD

North Atlantic Treaty Organization, 1977, "Manual on NATO Principles for the Storage of Ammunition and Explosives, Part III," AC/258-D/258, Group of Experts on the Safety Aspects of Transportation and Storage of Military Ammunition and Explosives (AC/258).

Millington, Charles, 1985, "The Ernestelle Report," Preliminary AWRE Report UK(ST)IWP 205, 0/1/85, AWRE (Foulness), Ministry of Defence, United Kingdom.

Rinehart, John S., 1960, "On Fractures Caused By Explosions and Impacts," Quarterly Of The Colorado School Of Mines, Volume 55, Number 4, Colorado School of Mines, Golden, CO

Schneider, Kenneth D., 1988, "Summary Report From Shallow Underground Tunnel/Chamber Test - China Lake," S-Cubed, Inc., Albuquerque, NM

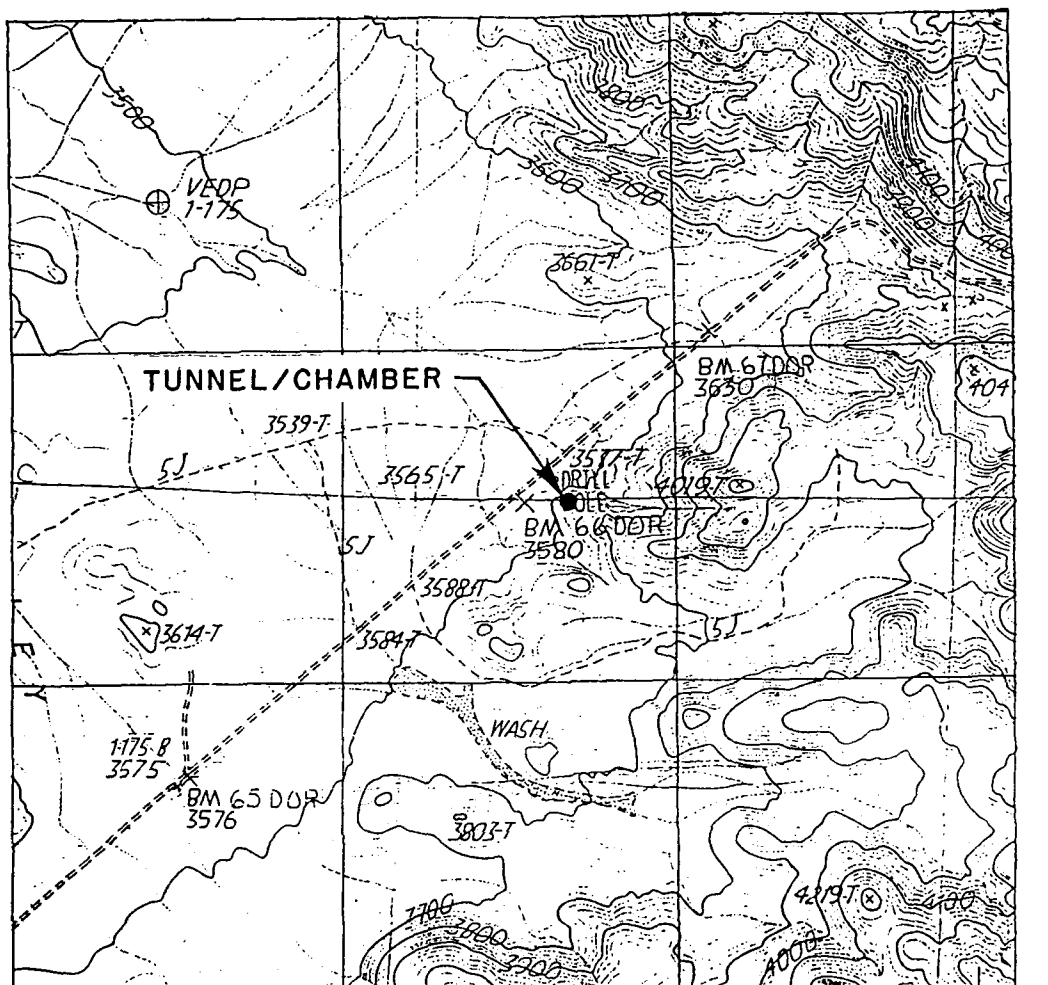
Skjeltorp, A. T.; Hegdahl, T.; and Jenssen, A.; 1975, "Underground Ammunition Storage, I, IIA, IIIA, IVA, and VA," Report Numbers 80/72, 81/72, 83/72, and 84/72, Norwegian Defence Construction Service, Oslo Norway.

Smith, Dennis R.; Joachim, Charles E.; Davis, Landon K.; and McMahon, Gordon W.; 1989, "Effects of Explosions in Underground Magazines," Technical Report SL-89-15, U.S. Army Engineer, Waterways Experiment Station, Vicksburg, MS.

Swizdak, Michael M., 1975, "Explosion Effects and Properties, Part I: Explosion Effects In Air," NSWC/WOL/TR 75-116, Naval Surface Weapons Center, Silver Spring, MD.

Vretblad, Bengt, 1988, "Data From The 1987 Klotz Club Test In Sweden," Report C3:88, Royal Swedish Fortifications Administration, Eskilstuna, Sweden.

Weibull, H. R. W., 1968, "Pressures Recorded in Partially Closed Chambers at Explosions of TNT Charges," Annual of the New York Academy of Sciences, Vol. 152.



SCALE 1:24 000

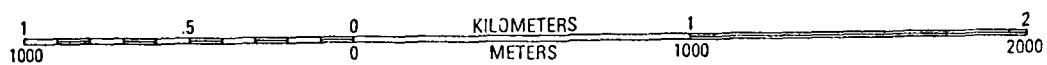


Figure 1. Site contour map

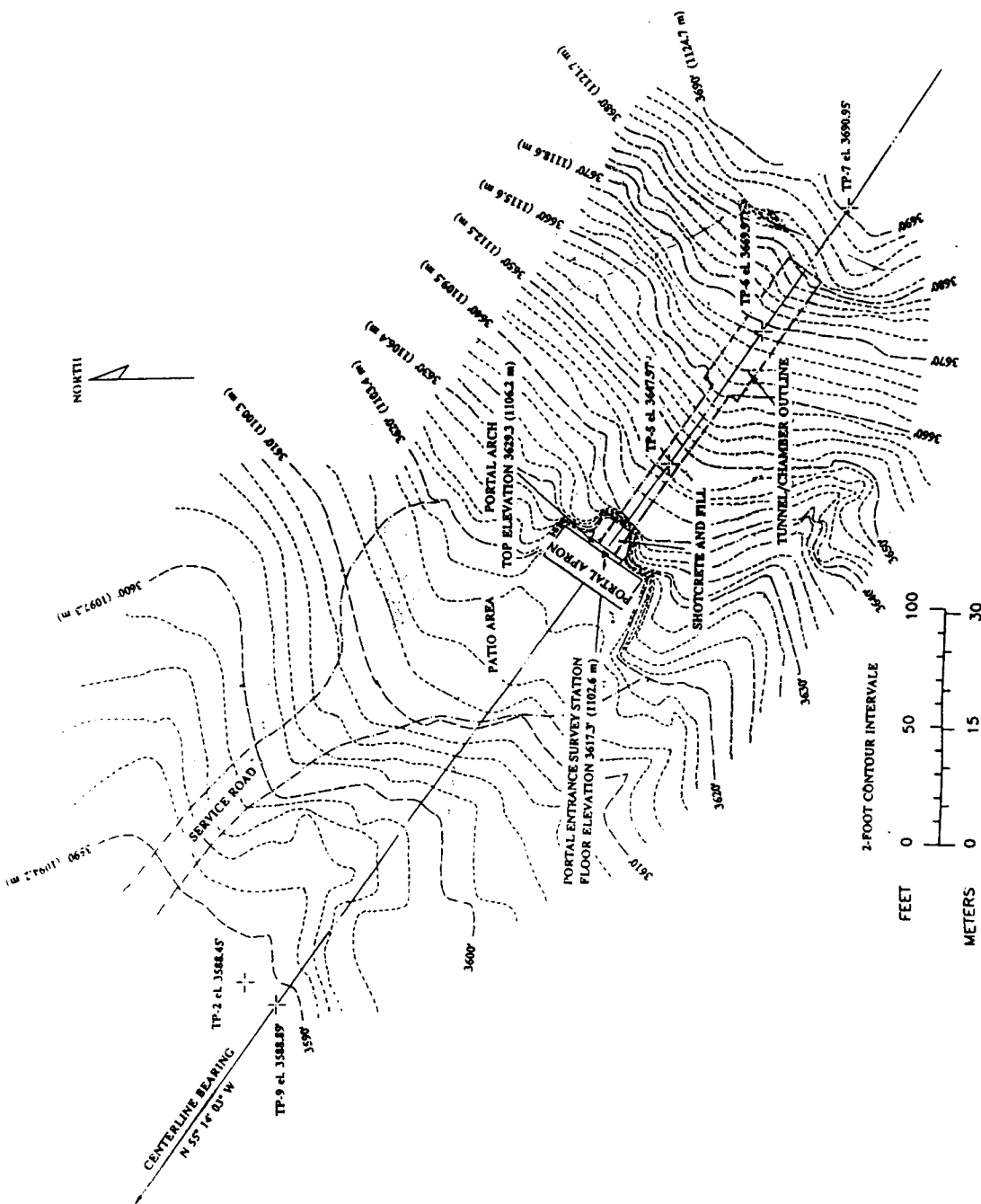


Figure 2. Site contour map for Shallow Underground Tunnel/Chamber Explosion Test Program.

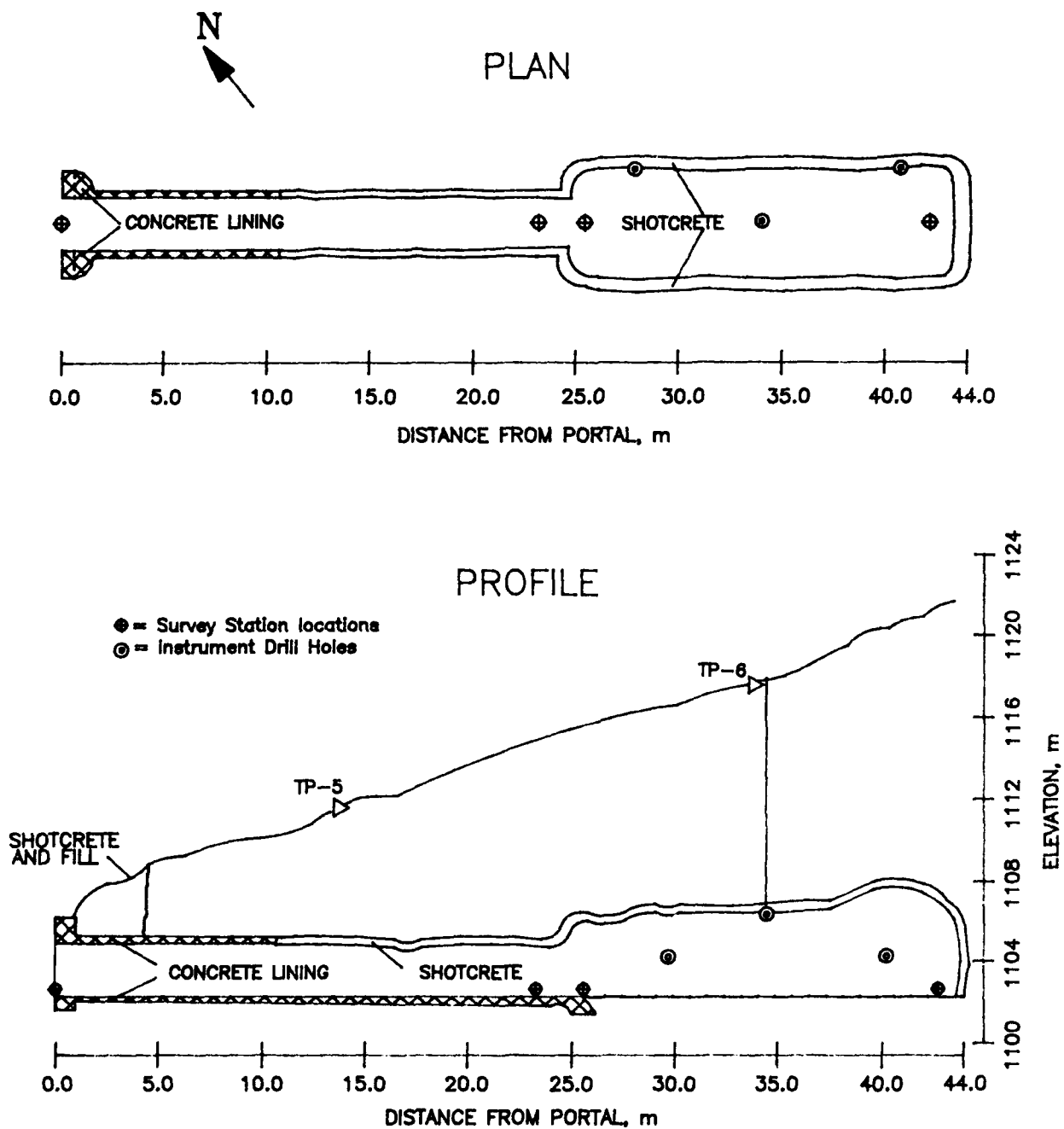


Figure 3. Tunnel/Chamber longitudinal cross-sections (plan and profile).

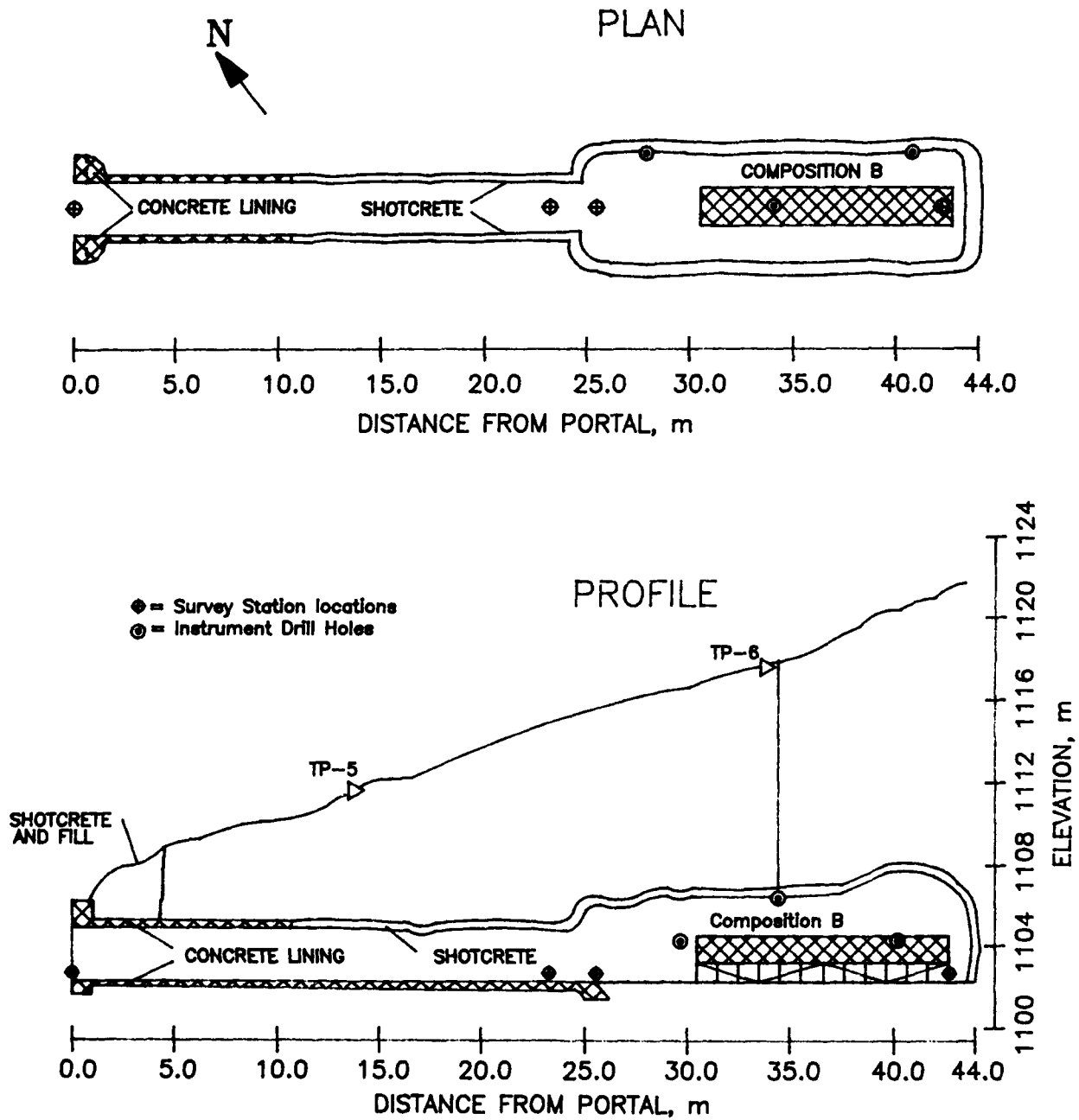


Figure 4. Location of 20,000-kg Composition B explosive charge for Shallow Underground Tunnel/Chamber Explosion Test Program (plan and profile).

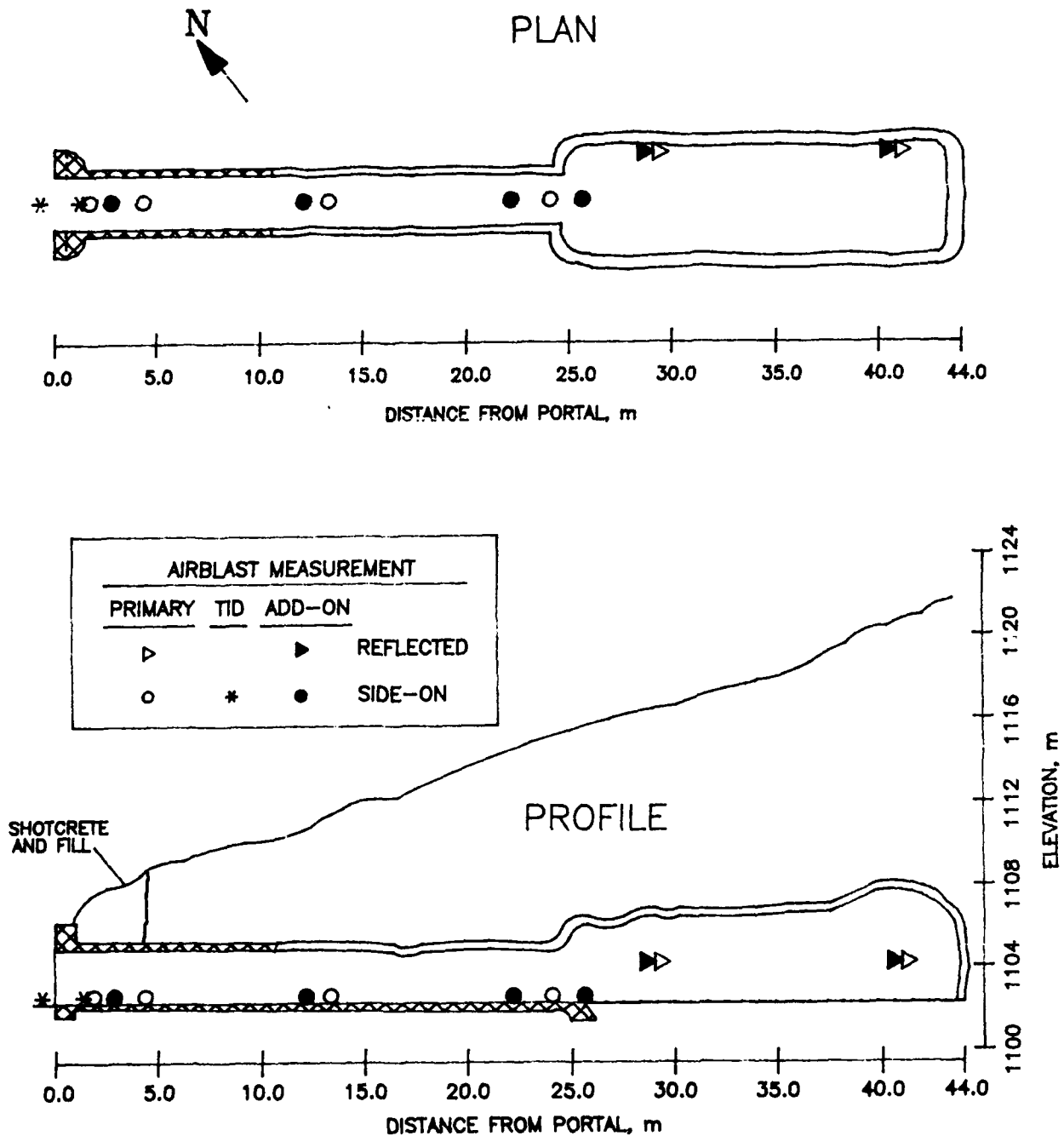


Figure 5. Interior pressure transducer locations for Shallow Underground Tunnel/Chamber Test Program.

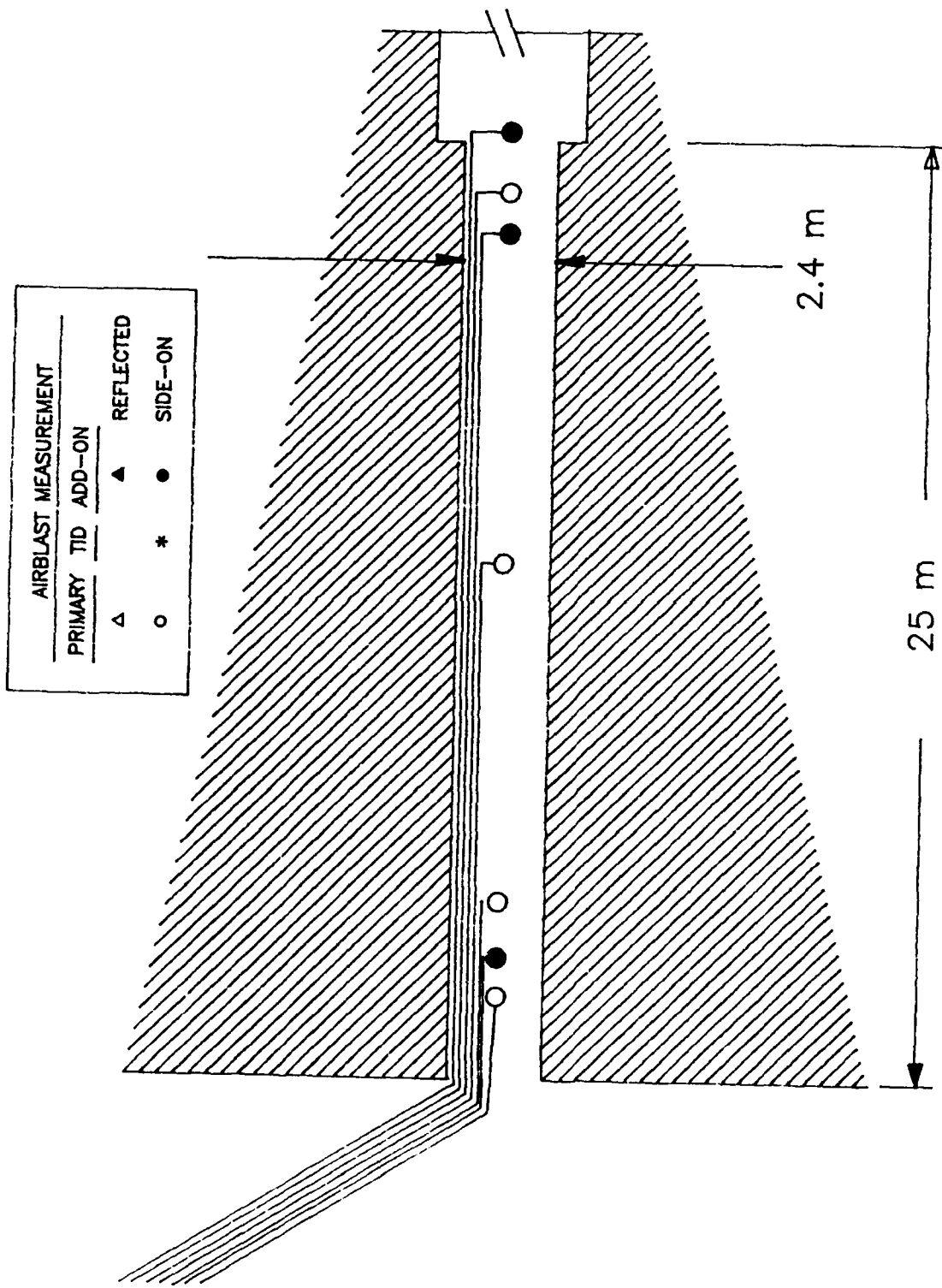


Figure 6. Cable protection schematic for interior airblast gage signal lines on Shallow Underground Tunnel/Chamber Test Program.

4 - 5000 KG TNT SPHERES

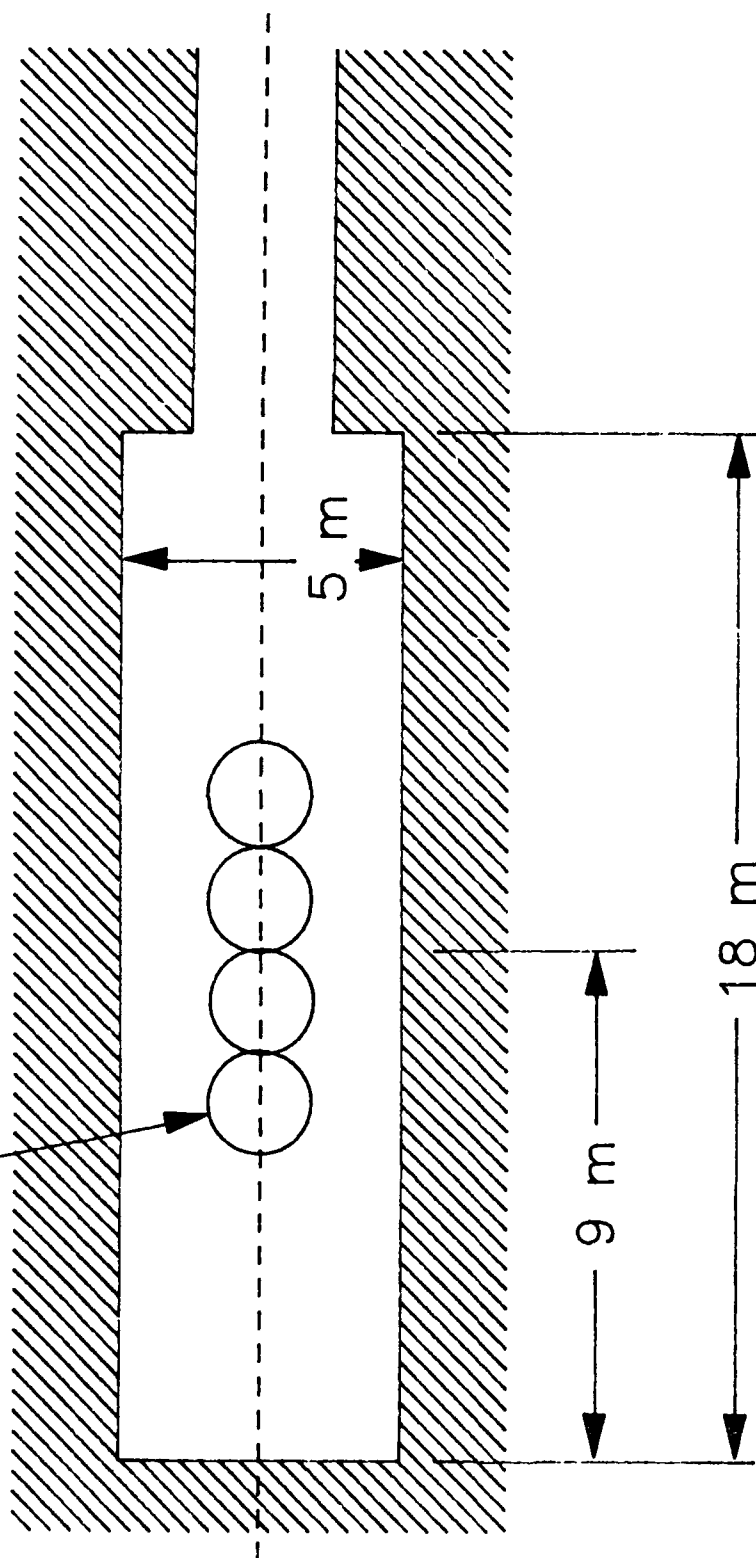


Figure 7. Charge and Chamber configuration for BLASTIN calculation.

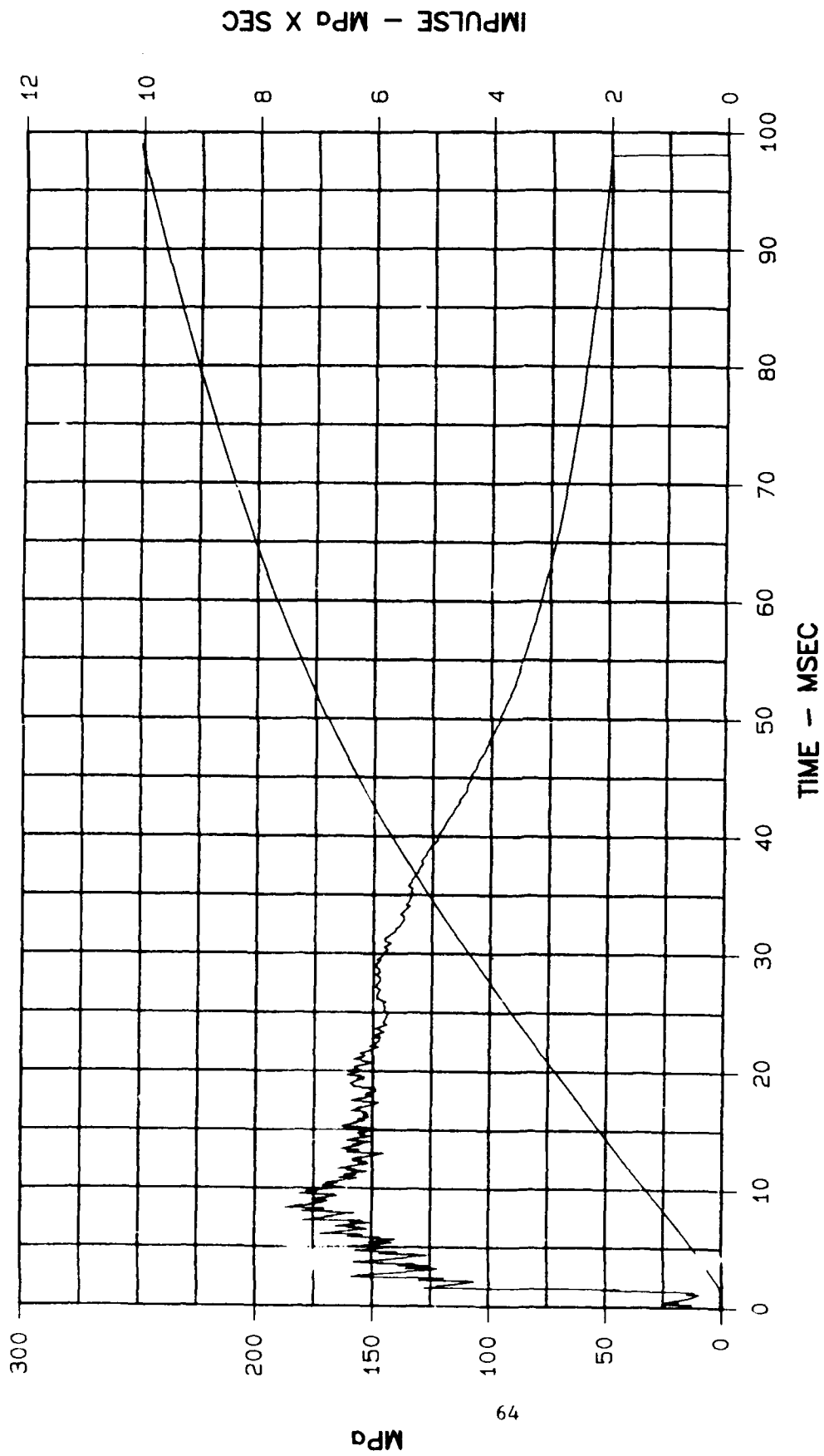


Figure 8. Predicted airblast overpressure record (gas plus shock) at station C.5, at tunnel/chamber interface as calculated by WES's BLASTIN code.

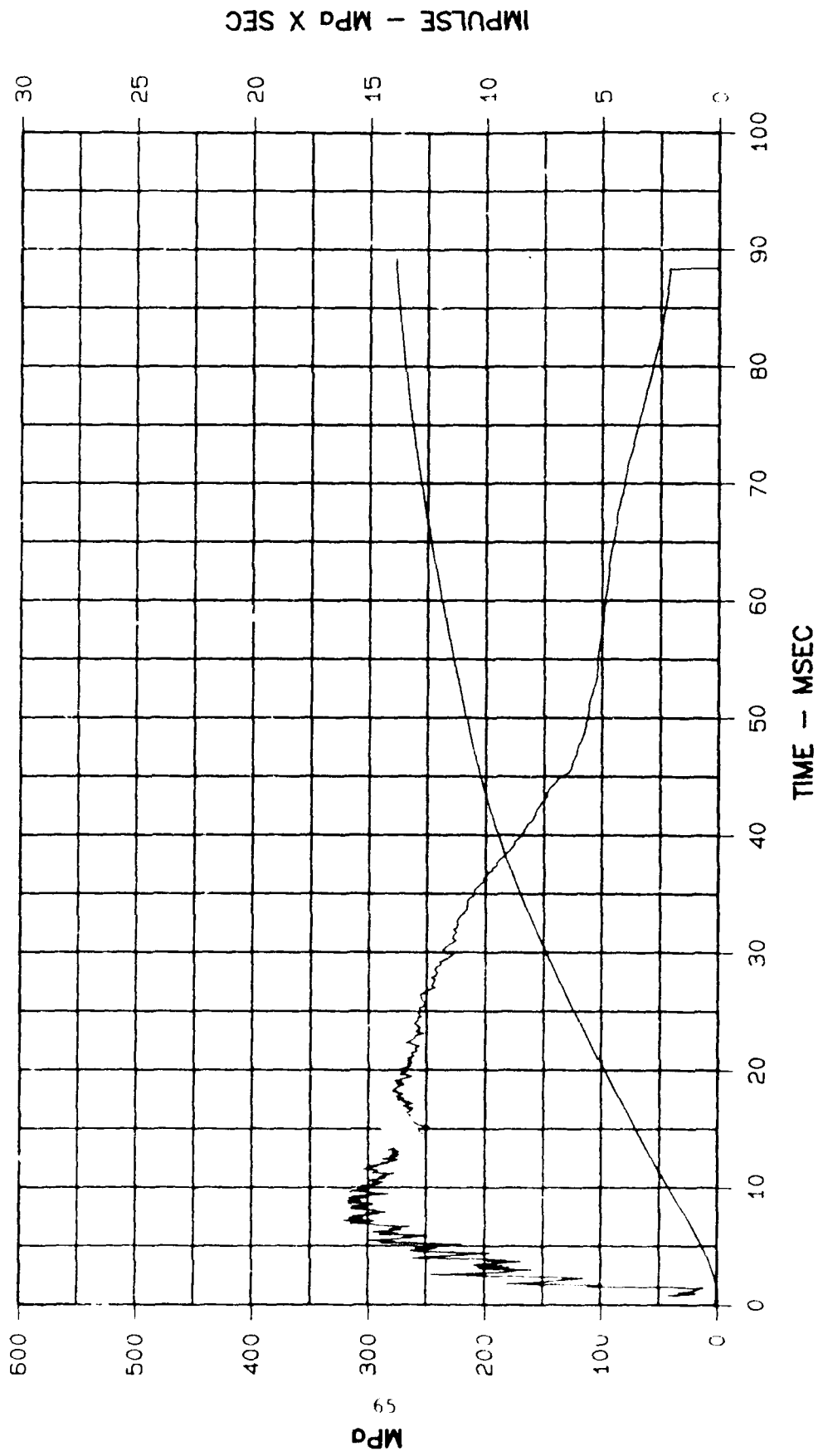


Figure 9. Chamber reflected airblast (gas plus shock) at stations C.1 and C.2.

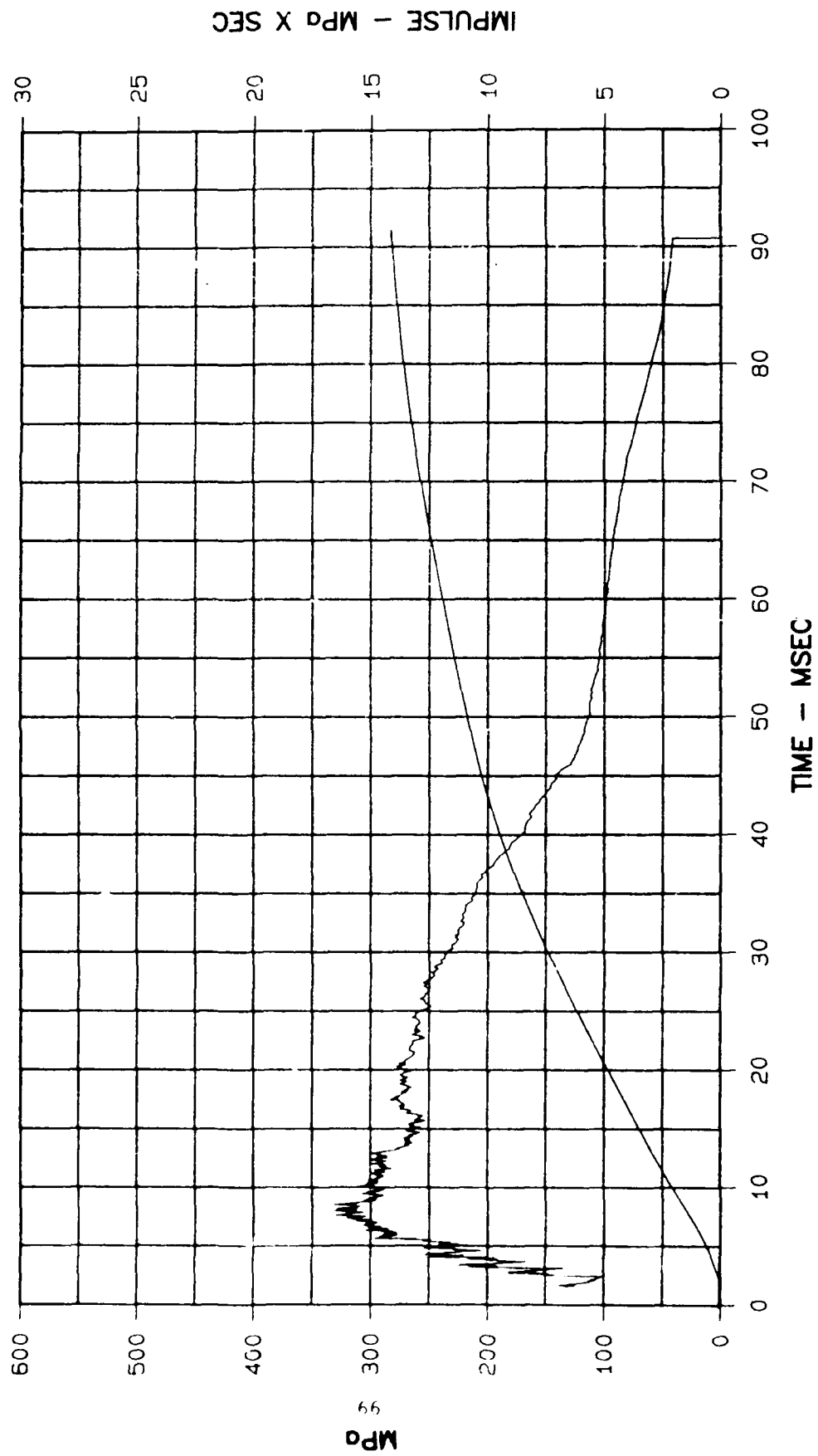


Figure 10. Reflected airblast (gas plus shock) at stations C.3 and C.4.

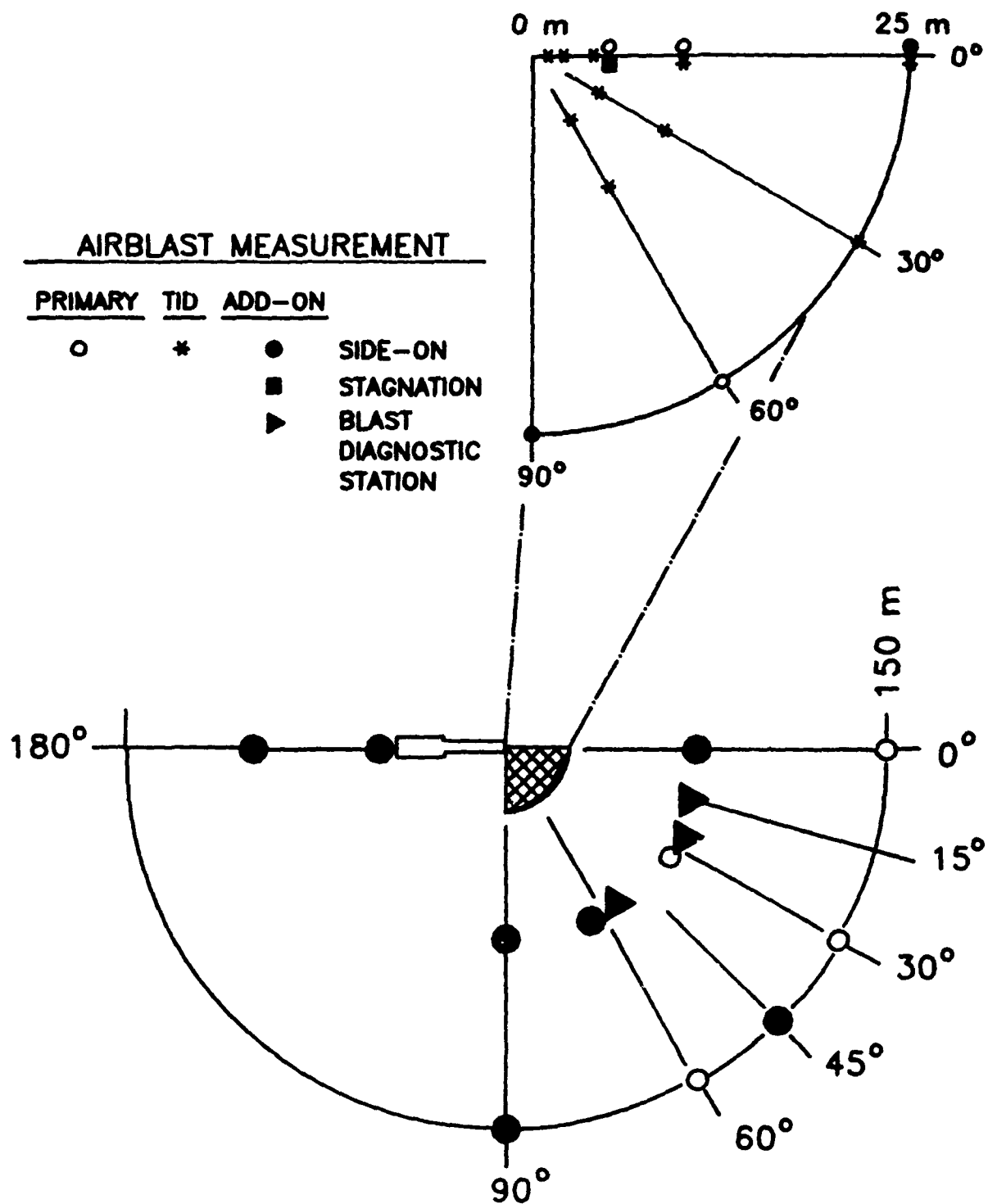


Figure 11. Free-field close-in airblast gage locations for Shallow Underground Tunnel/Chamber Explosion Test Program. Upper figure is enlargement of cross-hatched area.

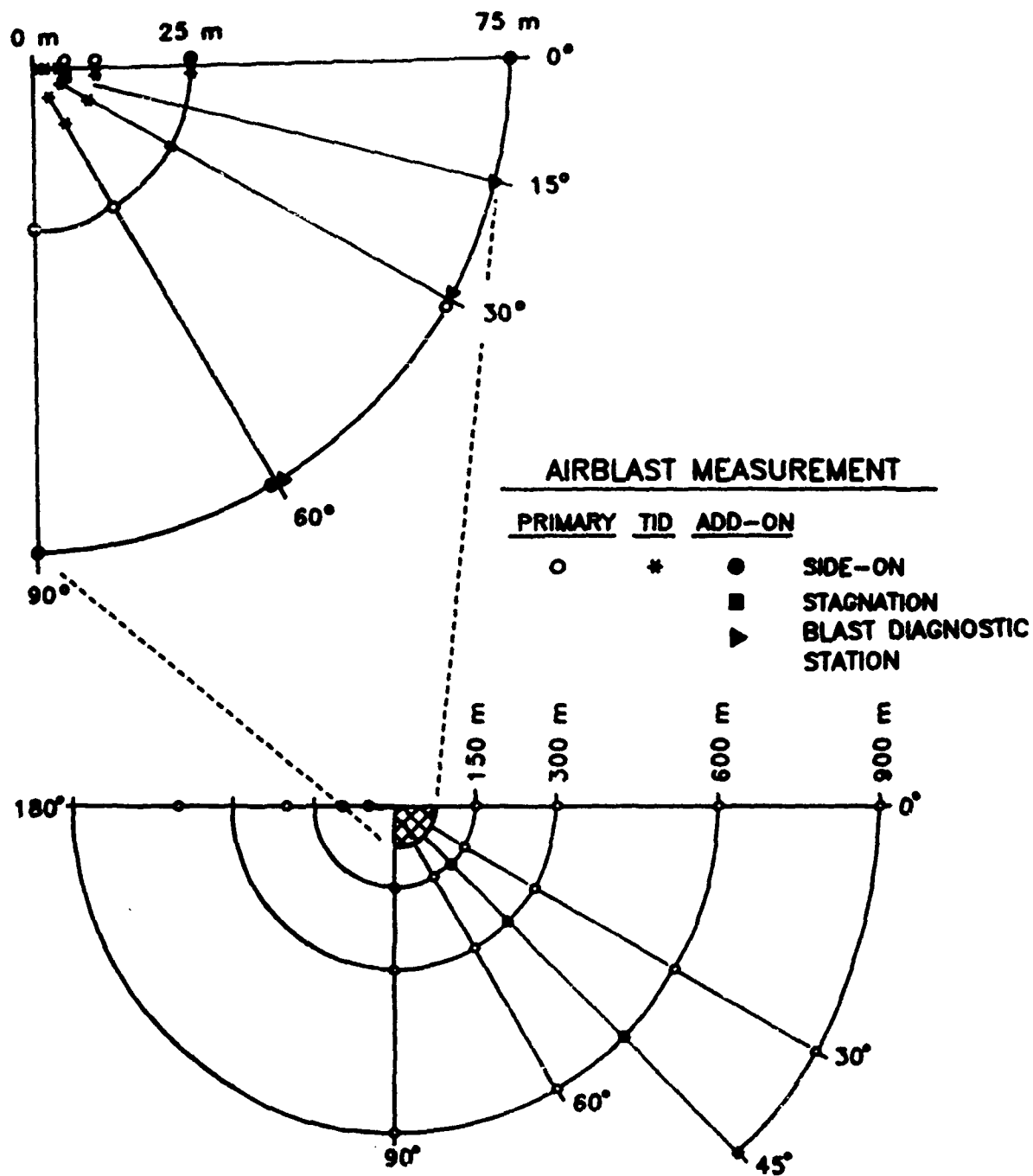


Figure 12. Free-field airblast gage locations for Shallow Underground Tunnel/Chamber Explosion Test Program. Upper figure is enlargement of cross-hatched area.

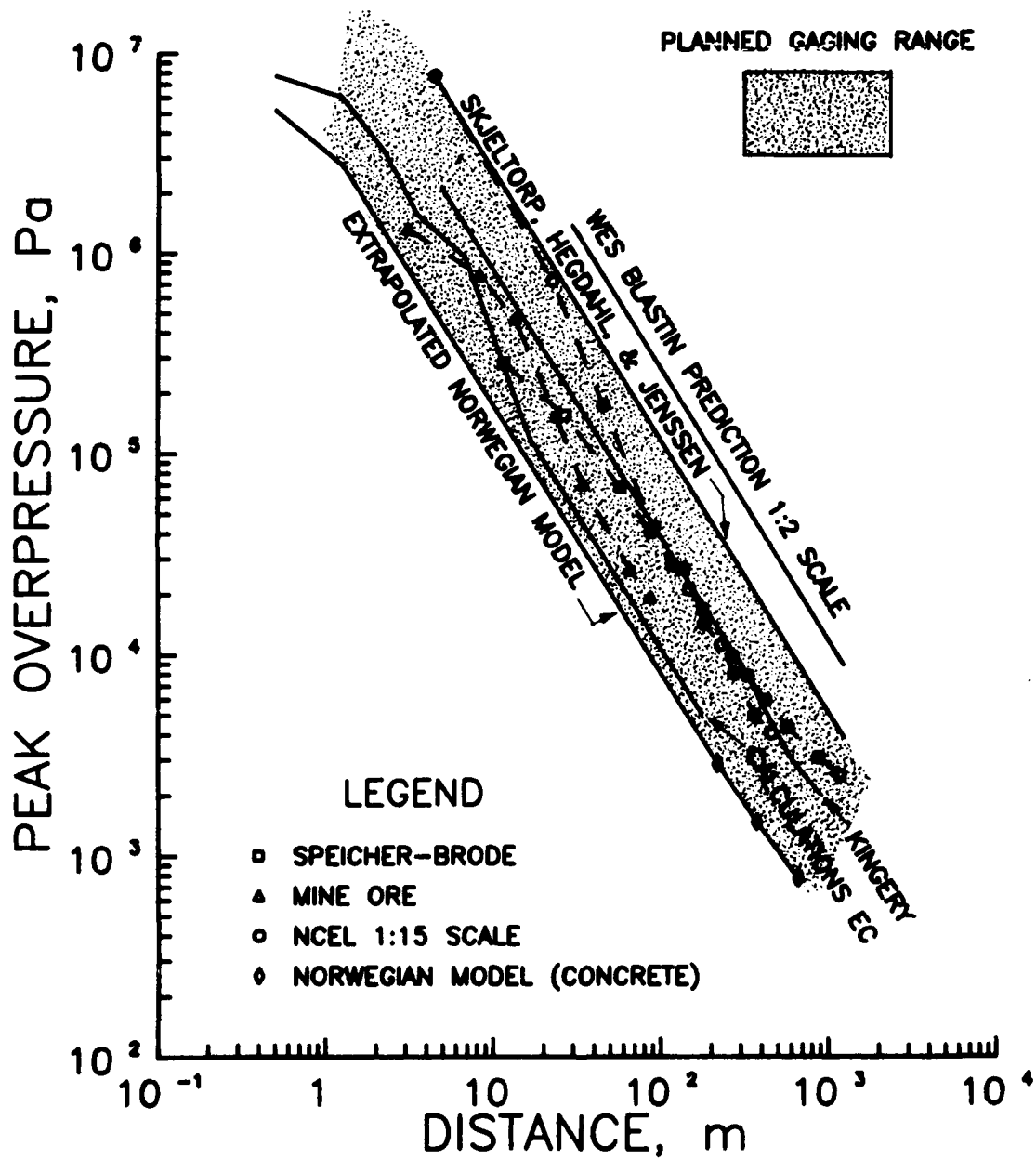


Figure 13. Free-field overpressure scaled to Shallow Underground Tunnel/Chamber Explosion Test parameters.

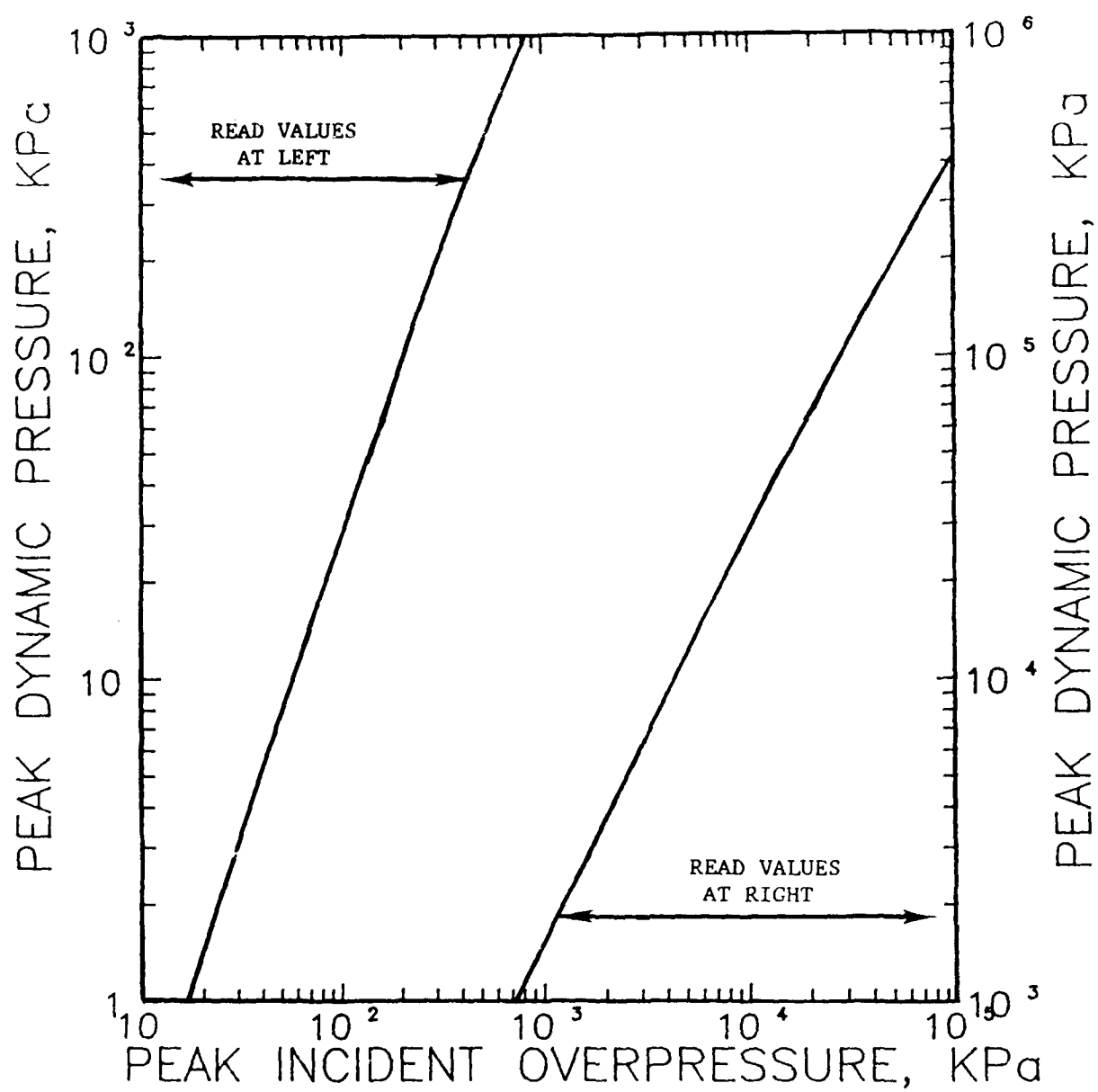


Figure 14. Peak incident pressure versus peak dynamic pressure, TM 5-855-1.

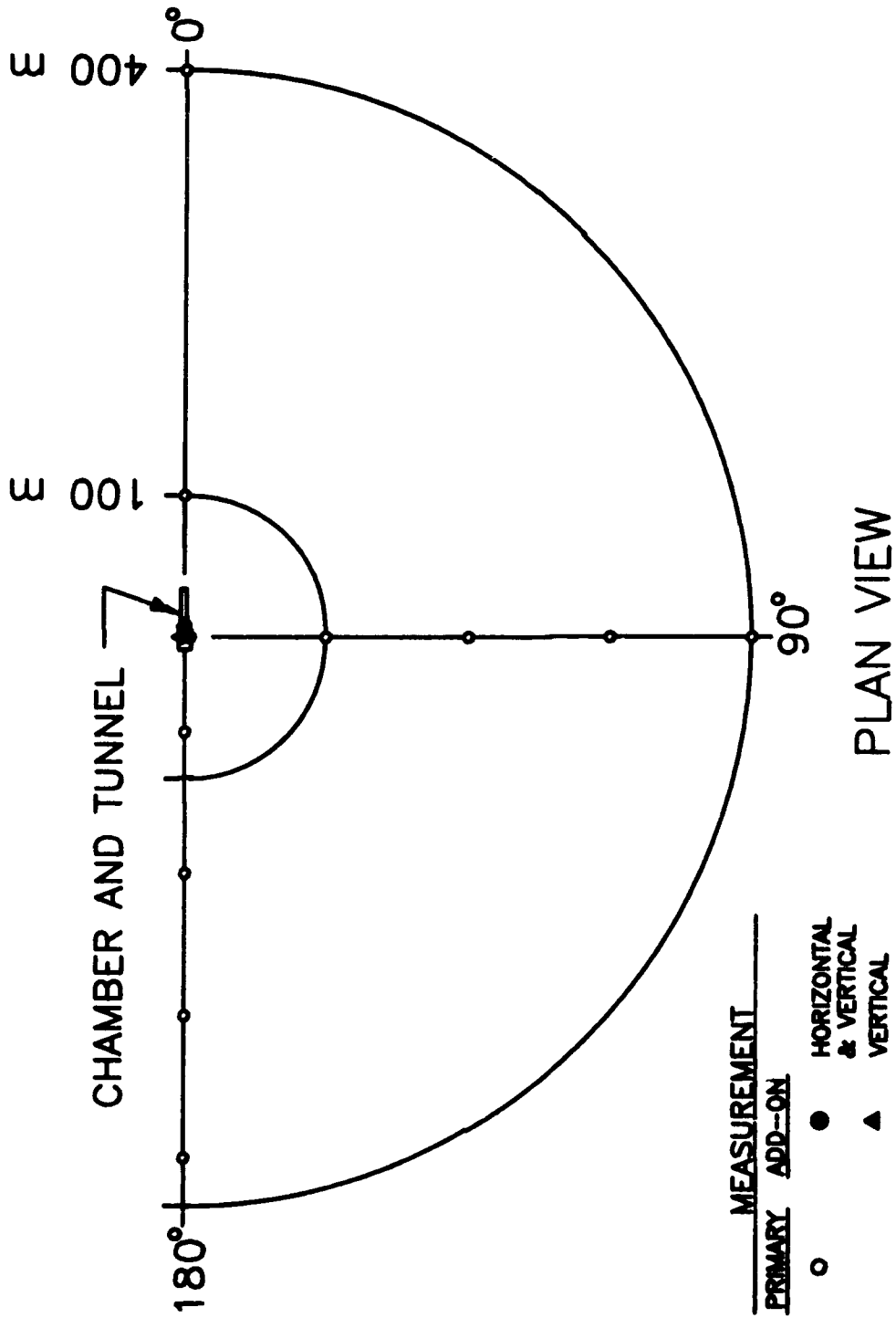


Figure 15. Free-field ground motion gage locations for Shallow Underground Tunnel/Chamber Explosion Test Program.

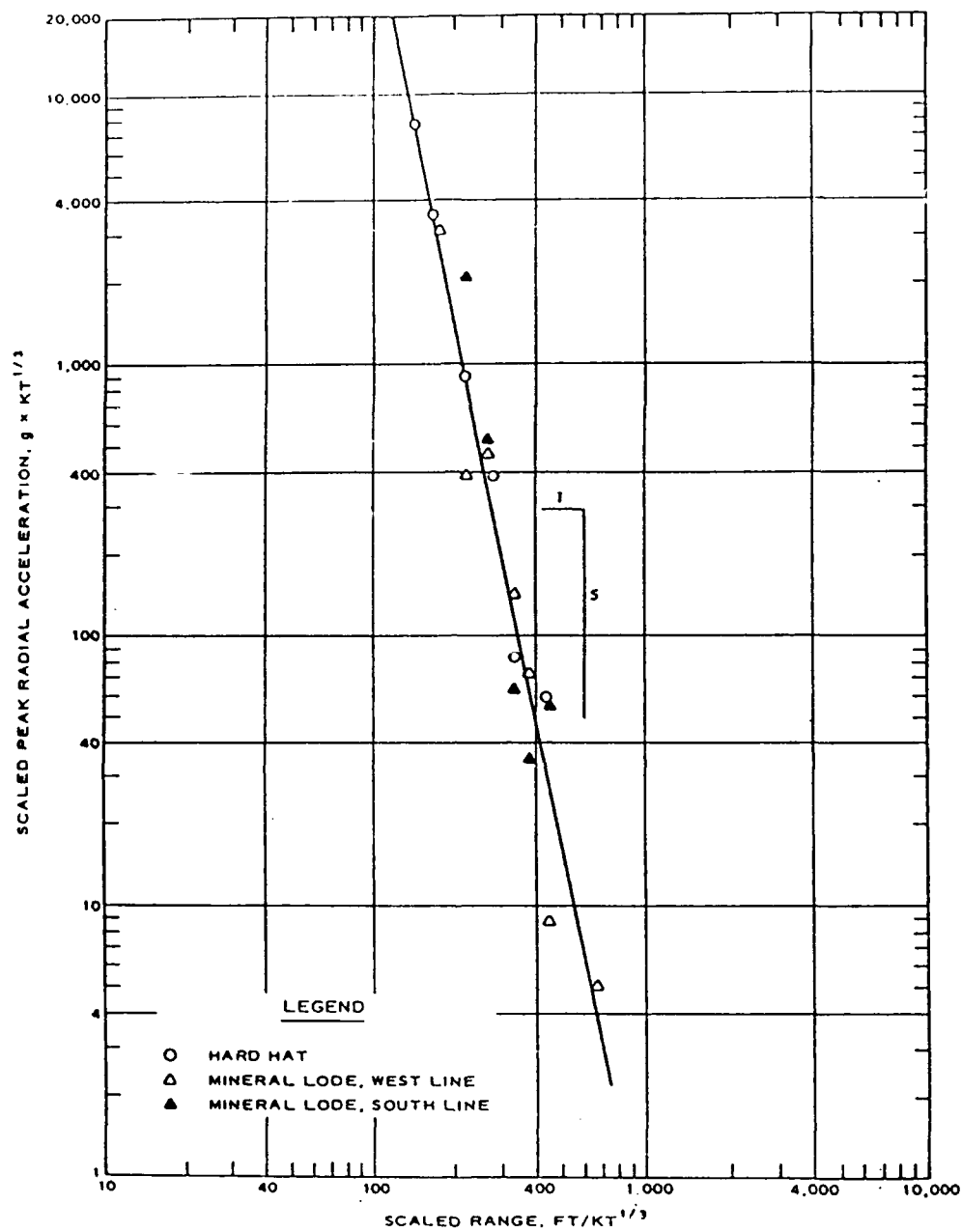


Figure 16. Scaled radial particle acceleration in rock, from HARD HAT (nuclear) and MINERAL LODE (high explosive) detonations.

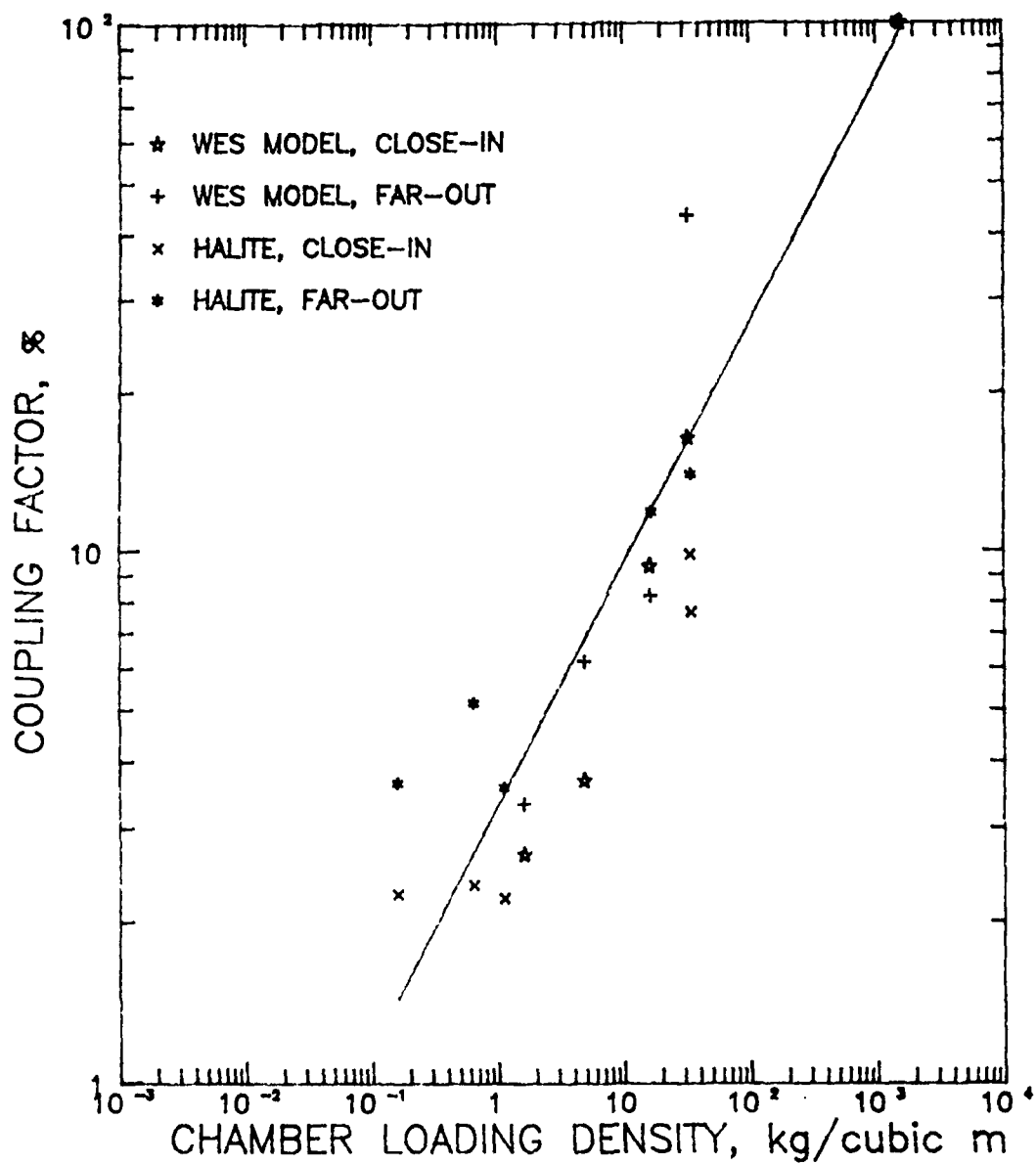


Figure 17. Coupling factor versus loading density.

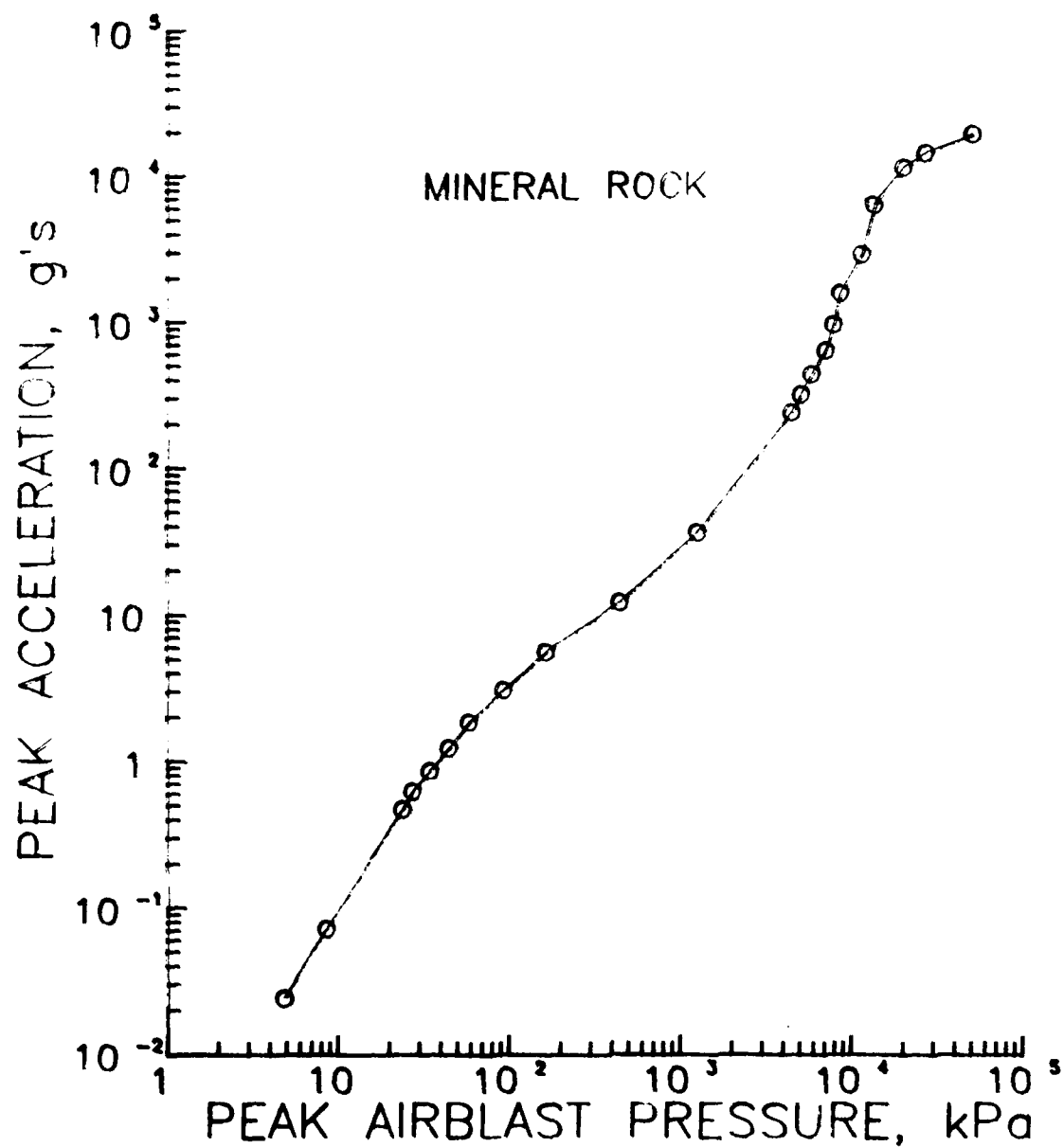


Figure 18. Airblast-induced acceleration in granite versus free-field airblast pressure, from the 100-ton MINERAL ROCK surface detonation.

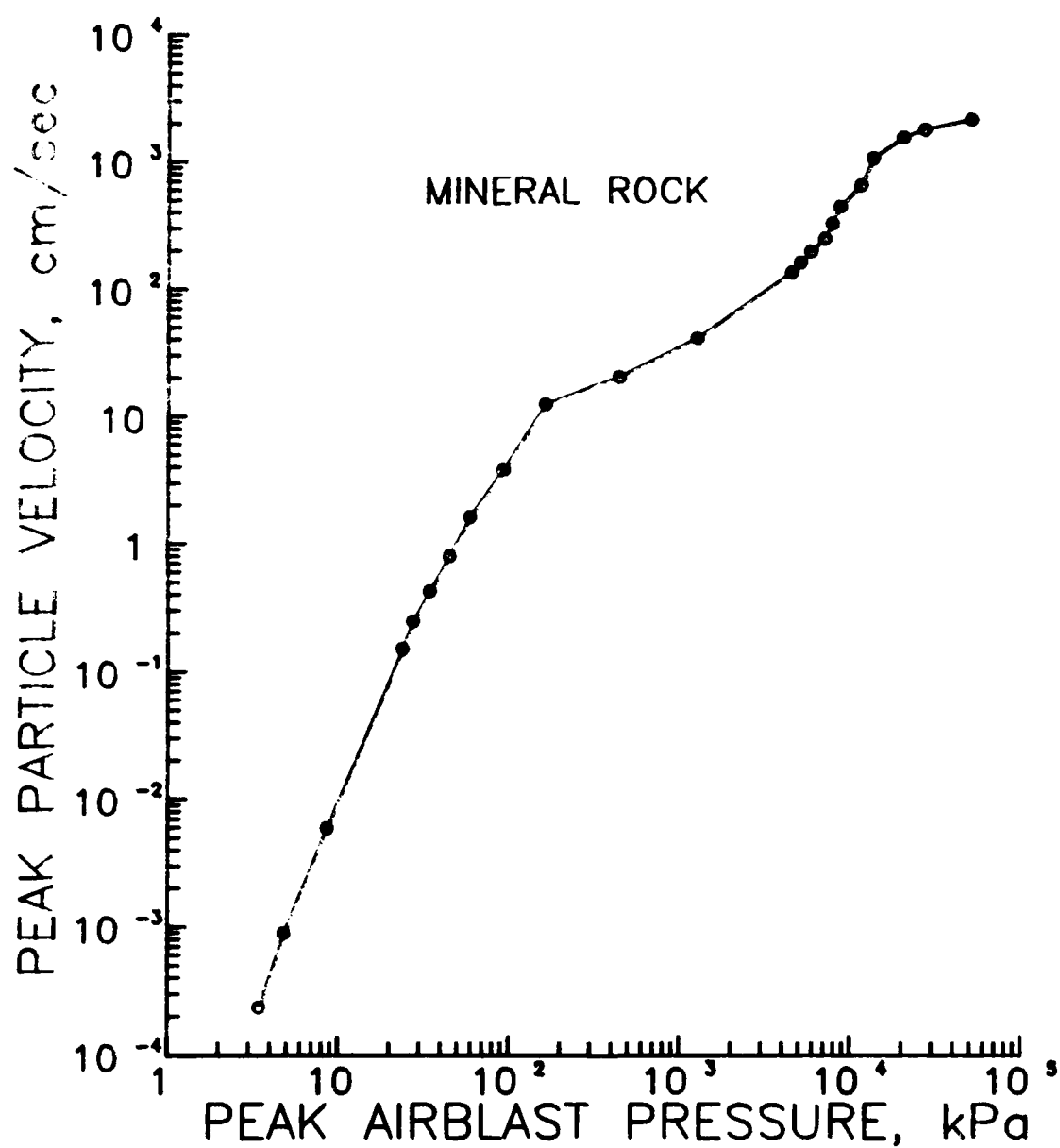


Figure 19. Peak airblast-induced particle velocity in rock versus free-field airblast pressure, from the MINERAL ROCK event.

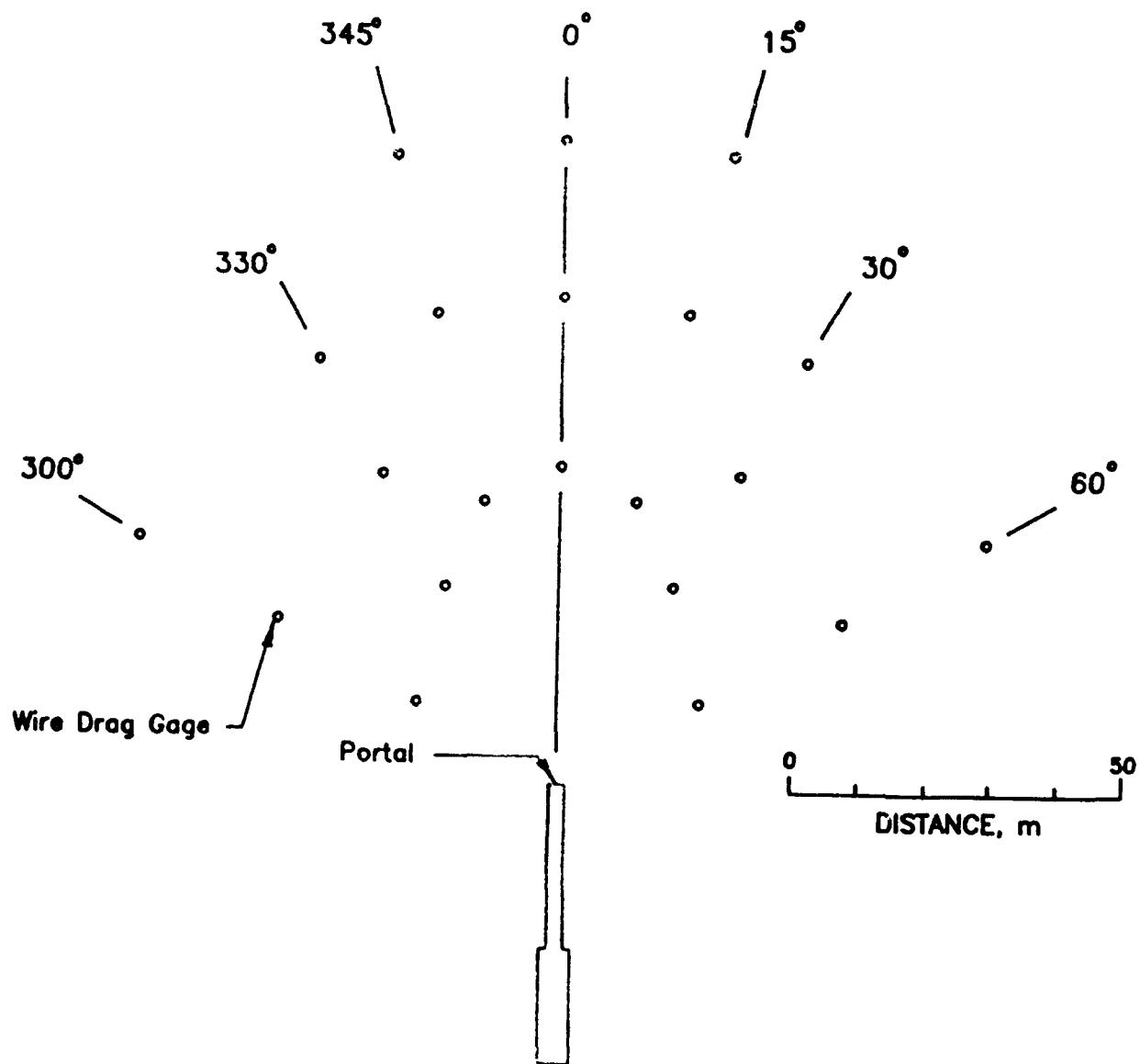


Figure 20. Wire drag gage locations for Shallow Underground Tunnel/Chamber Explosion Test.

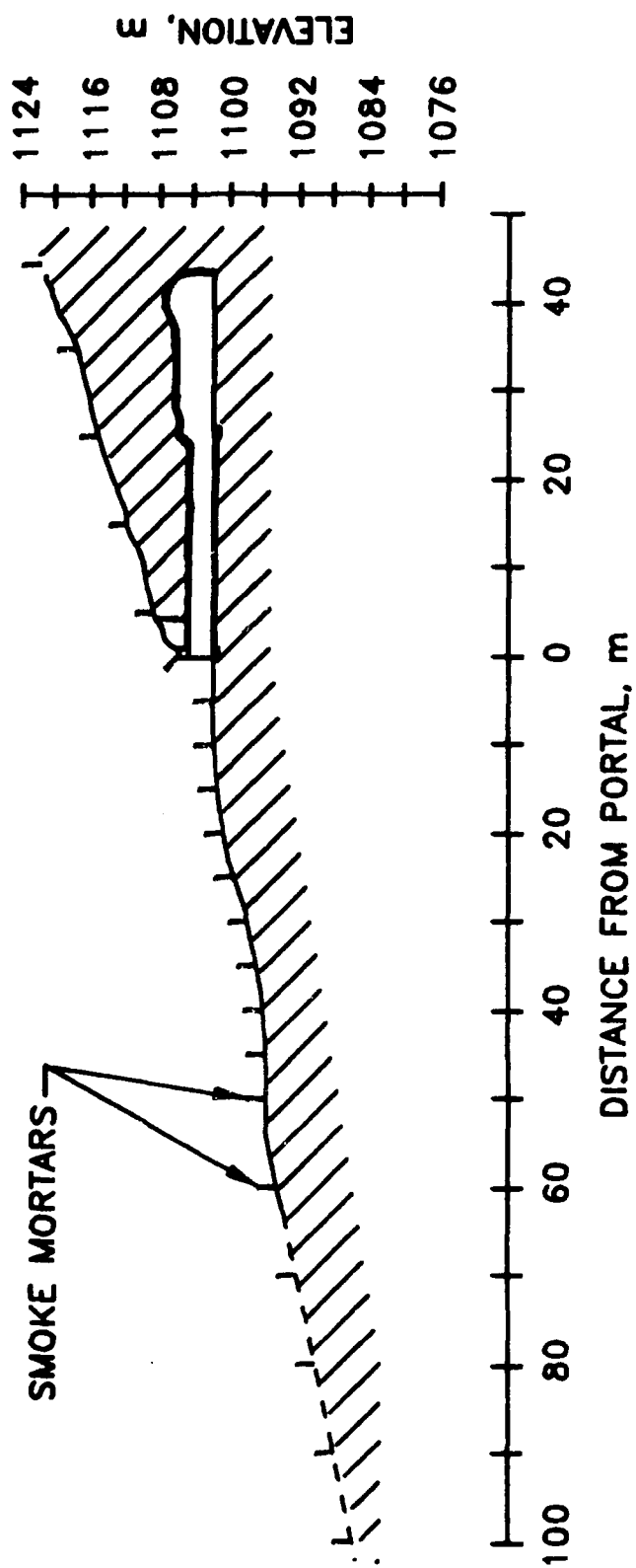


Figure 21. Smoke mortar locations for Shallow Underground Tunnel/Chamber Test.

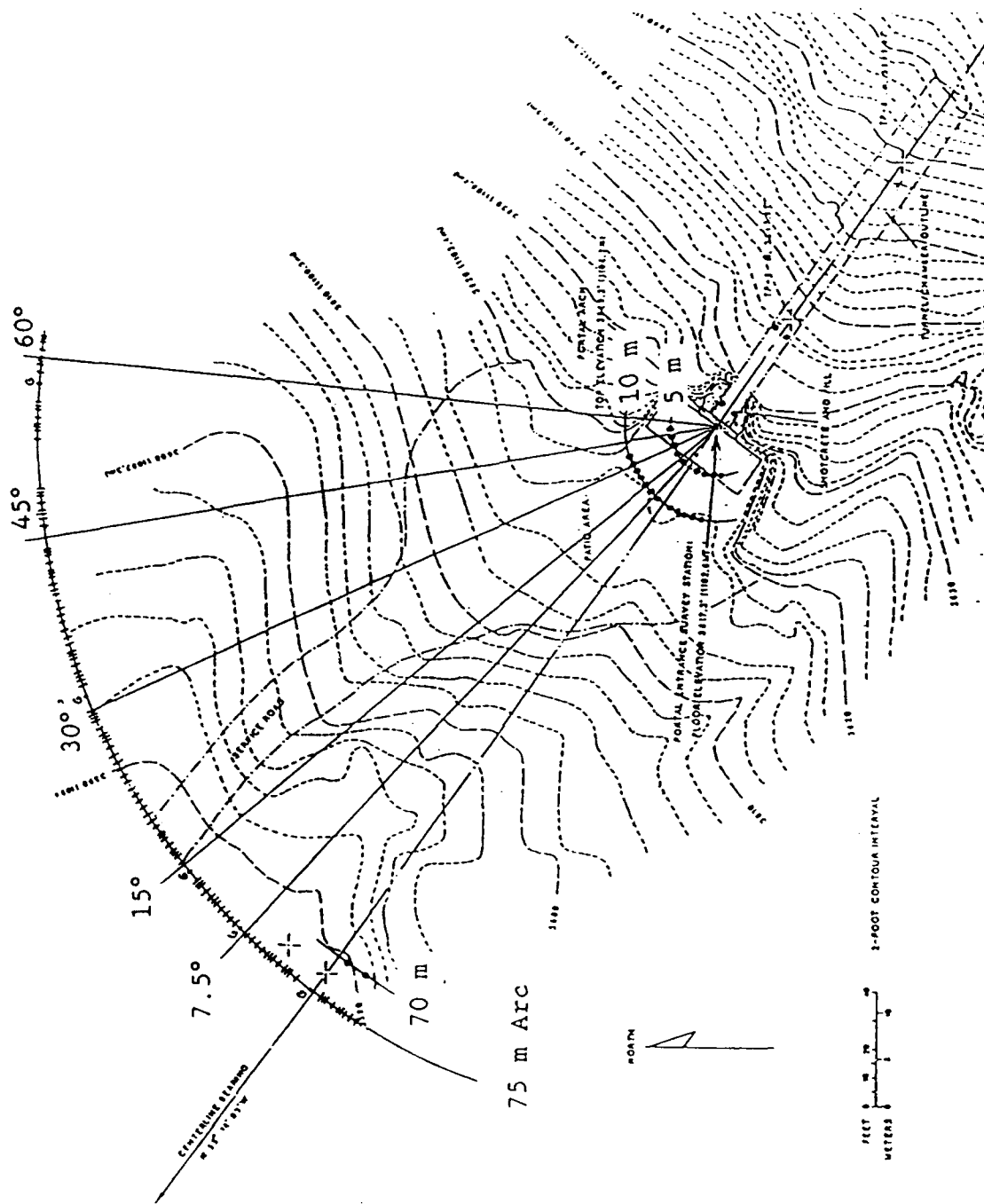


Figure 22. Contour map of test area showing pretest locations of blast cubes.

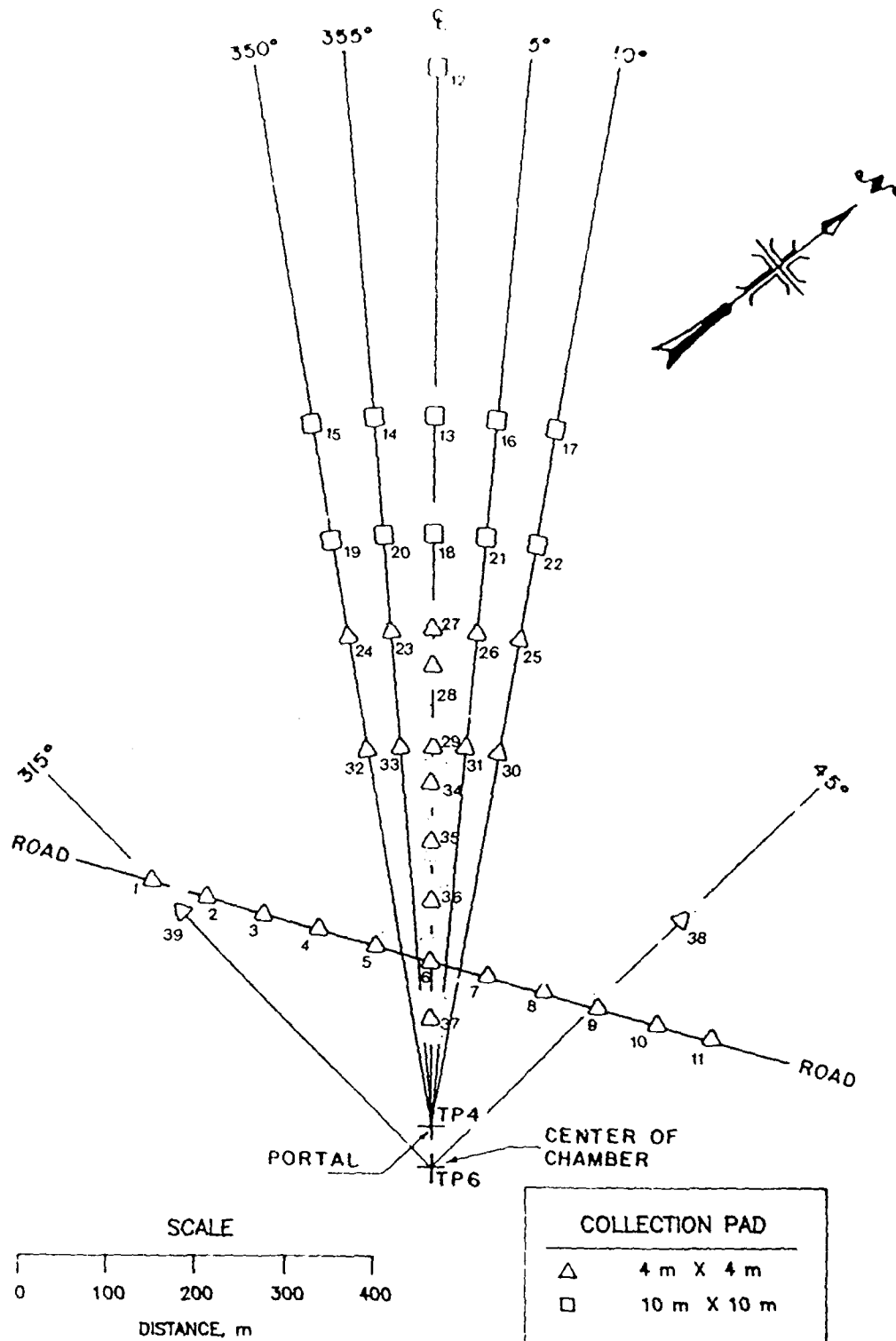


Figure 23. Ejecta collection pad locations. Numbers refer to corresponding stations in Table 9. Pads 1-5, 6-11, and 38-39 are referenced to the center of chamber. All other pads are referenced to tunnel portal.

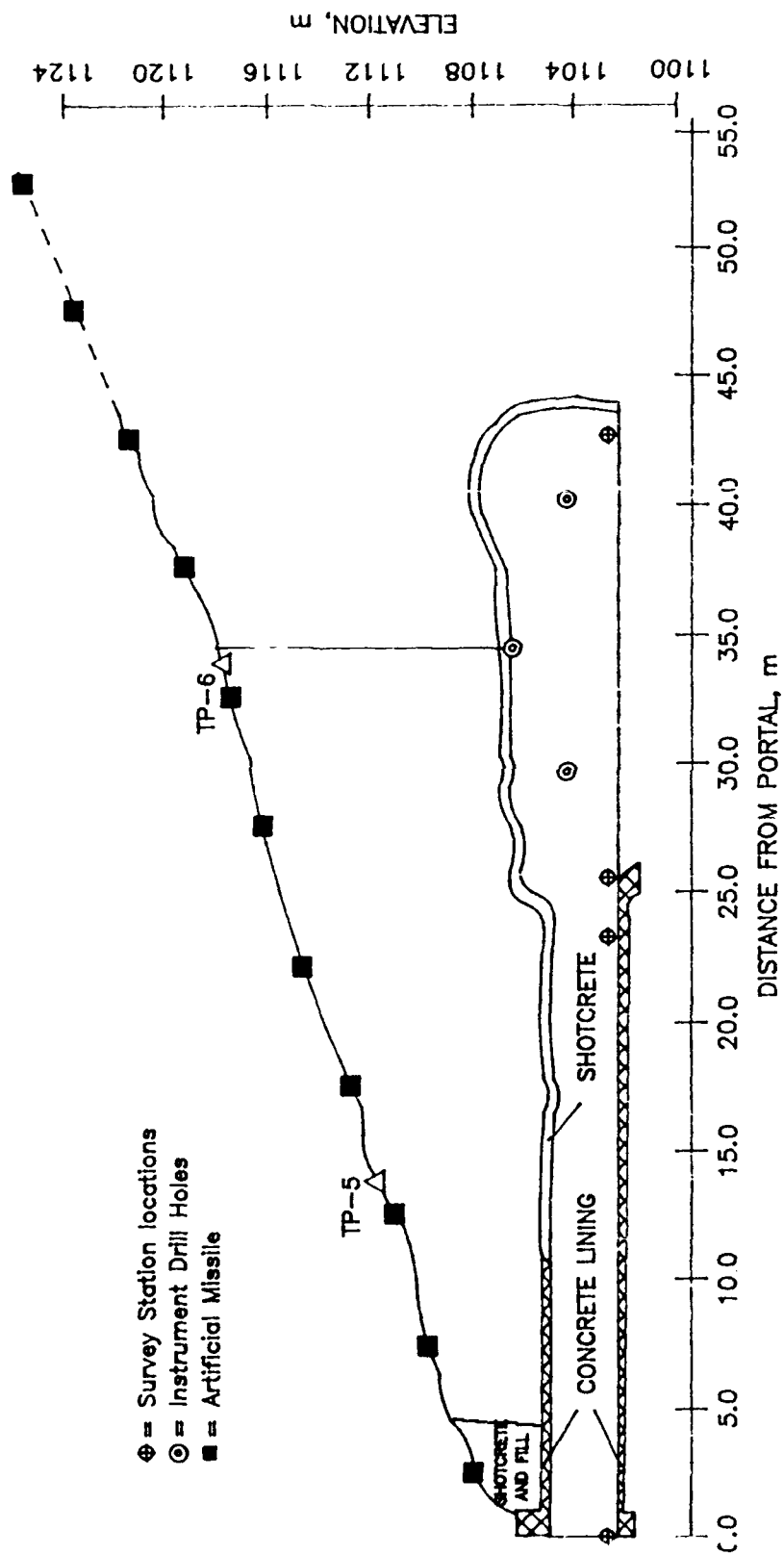


Figure 24. Pre-test locations of artificial missiles on overburden surface above tunnel/chamber centerline.

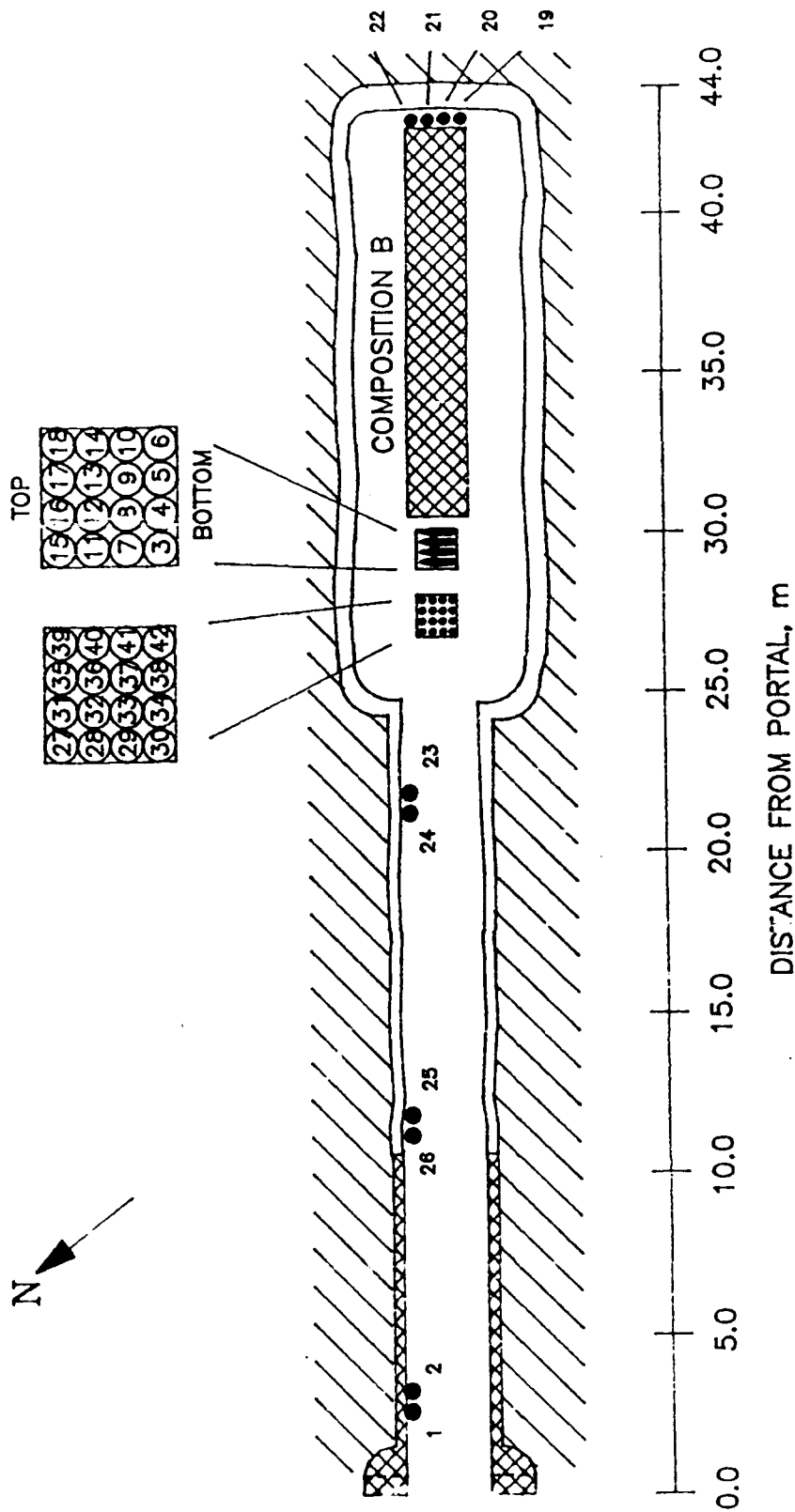


Figure 25. Pre-test locations of inert 155-mm artillery rounds for Shallow Underground Tunnel/Chamber Test Program. Each inert round was coded for identification.

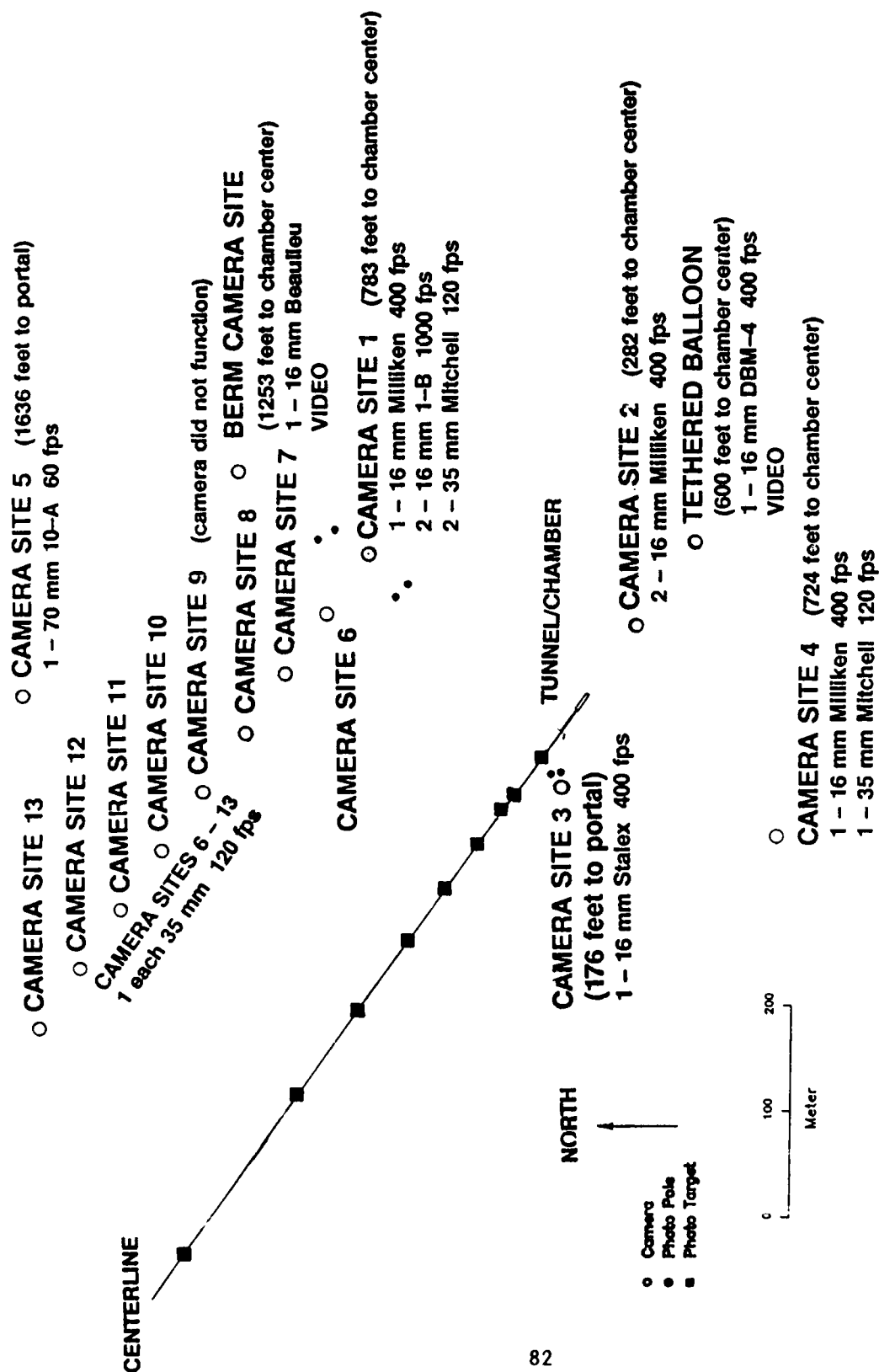


Figure 26. Camera, photo pole and photo target locations for Shallow Underground Tunnel/Chamber Explosion Test.

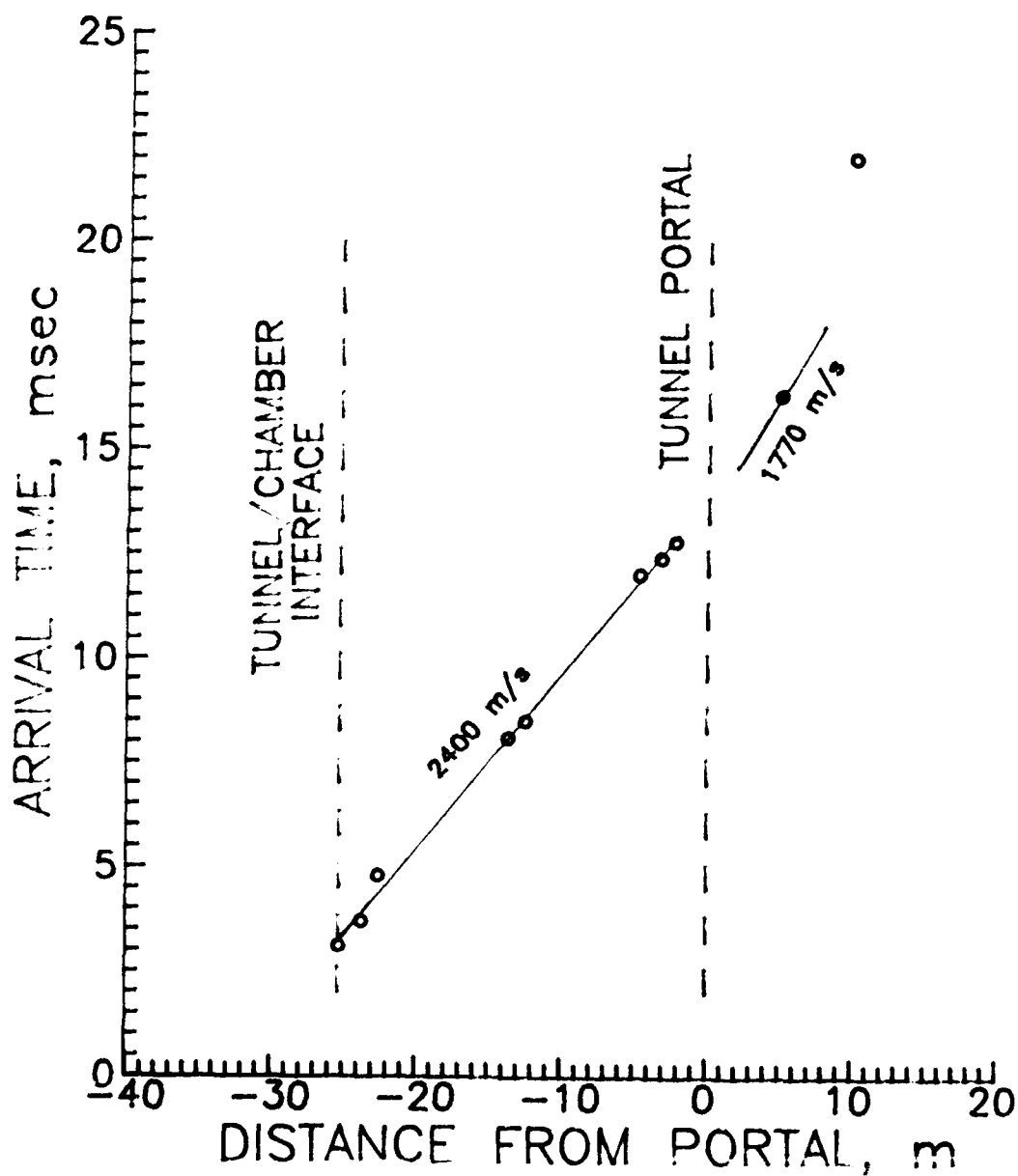


Figure 27. Shock wave arrival time in and just outside the access tunnel. The shock velocity at Gage A.2 (5 m outside the tunnel) was calculated from measured stagnation pressure.

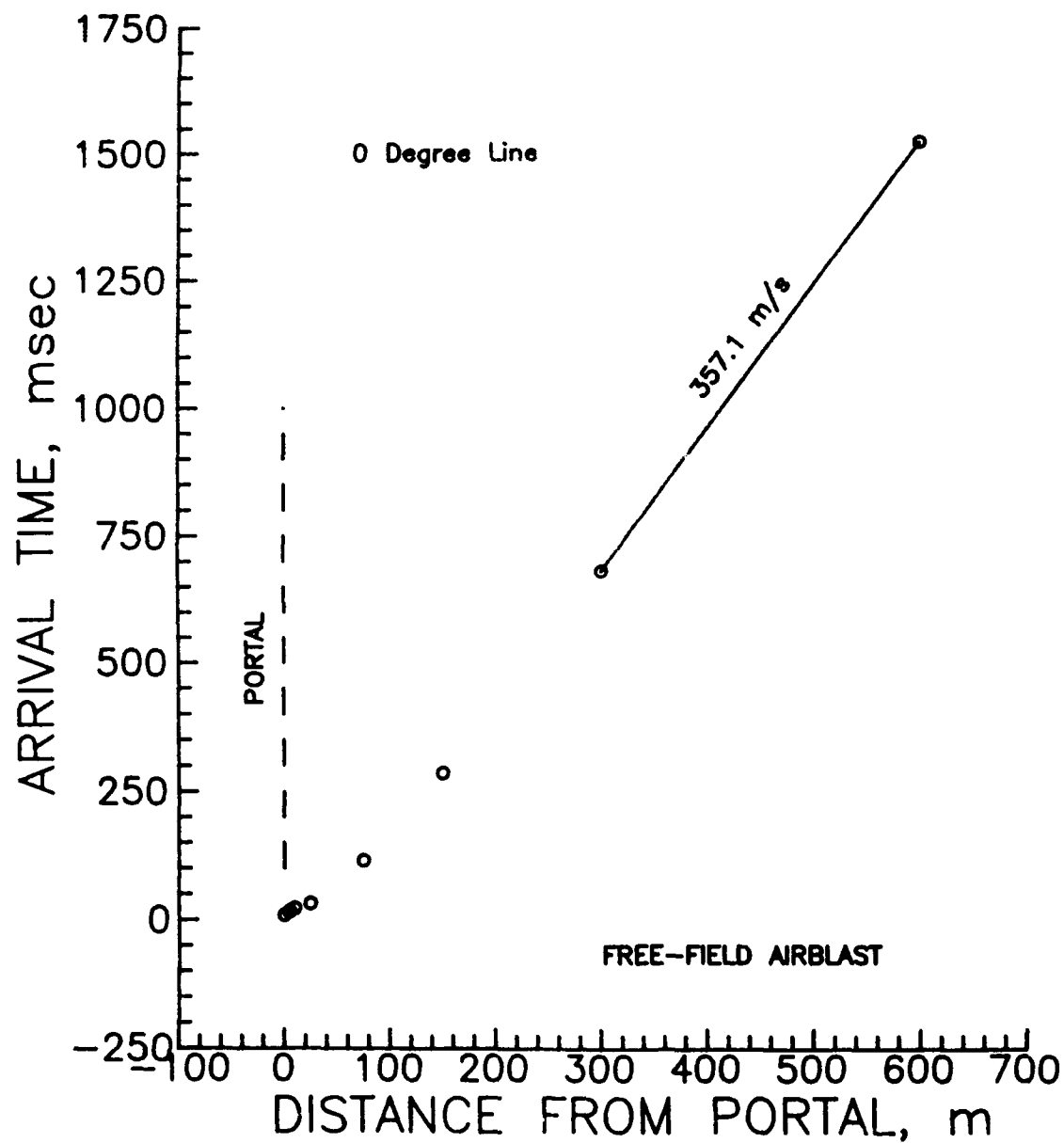


Figure 28. Free-field airblast shock wave arrival time versus distance from tunnel portal along the extended tunnel/chamber centerline, Shallow Underground Tunnel/Chamber Explosion Test.

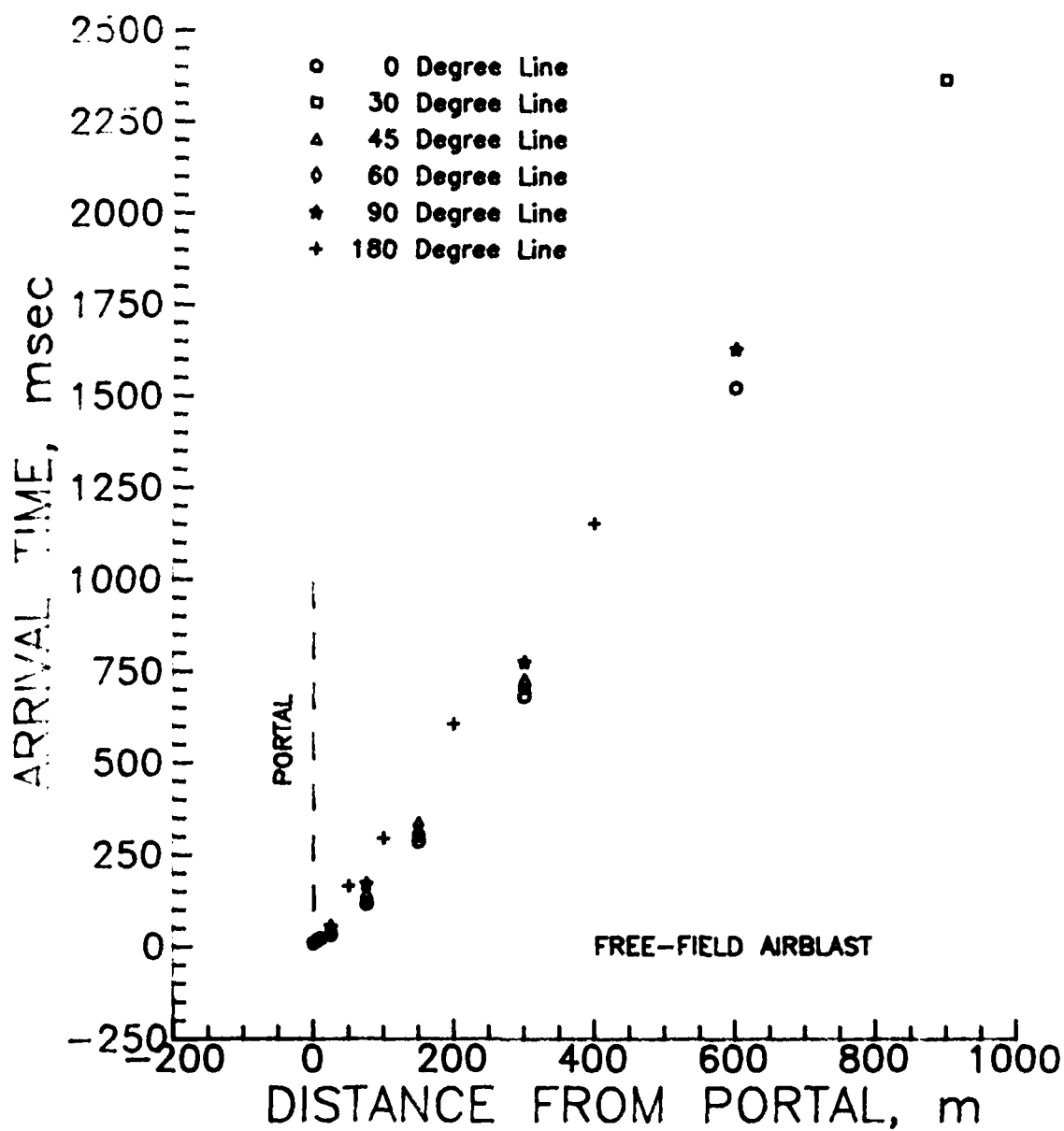


Figure 29. Free-field airblast shock wave arrival time versus distance from tunnel portal, Shallow Underground Tunnel/Chamber Explosion Test.

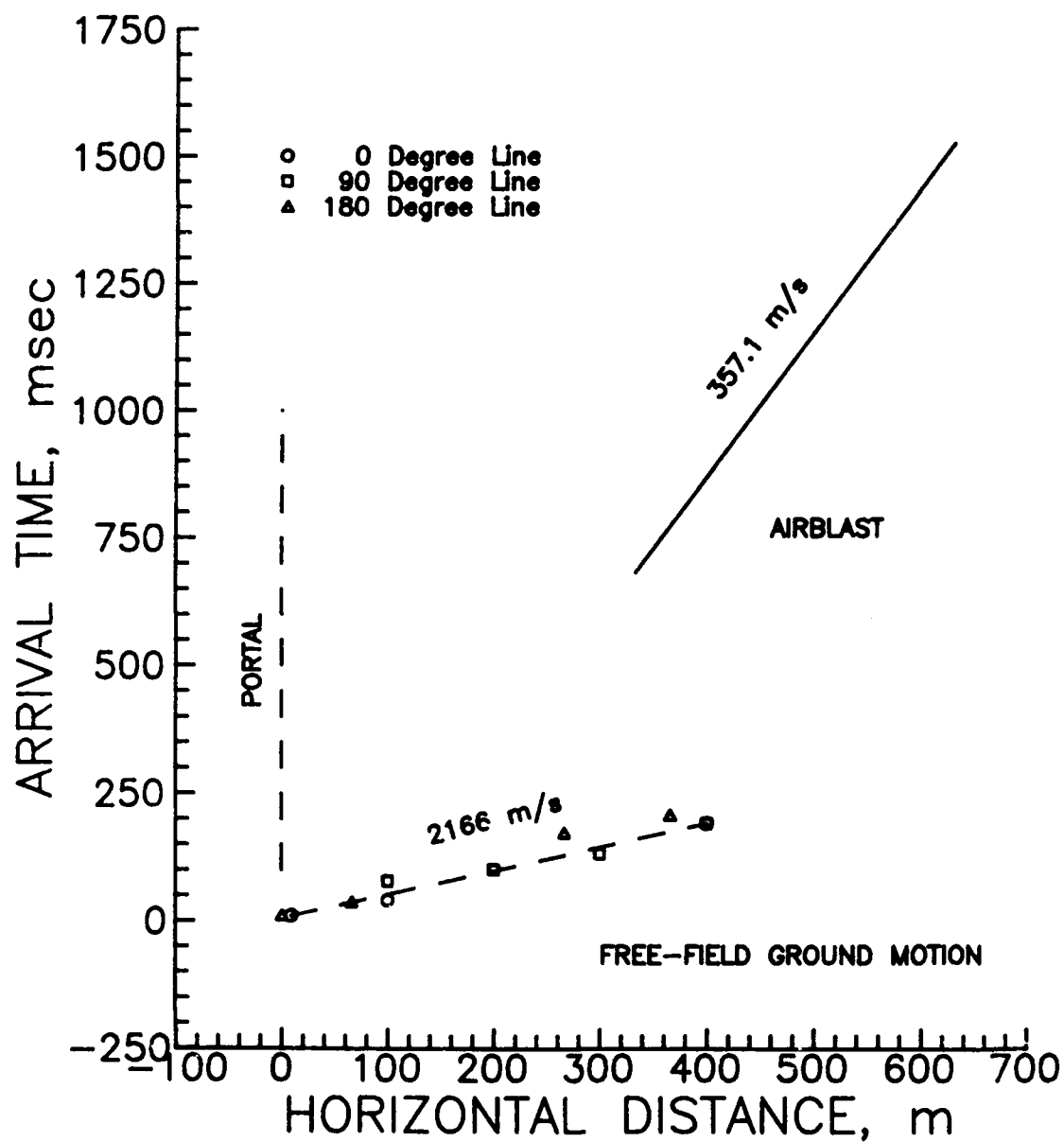


Figure 30. Free-field ground shock arrival time versus distance from center of chamber, Shallow Underground Tunnel/Chamber Explosion Test. Long-range free-field airblast arrival along 0-degree line is shown for comparison.

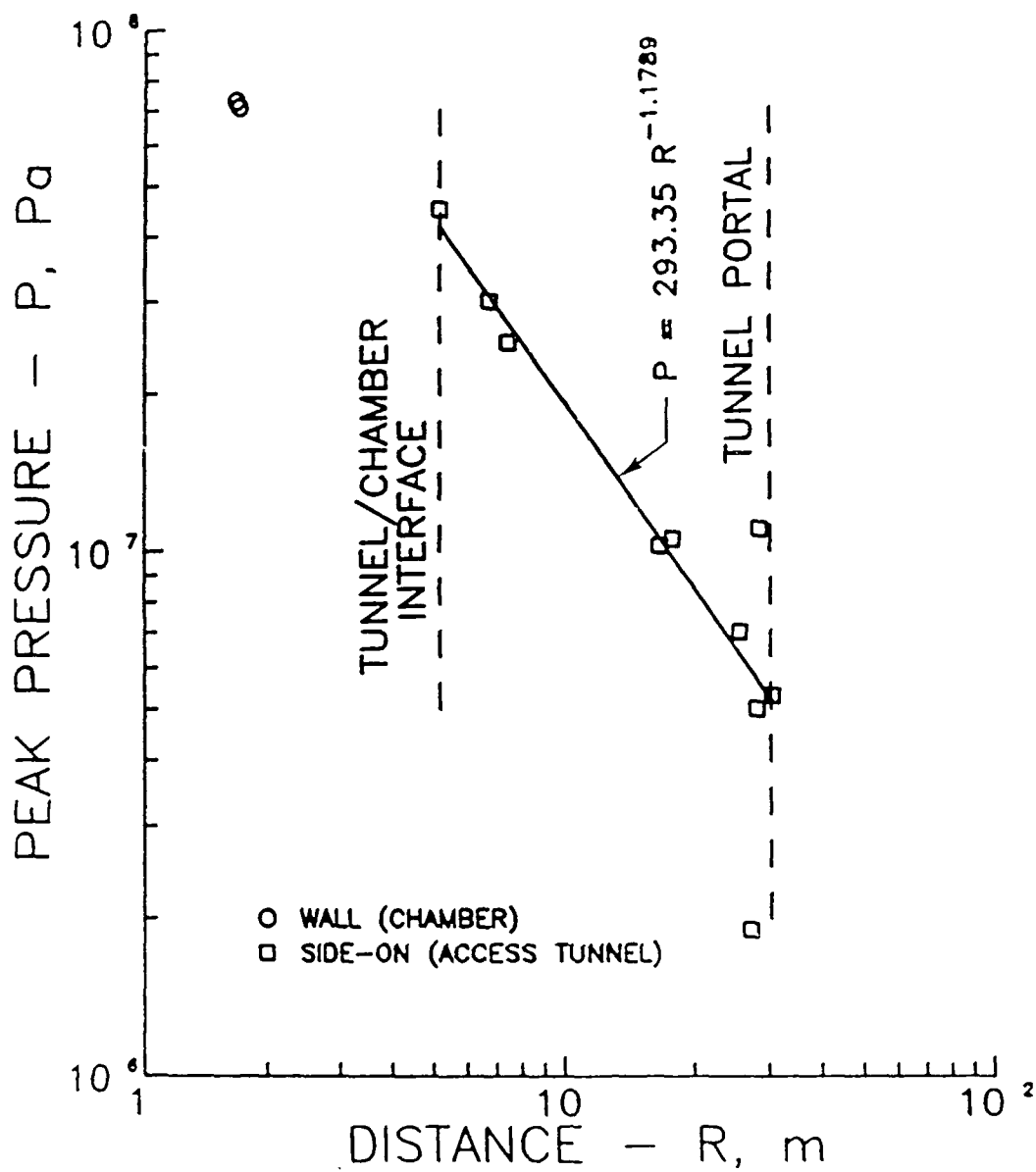


Figure 31. Peak side-on overpressure versus distance from the initiation end of the explosive charge, Shallow Underground Tunnel/Chamber Explosion Test. A least square fit to the peak tunnel pressure data gives an estimated exit pressure of 5.2 MPa.

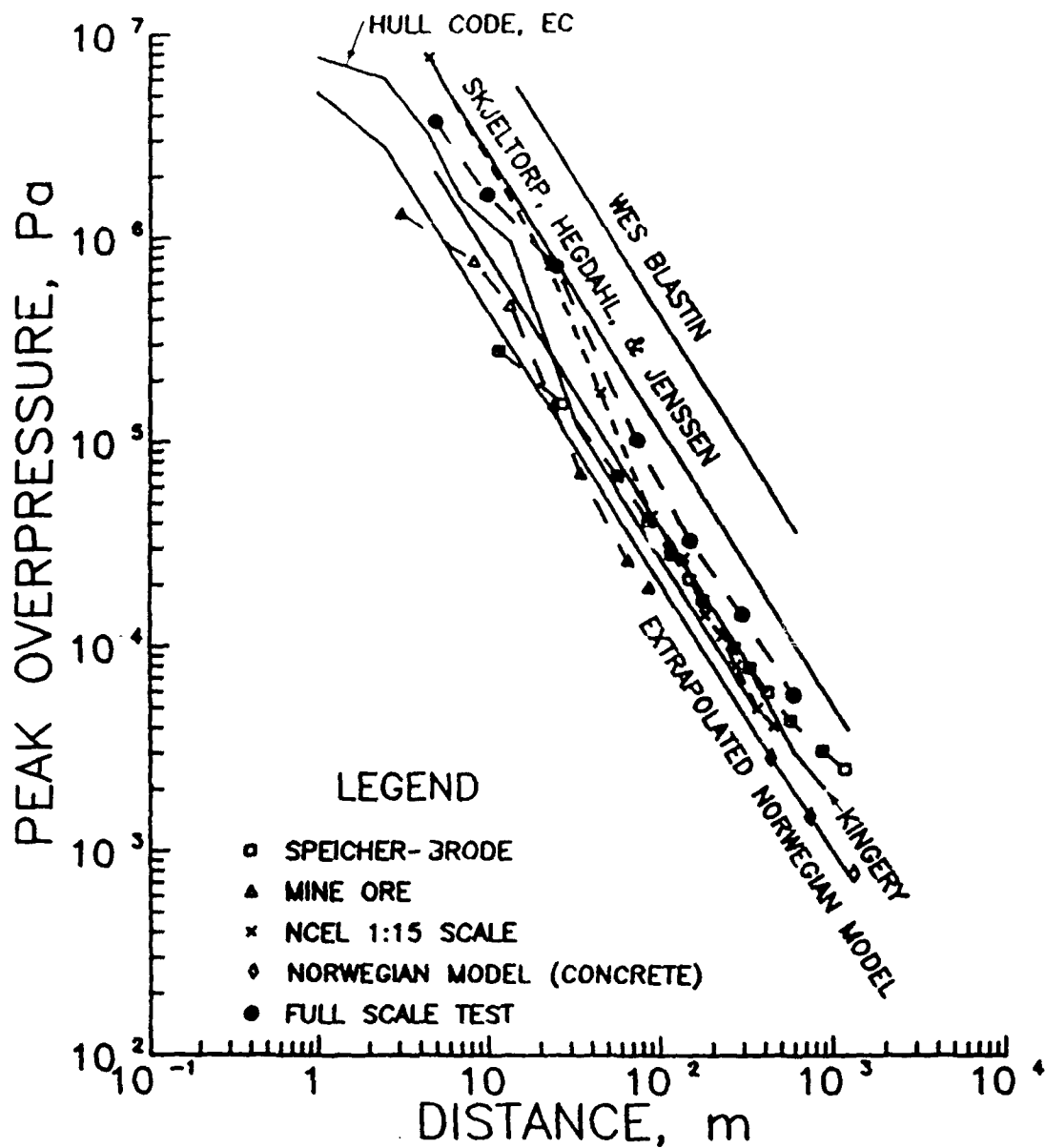


Figure 32. Comparison of predictions with measured free-field airblast data (0-degree azimuth) from Shallow Underground Tunnel/Chamber Explosion Test. Empirical relations (Skjeltorp and Kingery) use empirically calculated exit pressure. WES BLASTIN curve used 1/4 of code-predicted exit pressure in Skjeltorp free-field equation.

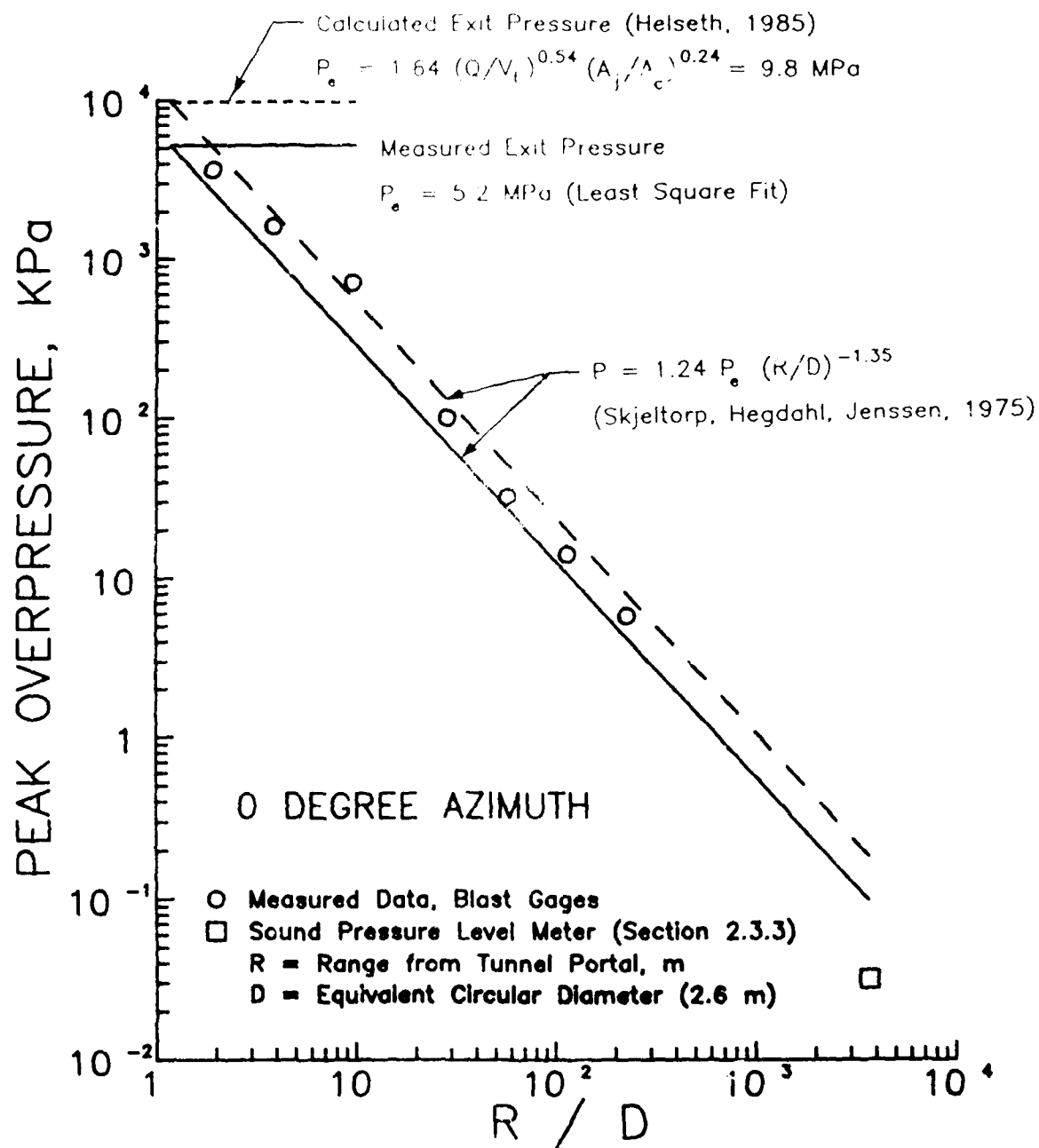


Figure 33. Comparison of measured full-scale and calculated free-field airblast data, 0° azimuth, Shallow Underground Tunnel/Chamber Explosion Test. Calculated (Helseth, 1985) and measured (least square fit to tunnel pressure data) exit pressures were used in the free-field airblast calculations.

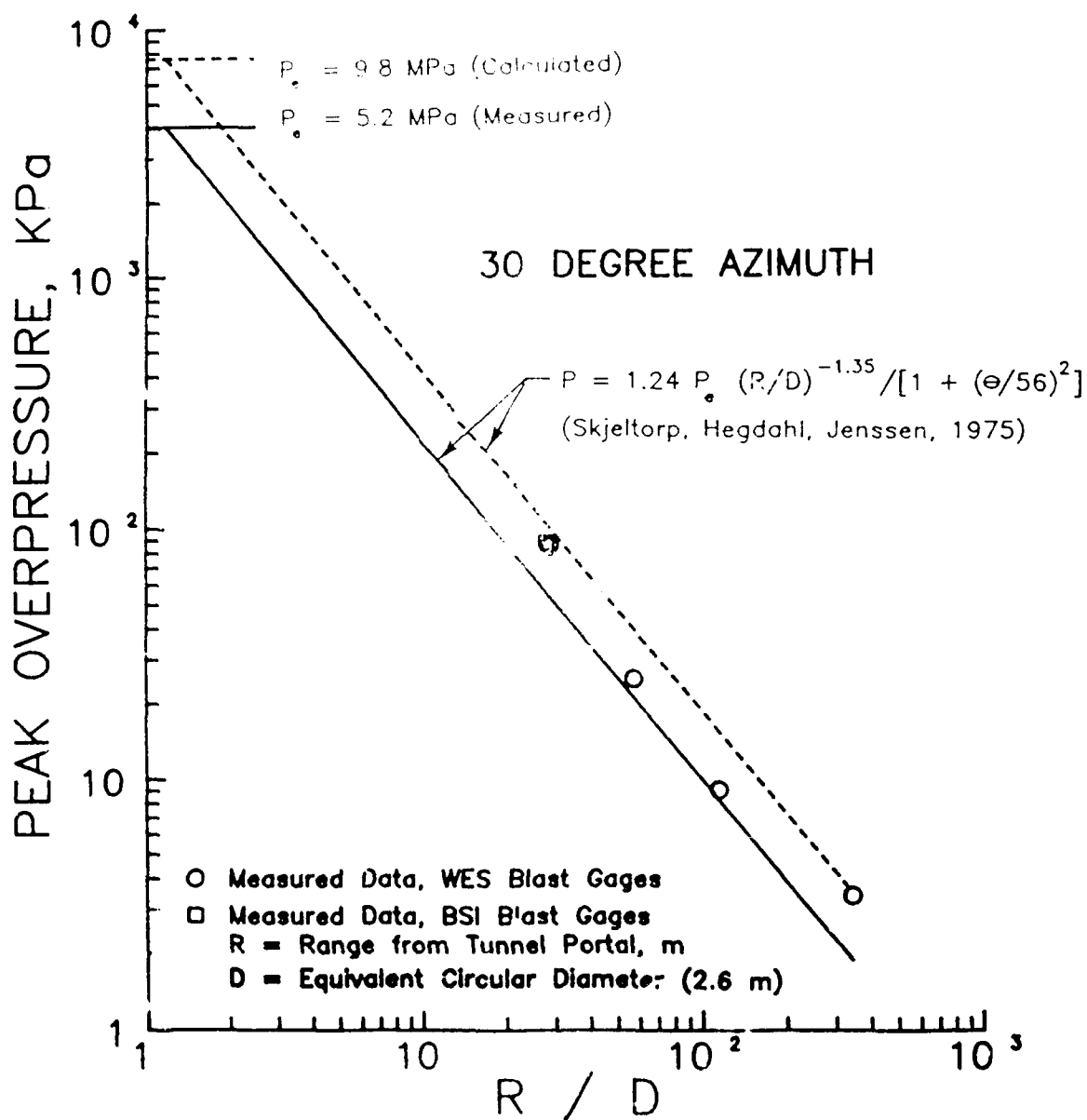


Figure 34. Comparison of measured full-scale and calculated free-field airblast data, 30° azimuth, Shallow Underground Tunnel/Chamber Explosion Test. Calculated (Helseth, 1985) and measured (least square fit to tunnel pressure data) exit pressures were used in the free-field airblast calculations.

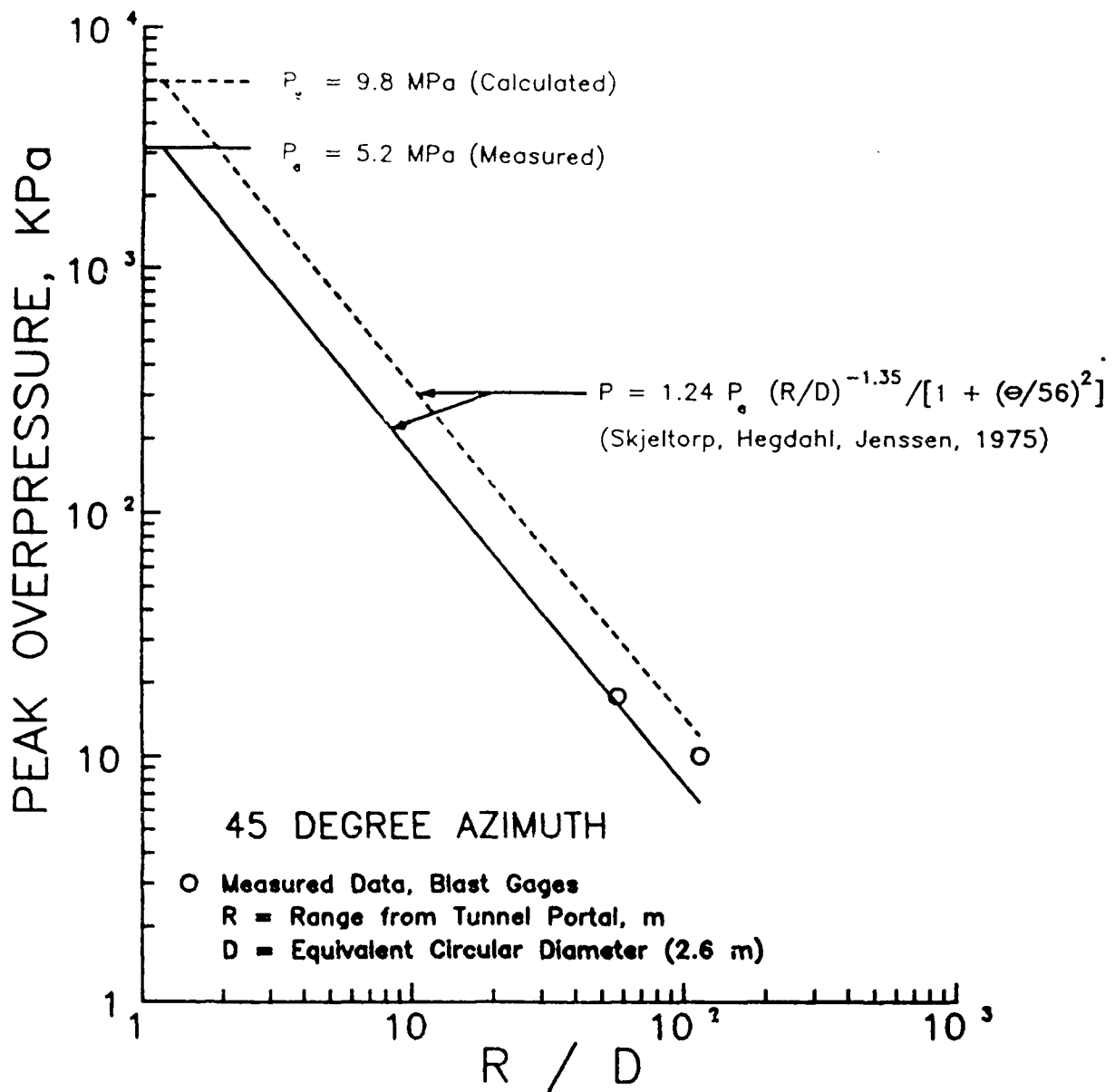


Figure 35. Comparison of measured full-scale and calculated free-field airblast data, 45° azimuth, Shallow Underground Tunnel/Chamber Explosion Test. Calculated (Helseth, 1985) and measured (least square fit to tunnel pressure data) exit pressures were used in the free-field airblast calculations.

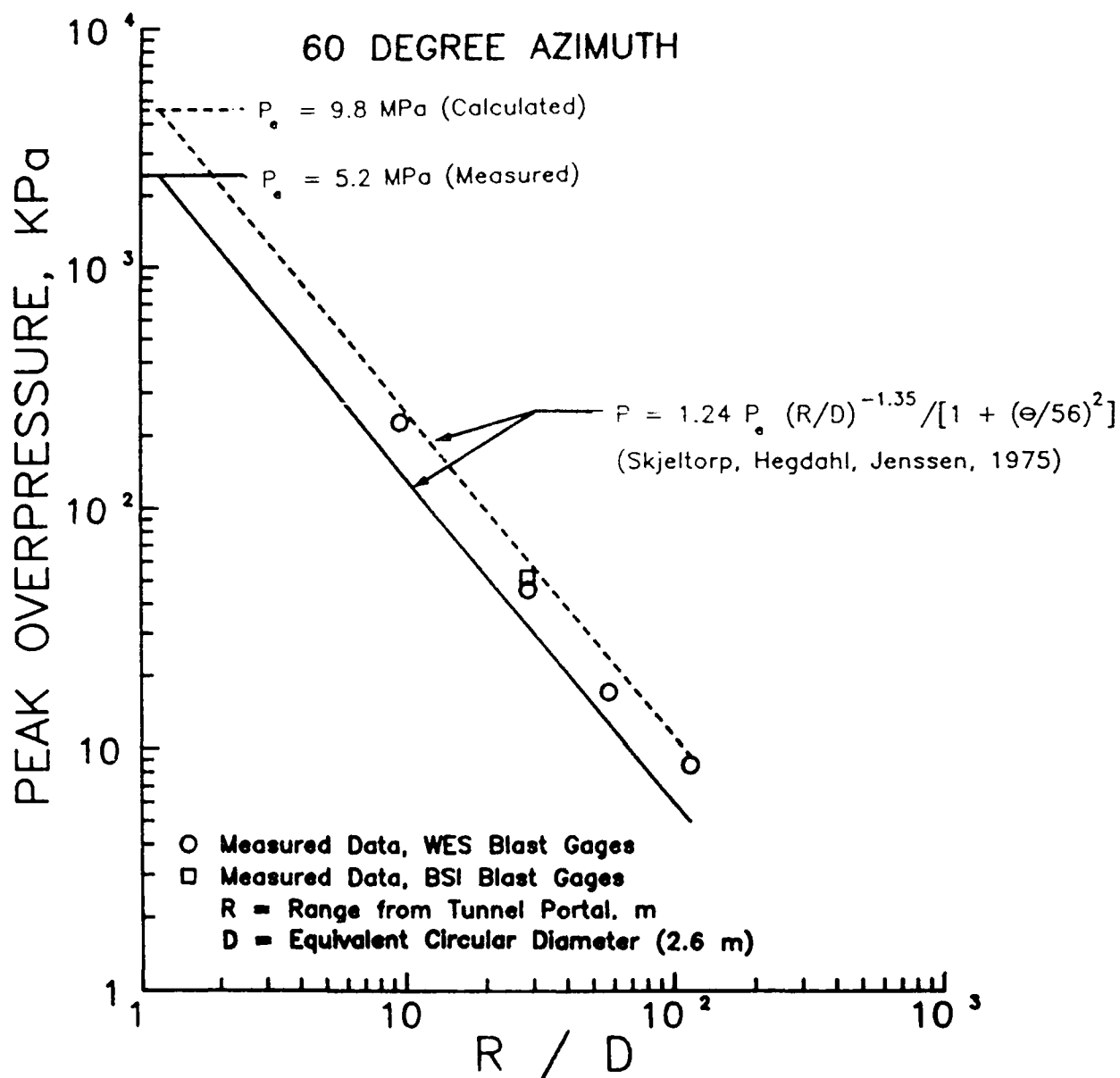


Figure 36. Comparison of measured full-scale and calculated free-field airblast data, 60° azimuth, Shallow Underground Tunnel/Chamber Explosion Test. Calculated (Helseth, 1985) and measured (least square fit to tunnel pressure data) exit pressures were used in the free-field airblast calculations.

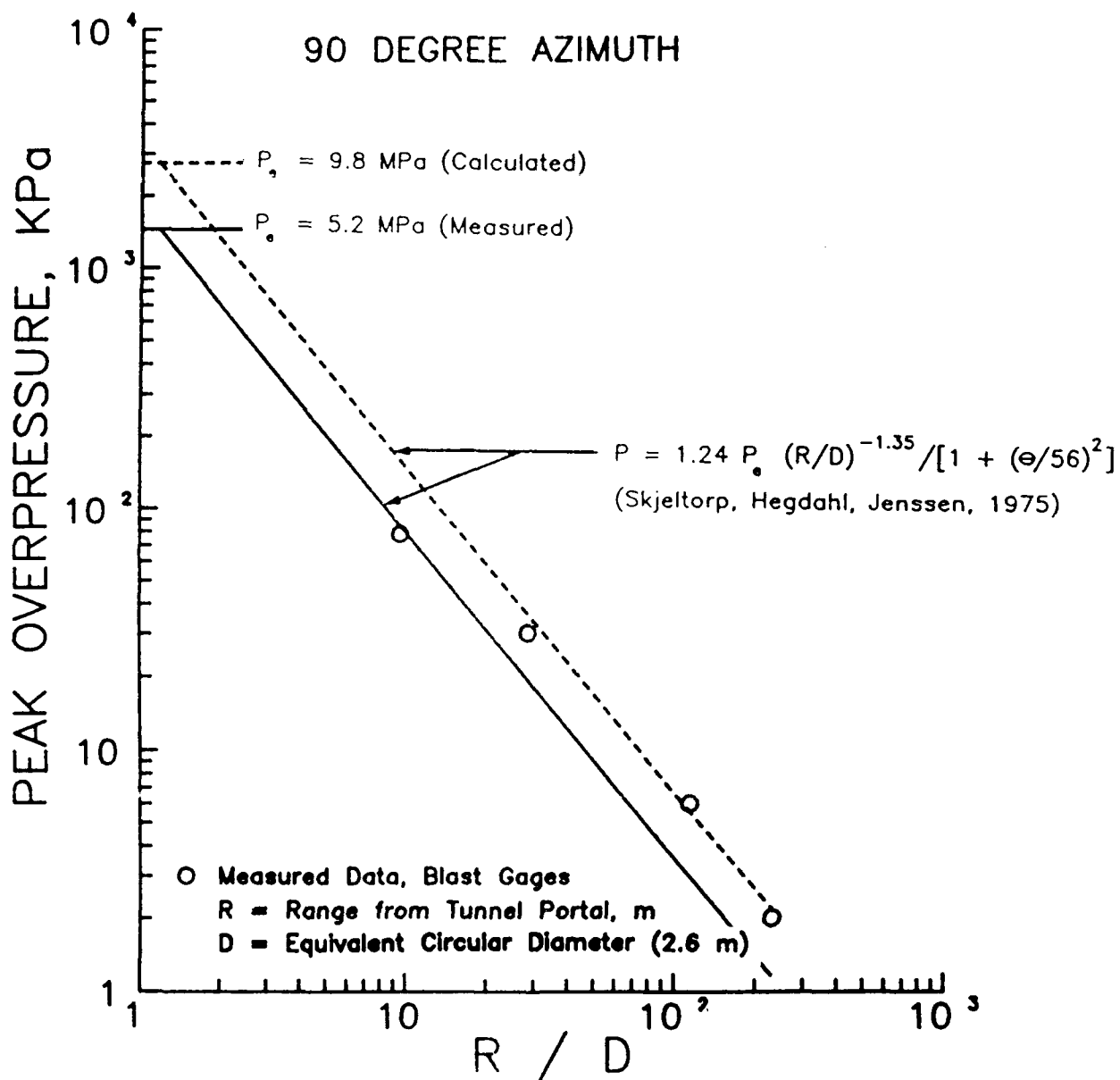


Figure 37. Comparison of measured full-scale and calculated free-field airblast data, 90° azimuth, Shallow Underground Tunnel/Chamber Explosion Test. Calculated (Helseth, 1985) and measured (least square fit to tunnel pressure data) exit pressures were used in the free-field airblast calculations.

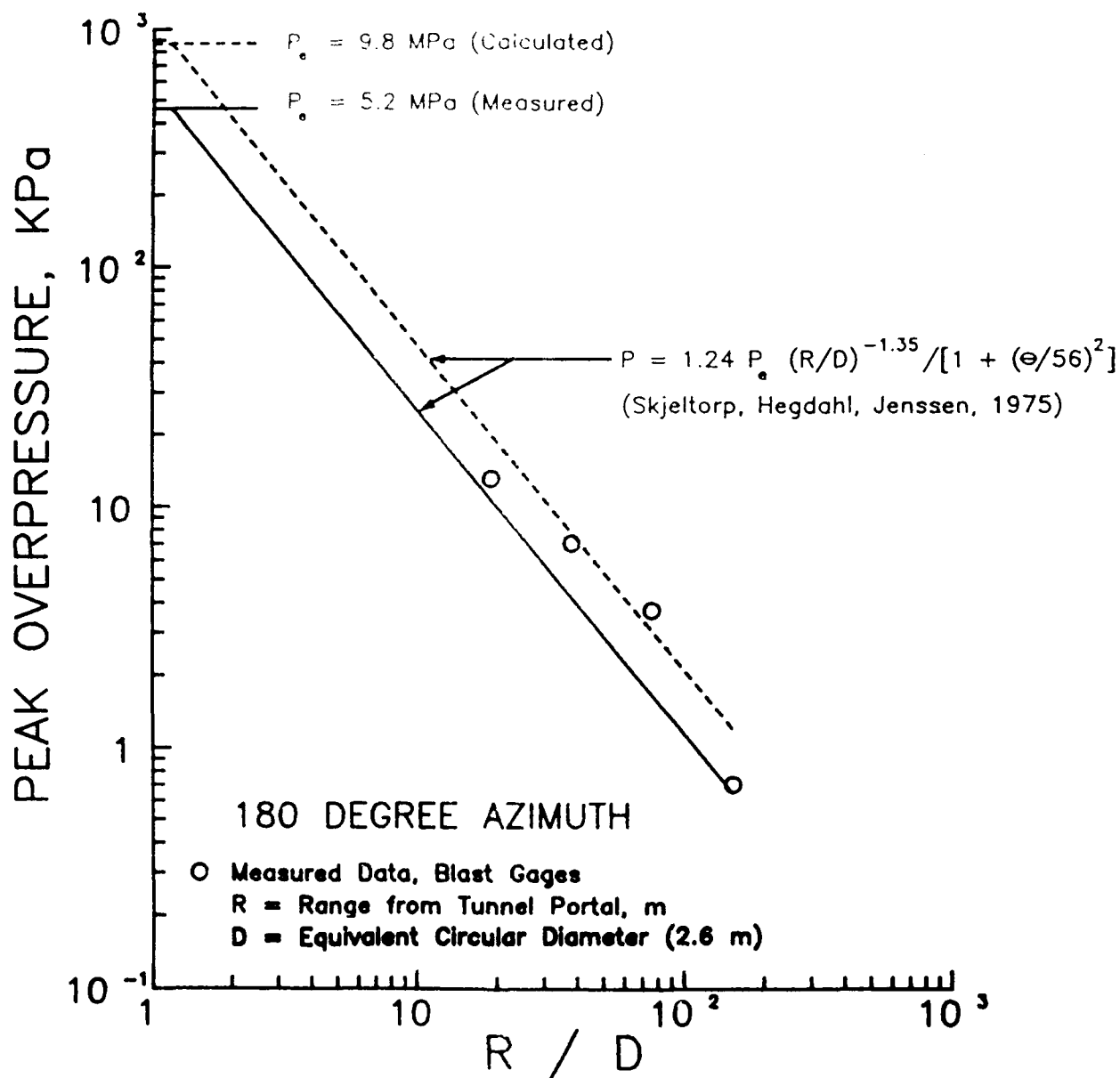


Figure 38. Comparison of measured full-scale and calculated free-field airblast data, 180° azimuth, Shallow Underground Tunnel/Chamber Explosion Test. Calculated (Helseth, 1985) and measured (least square fit to tunnel pressure data) exit pressures were used in the free-field airblast calculations.

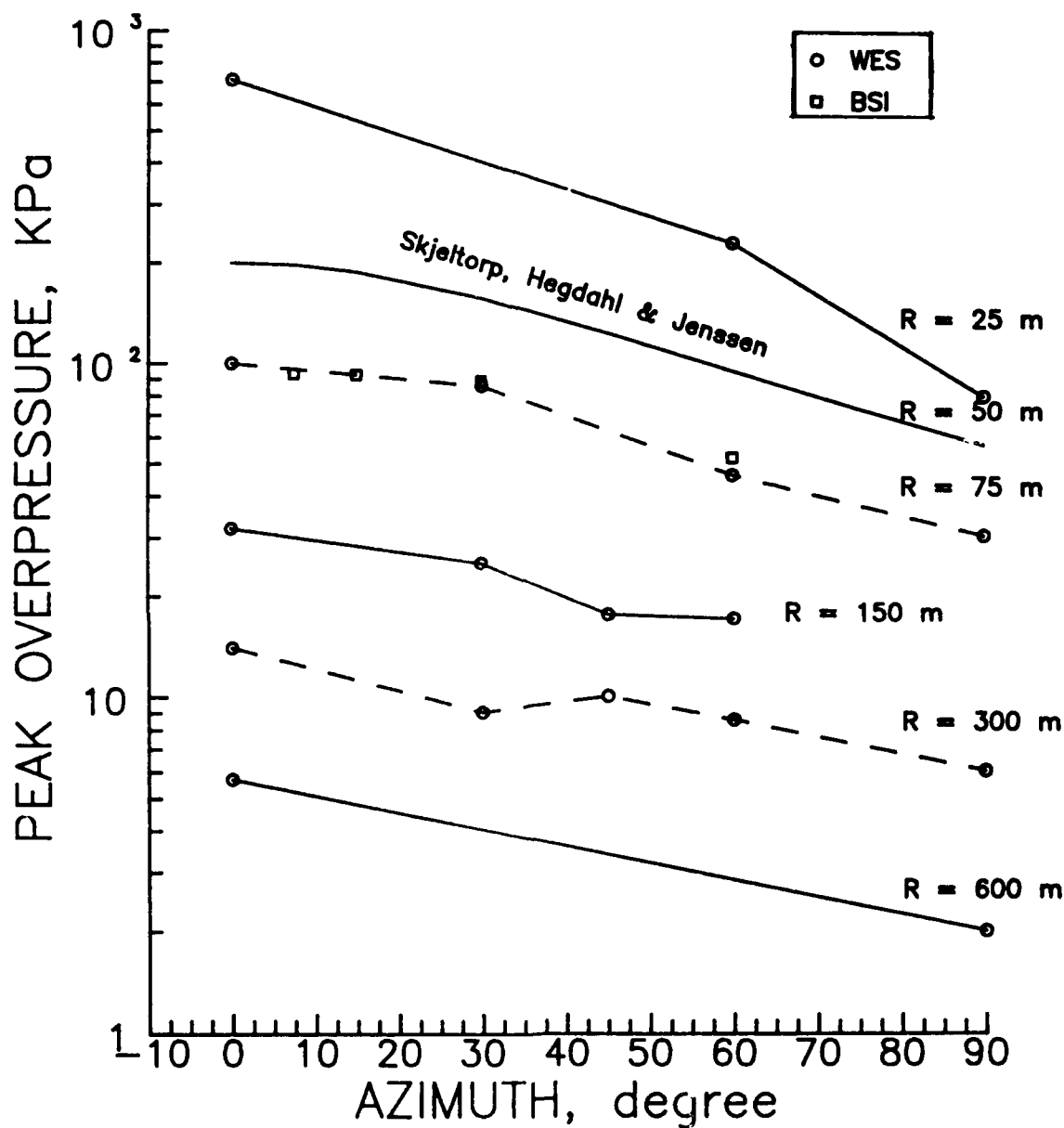


Figure 39. Peak overpressure versus azimuth, Shallow Underground Tunnel/Chamber Explosion Test. A comparison is shown between measured and calculated data using the azimuth parameter developed by Skjeltorp, Hegdahl and Jenssen (1975).

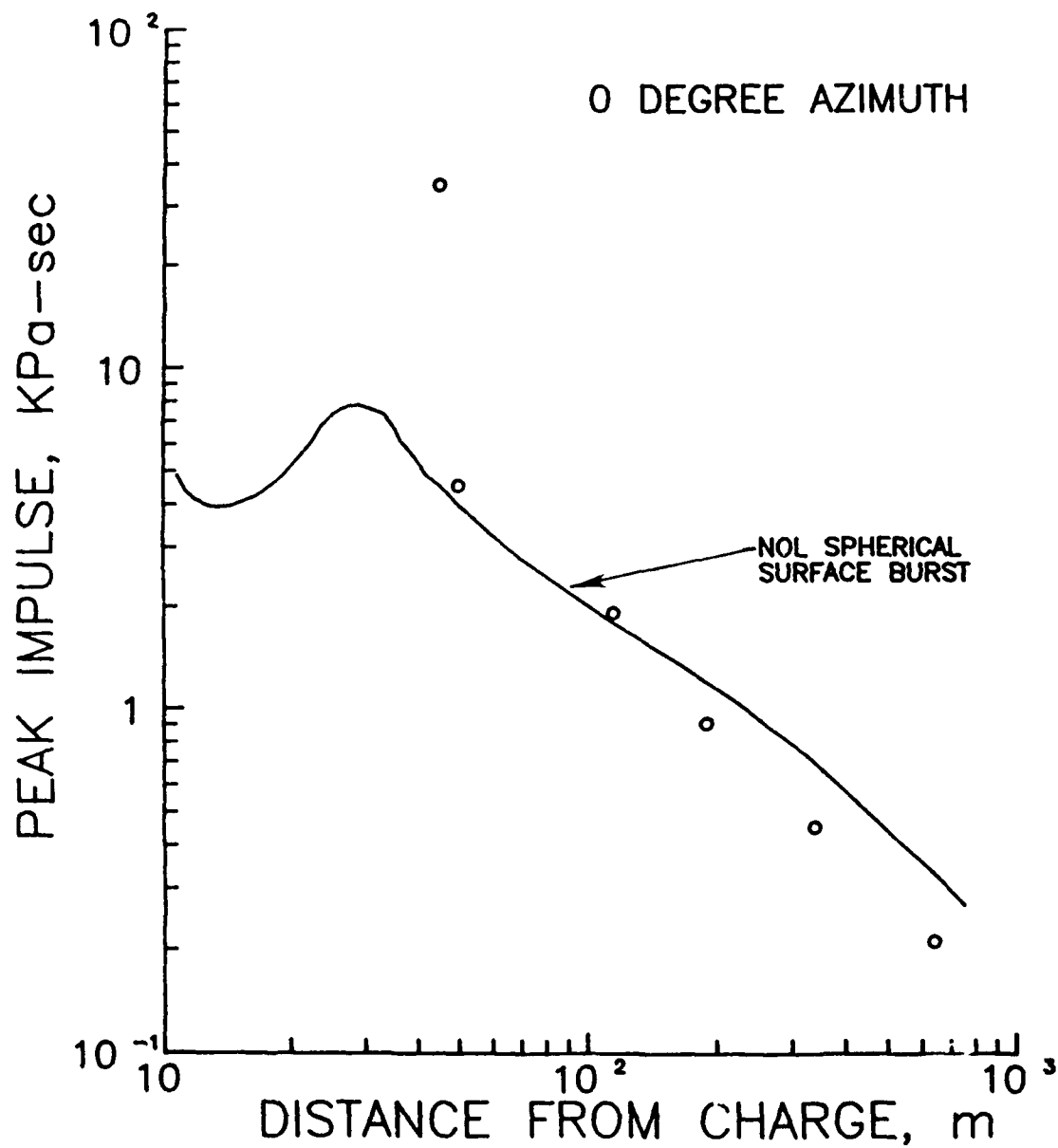


Figure 40. Peak impulse versus distance from the center of the charge, Shallow Underground Tunnel/Chamber Explosion Test. Comparison is shown between measured data and NOL spherical surface burst curve.

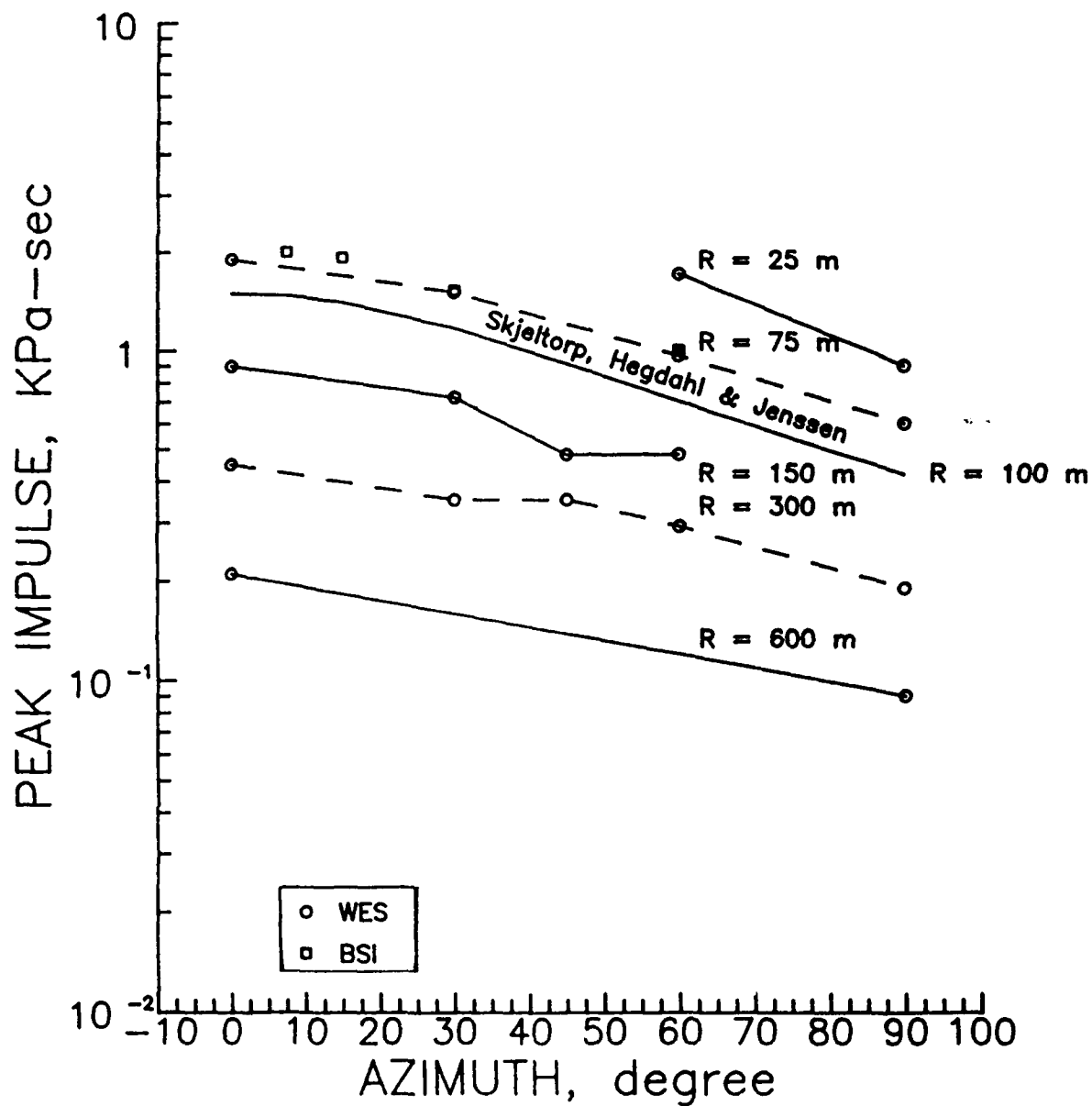


Figure 41. Peak impulse versus azimuth, Shallow Underground Tunnel/Chamber Explosion Test. A comparison is shown between measured and calculated data using the azimuth parameter developed by Skjeltnorp, Hegdahl and Jenssen (1975).

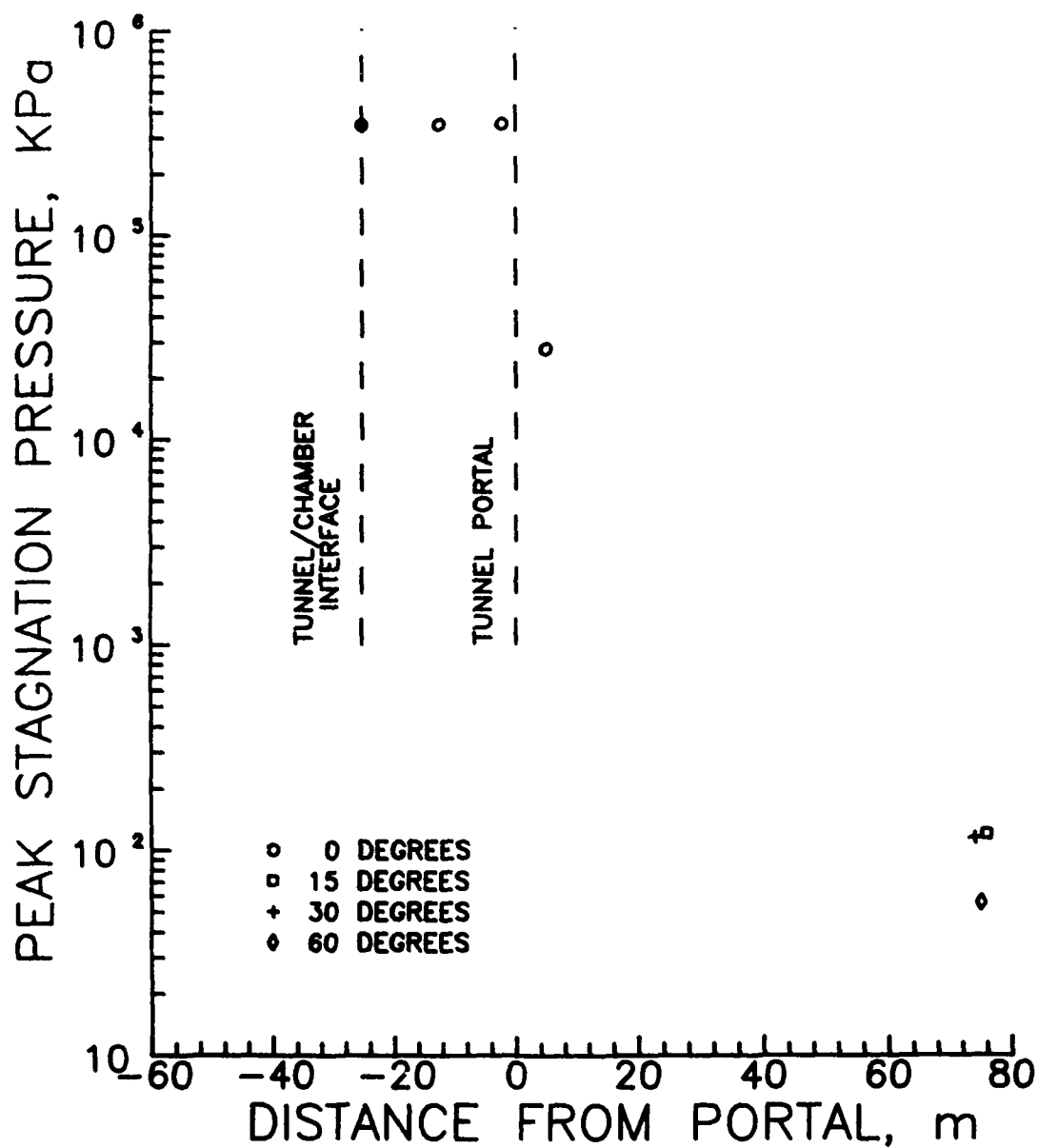


Figure 42. Peak stagnation pressure versus distance from the tunnel portal, Shallow Underground Tunnel/Chamber Explosion Test.

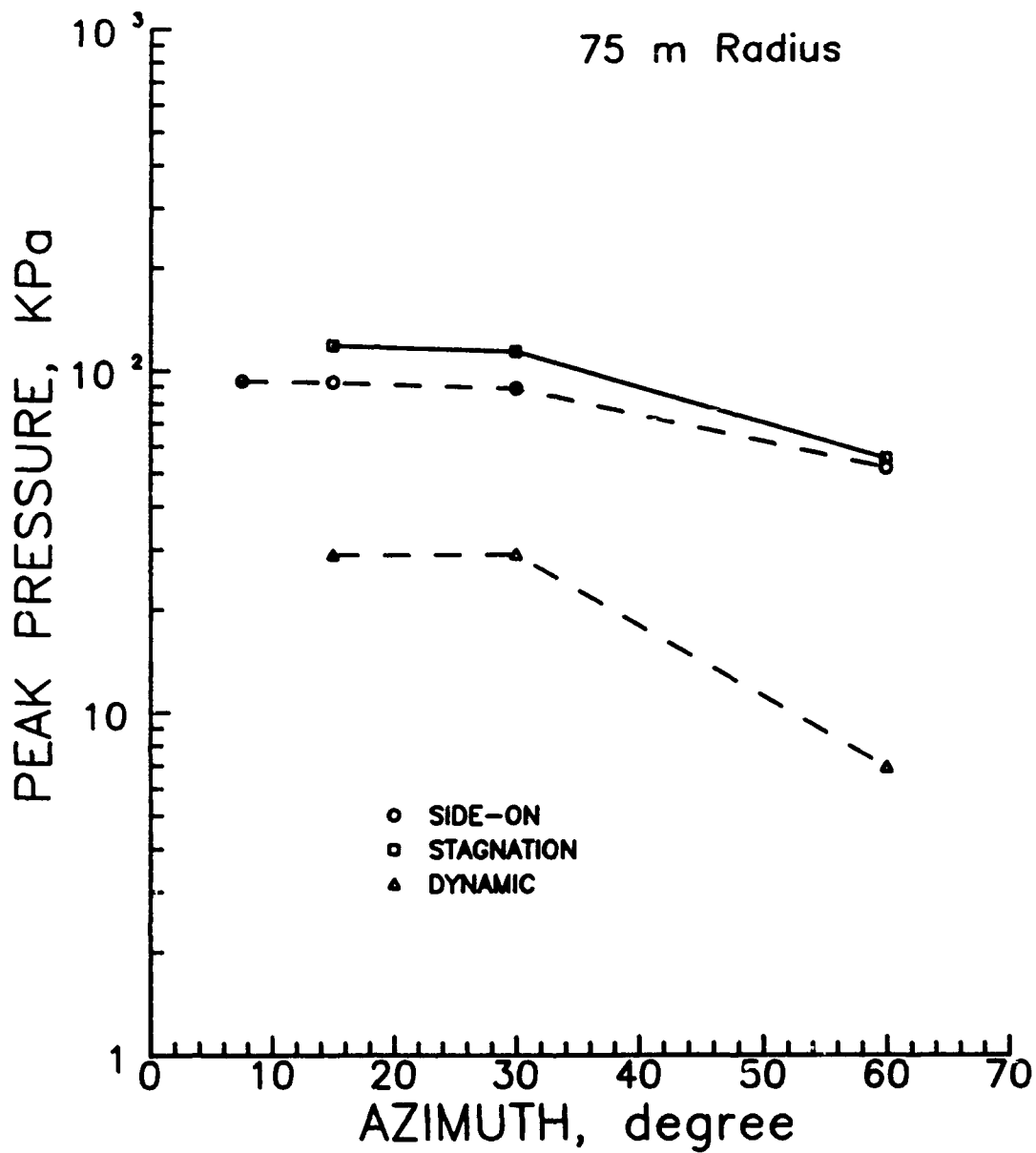


Figure 43. A comparison of peak stagnation, side-on and dynamic pressure at the 75-m range, Shallow Underground Tunnel/Chamber Explosion Test.

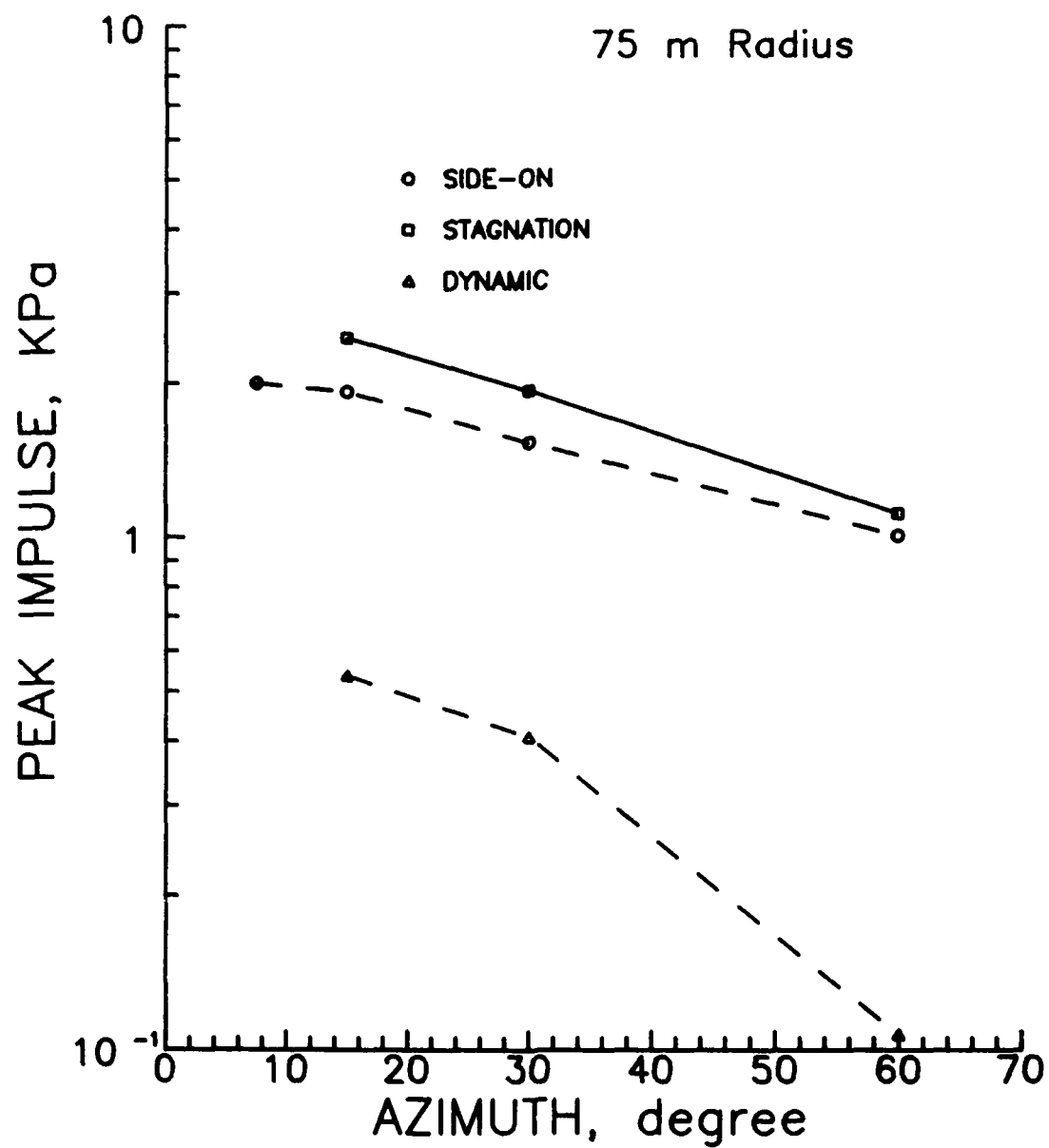


Figure 44. A comparison of peak stagnation, side-on, and dynamic impulse at the 75-m range, Shallow Underground Tunnel/Chamber Explosion Test.

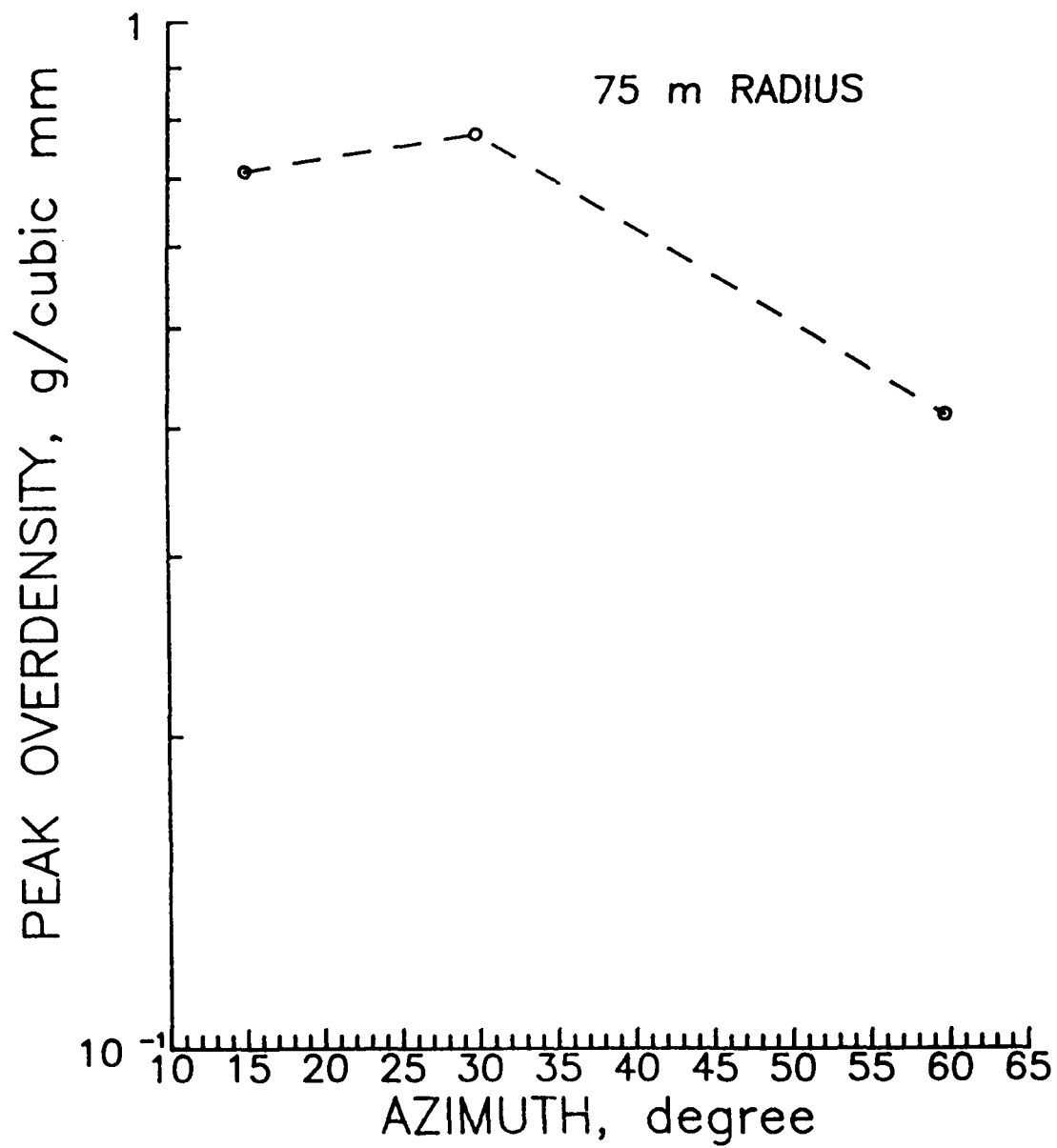


Figure 45. Overdensity versus azimuth at the 75-m range, Shallow Underground Tunnel/Chamber Explosion Test.

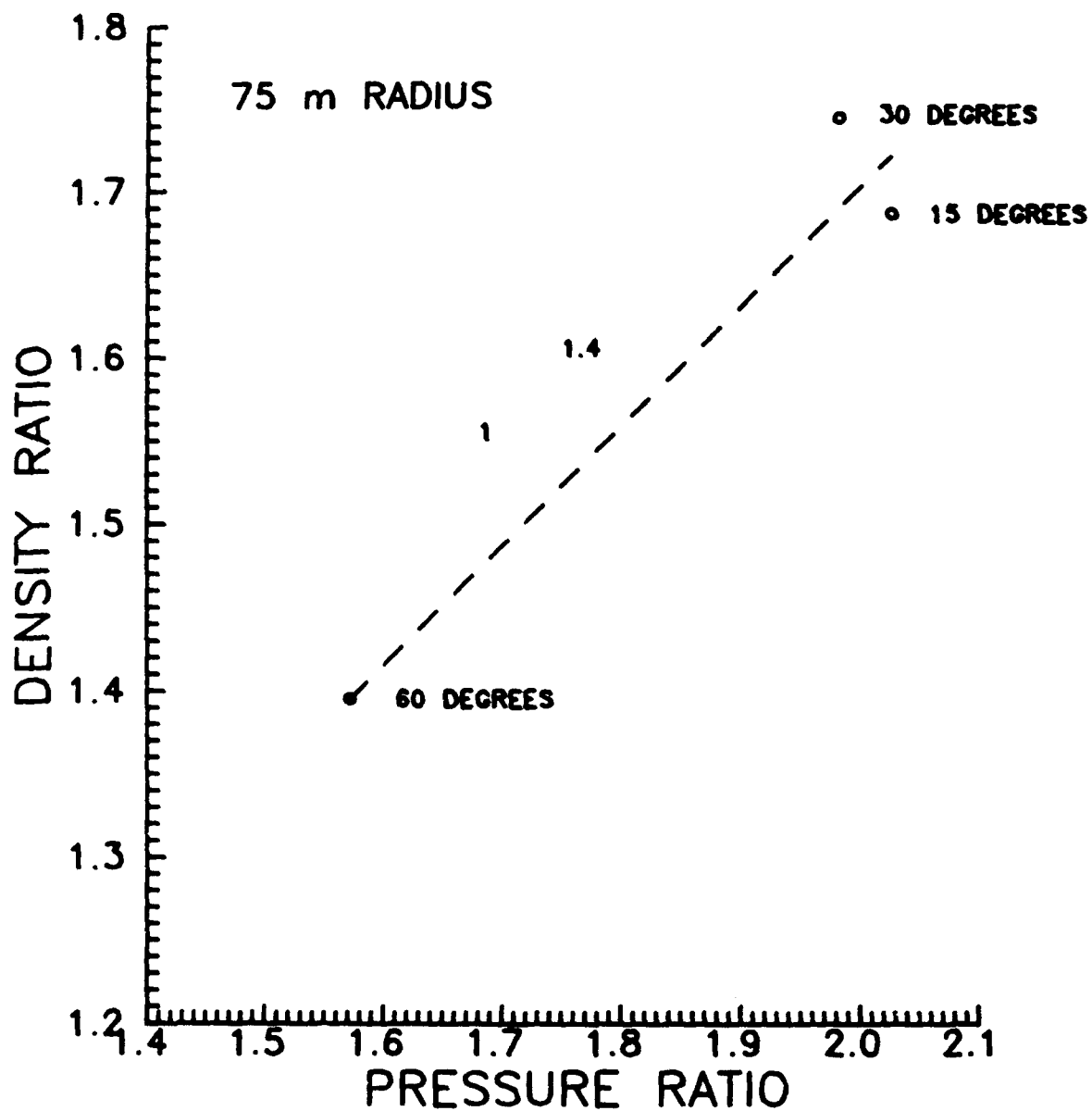


Figure 46. Density ratio versus pressure ratio, Shallow Underground Tunnel/Chamber Explosion Test.

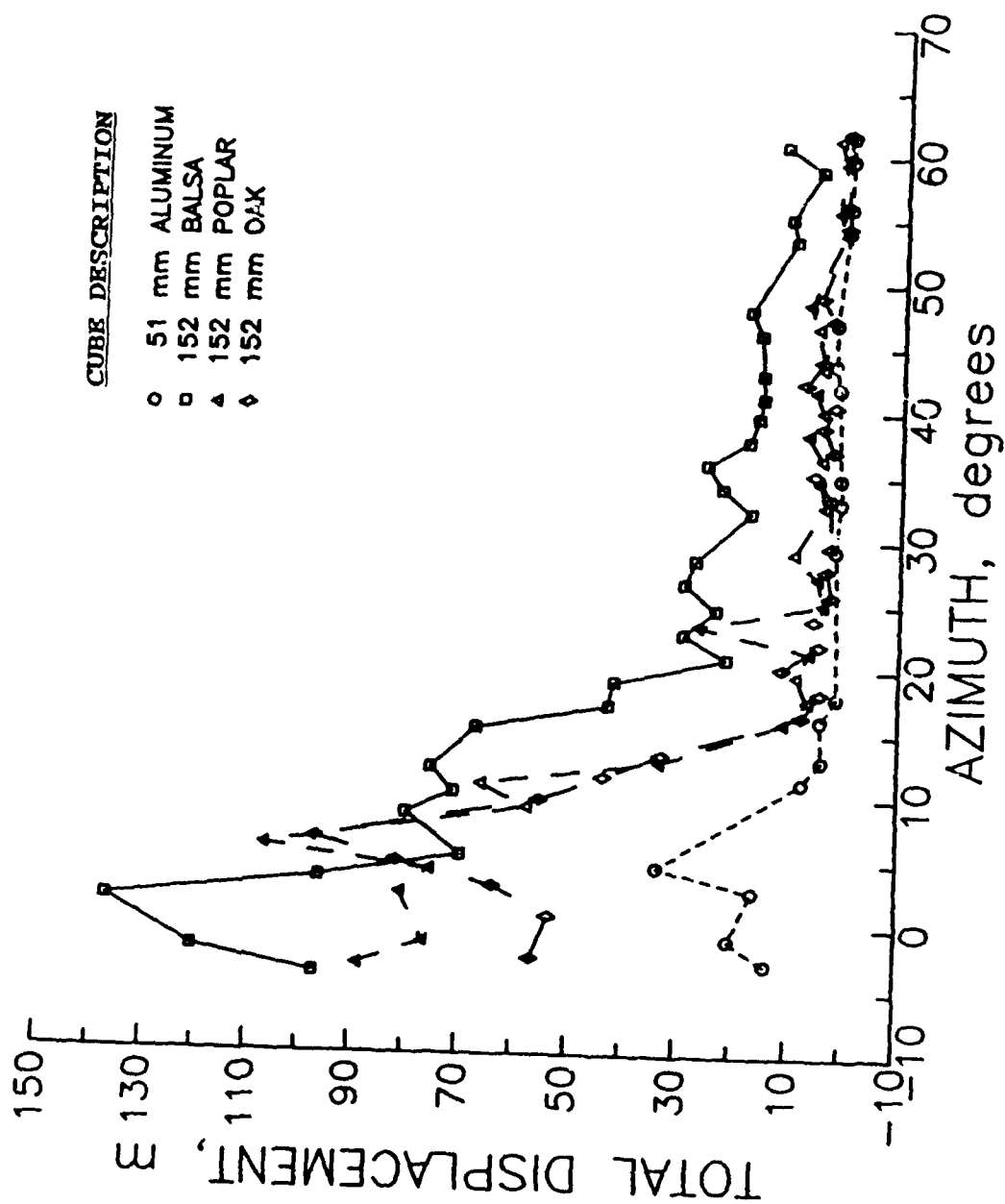


Figure 47. Total blast cube displacement versus azimuth at the 75-m range, Shallow Underground Tunnel/Chamber Explosion Test.

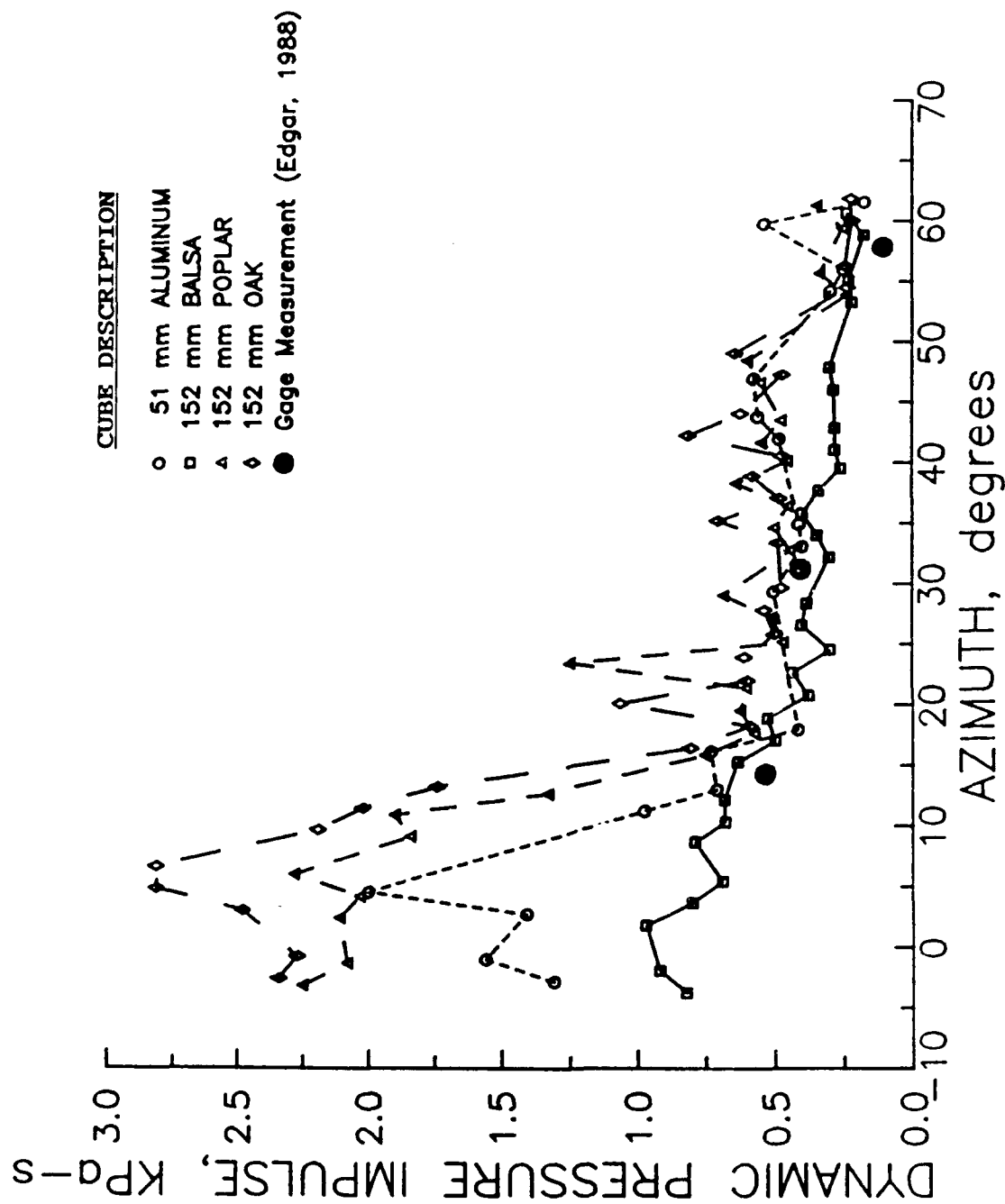


Figure 48. Blast cube dynamic pressure impulse versus azimuth at the 25-m range, Shallow Underground Tunnel/Chamber Explosion Test.

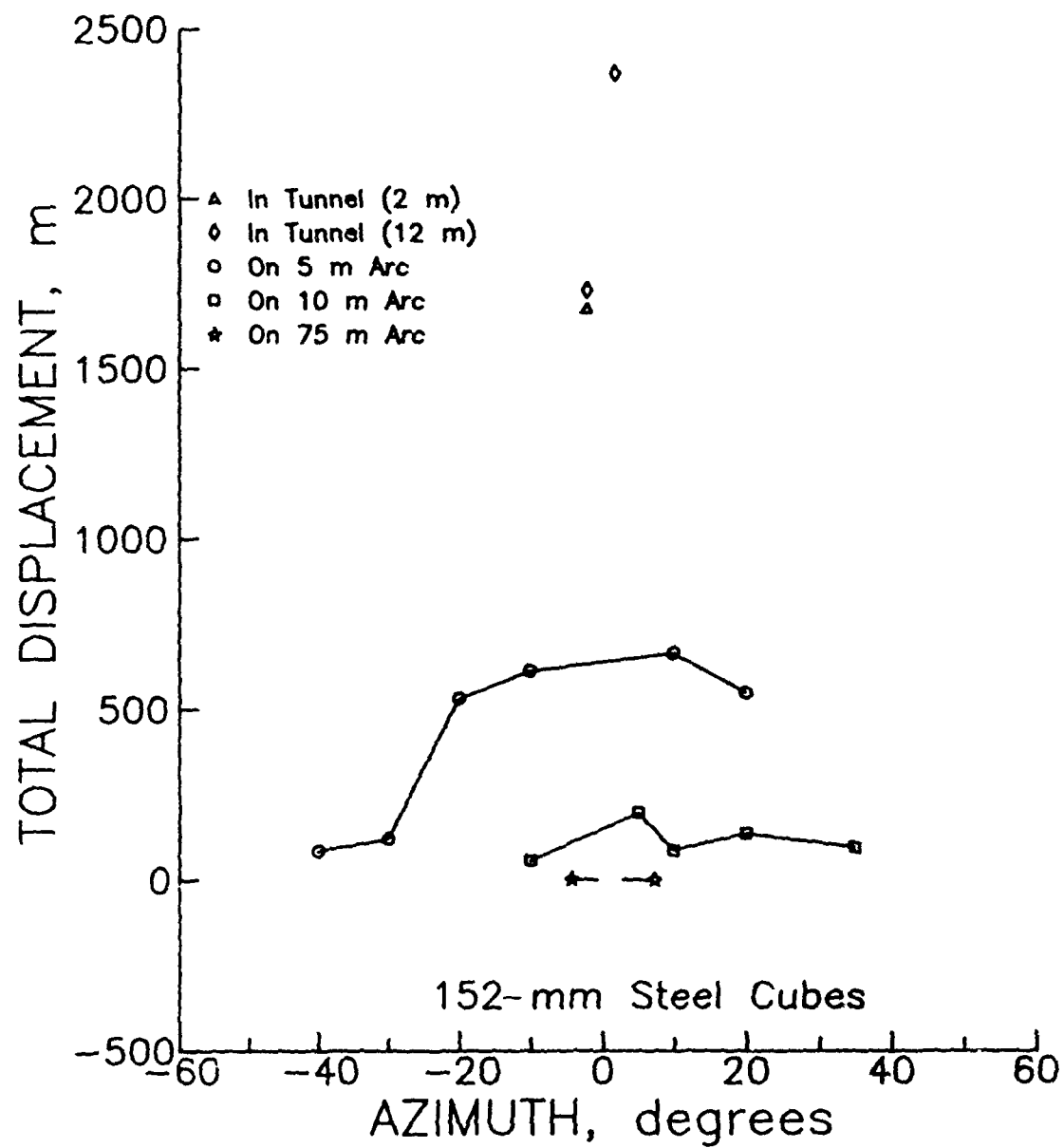


Figure 49. Steel blast cube total displacement versus azimuth, Shallow Underground Tunnel/Chamber Explosion Test.

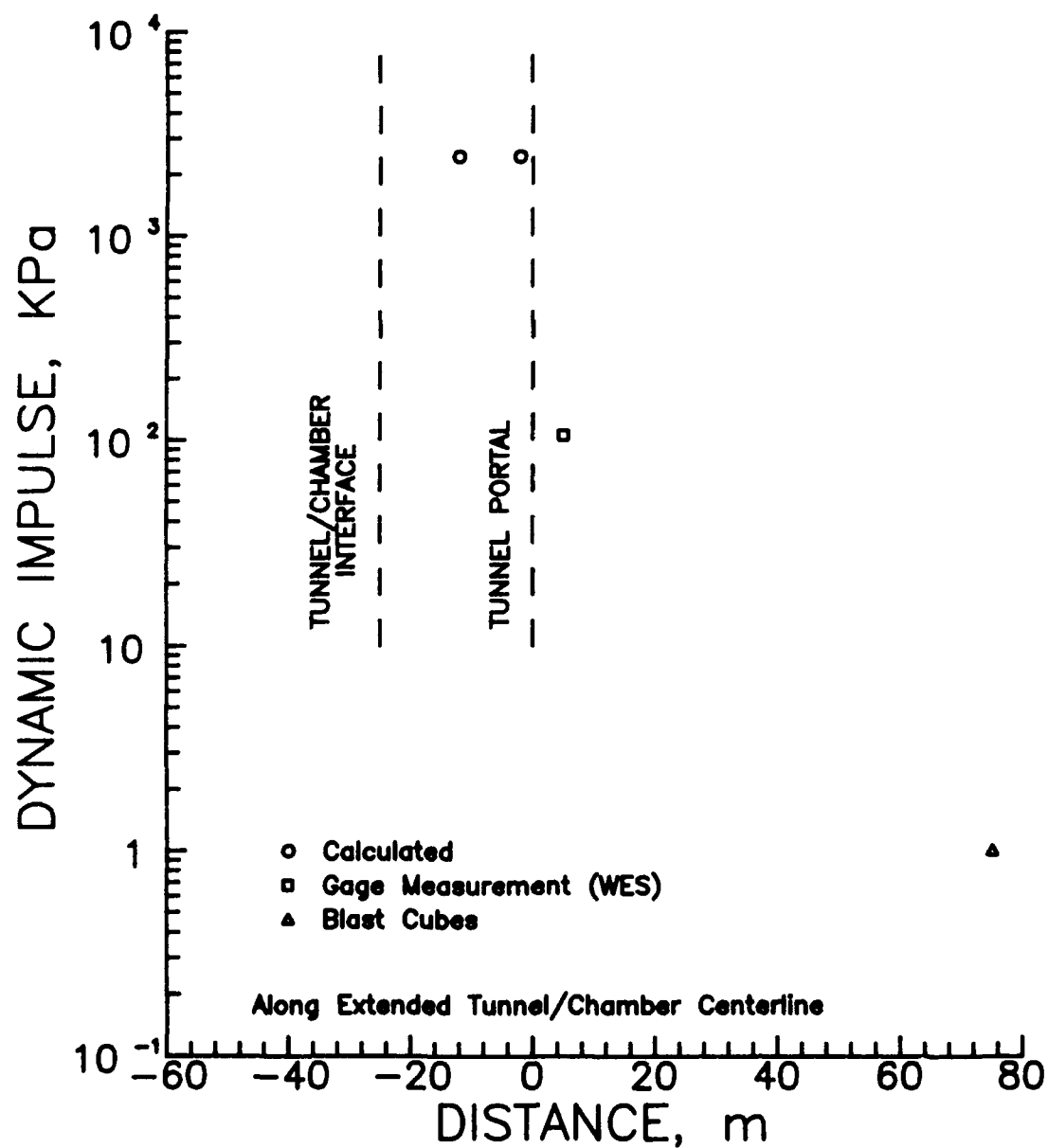


Figure 50. Inferred dynamic impulse versus distance along the tunnel/chamber extended centerline, Shallow Underground Tunnel/Chamber Explosion test.

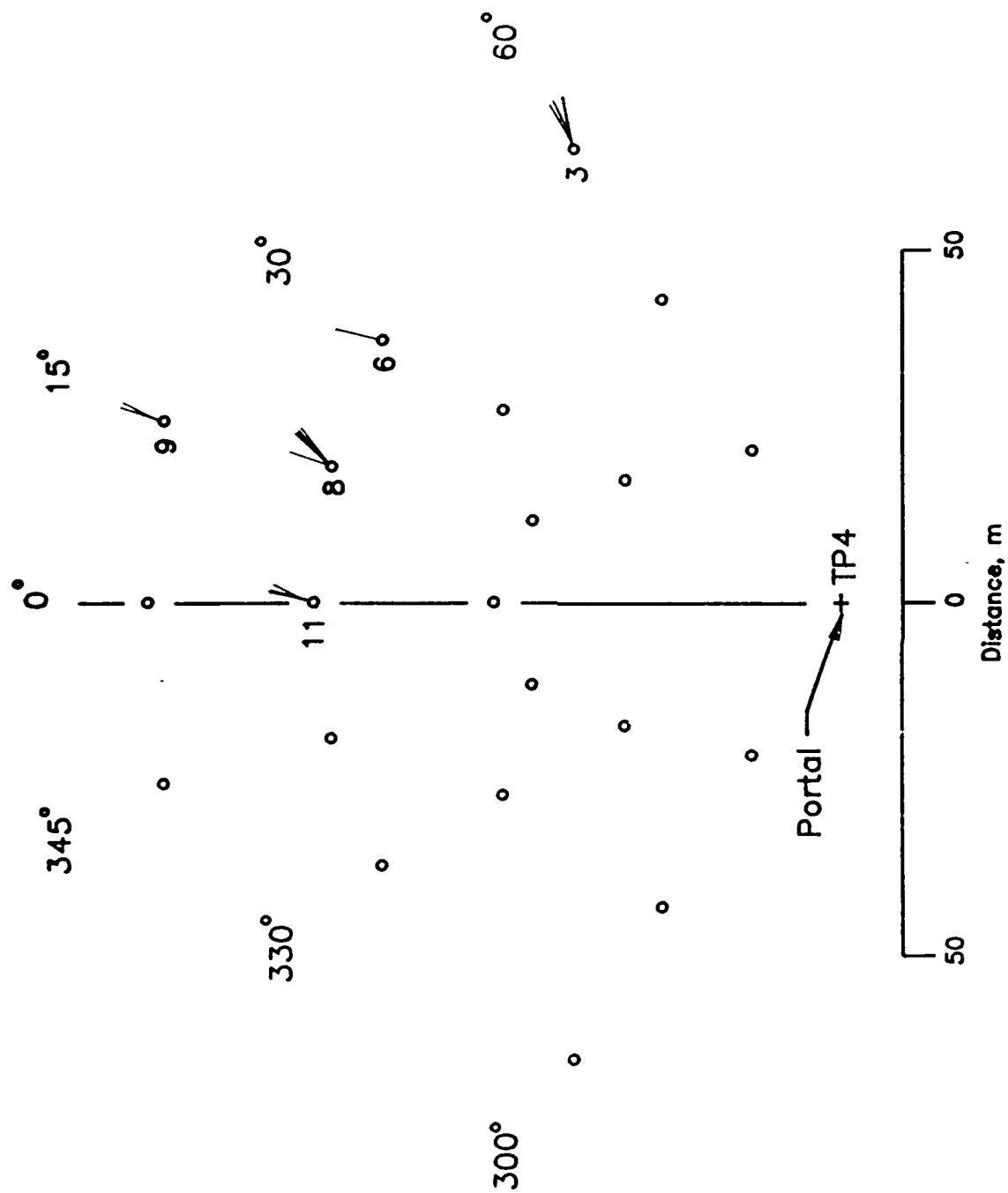


Figure 51. Free-field airblast flow direction as indicated by wire drag gages, Shallow Underground Tunnel/Chamber Explosion Test.

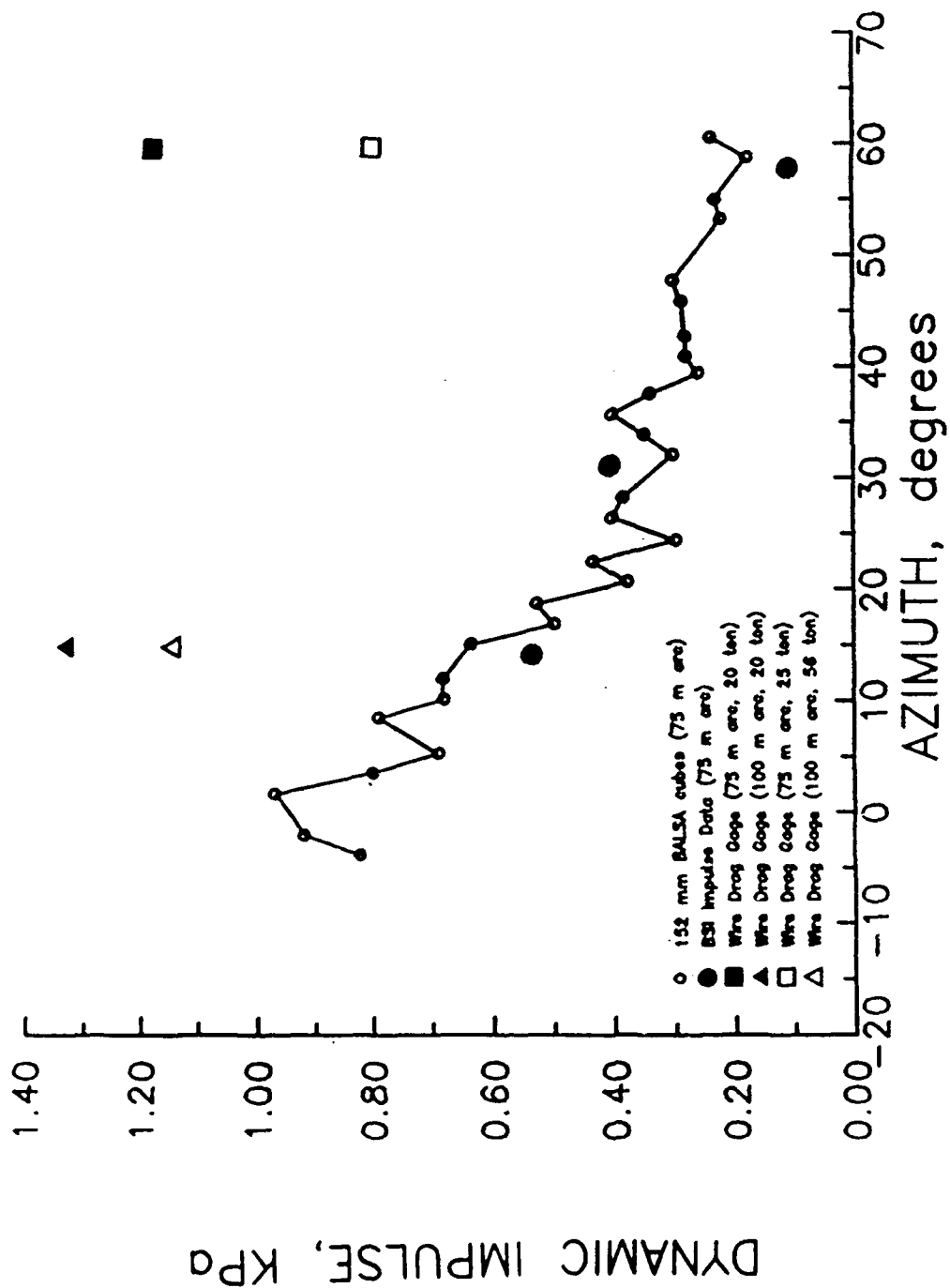


Figure 52. Comparison of dynamic impulse measured by BSI and data inferred by blast cubes and wire drag gages, Shallow Underground Tunnel/Chamber Explosion Test.

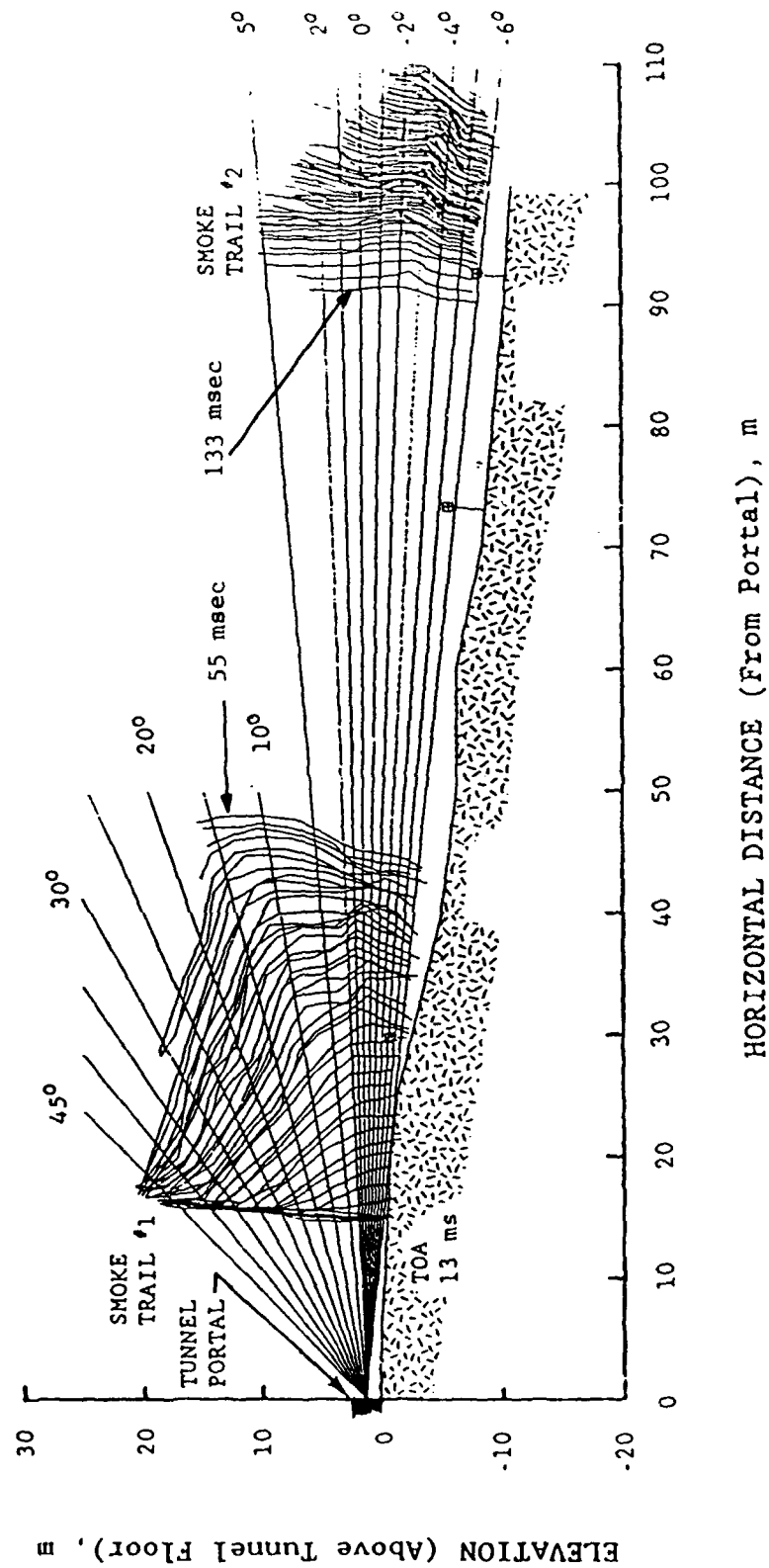


Figure 53. Smoke puff location-time contours (from Dewey, 1989), Shallow Underground Tunnel/Chamber Explosion Test.

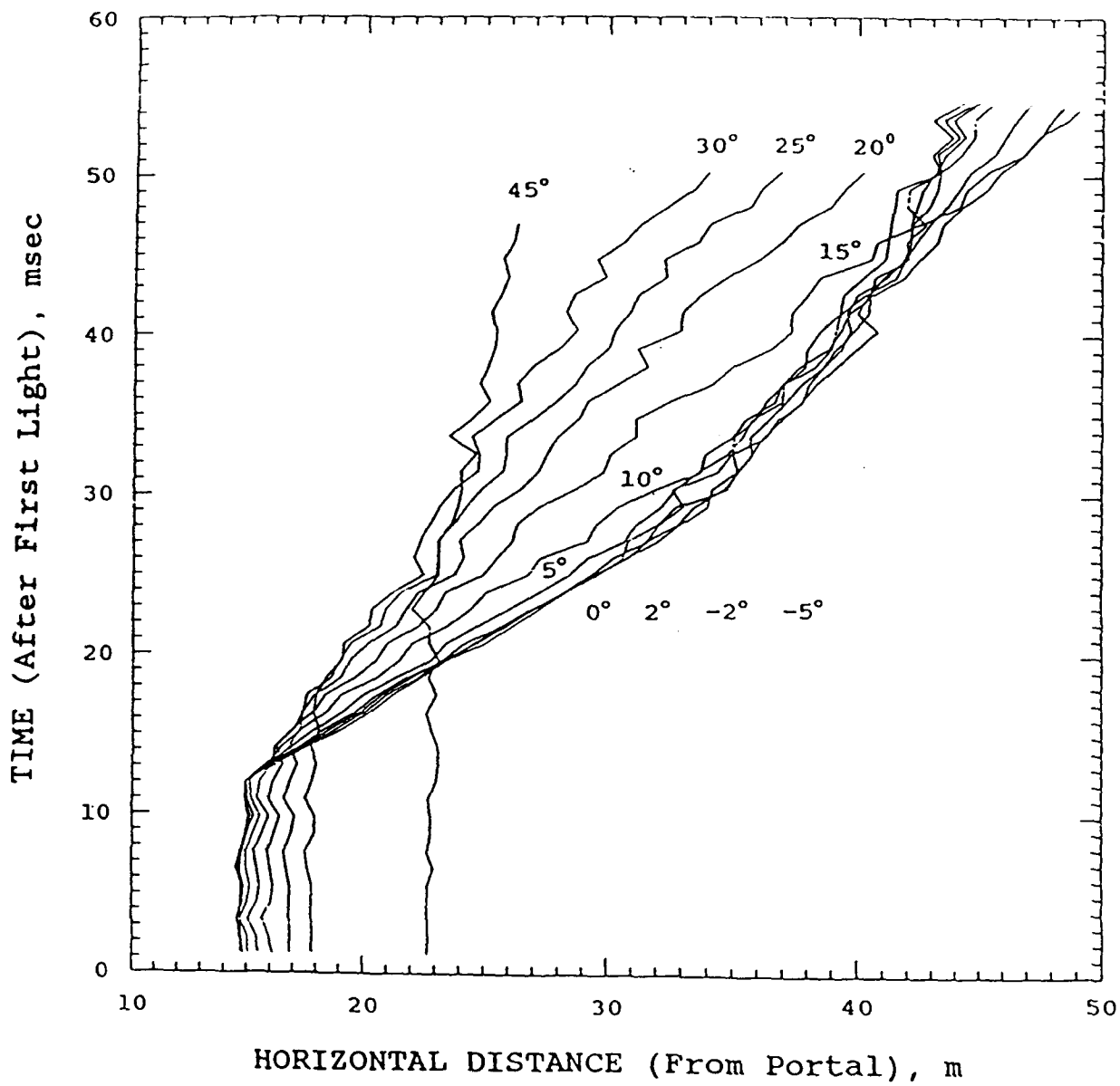


Figure 54. Particle trajectories measured from positions of Smoke Trail #1 (15 m). Dewey (1989), Shallow Underground Tunnel/Chamber Explosion Test. Vertical angles are those shown in Figure 53.

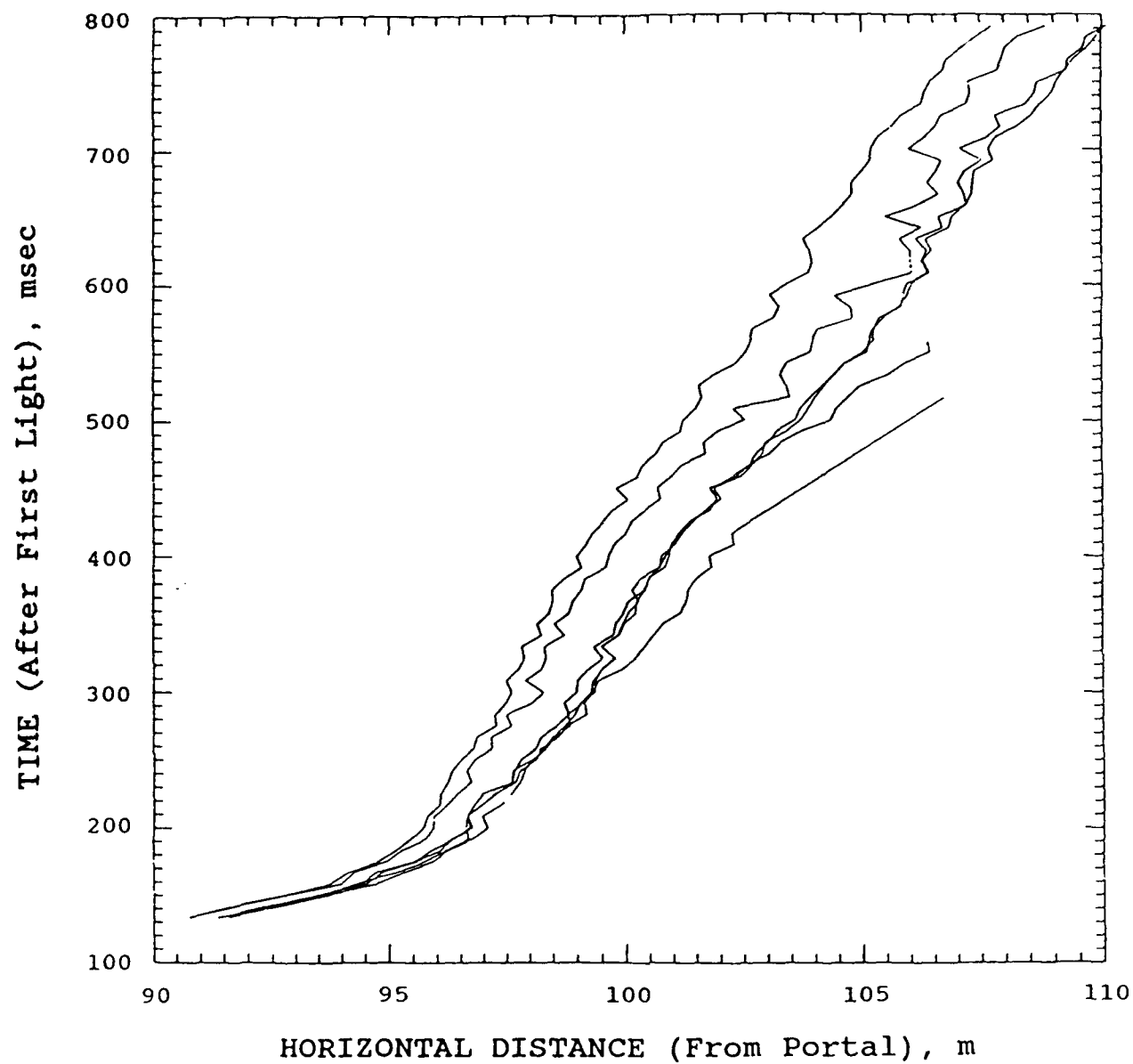


Figure 55. Particle trajectories measured from positions of Smoke Trail #2 (90 m), Dewey (1989), Shallow Underground Tunnel/Chamber Explosion Test.

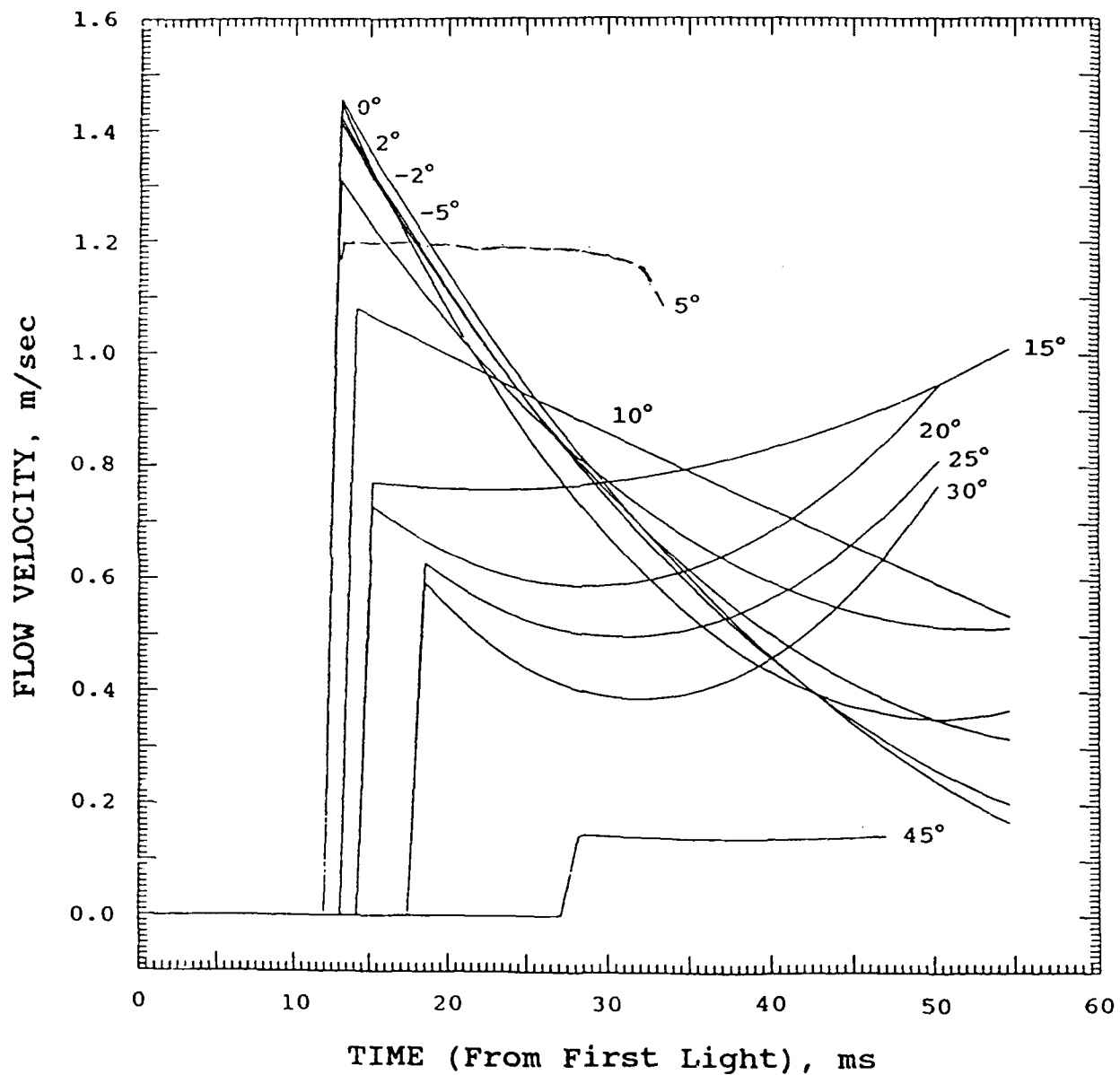


Figure 56. Measured smoke trail particle flow velocities along Smoke Trail #1, Dewey (1989), Shallow Underground Tunnel/Chamber Explosion Test. Vertical angles are those shown in Figure 53.

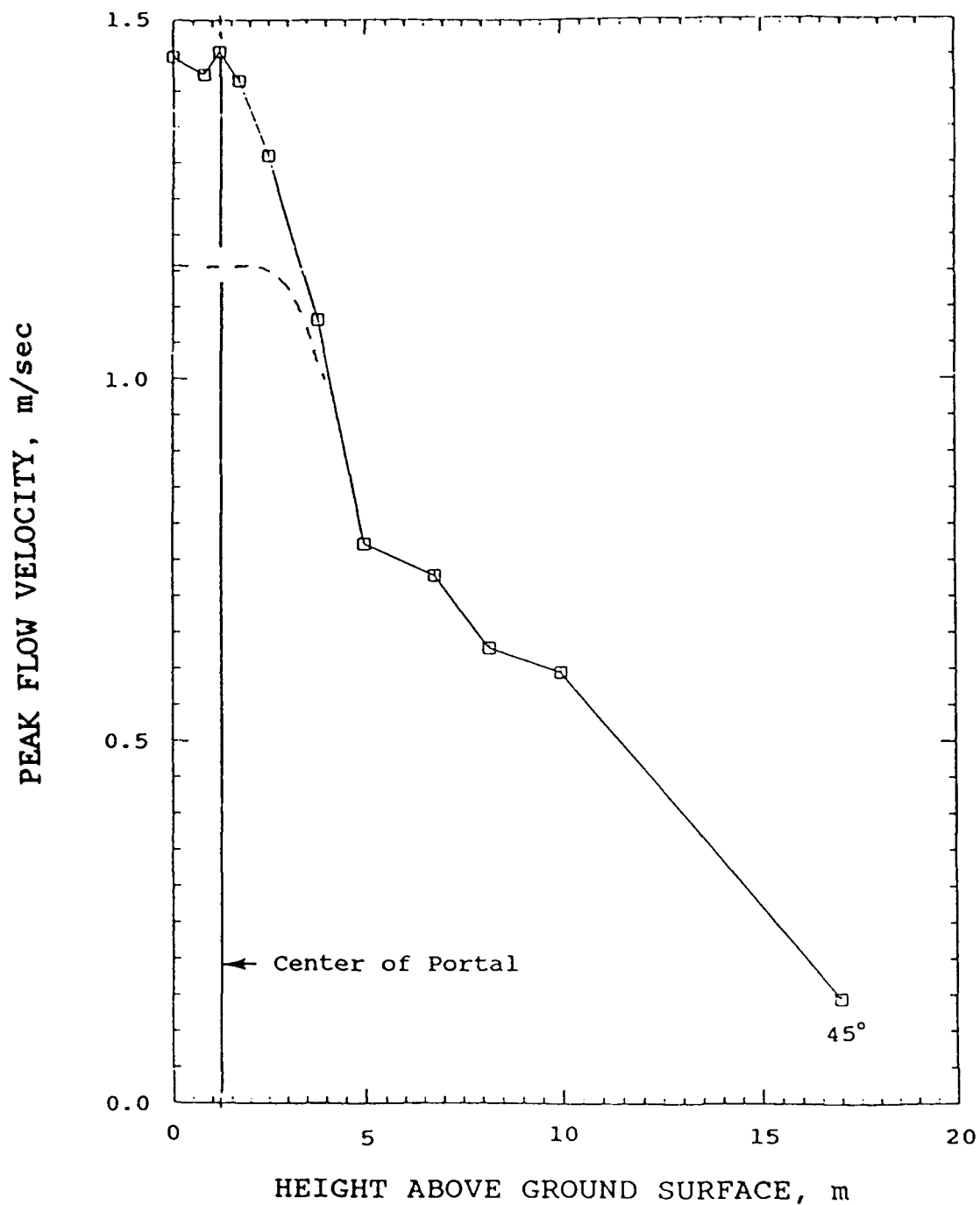


Figure 57. Initial smoke trail particle velocities along Smoke Trail #1 as a function of height above the ground surface, Dewey (1989), Shallow Underground Tunnel/Chamber Explosion Test.

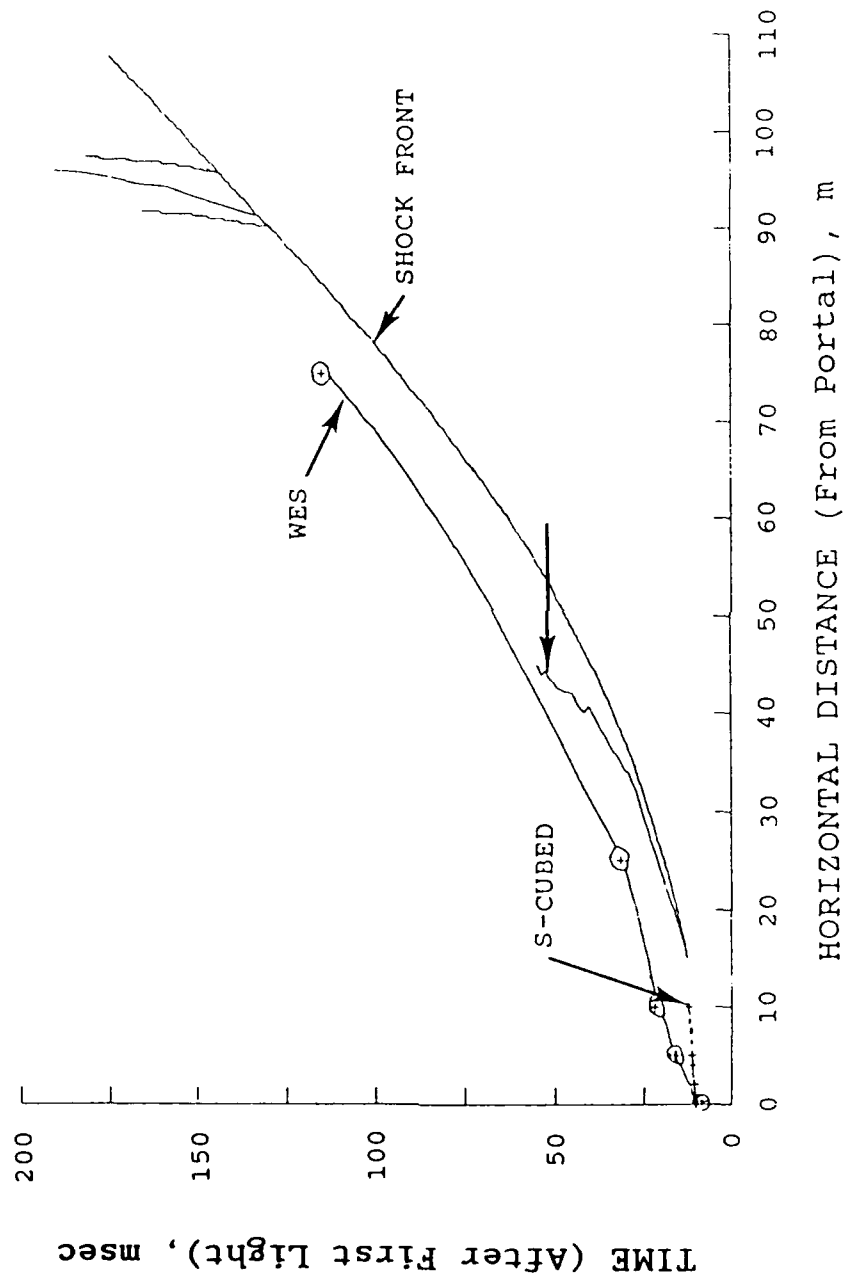


Figure 58. Blast wave reconstructed from smoke puff trails compared to wave fronts measured by WES and calculated by S-CUBED, Inc. Shallow Underground Tunnel/Chamber Explosion Test.

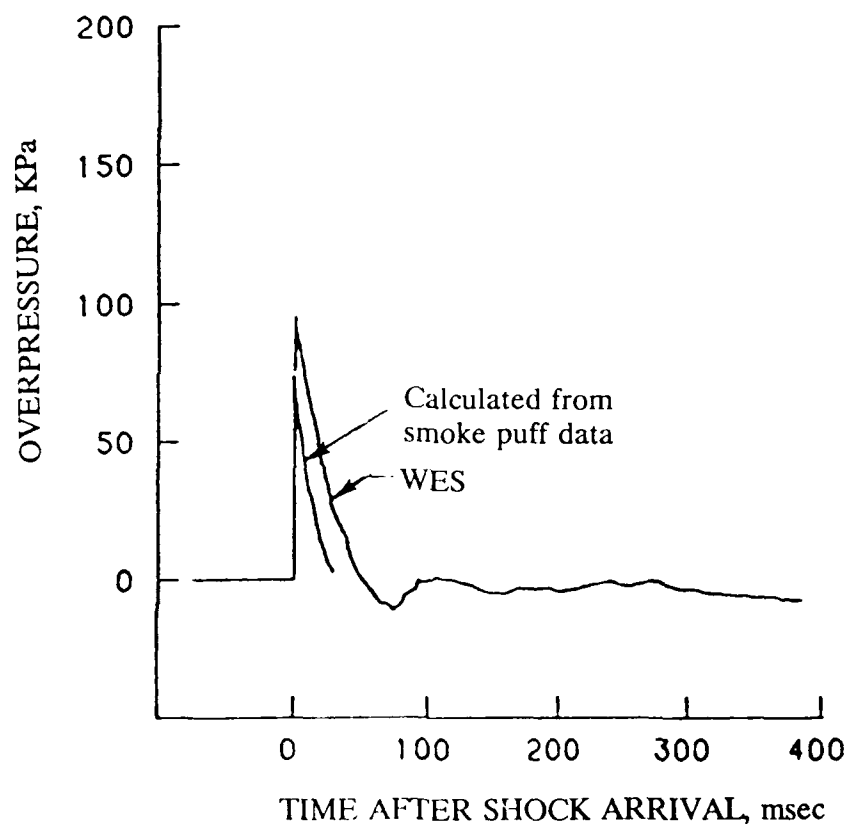


Figure 59. Comparison of WES measured and smoke puff calculated-time history at the 75 m radial, Dewey (1989), Shallow Underground Tunnel/Chamber Explosion Test.

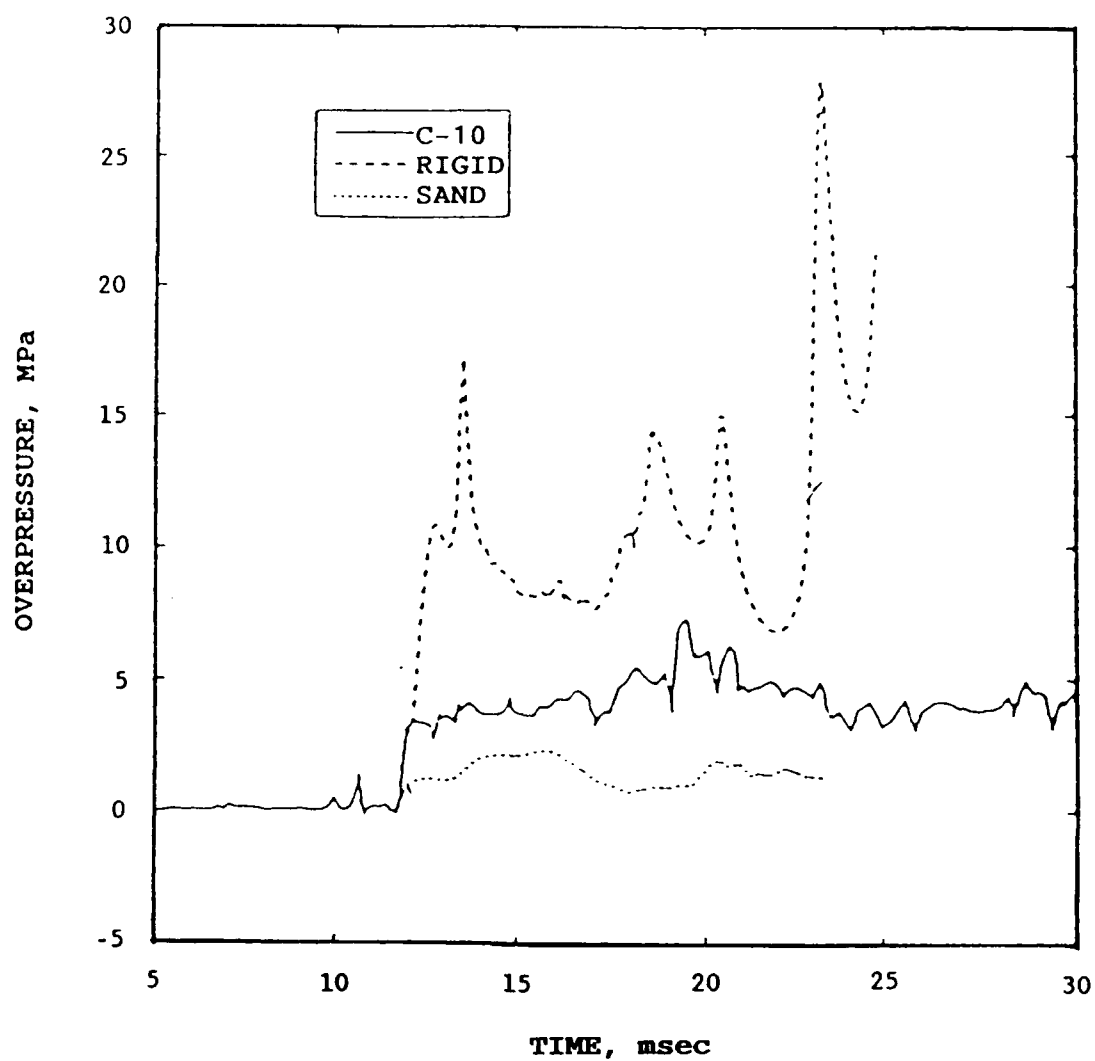


Figure 60. Comparison of overpressure-time histories from experimental record and two calculations (rigid and sand models) inside access tunnel 4 m from portal (gage station C-10, 4.7 m), Shallow Underground Tunnel/Chamber Explosion Test.

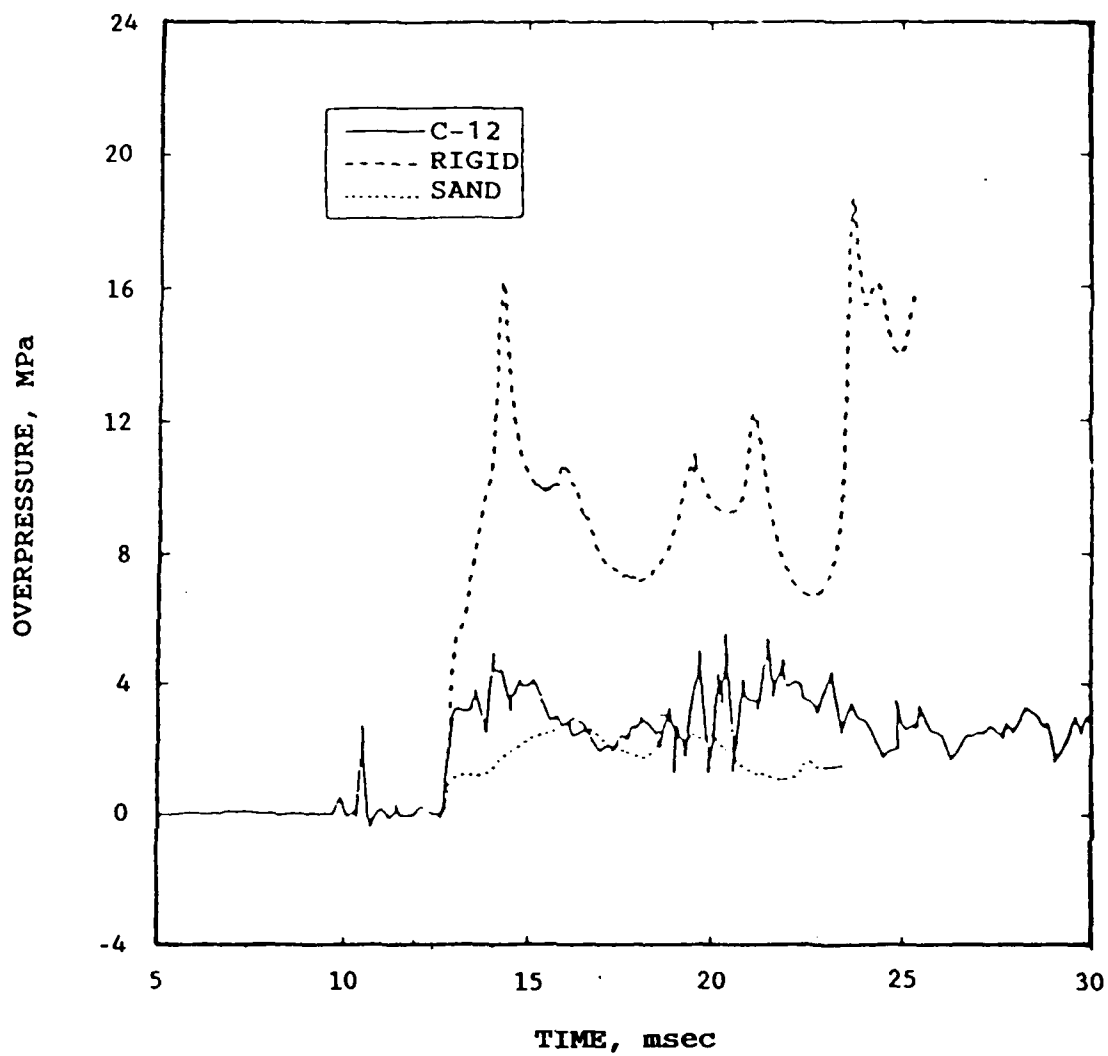


Figure 61. Comparison of overpressure-time histories from experimental record and two calculation (rigid and sand models) inside access tunnel 2.5 m from portal (gage station C-12, 2.2 m), Shallow Underground Tunnel/Chamber Explosion Test.

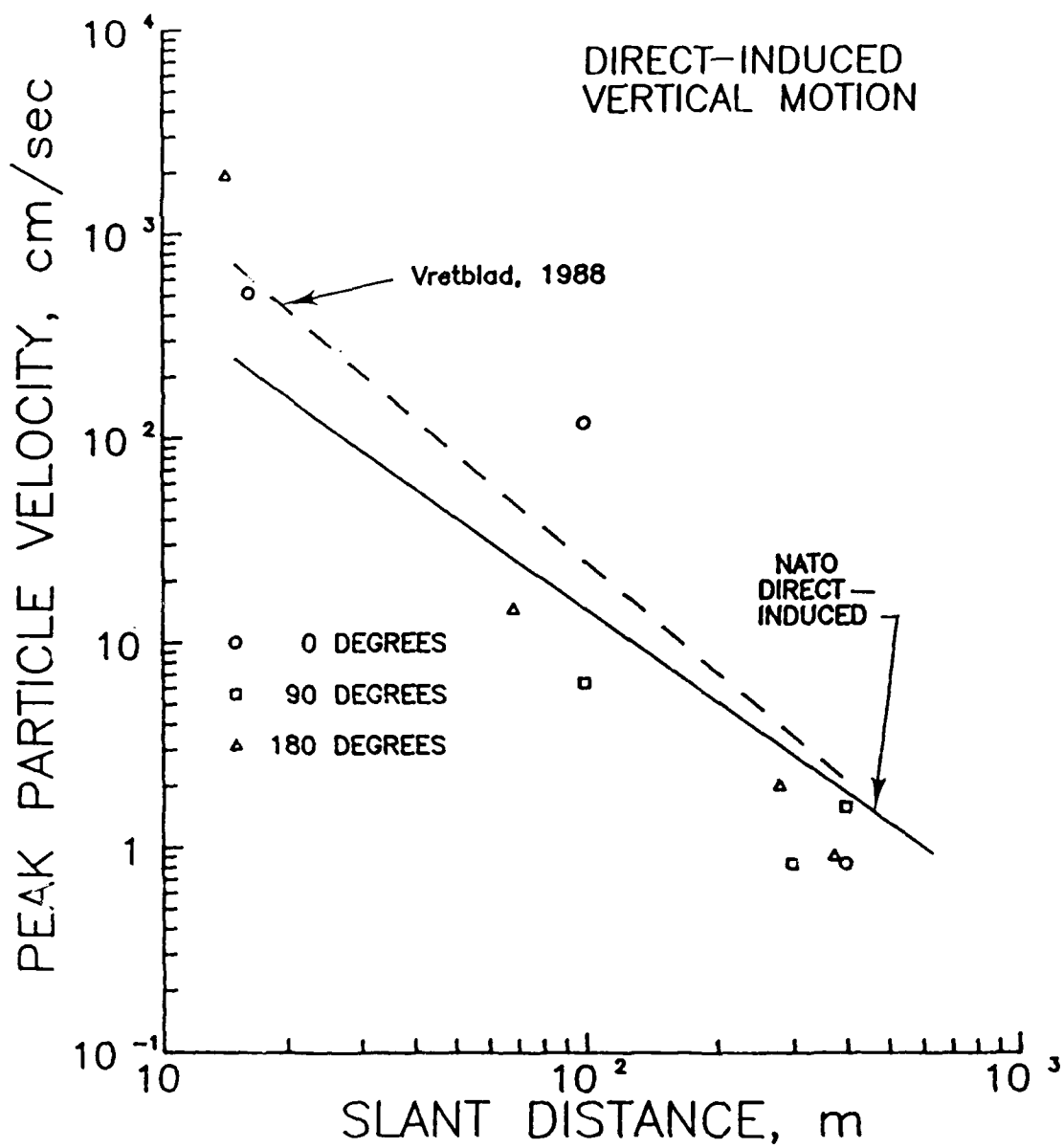


Figure 62. Peak, direct-induced, particle velocity versus slant distance from the center of the charge, Shallow Underground Tunnel/Chamber Explosion Test.

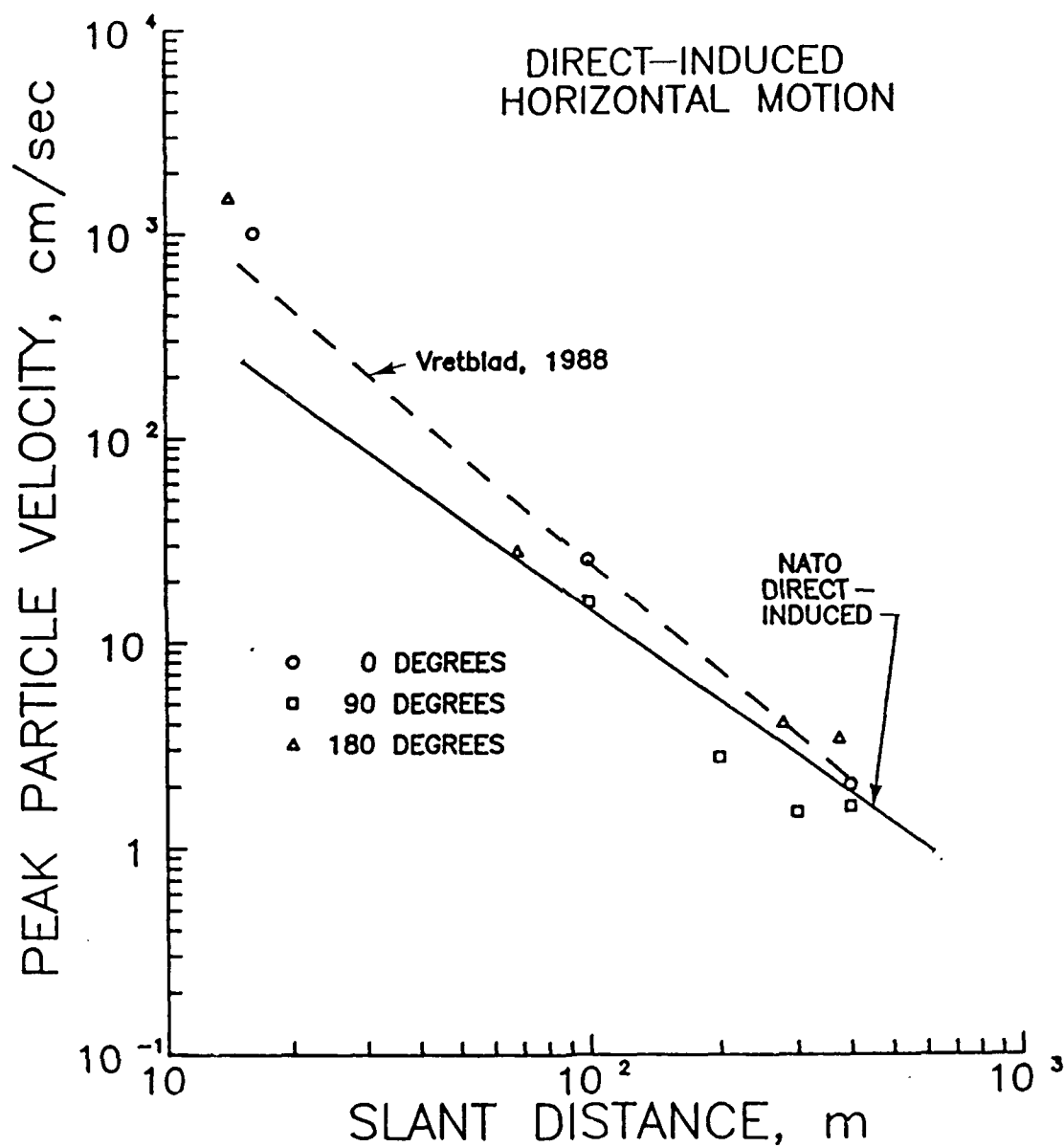


Figure 63. Peak, direct-induced, horizontal partical velocity versus slant distance from the center of the charge, Shallow Underground Tunnel/Chamber Explosion Test.

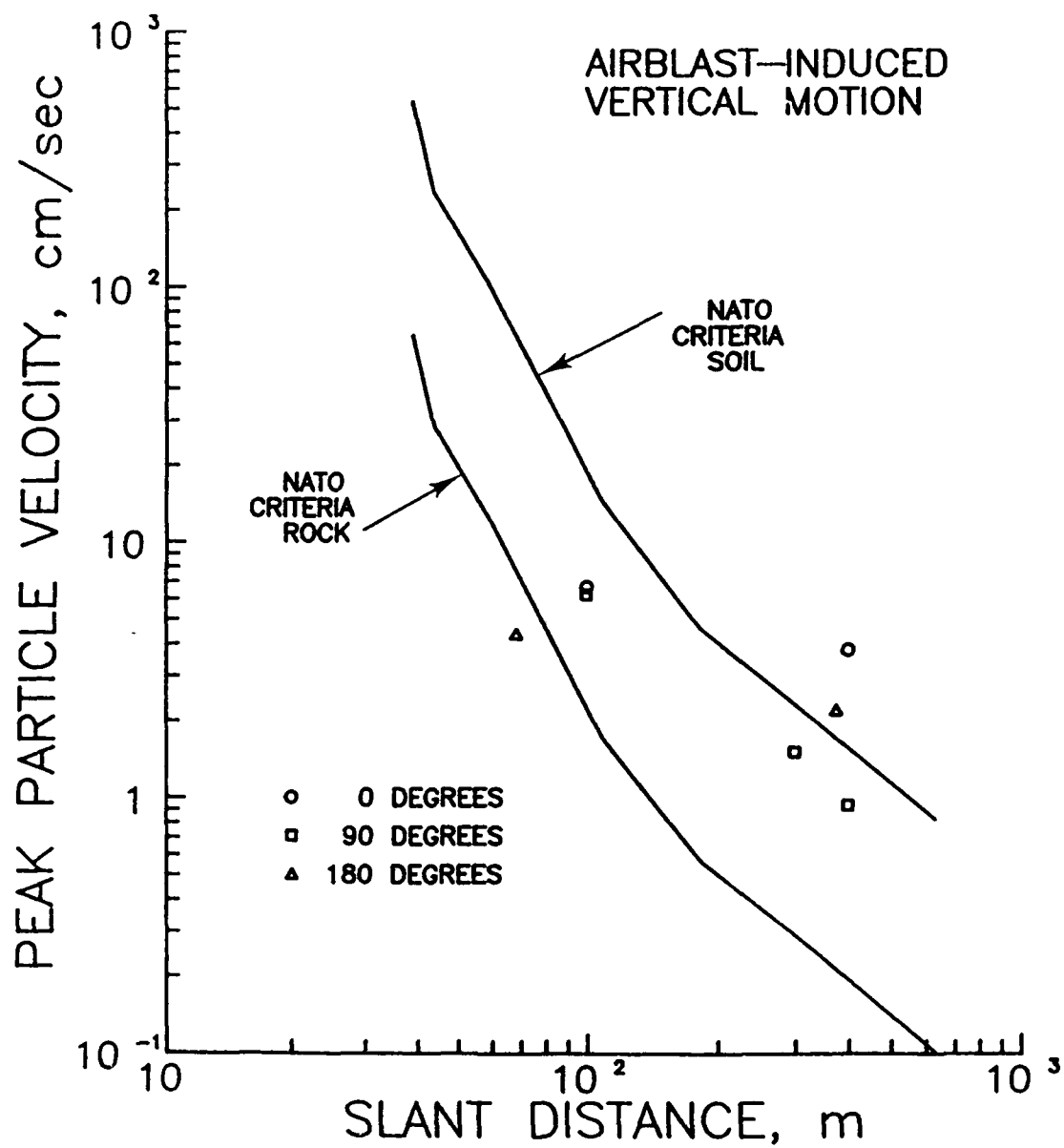


Figure 64. Peak, airblast-induced, vertical particle velocity versus slant distance from the center of the center of the charge, Shallow Underground Tunnel/Chamber Explosion Test.

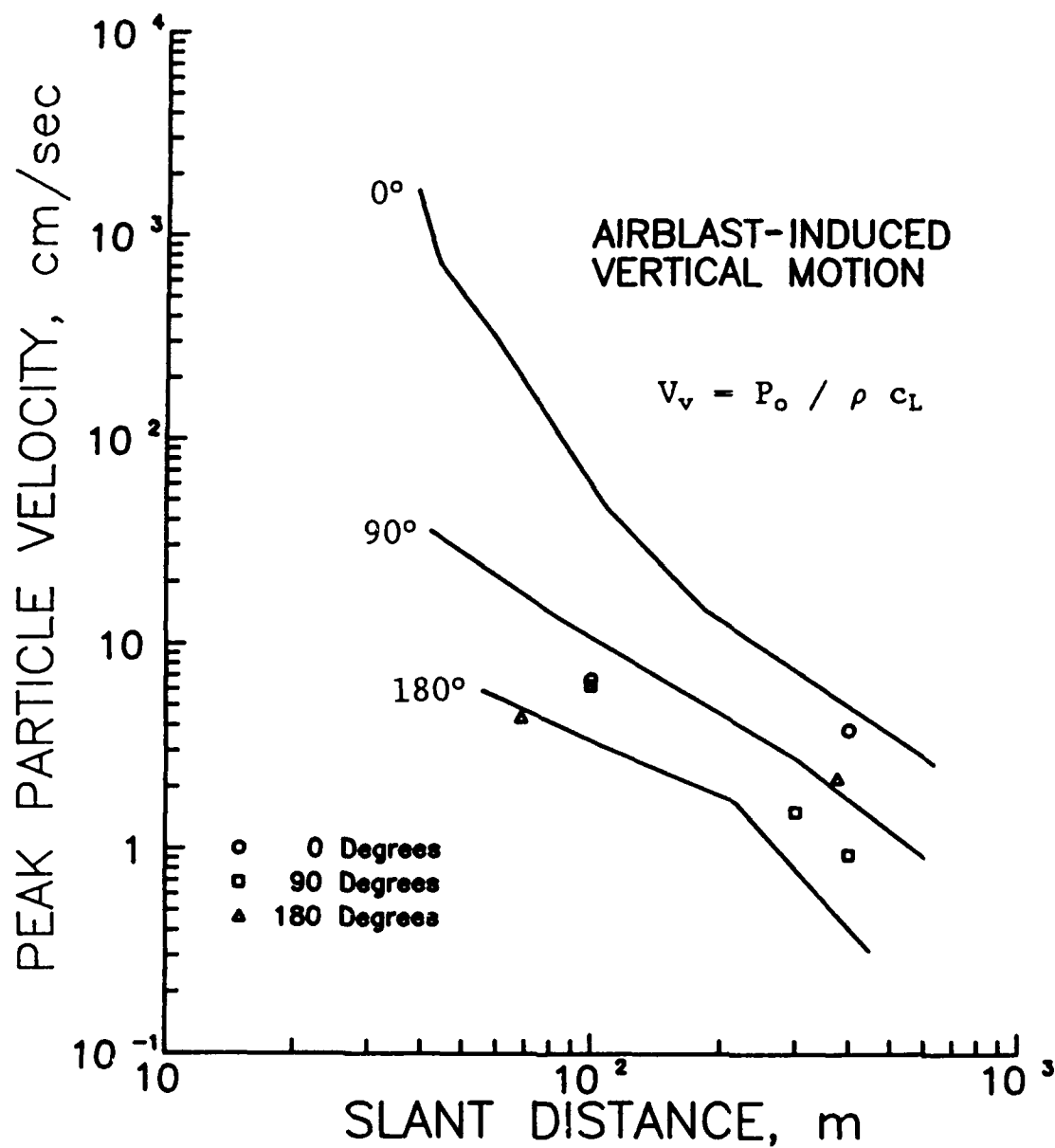


Figure 65. Comparison of predicted and measured peak, airblast induced, vertical particle velocity versus slant distance to the center of the explosive charge, Shallow Underground Tunnel/Chamber Explosion Test. See Section 3.6 for definition of prediction equation parameters.

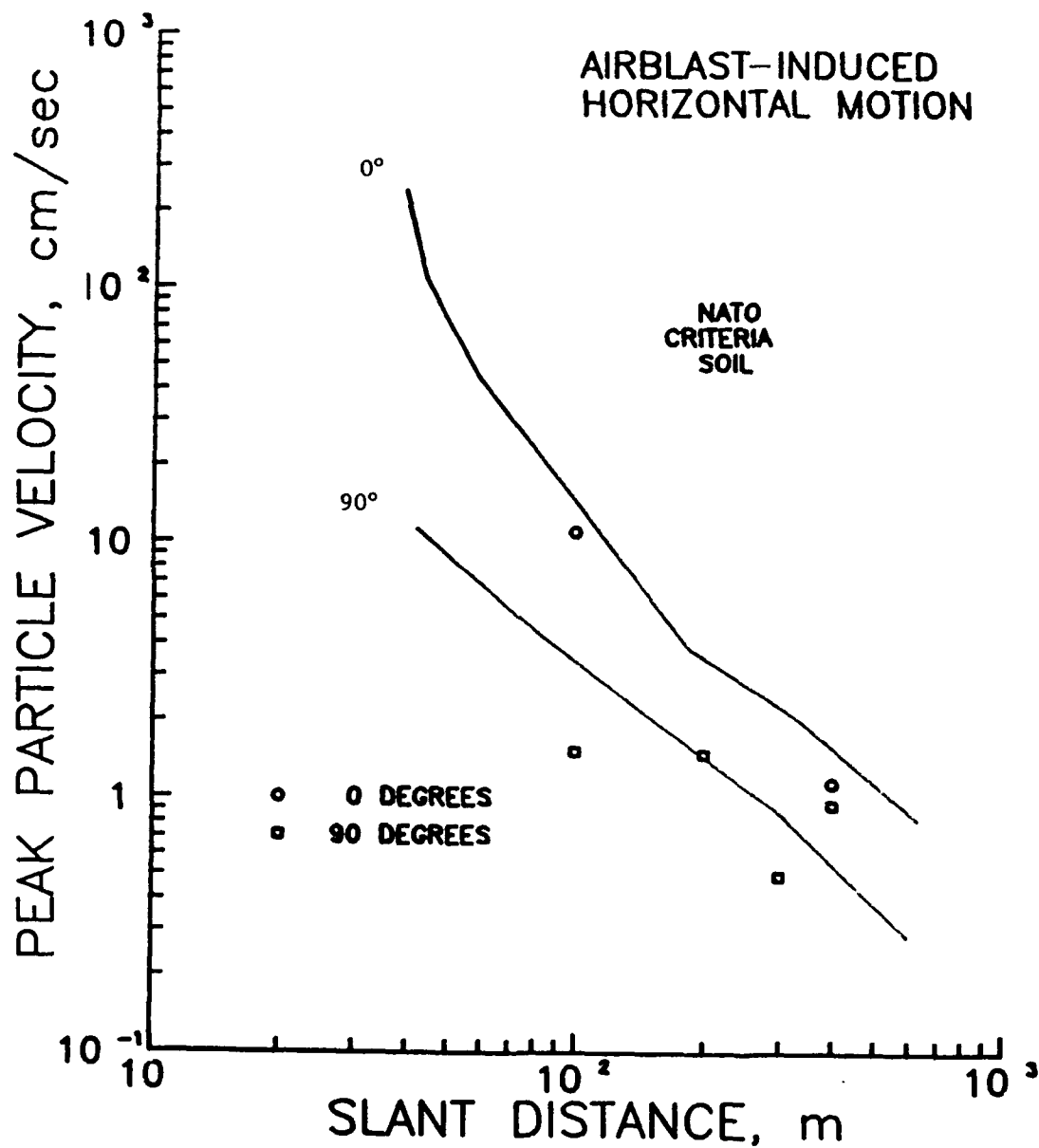


Figure 66. Peak, airblast-induced, horizontal particle velocity versus slant distance from the center of the charge, Shallow Underground Tunnel/Chamber Explosion Test.

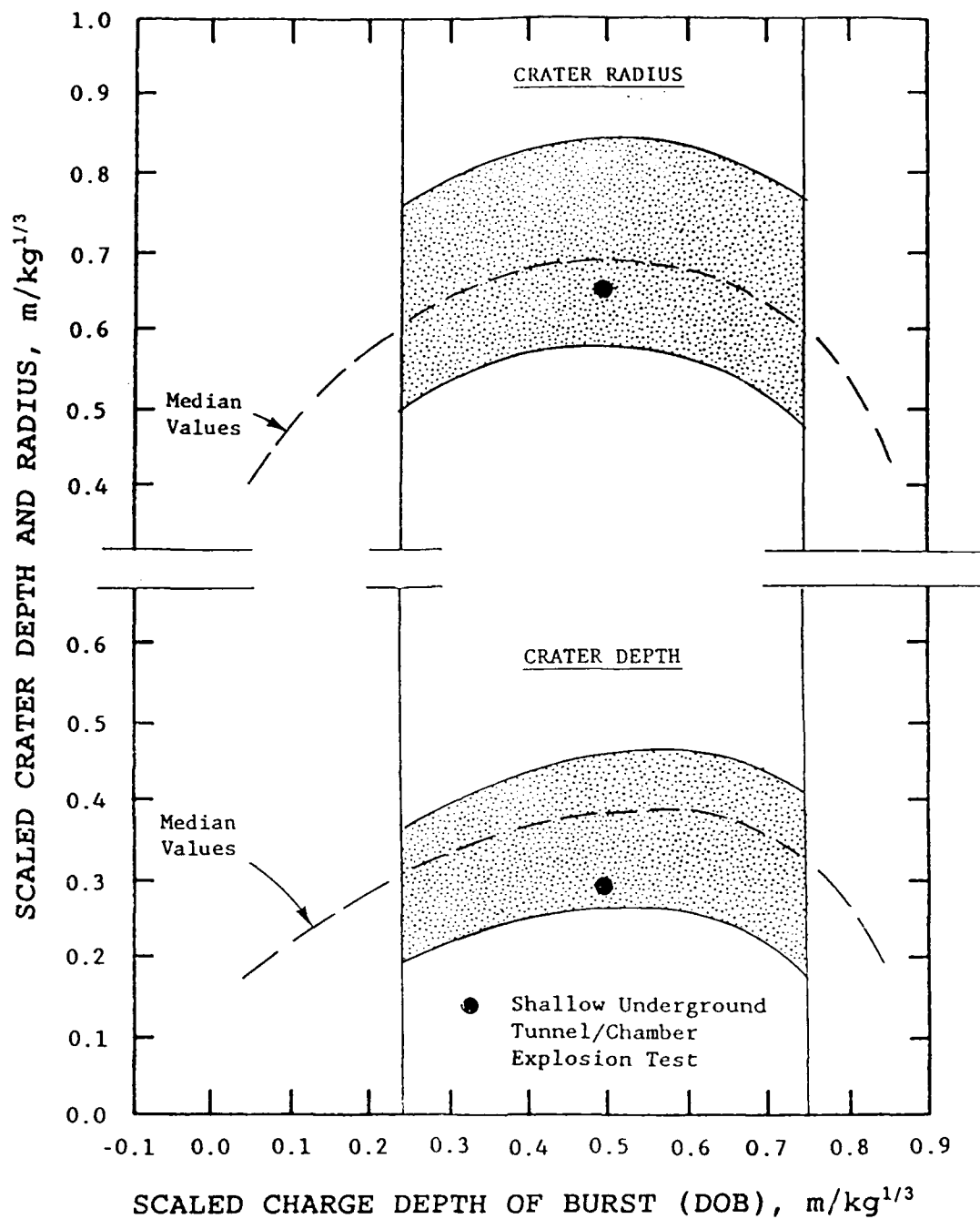


Figure 67. Scaled crater dimensions versus scaled depth of burst in rock; comparison of crater from Shallow Underground Tunnel/Chamber Explosion Test with data bands from previous, fully-coupled detonations in rock.

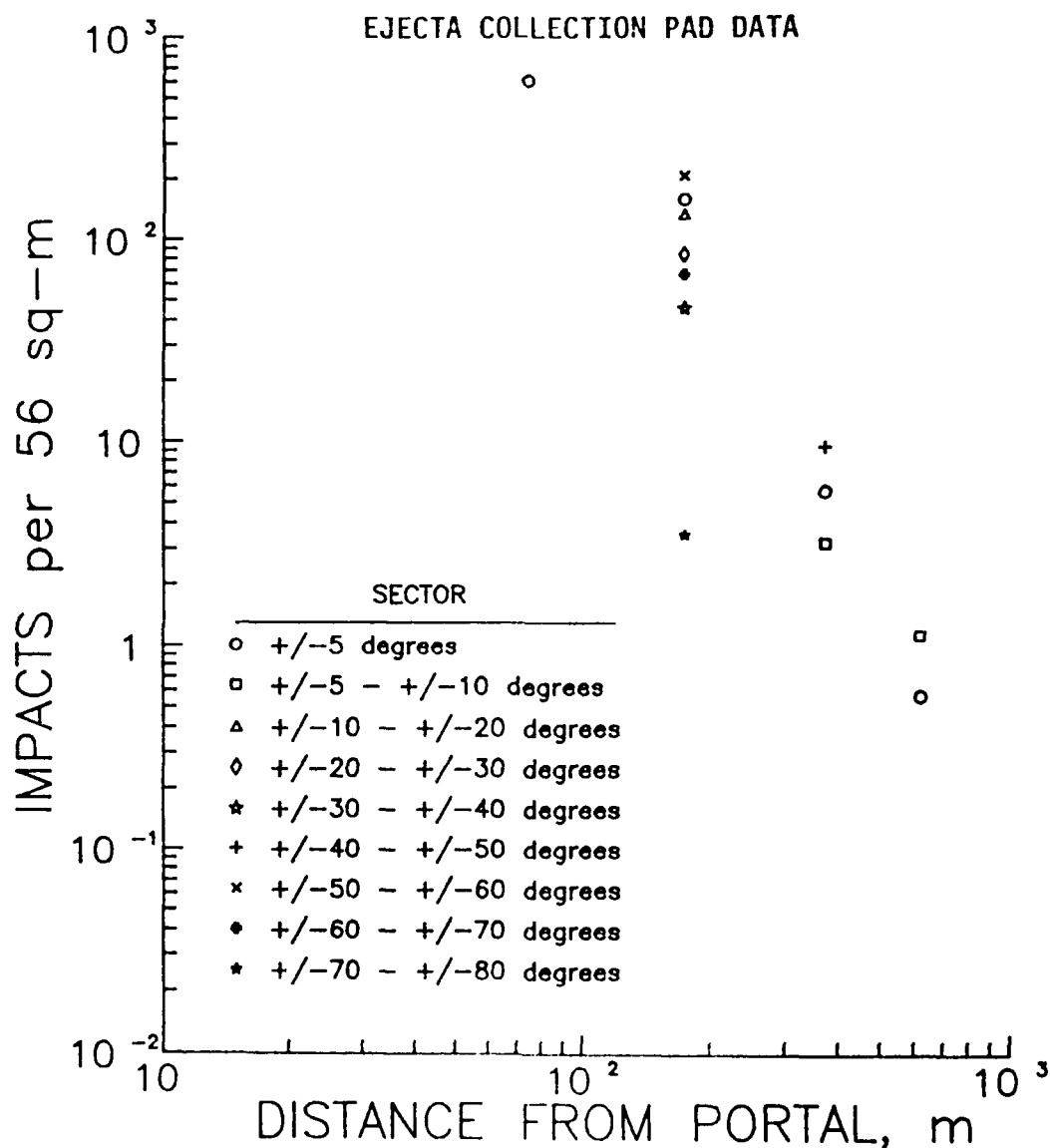


Figure 68. Impact density for ejecta missiles found on collection pads, as a function of distance from the tunnel portal; for Shallow Underground Tunnel/Chamber Explosion Test.

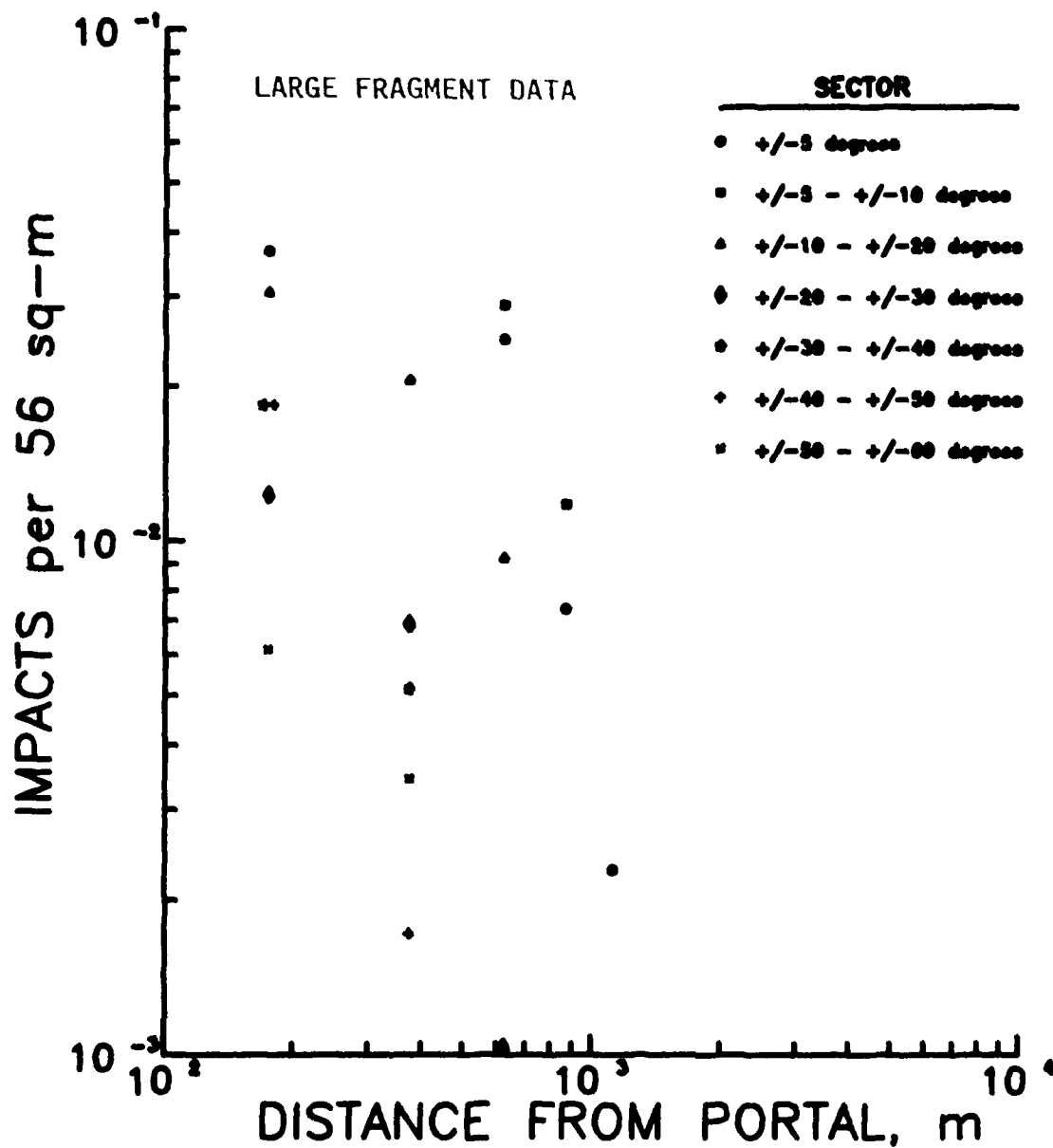


Figure 69. Large fragment impact as a function of distance from the tunnel portal, Shallow Underground Tunnel Chamber Explosion Test.

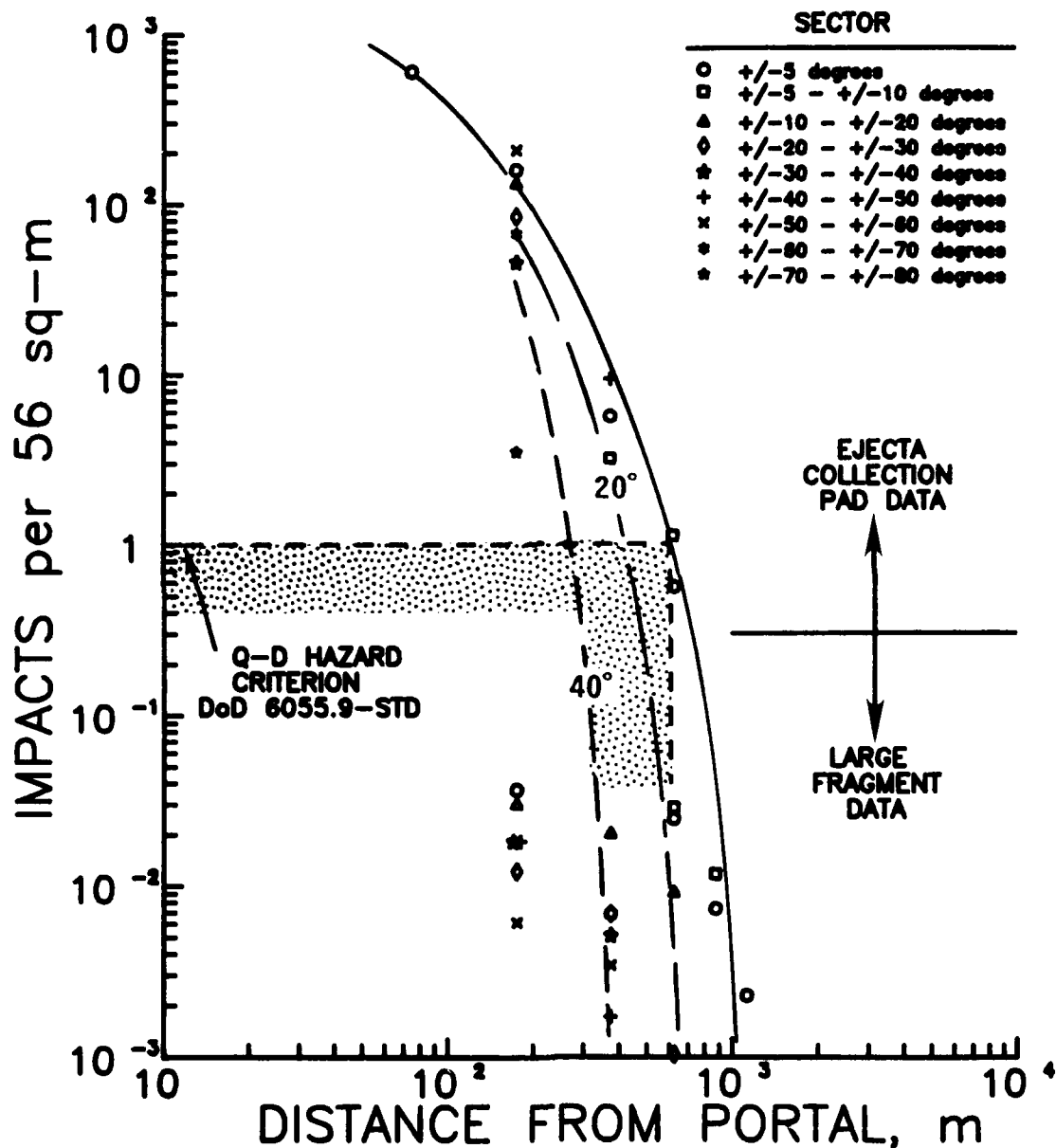


Figure 70. Ejecta/debris missile impact density versus distance from the portal, Shallow Underground Tunnel/Chamber Explosion Test. Curves show general limits of missile density ranges along extended tunnel axis (0-degree azimuth) and with ± 20 degree and ± 40 degree sectors.

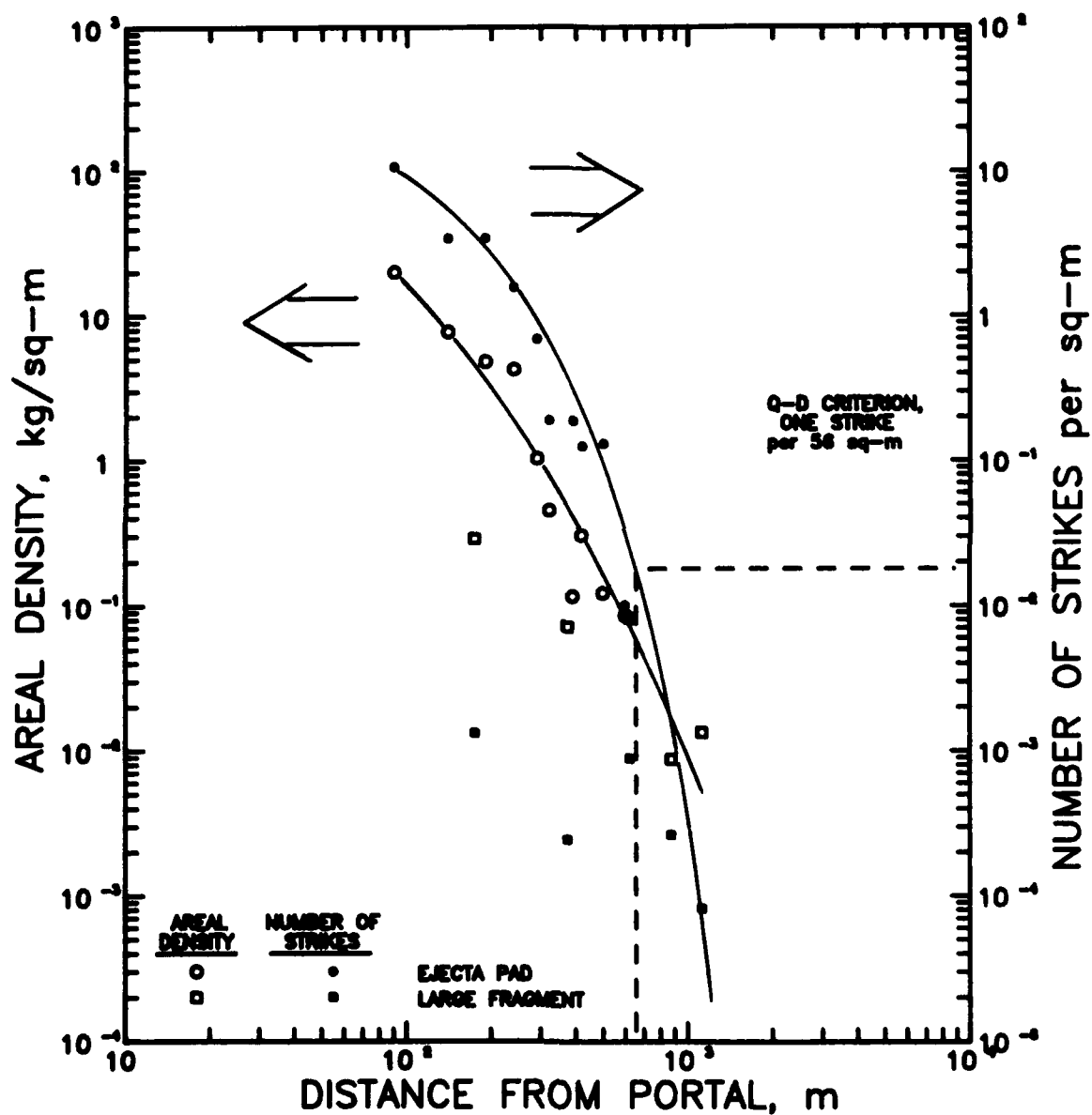


Figure 71. Areal density and number of strikes of natural missiles versus distance from tunnel portal, Shallow Underground Tunnel/Chamber Explosion Test.

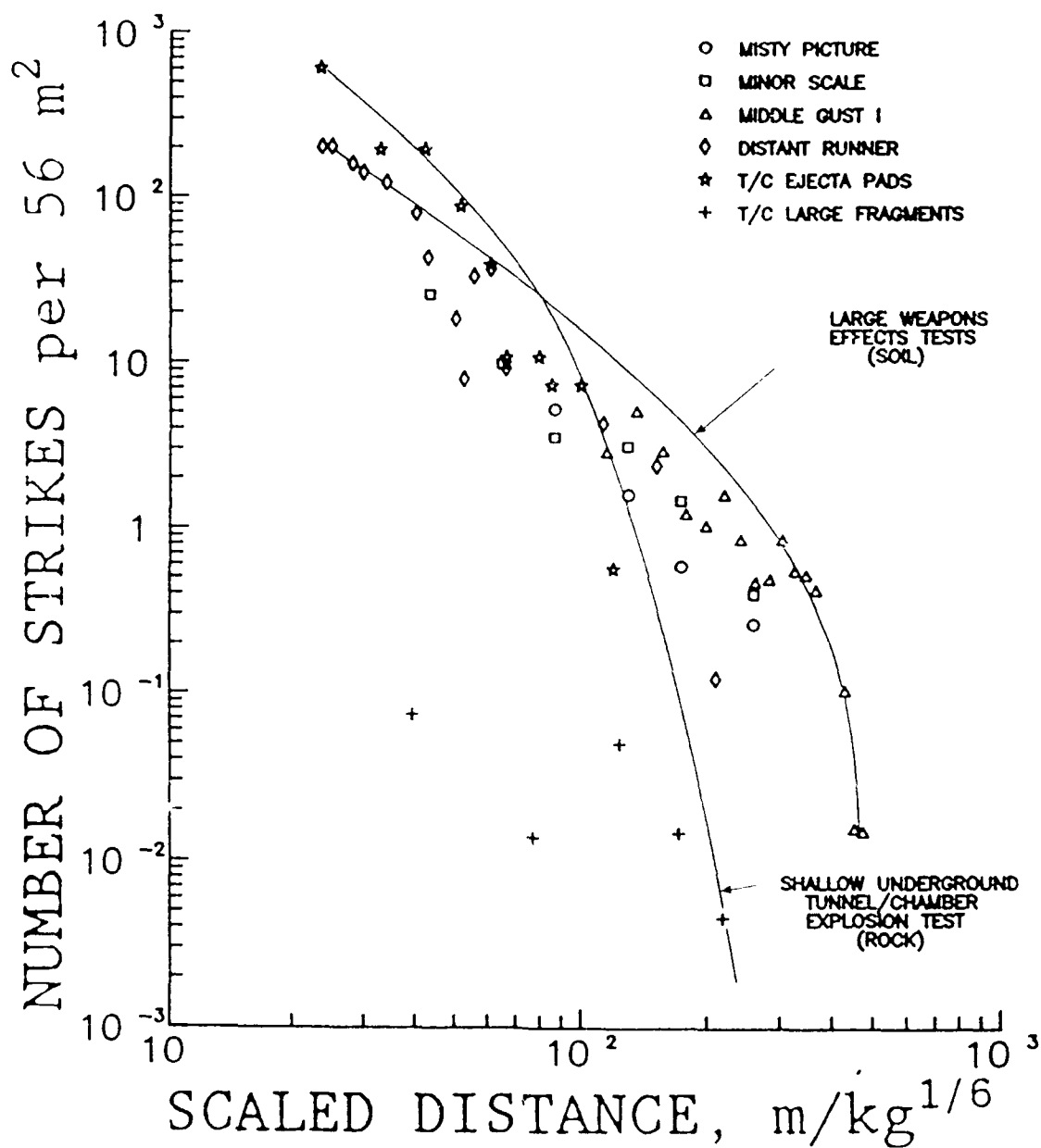


Figure 72. Comparison of the number of strikes versus scaled distance from the charge for large-yield surface burst explosion tests and the Shallow Underground Tunnel/Chamber Explosion Test (decoupled buried explosive charge).

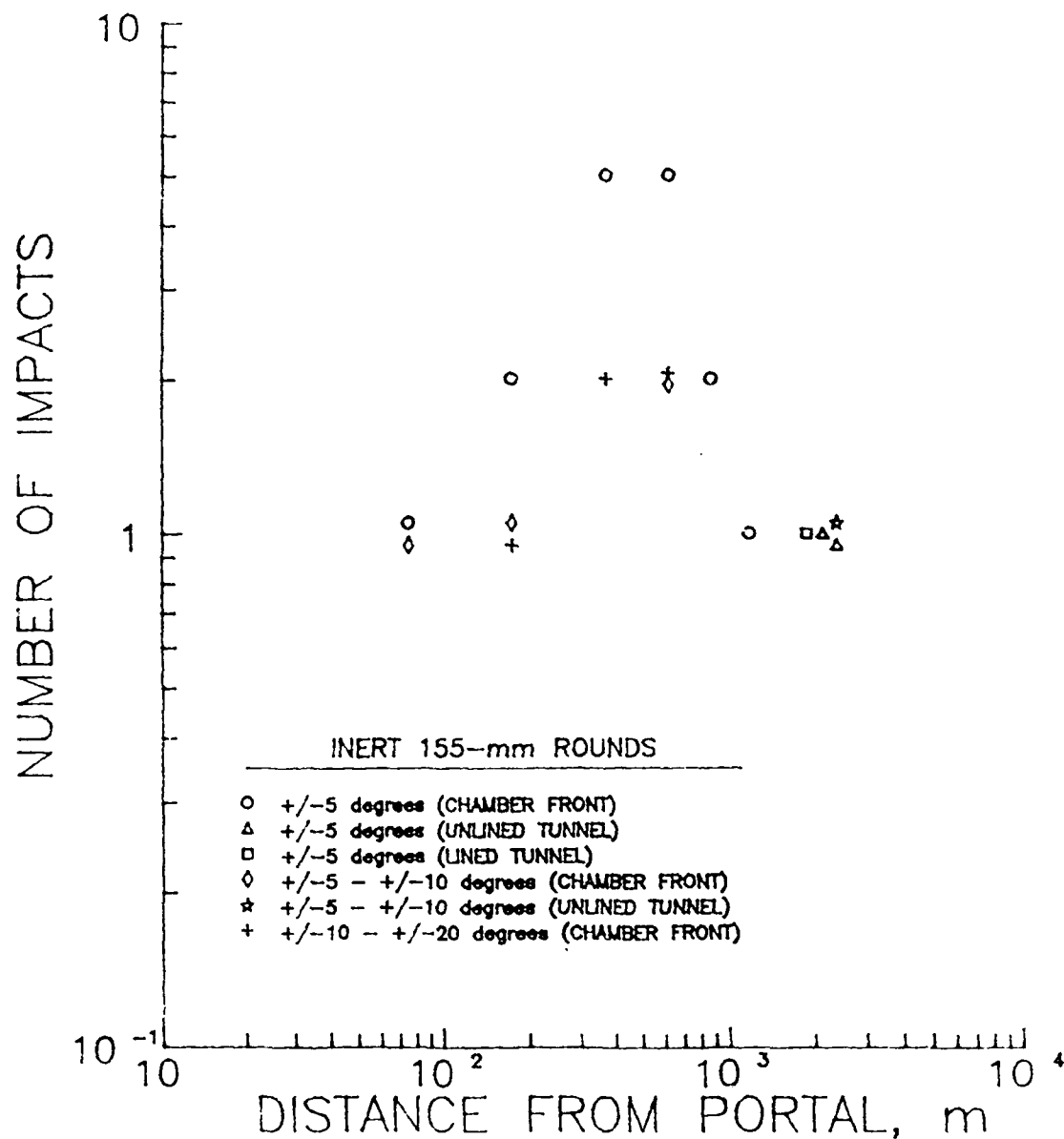


Figure 73. Number of inert 155-mm round impacts as a function of distance from the tunnel portal, Shallow Underground Tunnel/Chamber Explosion Test. Symbols identify pretest round location. Note: rounds placed in chamber behind explosive charge were not found post-test.

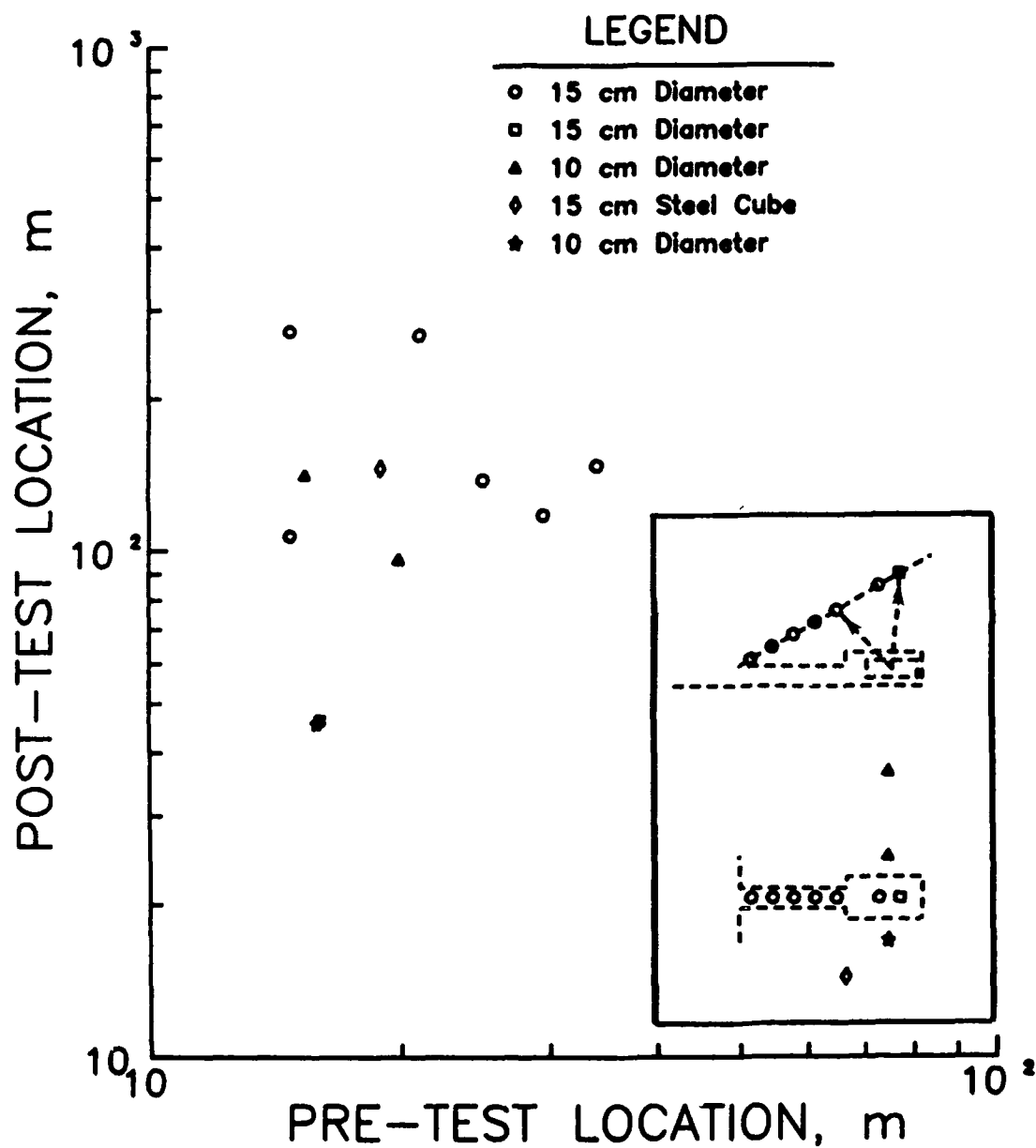


Figure 74. Artifical missile post-test versus pretest slant distance, Shallow Underground Tunnel/Chamber Explosion Test. Missiles were 10 and 15 cm diameter aluminum cylinders, 10 and 15 cm long, respectively. One 15 cm steel cube was also recovered.

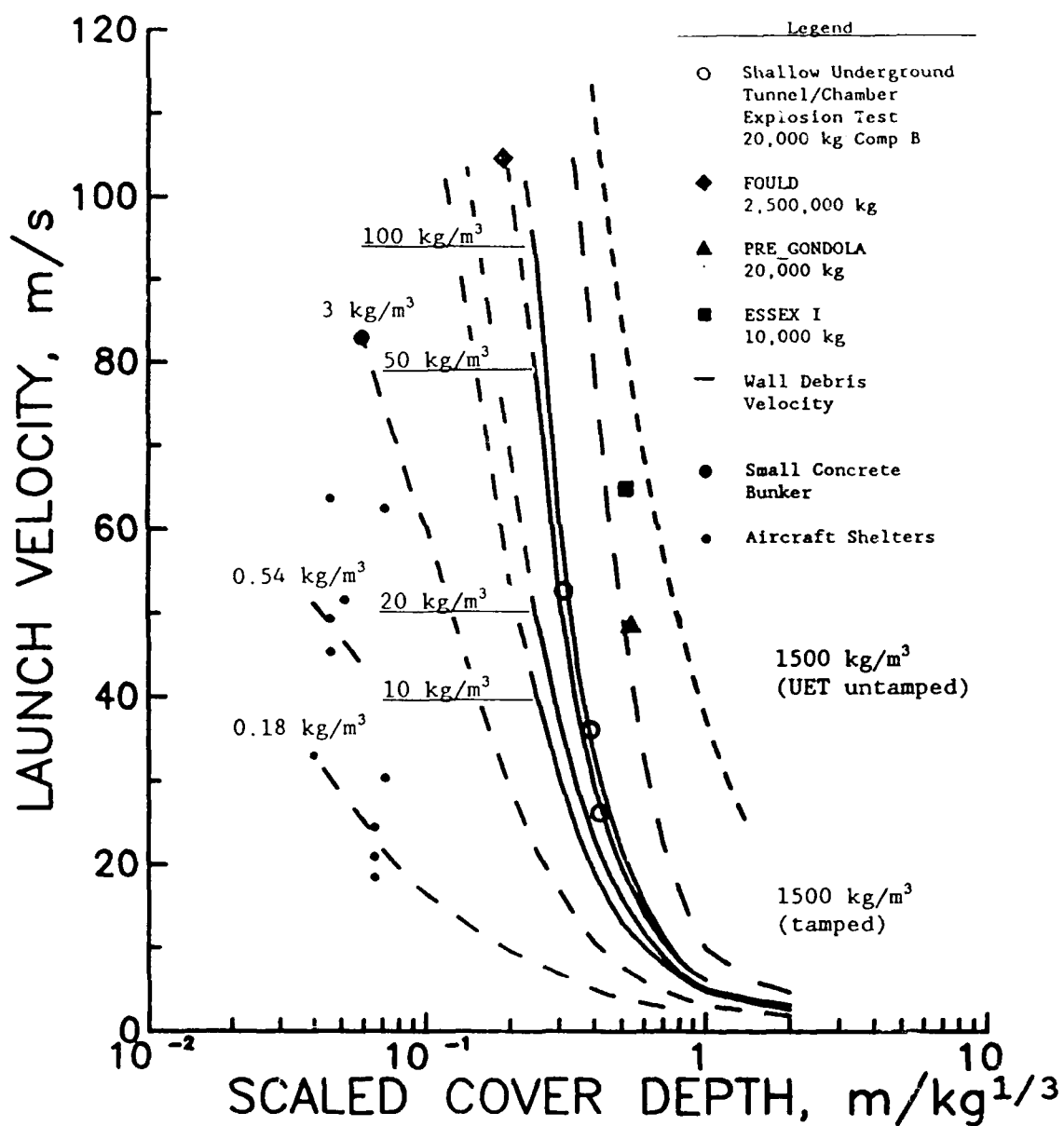


Figure 75. Launch velocity of cover rock ejecta from Shallow Underground Tunnel/Chamber Test, compared to ejecta velocities from other sources on previous explosive tests. (from Helseth, 1982). Scaled cover depth for Tunnel/Chamber Test varied from front of chamber to rear.

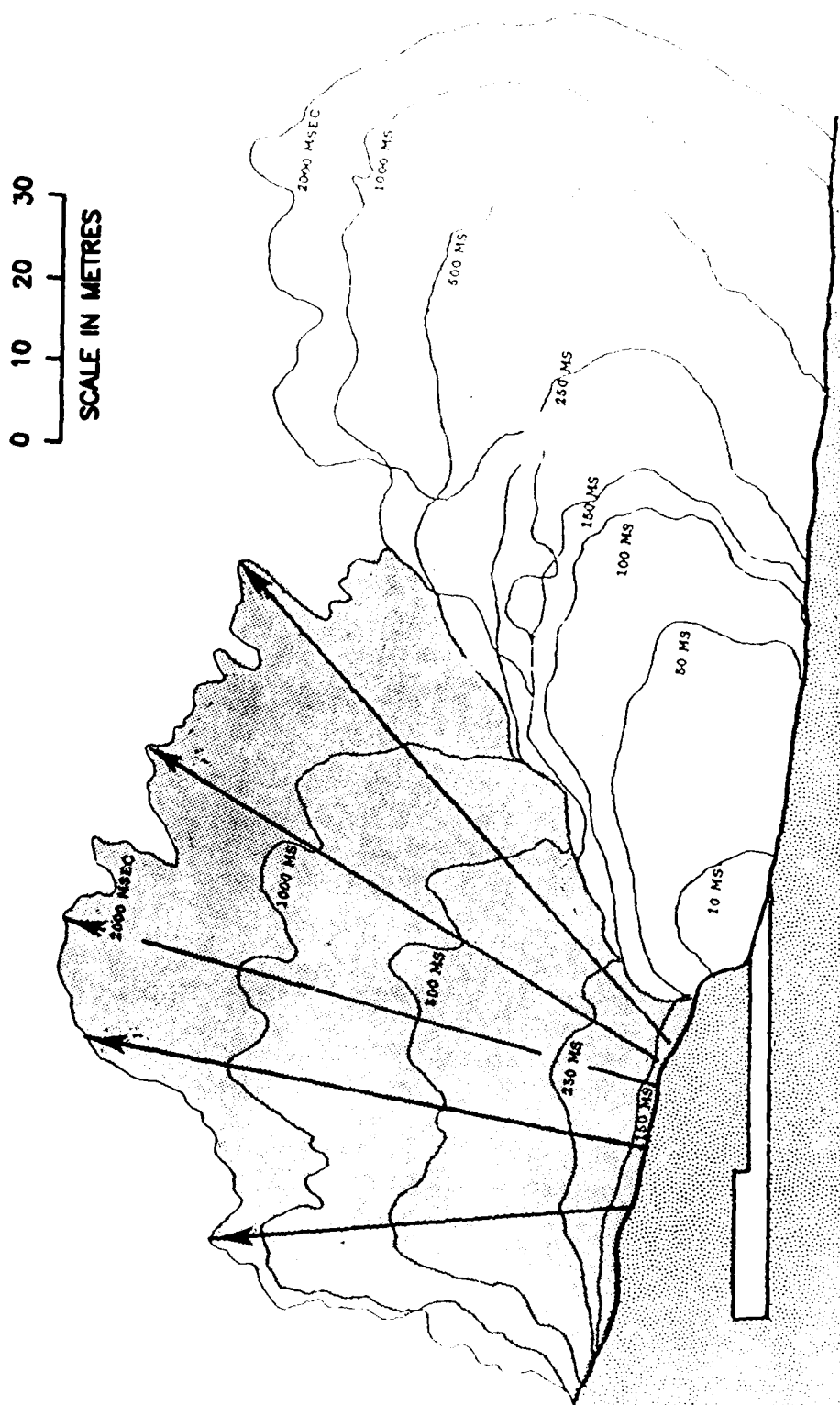


Figure 76. Growth rates of fireball (detonation products) clouds from tunnel portal (light area) and ejecta cloud from breach of rock cover over magazine (dark area). Time/position contours are in units of milliseconds after detonation. Initial overburden velocity was 19 m/s above the storage chamber.

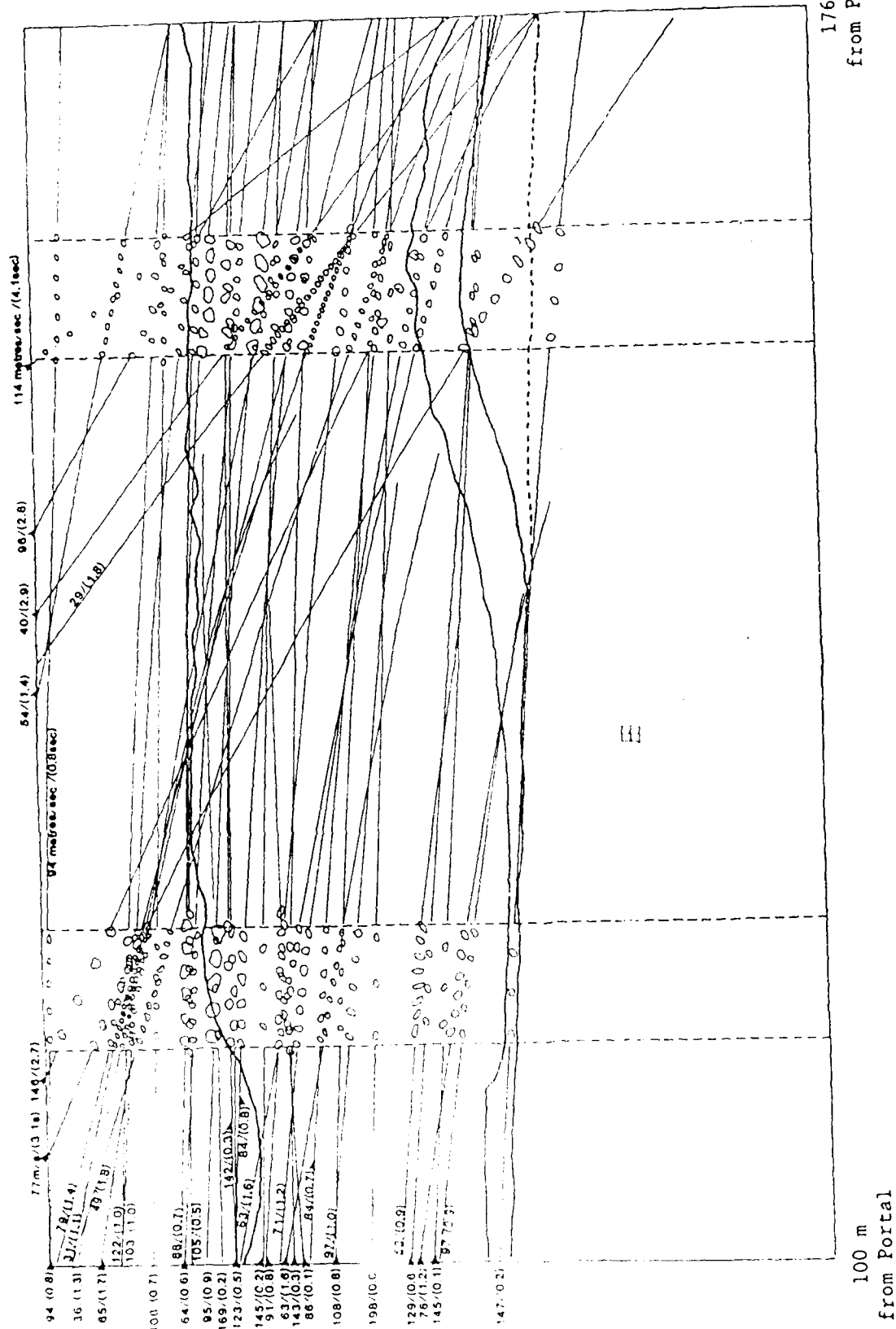


Figure 78. Ejecta missile paths recorded by camera Station 7. Center of field of view is 138 m from portal along 0-degree bearing. Notation gives computed particle velocity followed by relative arrival time (time after first particle passes edge of field of view), in seconds (shown in parentheses). Vertical sections show sizes and positions of missiles at single-frame intervals.

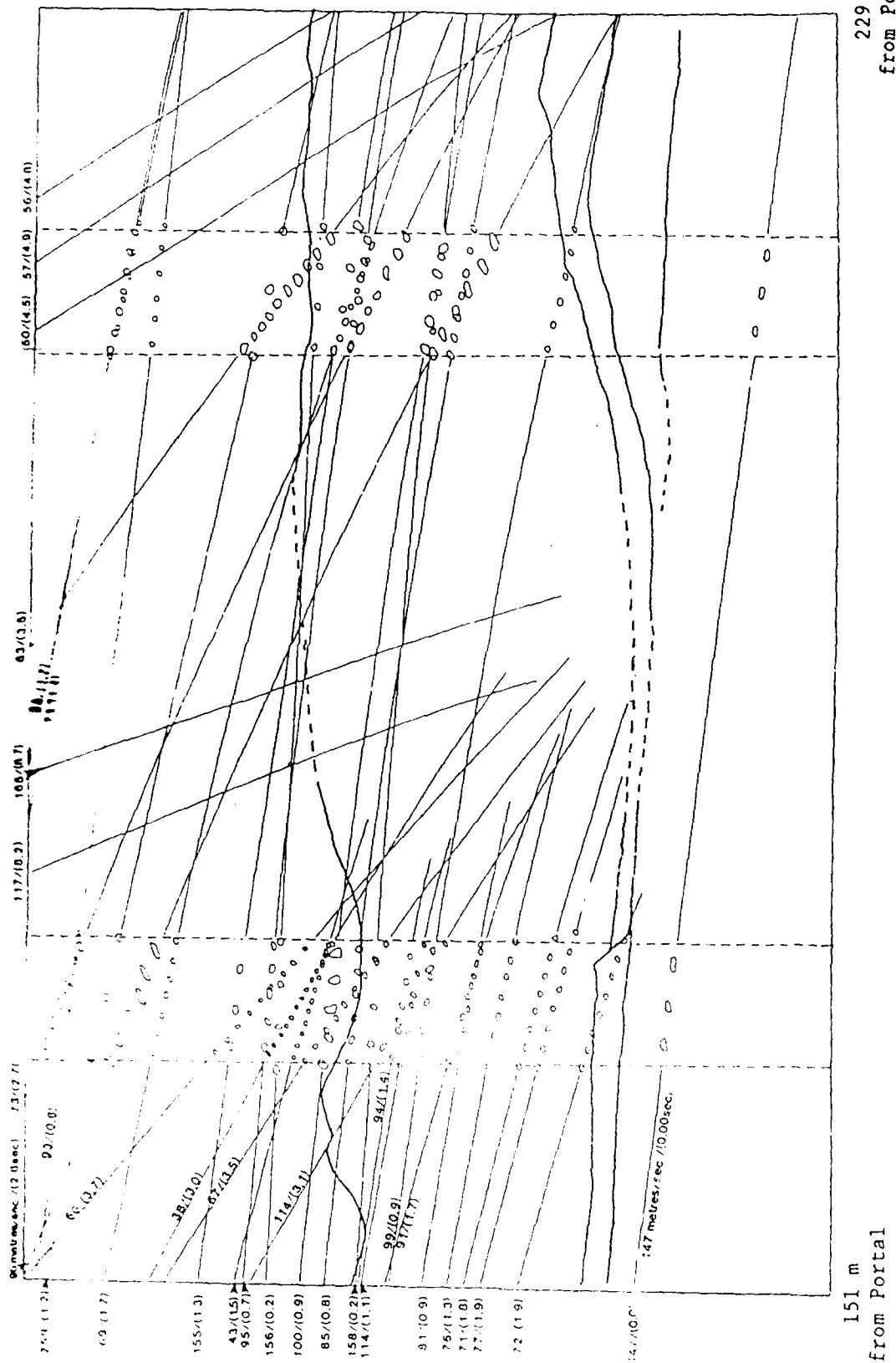
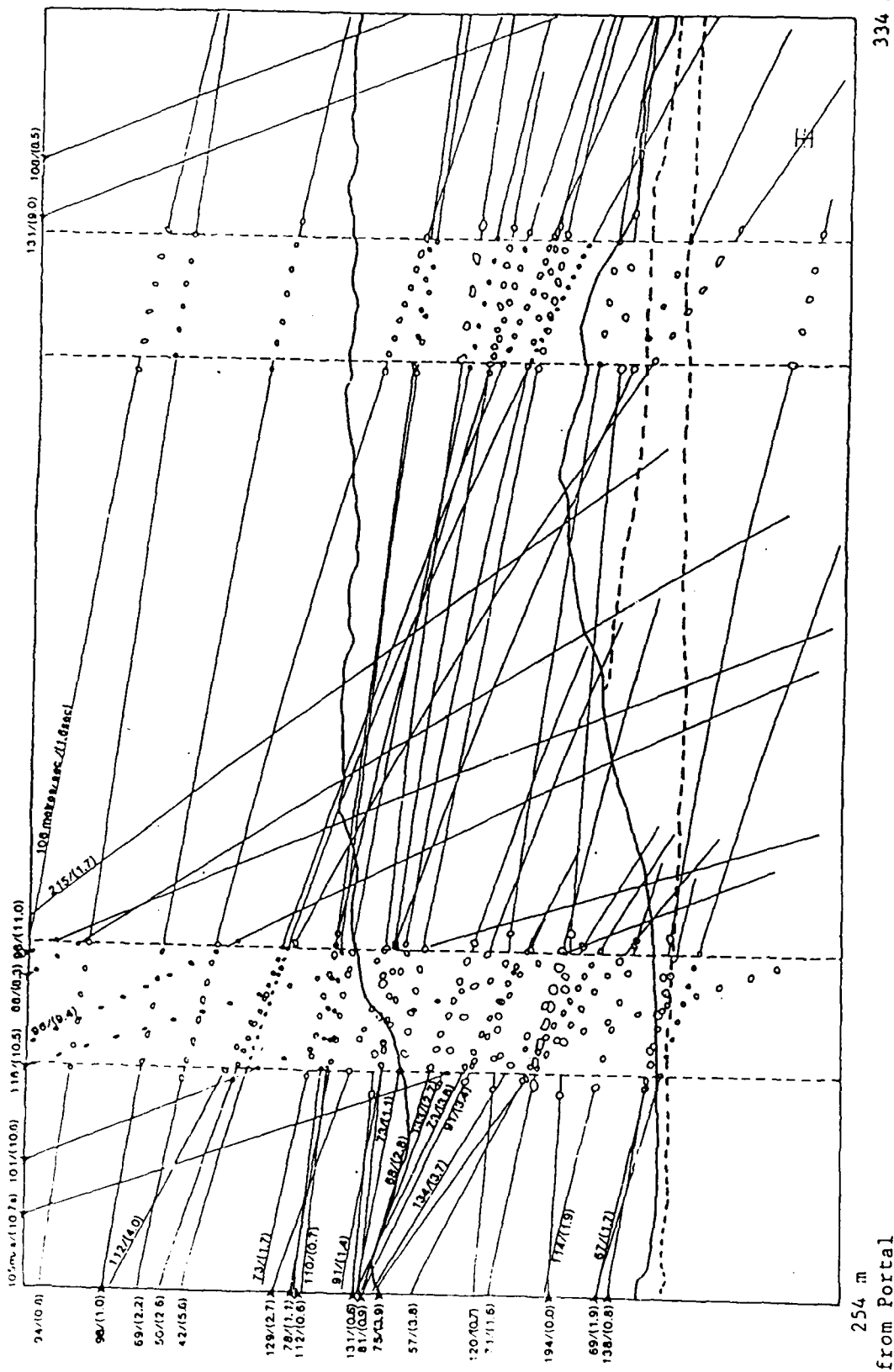


Figure 79. Ejecta missile paths recorded by camera Station 8. Center of field of view is 190 m from portal along 0-degree bearing. Notation gives computed particle velocity followed by relative arrival time (time after first particle passes edge of field of view), in seconds (shown in parentheses). Vertical sections show sizes and positions of missiles at single-frame intervals.



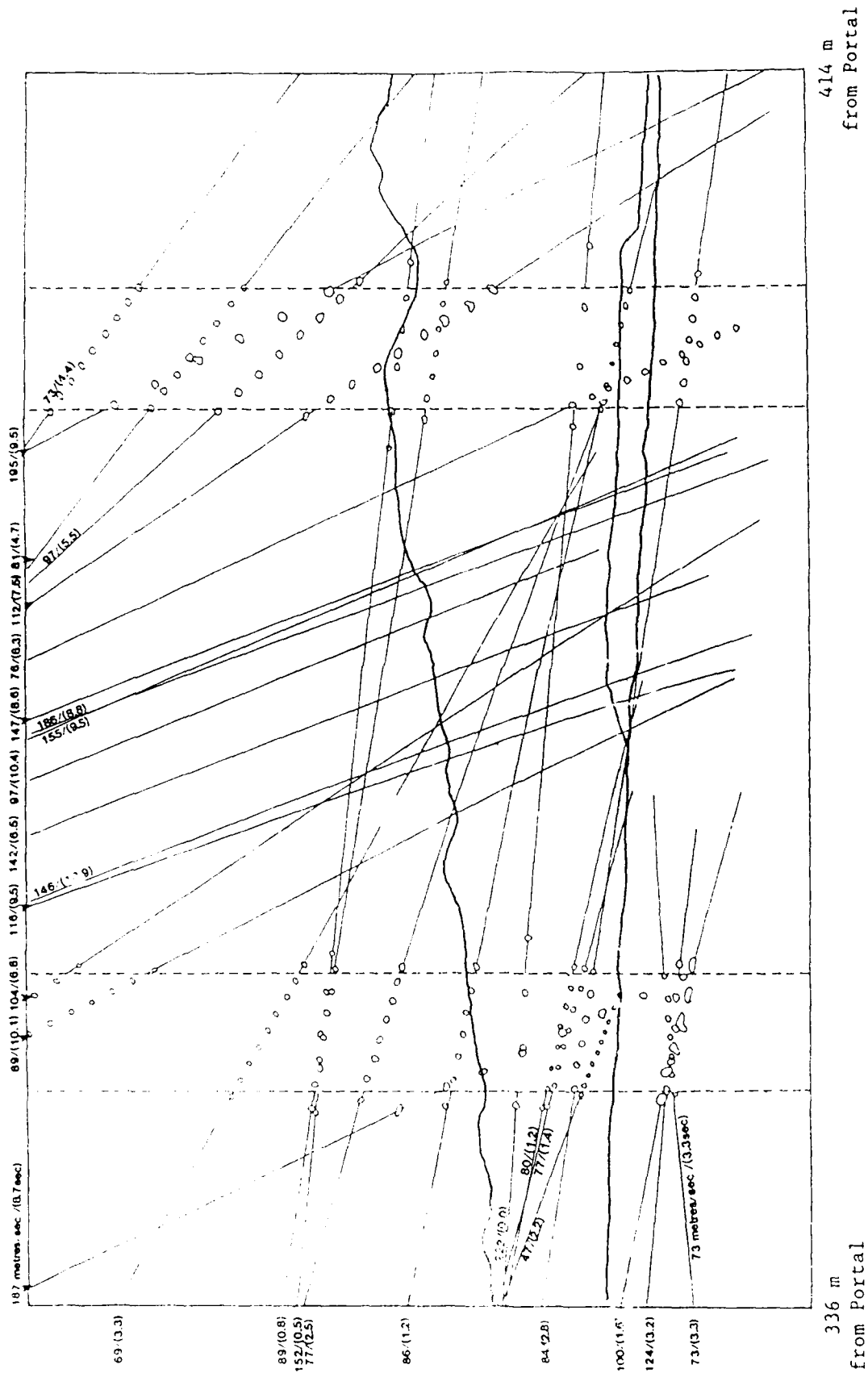


Figure 81. Ejecta missile paths recorded by camera Station 11. Center of field of view is 375 m from portal along 0-degree bearing. Notation gives computed particle velocity followed by relative arrival time (time after first particle passes edge of field of view), in seconds (shown in parentheses). Vertical sections show sizes and positions of missiles at single-frame intervals.

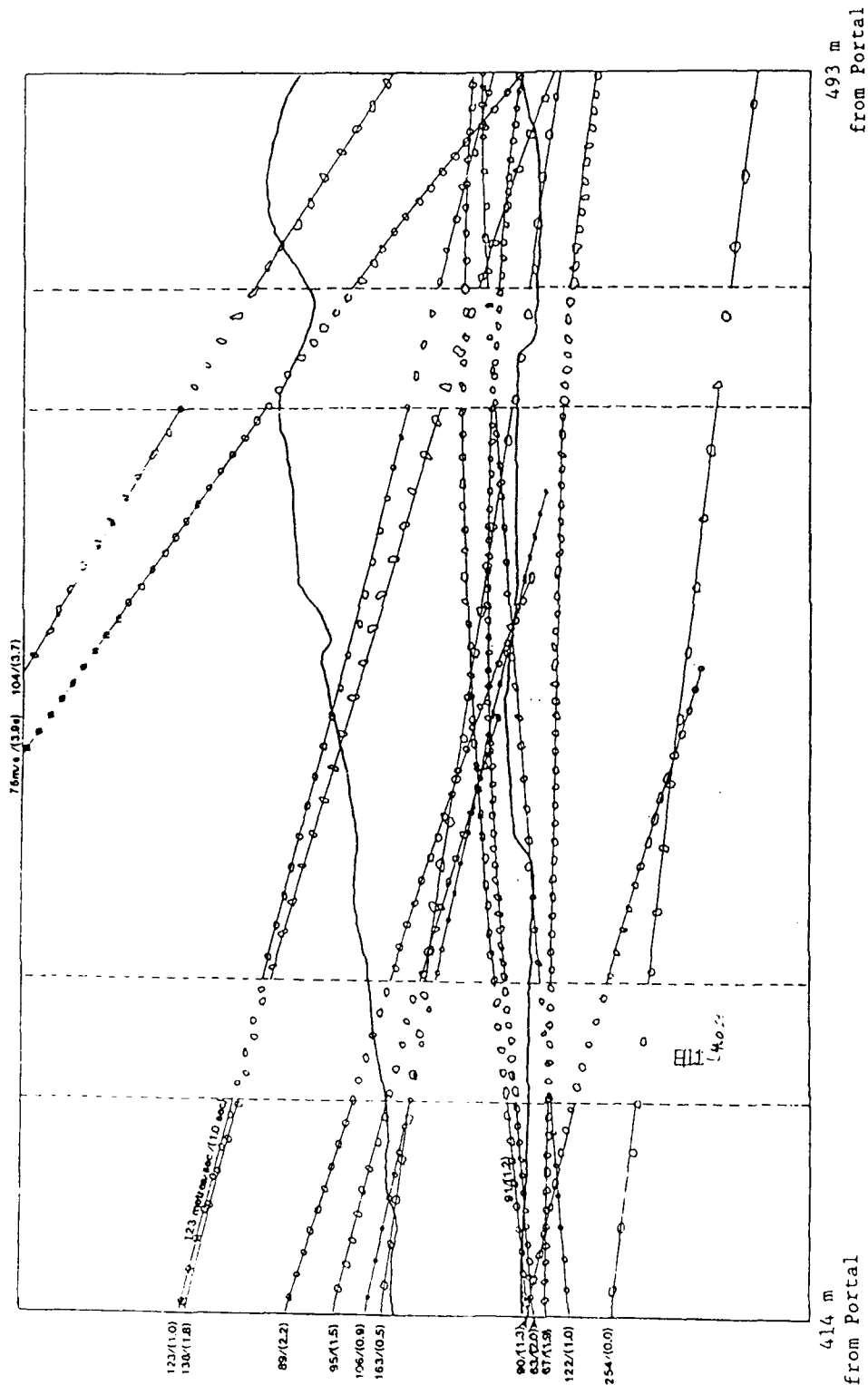


Figure 82. Ejecta missile paths recorded by camera Station 12. Center of field of view is 454 m from portal along 0-degree bearing. Notation gives computed particle velocity followed by relative arrival time (time after first particle passes edge of field of view), in seconds (shown in parentheses). Vertical sections show sizes and positions of missiles at single-frame intervals.

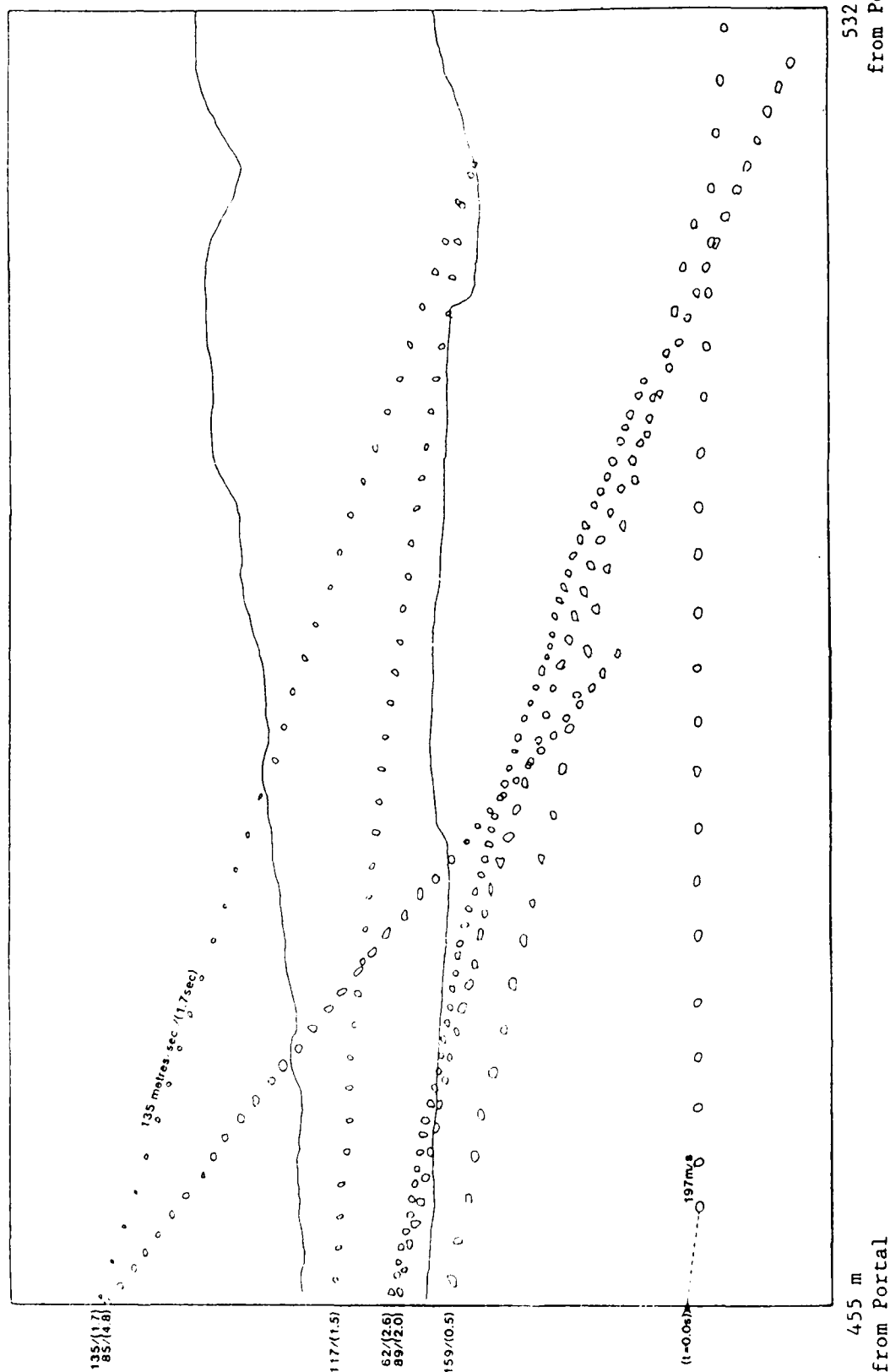


Figure 83. Ejecta missile paths recorded by camera Station 13. Center of field of view is 494 m from portal along 0-degree bearing. Notation gives computed particle velocity followed by relative arrival time (time after first particle velocity passes edge of field of view), in seconds (shown in parentheses). Vertical sections show sizes and positions of missiles at single-frame intervals.

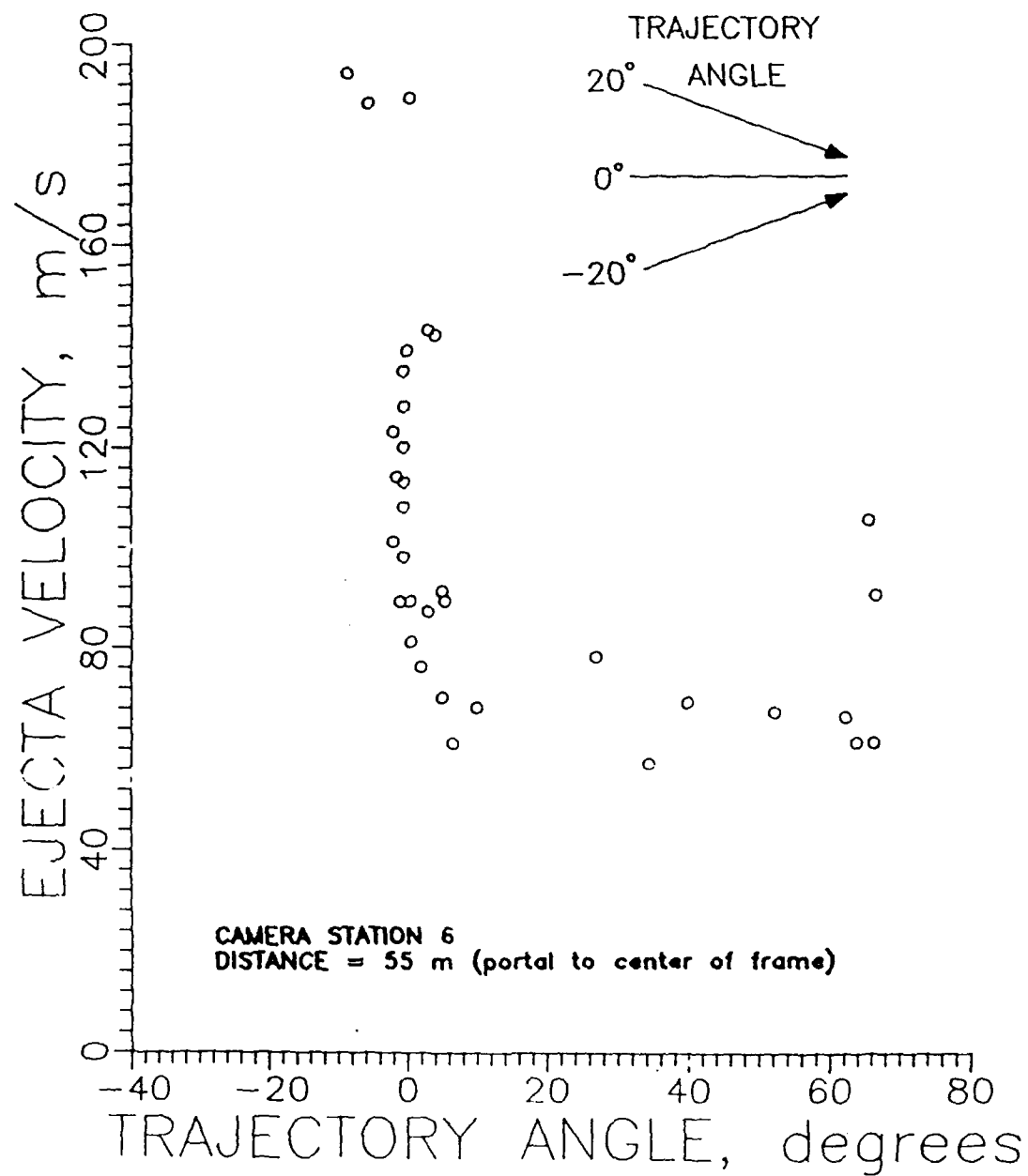


Figure 84. Ejecta missile velocity versus ballistic trajectory angle, as recorded by Camera Station 6. Negative angle indicates rising trajectory path.

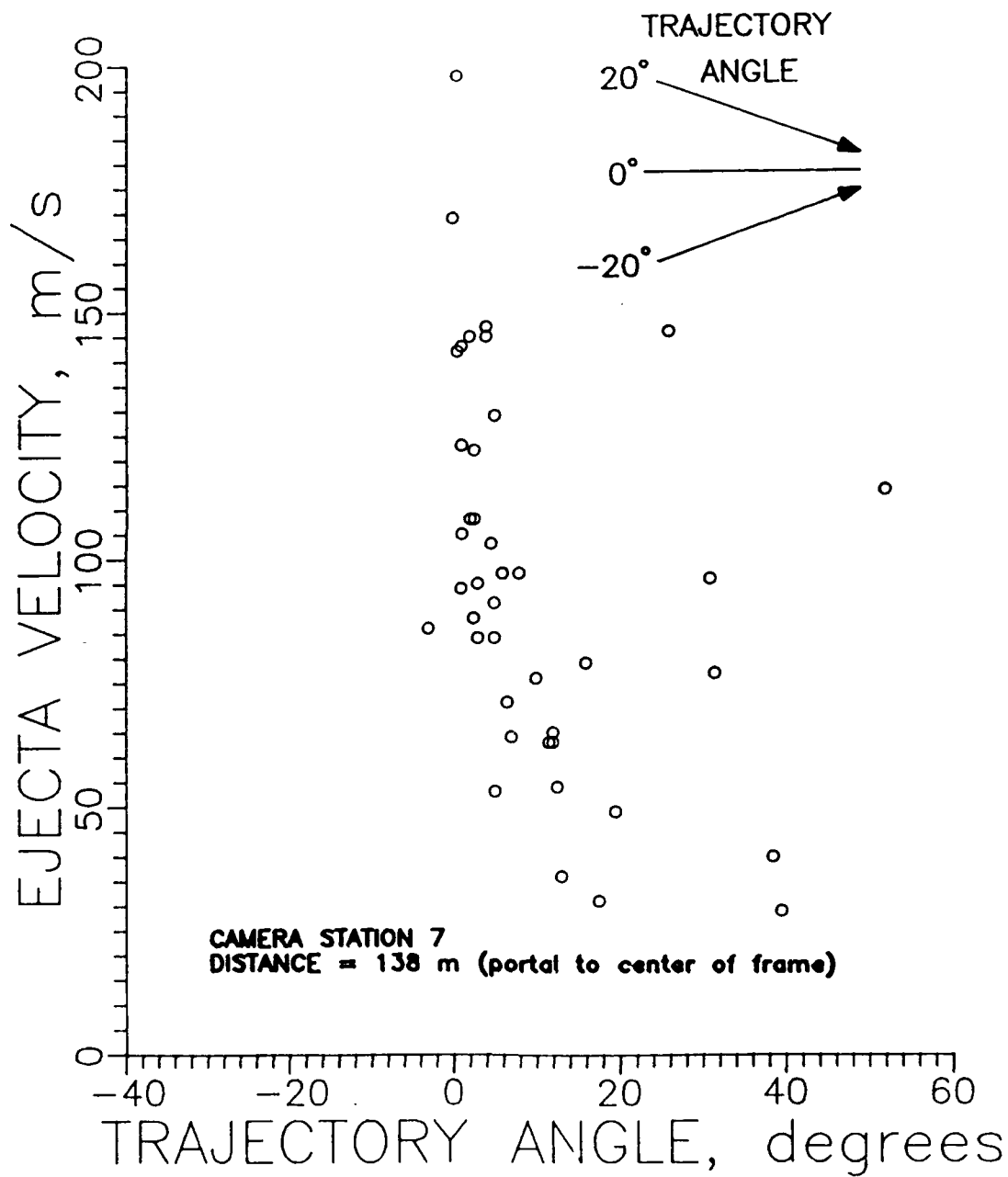


Figure 85 Ejecta missile velocity versus ballistic trajectory angle, as recorded by Camera Station 7.

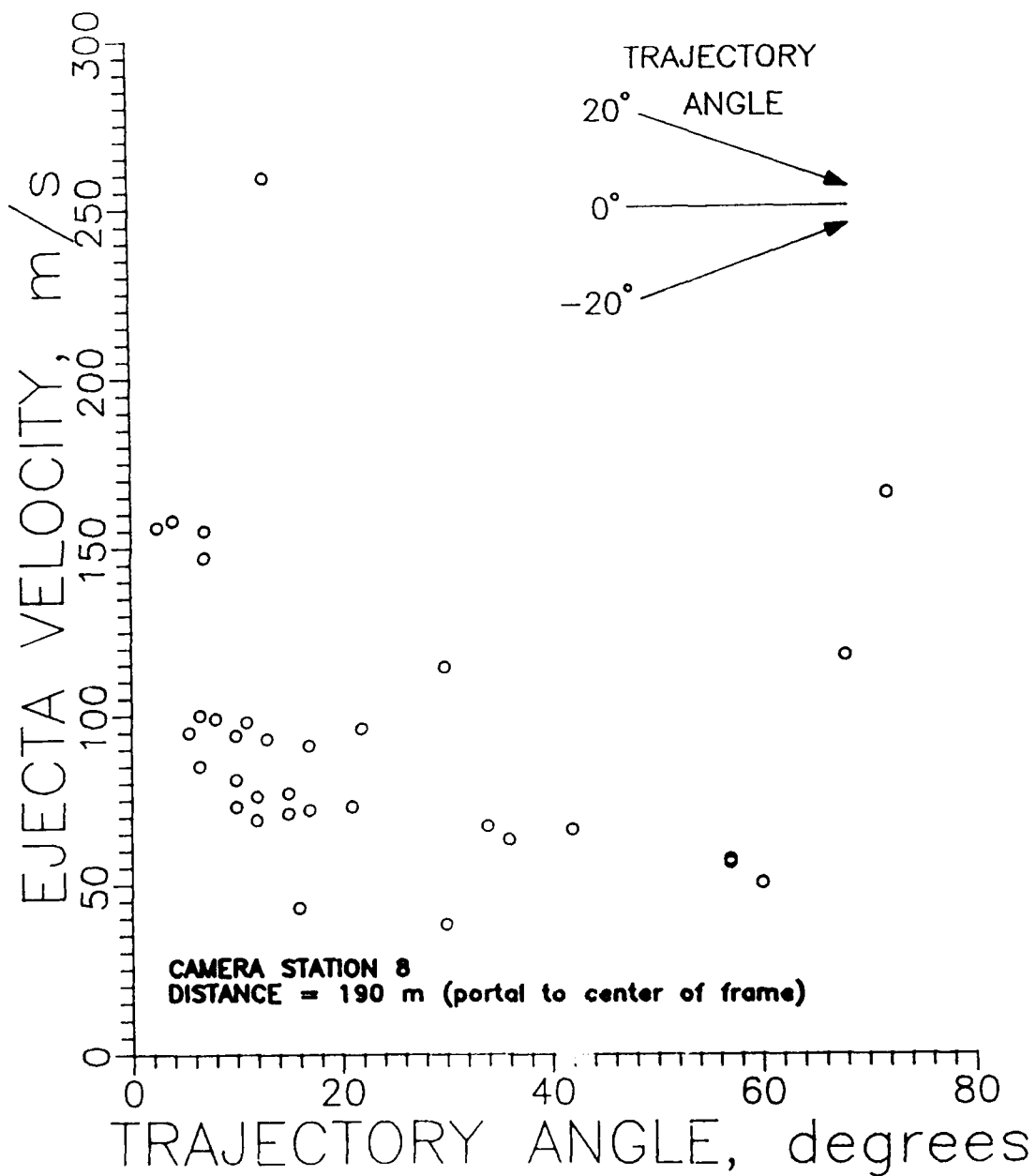


Figure 86. Ejecta missile velocity versus ballistic trajectory angle, as recorded by Camera Station 8.

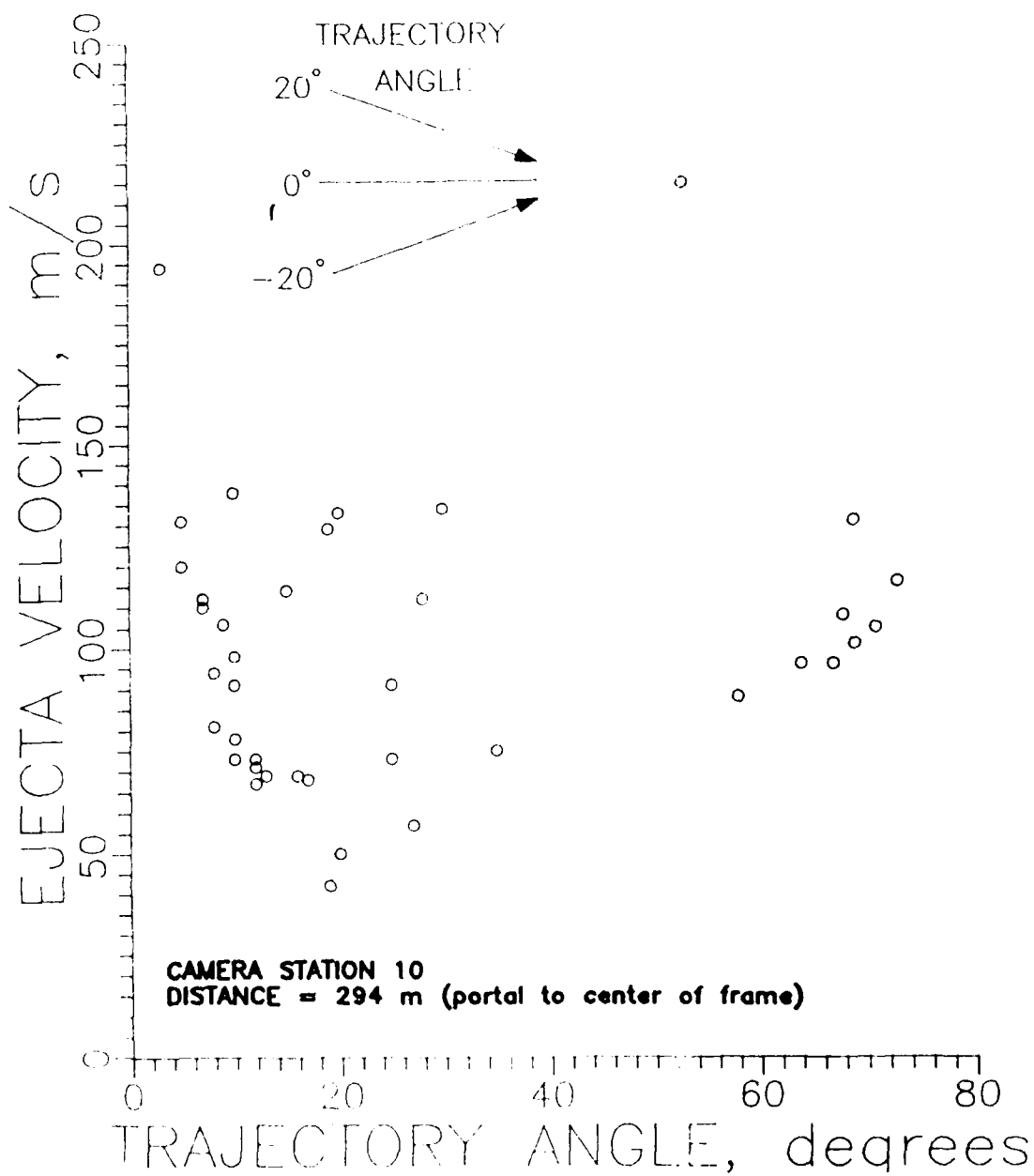


Figure 87. Ejecta missile velocity versus ballistic trajectory angle, as recorded by Camera Station 10.

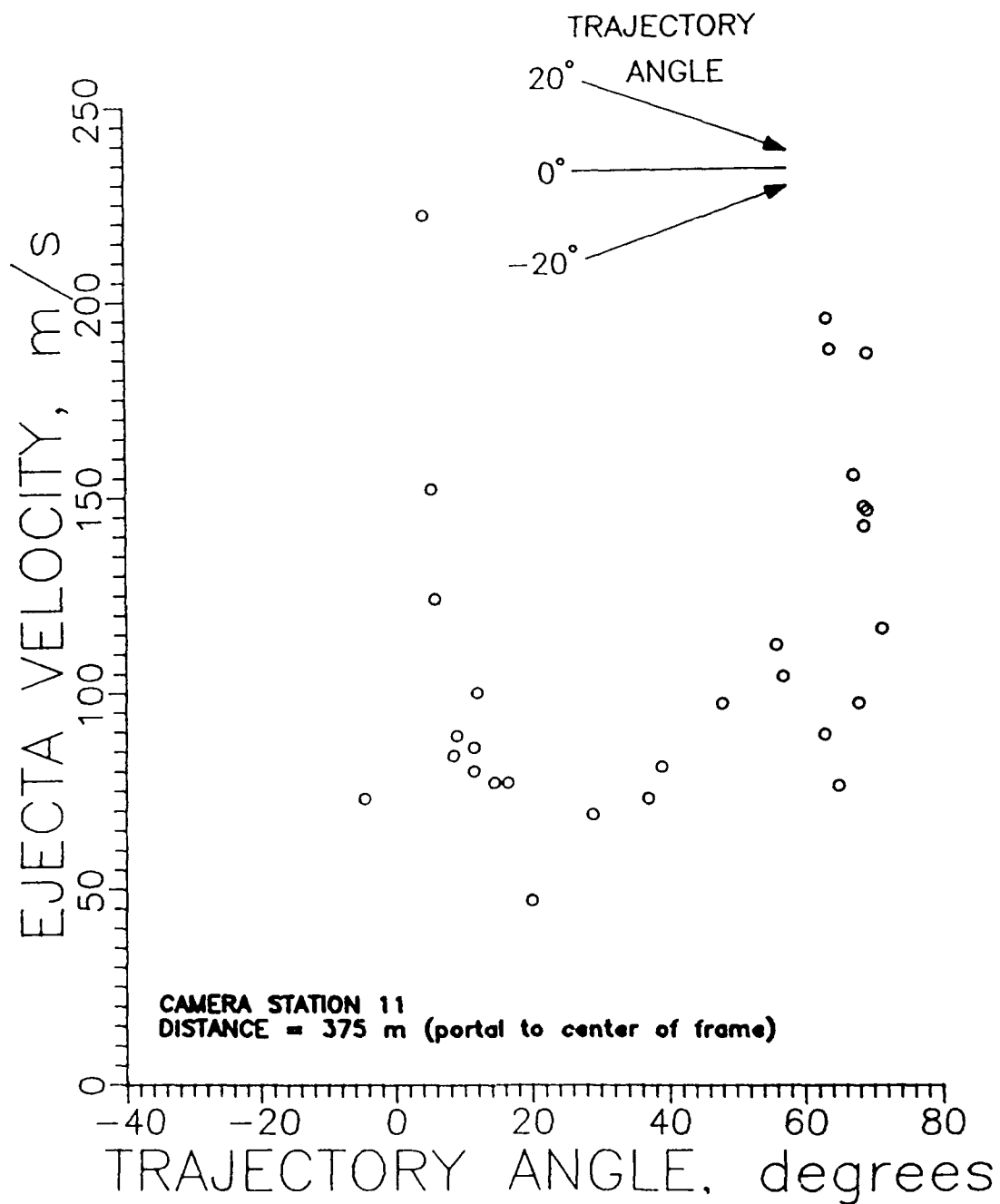


Figure 88. Ejecta missile velocity versus ballistic trajectory angle, as recorded by Camera Station 11.

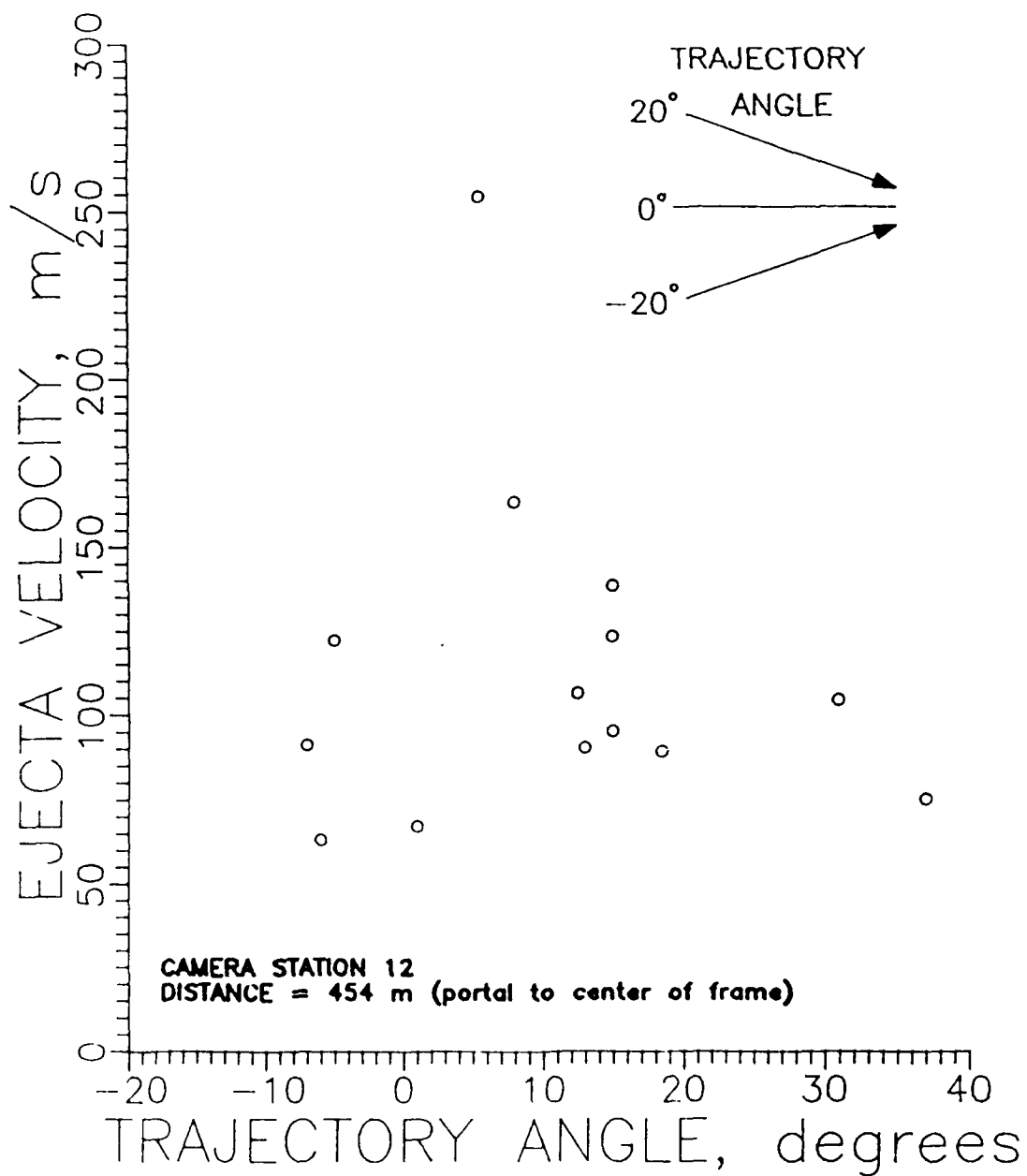


Figure 89. Ejecta missile velocity versus ballistic trajectory angle, as recorded by Camera Station 12.

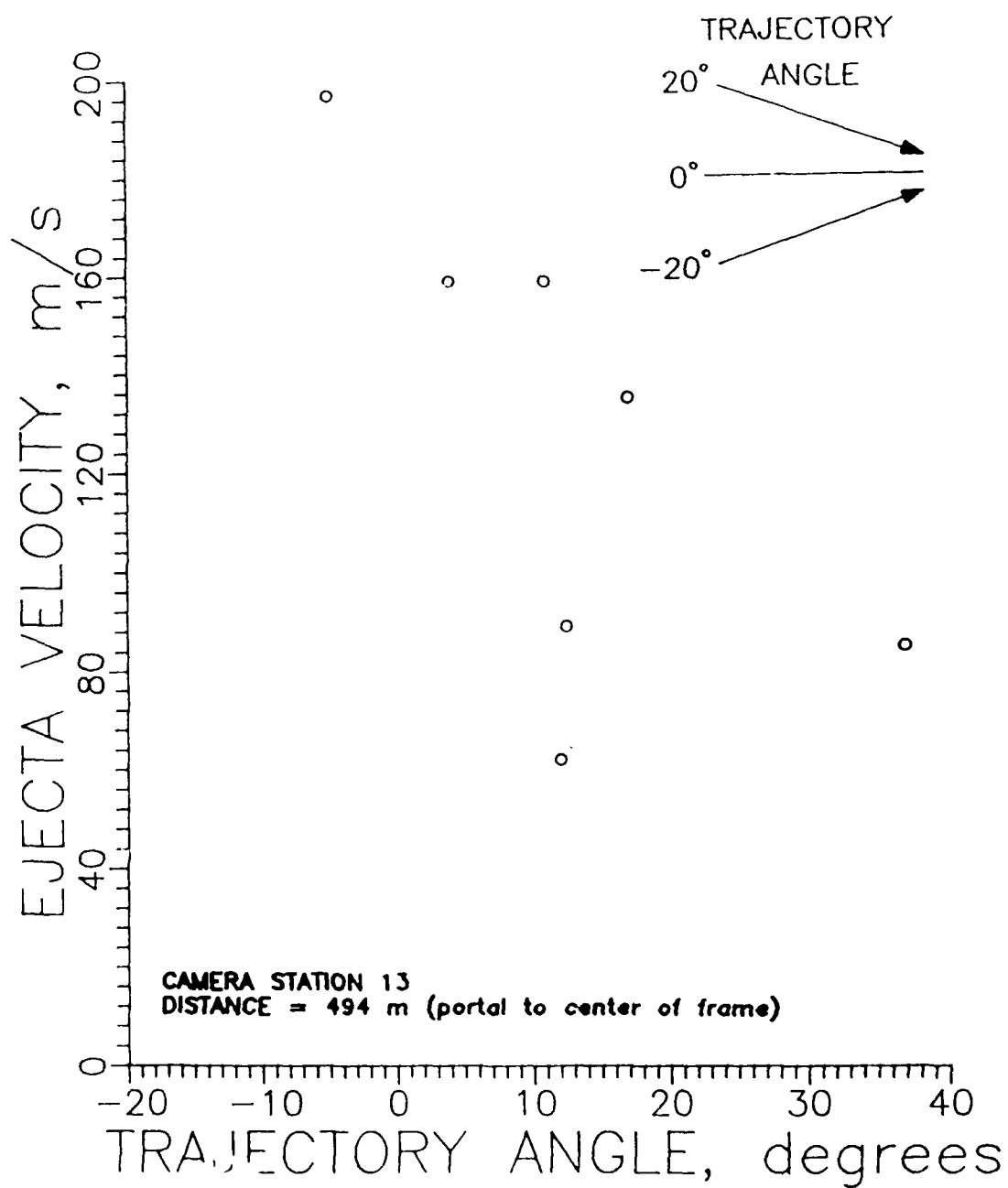


Figure 90. Ejecta missile velocity versus ballistic trajectory angle, as recorded by Camera Station 13.

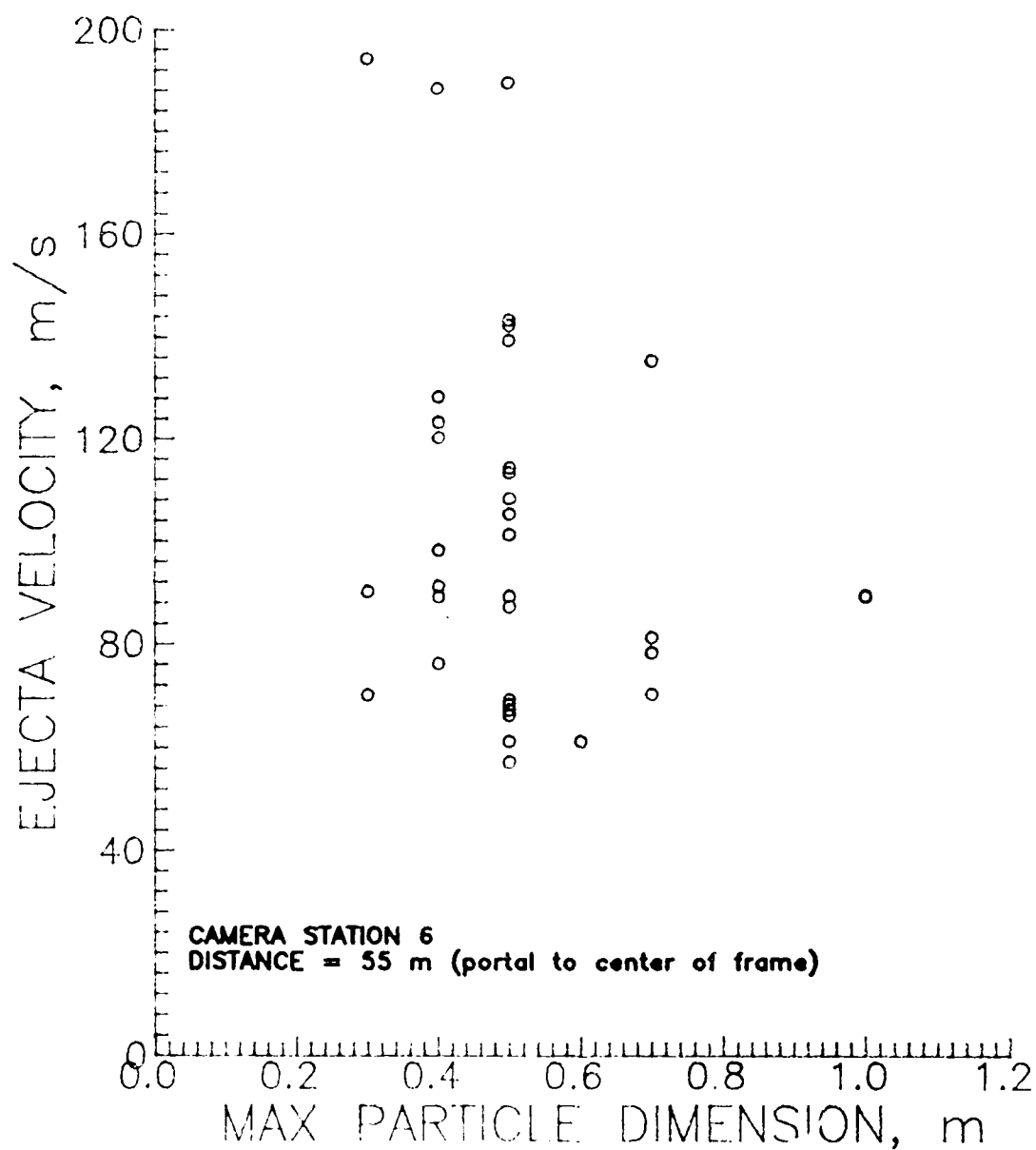


Figure 91. Ejecta missile velocity versus maximum particle dimension, as recorded by Camera Station 6.

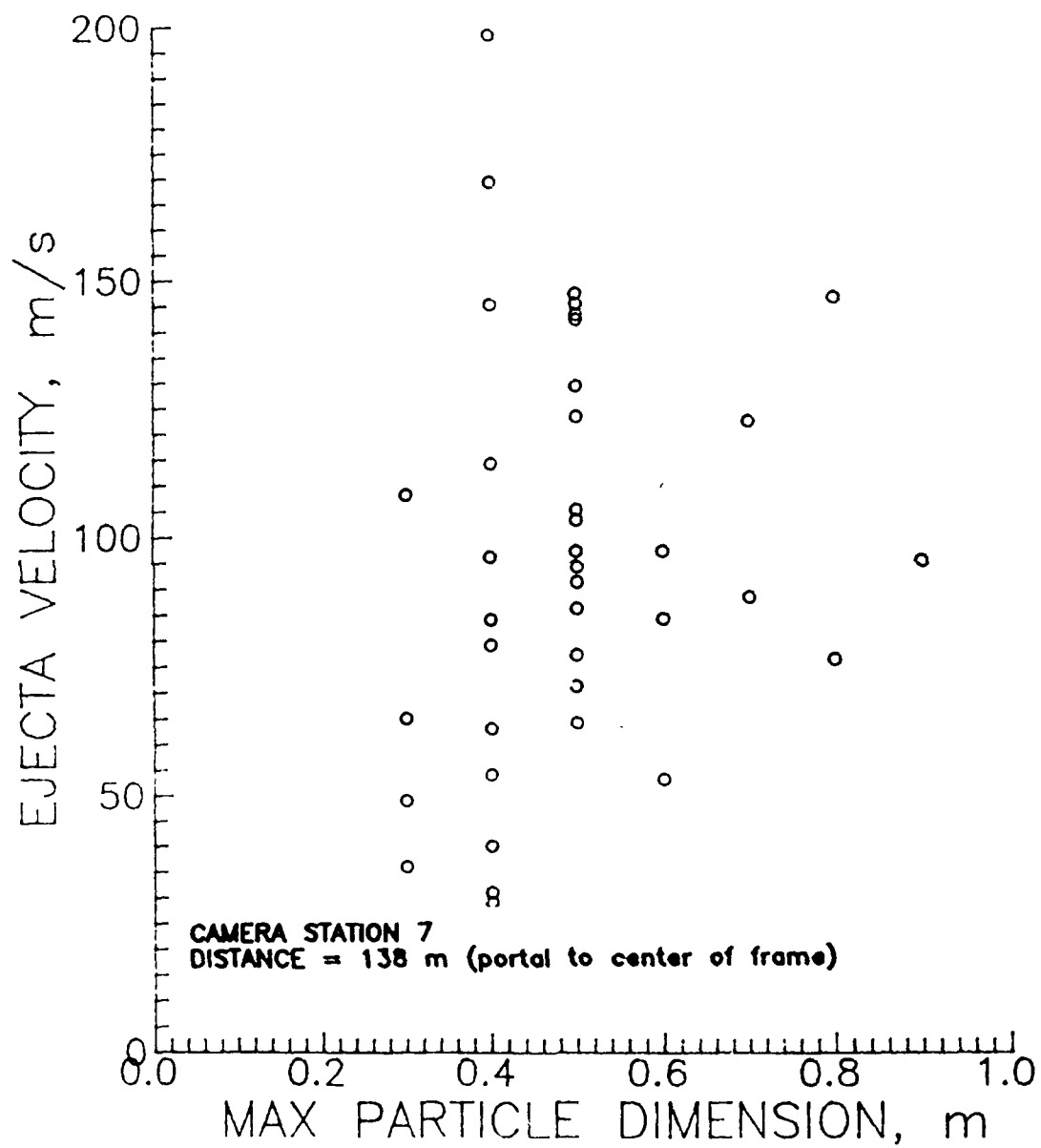


Figure 92. Ejecta missile velocity versus maximum particle dimension, as recorded by Camera Station 7.

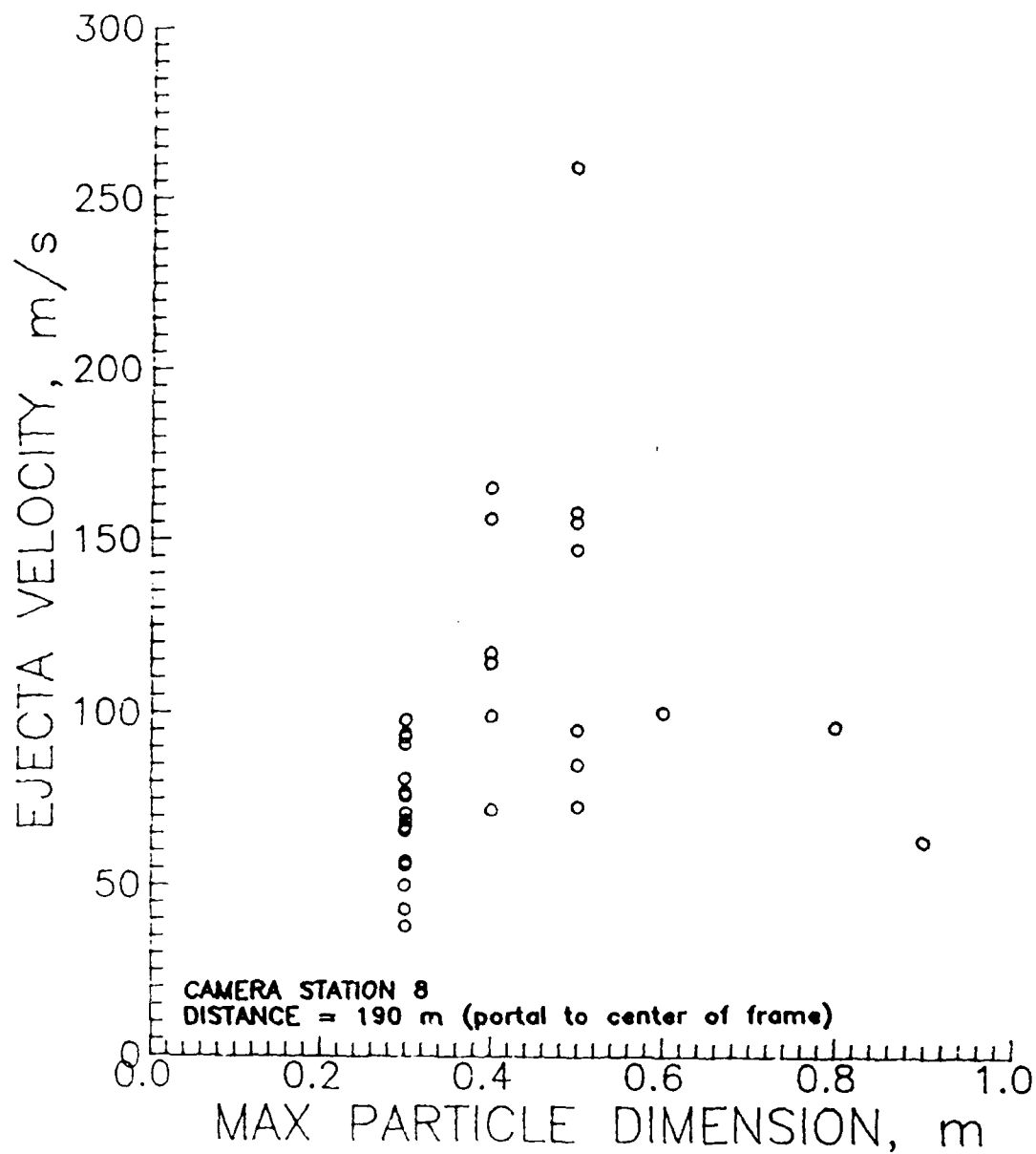


Figure 93. Ejecta missile velocity versus maximum particle dimension, as recorded by Camera Station 8.

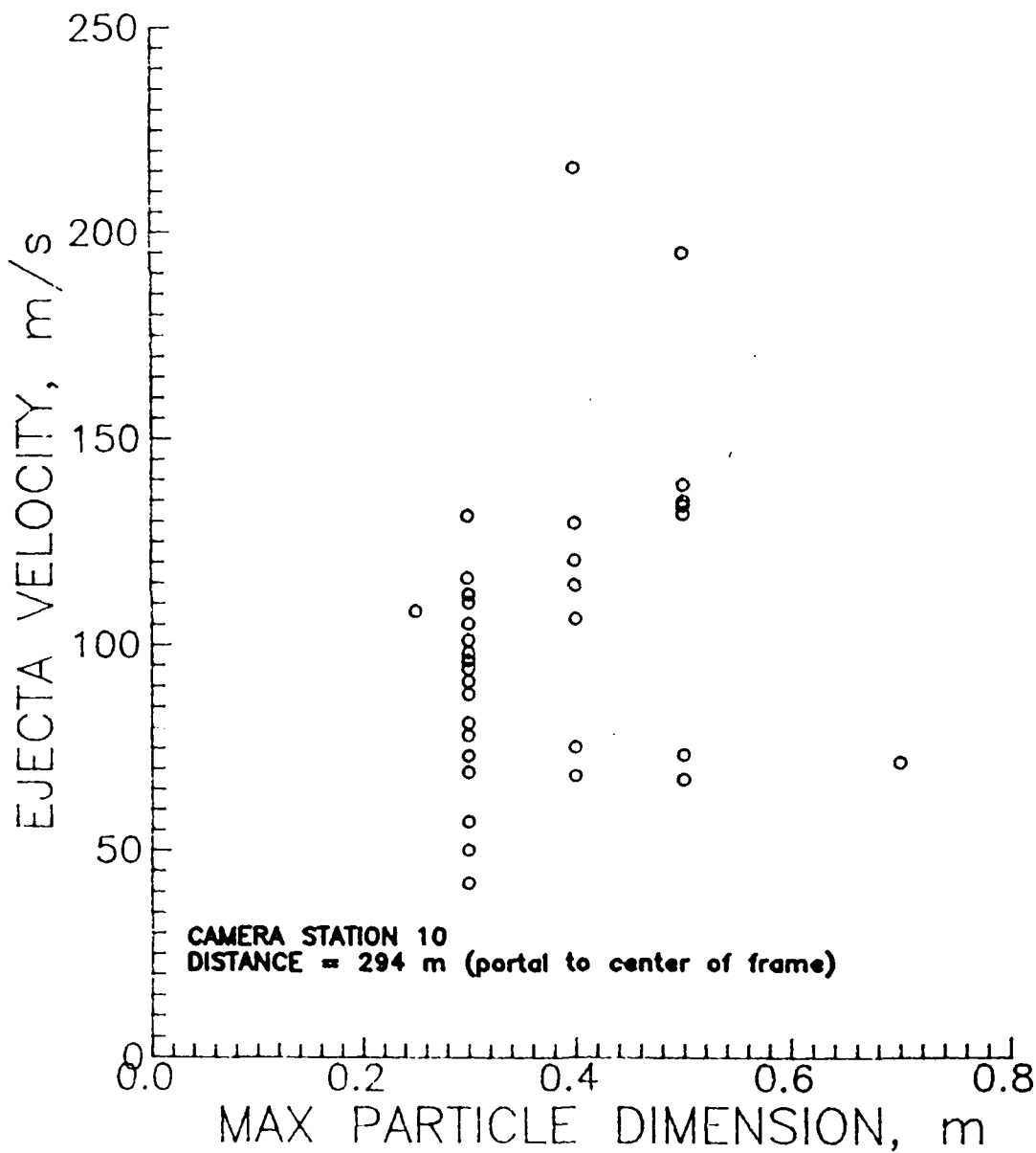


Figure 94. Ejecta missile velocity versus maximum particle dimension, as recorded by Camera Station 10.

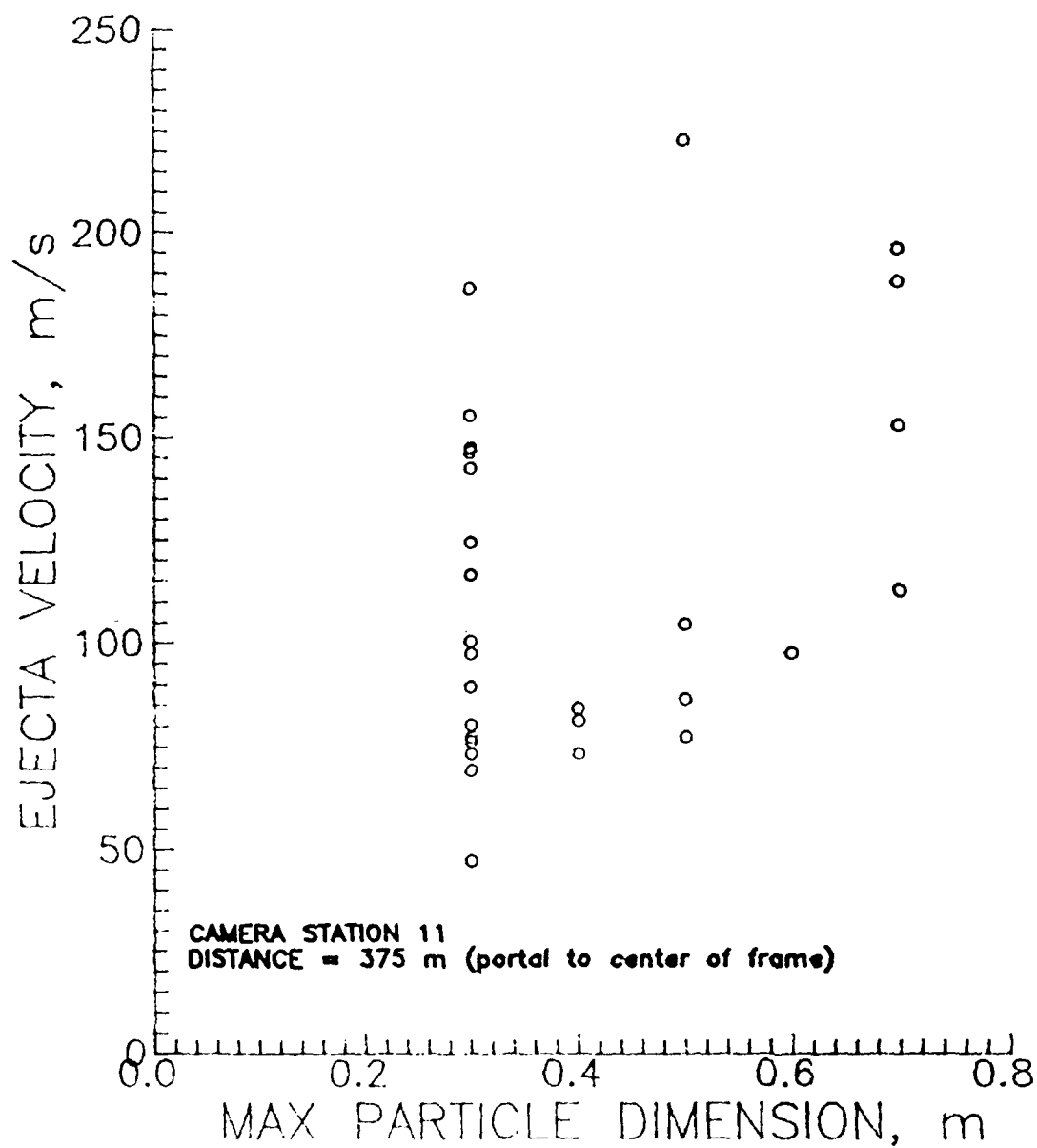


Figure 95. Ejecta missile velocity versus maximum particle dimension, as recorded by Camera Station 11.

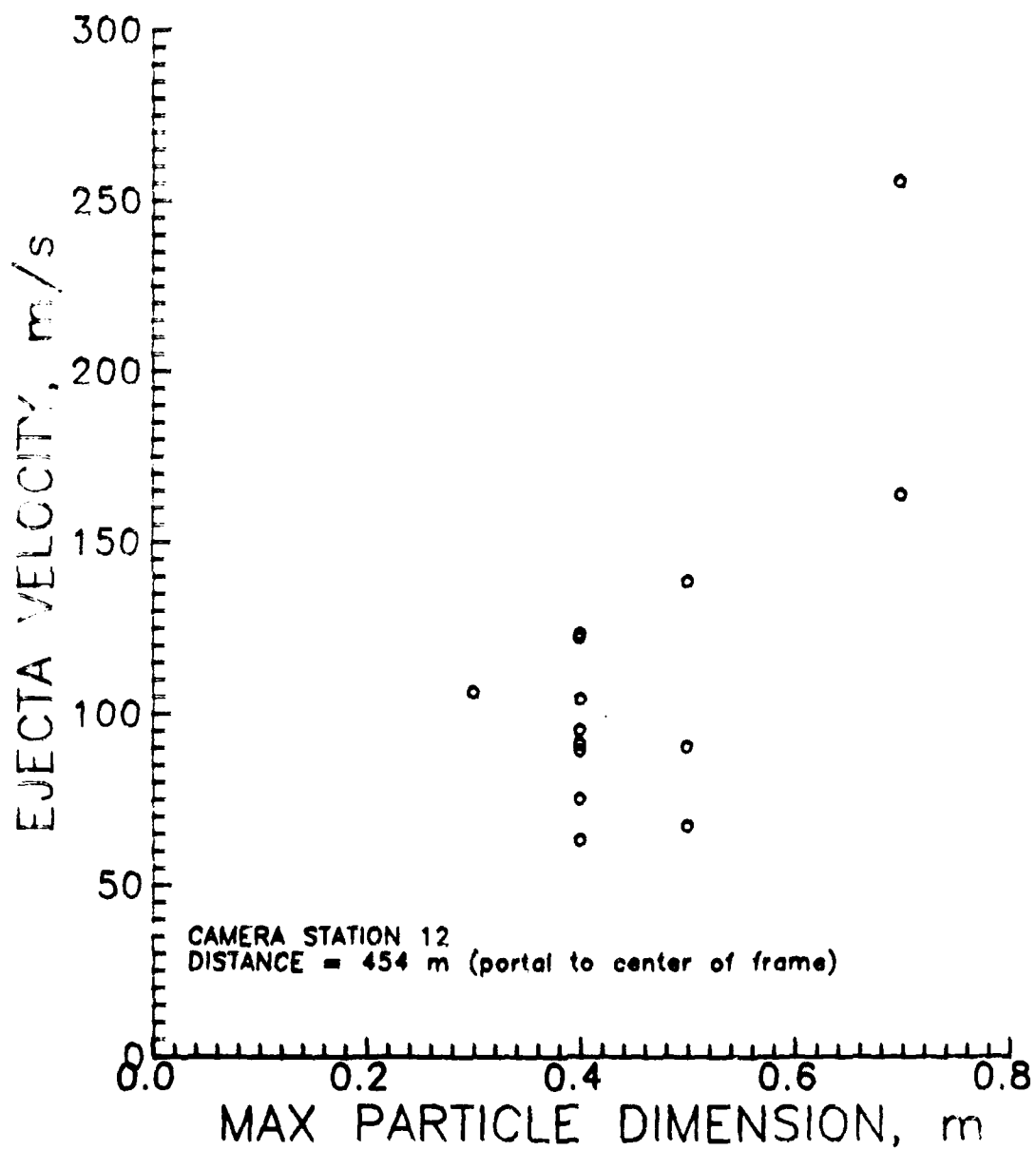


Figure 96. Ejecta missile velocity versus maximum particle dimension, as recorded by Camera Station 12.

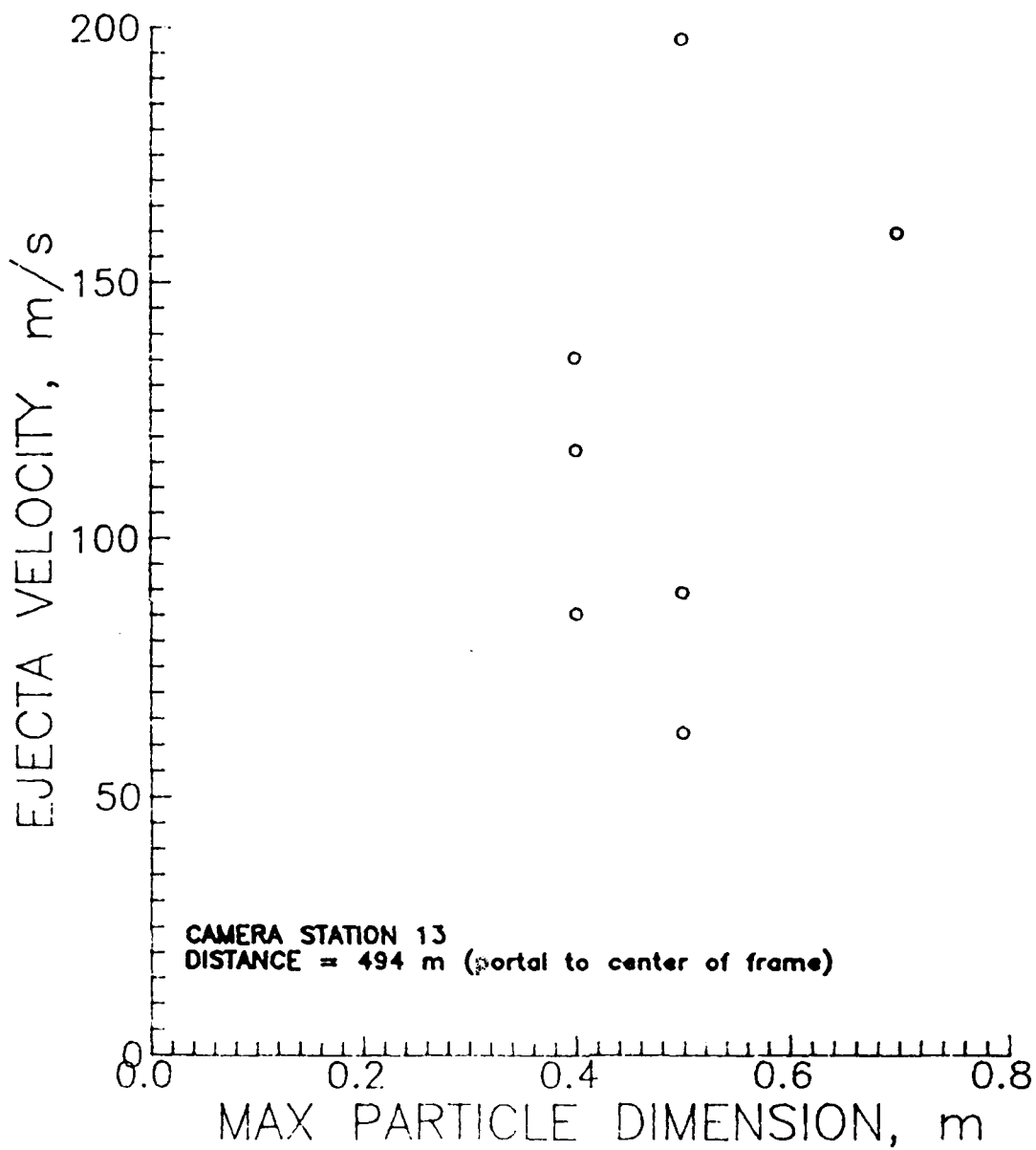


Figure 97. Ejecta missile velocity versus maximum particle dimension, as recorded by Camera Station 13.

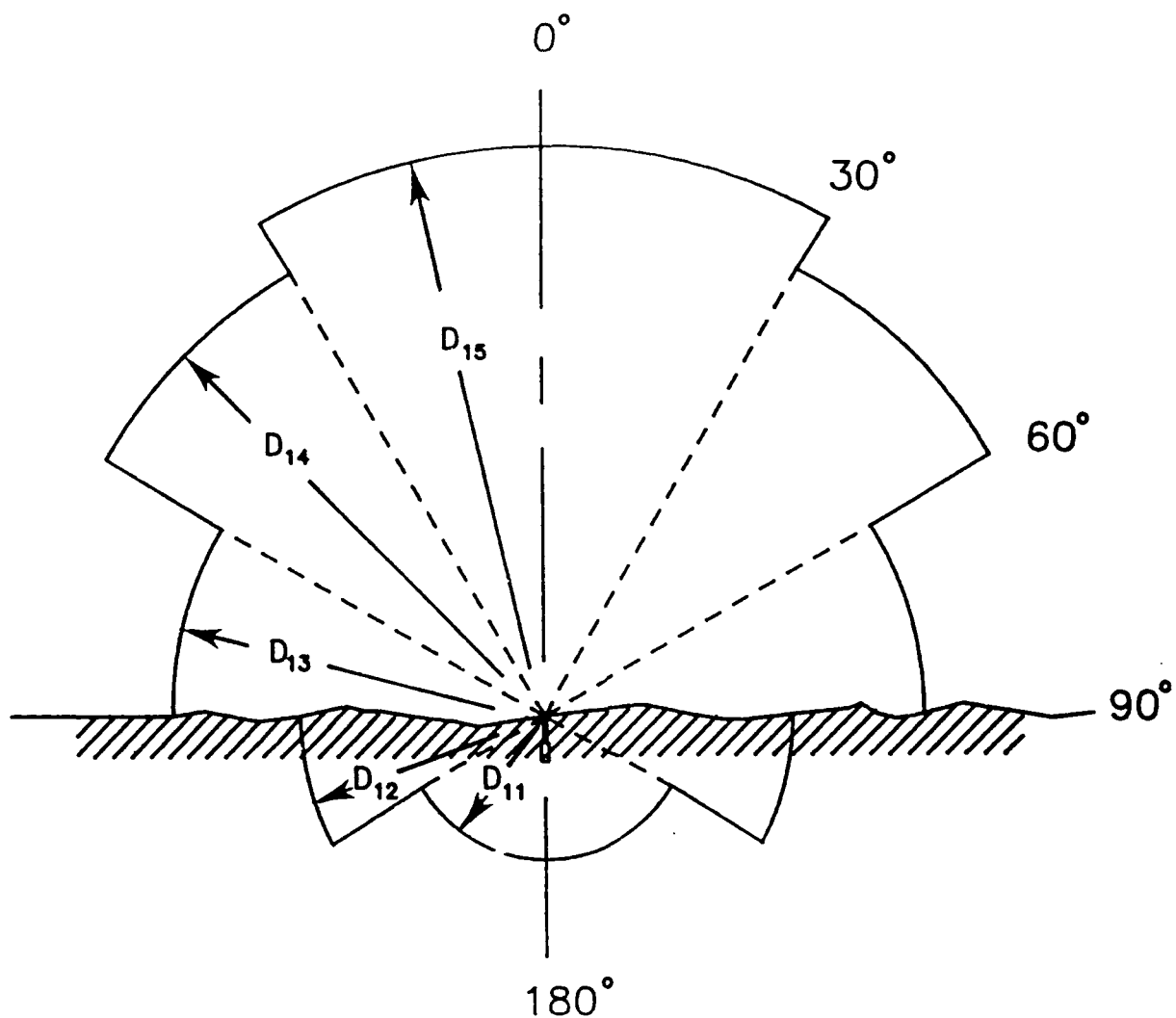


Figure 98. Geometry of Inhabited Building Distances for airblast from explosions in underground magazines; Ammunition and Explosives Safety Standards (DOD 6055.9-STD).

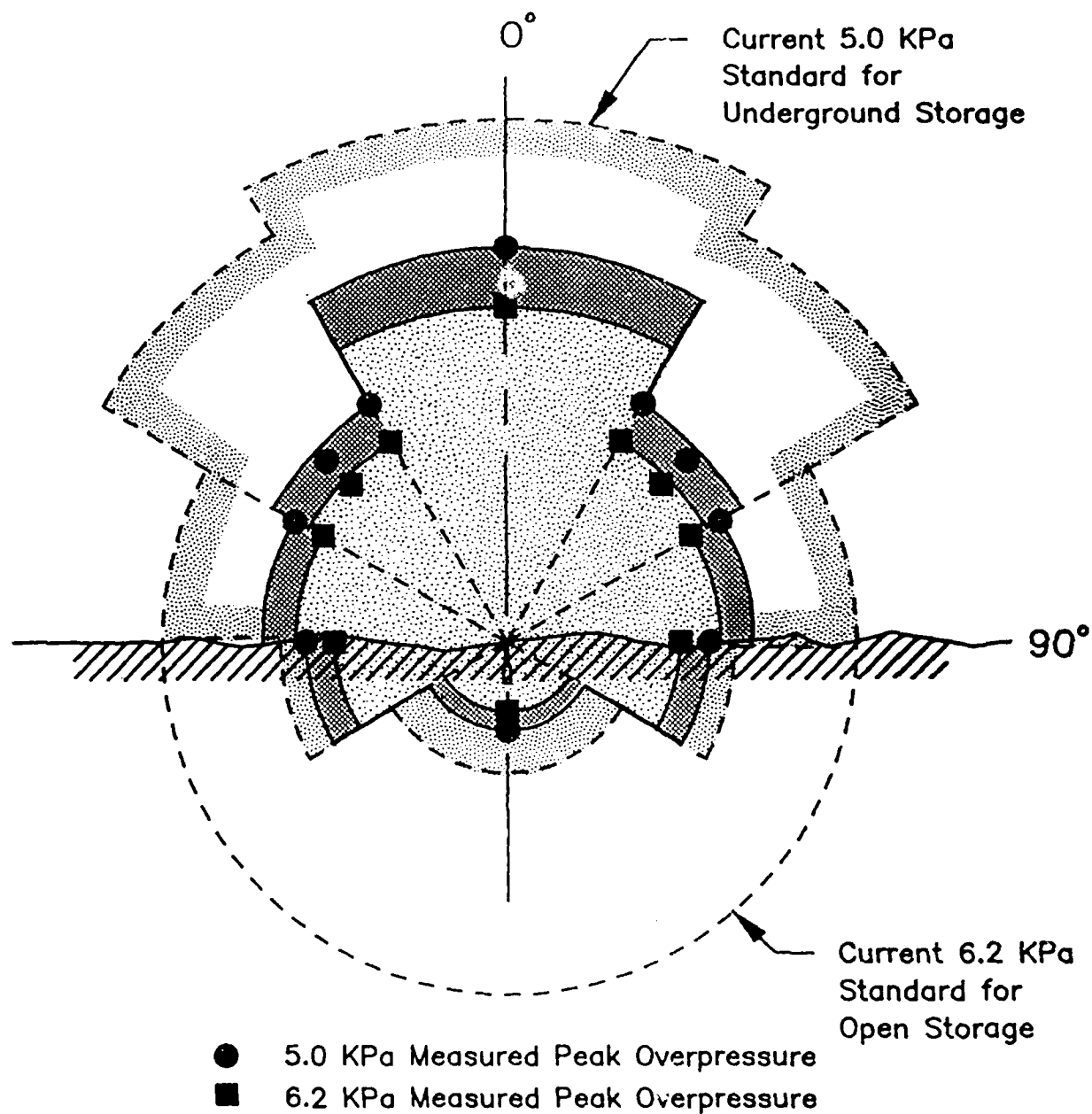


Figure 99. Airblast Inhabited Building Distances specified by Explosive Safety Standards (DOD 6055.9 STD) for open and underground munitions storage, compared to 5.0 and 6.2 kPa distances measured on Shallow Underground Tunnel Chamber Explosion Test (20,000 kg, Composition B, 66.4 kg/m³ (TNT equivalent) loading density).

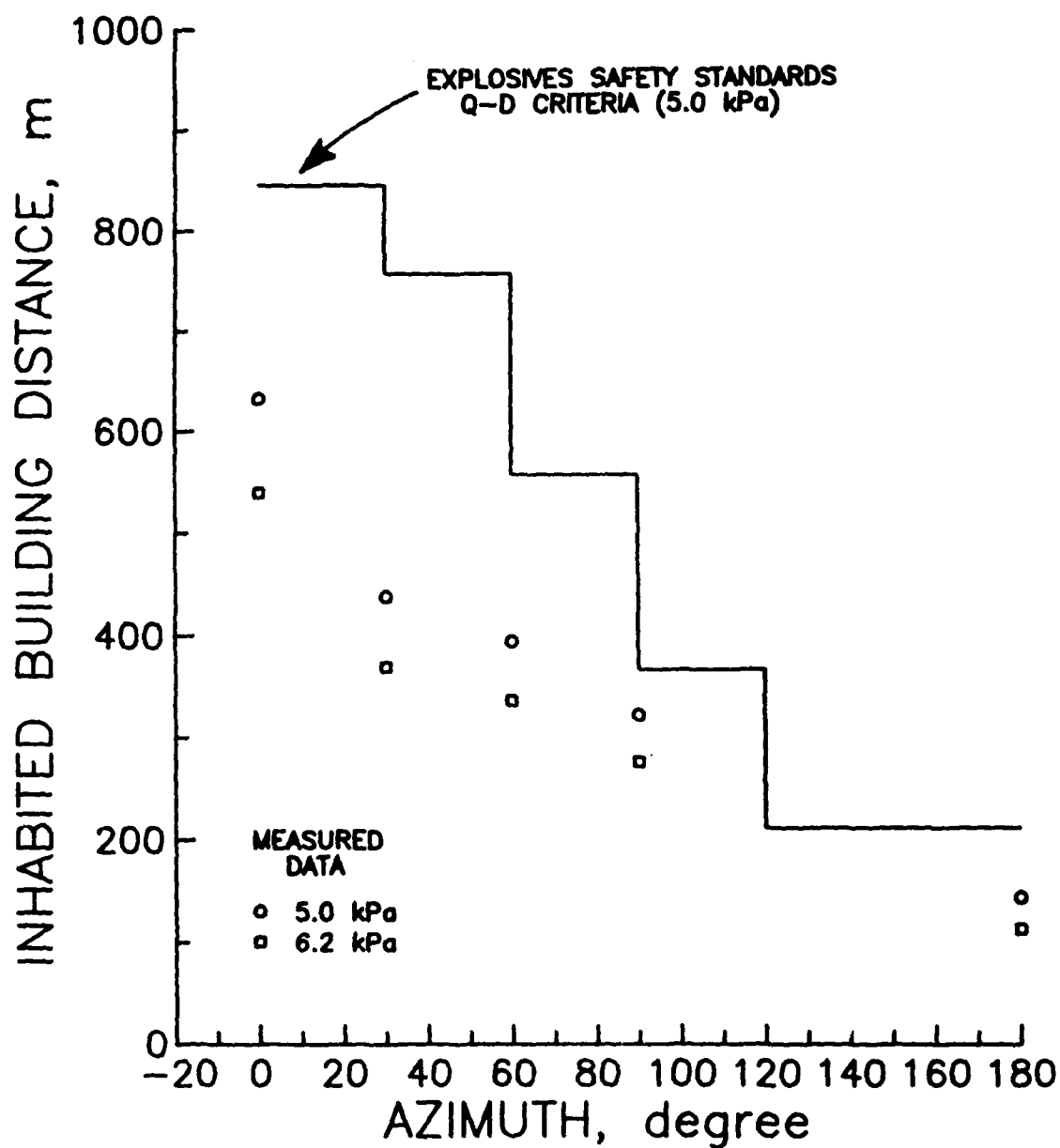


Figure 100. Airblast Inhabited Building Distances specified by Standards (DOD 6055.9-STD) compared to measured distances to 5.0 and 6.2 kPa pressure levels for the Shallow Underground Tunnel/Chamber Explosion Test (20,000 kg, Composition B, 66.4 kg/m³ (TNT equivalent) loading density).

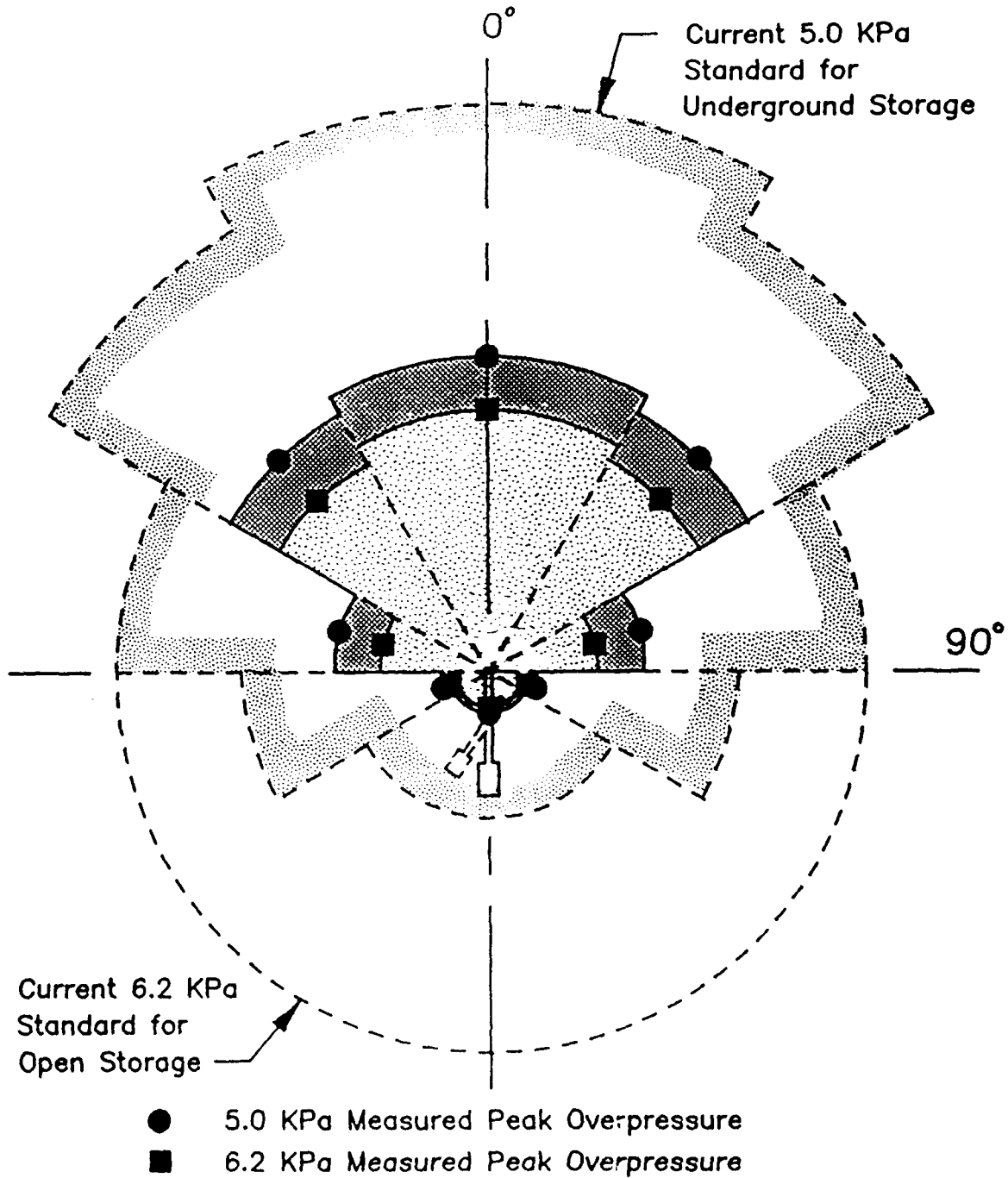


Figure 101. Airblast Inhabited Building Distances specified by Standards (DOD 6055.9-STD) for open and underground munitions storage, compared to 5.0 and 6.2 kPa distances measured in 1987 KLOTZ Club Test 8 at Alvdalen, Sweden (4540 kg ANFO, 12.7 kg/m³ (TNT equivalent) loading density).

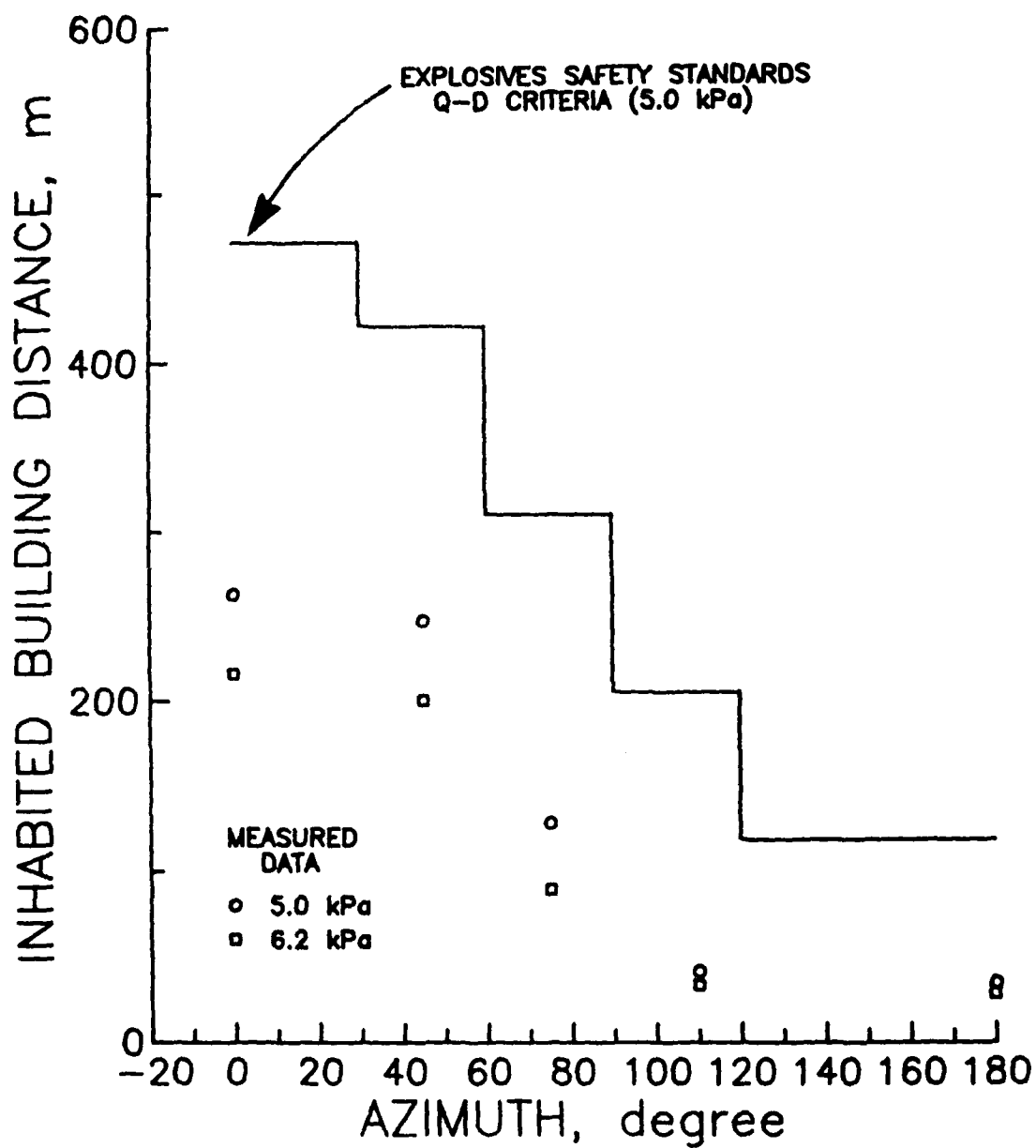


Figure 102. Airblast Inhabited Building Distances specified by Explosives Safety Standards for underground munitions storage, compared to measured distances to 5.0 and 6.2 kPa pressure levels, for 1987 KLOTZ Club Test 8 at Alvdalen, Sweden (4540 kg ANFO, 12.7 kg/m³ (TNT equivalent) loading density).

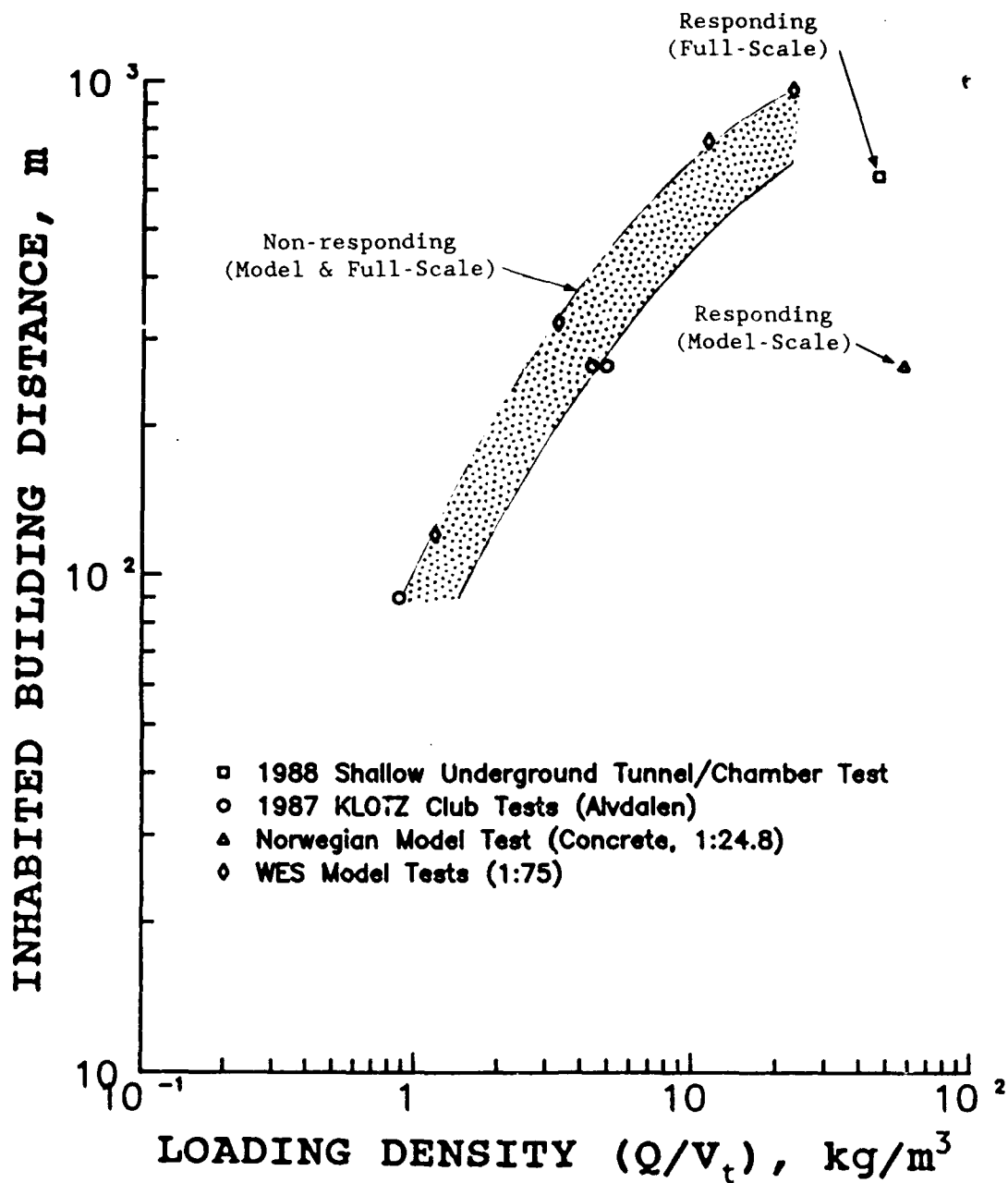


Figure 103. Airblast Inhabited Building Distance along the 0-degree azimuth (extended tunnel axis) as a function of loading density, as indicated by full-scale and model test data. (Note: Loading density is defined as charge weight, Q , divided by total volume, V_t , which is volume of the chamber plus the tunnel portion between the chamber and the portal).

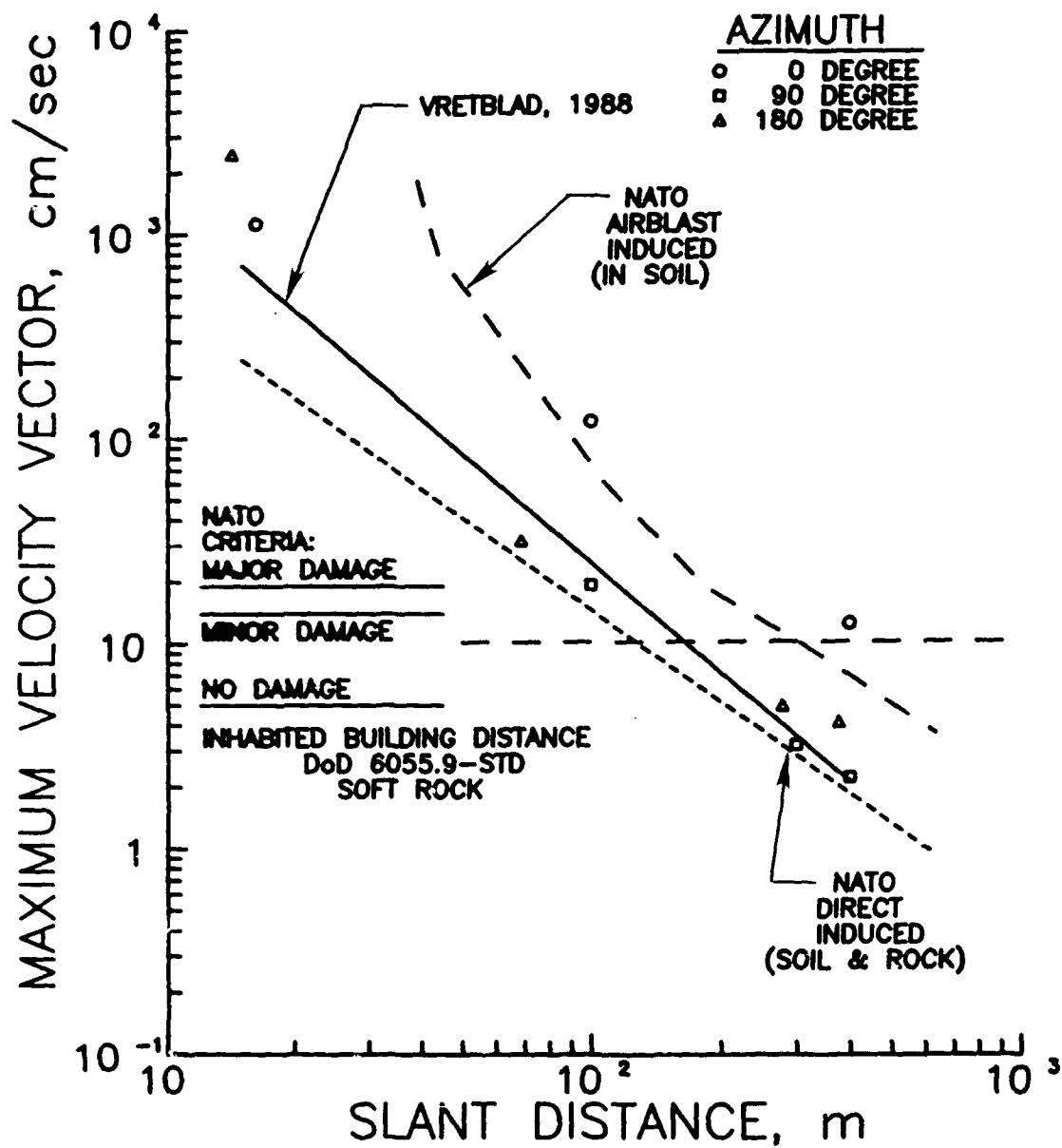


Figure 104. Maximum velocity vector versus slant distance from center of the charge; comparison of prediction curves with data from 0, 90, and 180-degree azimuths on Tunnel/Chamber Test.

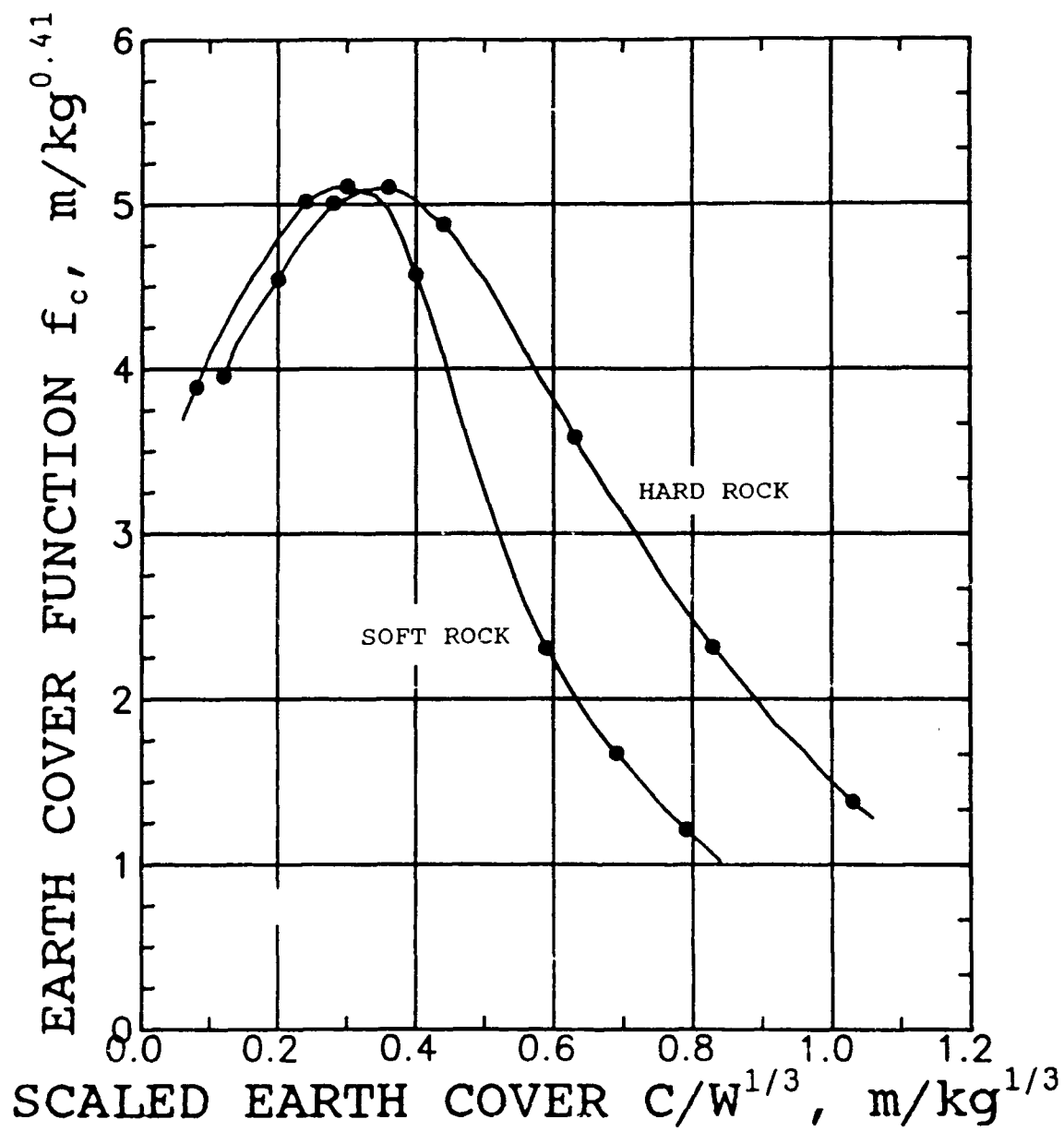


Figure 105. Earth cover function, f_c , for ejecta/debris versus scaled chamber earth cover depth, Ammunition and Explosives Safety Standards (A&ESS).

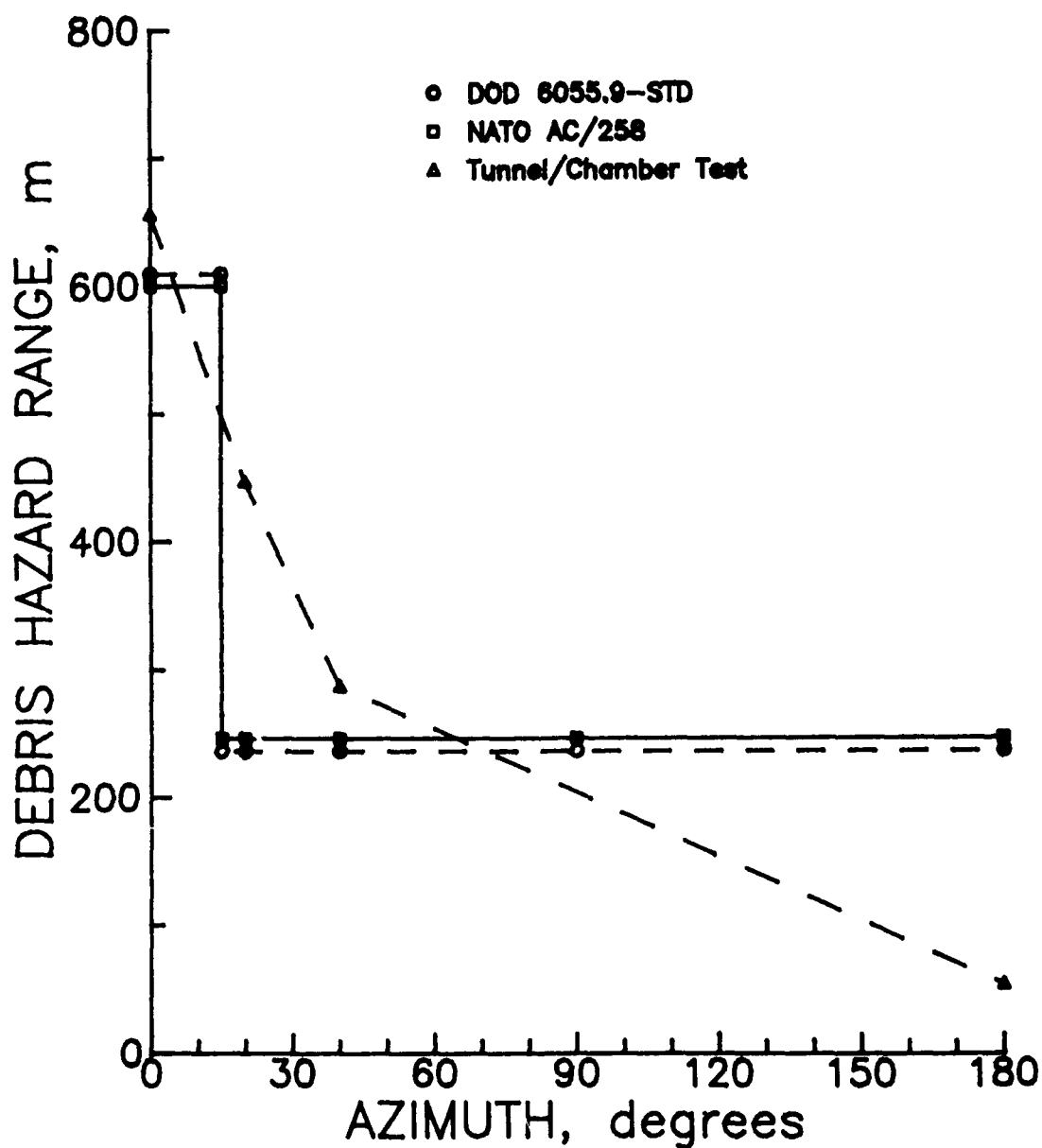


Figure 106. Inhabited Building Distances from debris hazards specified in the Explosives Safety Standards and NATO AC/258 for a 20,000-kg detonation, compared to ranges indicated by data collection on the Shallow Underground Tunnel/Chamber Explosion Test.

Table 1. Calculated Chamber Gas Pressures for a Range of Net Explosive Weights and Candidate Explosive Sources

TNT Explosive Mass (kg)	Chamber Gas Pressure* (MPa)	ANFO Explosive Mass (kg)	COMPOSITION B Explosive Mass (kg)
882	3.53	1,000	666.6
1,000	3.86	1,100	756.8
1,317	4.75	1,370	1,000.0
20,000	60.00	17,680	15,550.0
22,640	68.40	20,000	17,630.0
25,650	78.00	22,640	20,000.0

* Pressures calculated for 360-m³ chamber using the WES BLASTIN code.

Table 2. Locations and Peak Pressure Predictions
for Internal Airblast Measurements*

Station Number	Range (m)	Measurement Type	Predicted Peak Pressure (MPa)	Gage Position
C.1	-41.0	Reflected	152.0	Mid-height on chamber wall
C.2	-40.9	Reflected	152.0	Mid-height on chamber wall
C.3	-29.0	Reflected	152.0	Mid-Height on chamber wall
C.4	-28.9	Reflected	152.0	Mid-height on chamber wall
C.5	-25.3	Side-on	82.5	at chamber entrance
C.6	-23.7	Side-on	79.9	in access tunnel floor
C.7	-22.6	Side-on	78.7	in access tunnel floor
C.8	-13.7	Side-on	69.2	in access tunnel floor
C.9	-12.5	Side-on	68.3	in access tunnel floor
C.10	-4.7	Side-on	61.7	in access tunnel floor
C.11	-3.2	Side-on	60.7	in access tunnel floor
C.12	-2.2	Side-on	60.0	in access tunnel floor
C.13**	-1.7	Side-on	61.0	in access tunnel floor
C.14**	0.3	Side-on	59.6	in access tunnel floor

* All ranges measured from the tunnel portal; minus distances indicate internal gage locations; positive distances indicate external gages.

** Developmental (TID), self-recording gage package.

Table 3. Locations and Predicted Peak Pressures
for Free-Field Airblast Measurements

Station Number	Range (m)	Azimuth* (deg)	Predicted Peak Pressure (kPa)	Station Number	Range (m)	Azimuth (deg)	Predicted Peak Pressure (kPa)
A.1	5	0	15,000	A.17	600	45	14
A.2**	5	0	63,000	A.18	900	45	8
A.3	10	0	5,900	A.19	25	60	800
A.4	25	0	1,700	A.20	75	60	180
A.5	75	0	390	A.21	150	60	70
A.6	150	0	150	A.22	300	60	28
A.7	300	0	60	A.23	600	60	11
A.8	600	0	24	A.24	25	90	480
A.9	900	0	14	A.25	75	90	110
A.10	75	30	300	A.26	150	90	43
A.11	150	30	120	A.27	300	90	17
A.12	300	30	47	A.28	600	90	7
A.13	600	30	18	A.29	50	180	60
A.14	900	30	11	A.30	100	180	23
A.15	150	45	93	A.31	200	180	9
A.16	300	45	37	A.32	400	180	4

* All ranges and angles are referenced to the tunnel centerline at the portal.

** Stagnation pressure measurement.

Table 4. Sound Pressure Level Dosimeter Locations

<u>Station Number</u>	<u>Range* (km)</u>	<u>Measurement Location</u>
S.1	0.80	Test Site Visitor Parking Area
S.2	1.21	Beside access road, west of Test Site
S.3	1.61	Beside access road, west of Test Site
S.4	2.41	Beside access road, west of Test Site
S.5	3.22	Beside access road, west of Test Site
S.6	4.83	Cinder road at NWC site gate
S.7	9.66	Observation Point (Coso Rest Area)

* Range from tunnel portal.

Table 5. Location and Predicted Peak Values for
Surface Ground Motion Measurements

Station Number	Range* (m)	Azimuth (deg)	Predicted Acceleration (g's)	Predicted Velocity (cm/s)	Measurement Orientation
G.1V	9.0	0	1,190.000	---	Vertical
G.1H	9.0	0	1,190.000	---	Horizontal
G.2V	100.0	0	25.600	---	Vertical
G.2H	100.0	0	12.800	---	Horizontal
G.3V	400.0	0	3.000	---	Vertical
G.3H	400.0	0	1.500	---	Horizontal
G.4V	100.0	90	4.900	---	Vertical
G.4H	100.0	90	2.400	---	Horizontal
G.5V	200.0	90	1.800	1.500	Vertical
G.5H	200.0	90	0.880	0.770	Horizontal
G.6V	300.0	90	0.810	0.400	Vertical
G.6H	300.0	90	0.410	0.200	Horizontal
G.7V	400.0	90	0.410	0.140	Vertical
G.7H	400.0	90	0.210	0.068	Horizontal
G.8CV**	0	180	80,000.000	---	Vertical
G.9V	0	180	950.000	---	Vertical
G.9H	0	180	950.000	---	Horizontal
G.10V	66.0	180	1.300	0.880	Vertical
G.10H	66.0	180	0.640	0.440	Horizontal
G.11V	166.0	180	0.320	0.096	Vertical
G.11H	166.0	180	0.160	0.048	Horizontal
G.12V	266.0	180	0.120	0.025	Vertical
G.12H	266.0	180	0.061	0.012	Horizontal
G.13V	366.0	180	0.053	0.004	Vertical
G.13H	366.0	180	0.026	0.002	Horizontal
G.14 ⁺	6.5	0	1,870.000	---	Vertical

* All ranges and azimuths are referenced to the center of the chamber and the chamber/tunnel centerline.

** Gage G.8CV was installed in a drill hole at 2.5 m above the chamber roof. All other gages were shallow buried.

⁺ Developmental (TID), self-recording gage package cast in concrete-filled drum (artificial missile).

Table 6. Wire Drag Gage Locations (Dewey, 1989)

<u>Station Number</u>	<u>Range (m)</u>	<u>Azimuth* (deg)</u>	<u>Station Number</u>	<u>Range (m)</u>	<u>Azimuth (deg)</u>
1	25	60	12	99	0
2	50	60	13	45	345
3	75	60	14	75	345
4	35	30	15	100	345
5	55	30	16	35	330
6	75	30	17	53	330
7	45	15	18	75	330
8	75	15	19	25	300
9	100	15	20	50	300
10	49	0	21	75	300
11	75	0	---	--	---

* Range and azimuth measured from tunnel portal and centerline.

Table 7. Smoke Puff Launcher Locations

<u>Station Number</u>	<u>Range m</u>	<u>Azimuth degree</u>	<u>Station Number</u>	<u>Range m</u>	<u>Azimuth degree</u>
SP.1*	0	0	SP.12	60	0
SP.2	5	0	SP.13	70	0
SP.3	10	0	SP.14	80	0
SP.4	15	0	SP.15	90	0
SP.5	20	0	SP.16	100	0
SP.6	25	0	SP.17	5	180
SP.7	30	0	SP.18	15	180
SP.8	35	0	SP.19	25	180
SP.9	40	0	SP.20	35	180
SP.10	45	0	SP.21	45	180
SP.11	50	0	---	--	---

* Range and azimuth measured from tunnel portal and centerline.

** Smoke puff launcher located above tunnel portal at 45-degree angle to vertical, in direction of 0-degree azimuth.

Table 8. Blast Cube Pre-Test Locations (Ethridge, 1989)

Position on Arc	Cube Number	Cube Type	Arc (m)	Azimuth (deg)	Position on Arc	Cube Number	Cube Type	Arc (m)	Azimuth (deg)
1	010	Steel	5	320.00	22	016	Poplar	75	9.17
2	051	Steel	5	330.00	23	006	Oak	75	9.75
3	079	Steel	5	340.00	24	024	Balsa	75	10.32
4	008	Steel	5	350.00	25	024	Poplar	75	10.94
5	085	Steel	5	10.00	26	048	Aluminum	75	11.23
6	028	Steel	5	20.00	27	022	Oak	75	11.53
7	044	Steel	5	30.00	28	010	Balsa	75	12.14
8	025	Steel	5	40.00	29	015	Poplar	75	12.69
9	020	Steel	5	50.00	30	062	Aluminum	75	12.98
1	009	Steel	10	335.00	31	016	Oak	75	13.27
2	011	Steel	10	340.00	32	007	Balsa	75	15.27
3	003	Steel	10	345.00	33	014	Poplar	75	15.86
4	039	Steel	10	350.00	34	058	Aluminum	75	16.15
5	089	Steel	10	355.00	35	018	Oak	75	16.43
6	066	Steel	10	5.00	36	014	Balsa	75	17.04
7	029	Steel	10	10.00	37	013	Poplar	75	17.63
8	030	Steel	10	15.00	38	063	Aluminum	75	17.93
9	035	Steel	10	20.00	39	008	Oak	75	18.25
10	056	Steel	10	25.00	40	011	Balsa	75	18.88
11	040	Steel	10	30.00	41	025	Poplar	75	19.51
12	081	Steel	10	35.00	42	024	Oak	75	20.11
1	054	Steel	70	359.00	43	020	Balsa	75	20.77
2	080	Steel	75	357.00	44	004	Poplar	75	21.37
0	055	Steel	75	355.70	45	027	Oak	75	21.99
1	029	Balsa	75	356.24	46	002	Balsa	75	22.62
2	012	Poplar	75	356.85	47	030	Poplar	75	23.28
3	070	Aluminum	75	357.14	48	021	Oak	23	23.90
4	002	Oak	75	357.44	49	022	Balsa	75	24.52
5	030	Balsa	75	358.08	50	006	Poplar	75	25.13
6	010	Poplar	75	358.71	51	003	Oak	75	25.78
7	042	Aluminum	75	359.00	52	025	Balsa	75	26.53
8	026	Oak	75	359.29	53	021	Poplar	75	27.16
9	026	Balsa	75	1.81	54	067	Aluminum	75	27.48
10	001	Poplar	75	2.46	55	004	Oak	75	27.79
11	039	Aluminum	75	2.76	56	005	Balsa	75	28.35
12	010	Oak	75	3.07	57	007	Poplar	75	29.00

Table 8. Blast Cube Pre-Test Locations (Ethridge, 1989) (Concluded)

Position on Arc	Cube Number	Cube Type	Arc (m)	Azimuth (deg)	Position on Arc	Cube Number	Cube Type	Arc (m)	Azimuth (deg)
13	019	Balsa	75	3.66	58	043	Aluminum	75	29.32
14	008	Poplar	75	4.26	59	029	Oak	75	29.63
15	046	Aluminum	75	4.57	60	021	Balsa	75	32.17
16	017	Oak	75	4.89	61	002	Poplar	75	32.74
17	015	Balsa	75	5.42	62	069	Aluminum	75	33.05
18	018	Poplar	75	6.05	63	001	Oak	75	33.36
19	005	Oak	75	6.68	64	006	Balsa	75	34.00
20	031	Steel	75	7.25	65	020	Poplar	75	34.59
21	028	Balsa	75	8.67	66	049	Aluminum	75	34.89
67	025	Oak	75	35.19	88	014	Oak	75	47.22
68	003	Balsa	75	35.80	89	023	Balsa	75	47.84
69	011	Poplar	75	36.80	90	019	Poplar	75	48.42
70	011	Oak	75	37.04	91	045	Aluminum	75	48.73
71	008	Balsa	75	37.68	92	023	Oak	75	49.03
72	027	Poplar	75	38.28	93	009	Balsa	75	53.27
73	007	Oak	75	38.89	94	023	Poplar	75	53.88
74	027	Balsa	75	39.52	95	051	Aluminum	75	54.18
75	017	Poplar	75	40.09	96	009	Oak	75	54.48
76	030	Oak	75	40.52	97	001	Balsa	75	55.05
77	013	Balsa	75	41.03	98	003	Poplar	75	55.64
78	029	Poplar	75	41.63	99	041	Aluminum	75	55.96
79	040	Aluminum	75	41.91	100	020	Oak	75	56.28
80	028	Oak	75	42.21	101	018	Balsa	75	58.82
81	012	Balsa	75	42.84	102	005	Poplar	75	59.40
82	026	Poplar	75	43.46	103	044	Aluminum	75	59.72
83	054	Aluminum	75	43.74	104	013	Oak	75	60.03
84	012	Oak	75	44.03	105	017	Balsa	75	60.65
85	016	Balsa	75	45.97	106	029	Poplar	75	61.25
86	006	Poplar	75	46.59	107	047	Aluminum	75	61.56
87	053	Aluminum	75	46.91	108	015	Oak	75	61.85

(Sheet 2 of 2)

Table 9. Ejecta and Debris Collection Pad Locations

Station No.	Radius (m)	Azimuth (deg)	Collection Pad Area (m ²)	Station No.	Range (m)	Azimuth (deg)	Collection Pad Area (m ²)
1	344*	316	16	2	500	5	100
2	301*	320	16	22	500	10	100
3	261*	327	16	23	420	355	16
4	225*	335	16	24	420	350	16
5	195*	346	16	25	420	10	16
6	140	0	16	26	420	5	16
7	167*	17	16	27	420	0	16
8	174*	33	16	28	390	0	16
9	194*	48	16	29	320	0	16
10	224*	59	16	30	320	10	16
11	260*	67	16	31	320	5	16
12	900	0	100	32	320	350	16
13	600	0	100	33	320	355	16
14	600	355	100	34	290	0	16
15	600	350	100	35	240	0	16
16	600	5	100	36	190	0	16
17	600	10	100	37	90	0	16
18	500	0	100	38*	300	45	16
19	500	350	100	39*	300	315	16
20	500	355	100				

* Radius and azimuth referenced to center of chamber (TP 6).

Table 10. Artificial Missile Location Data

ID Number	Type	Horizontal Distance		Nominal	Mass (kg)
		From Portal (m)	From Centerline (m)	Dimensions (cm)	
014	Steel	25	15 (right side)	15 (cube)	--
034	Steel	43	15 (right side)	15 (cube)	--
049	Steel	34	15 (right side)	15 (cube)	--
075	Steel	43	15 (left side)	15 (cube)	--
076	Steel	25	15 (left side)	15 (cube)	--
098	Steel	34	15 (left side)	15 (cube)	--
1	Rock	25	15 (left side)	10 x 12 x 15	4.1
2	Rock	43	15 (right side)	10 x 11 x 15	3.6
3	Rock	43	15 (left side)	9 x 10 x 13.5	4.2
4	Rock	25	15 (right side)	11 x 12 x 16	5.6
5	Rock	34	15 (left side)	12 x 12 x 20	11.6
6	Rock	34	15 (right side)	15 x 18 x 22	17.0
6"-1	Aluminum	2.8	0	15 (cylinder)	--
6"-2	Aluminum	7.8	0	15 (cylinder)	--
6"-3	Aluminum	12.8	0	15 (cylinder)	--
6"-4	Aluminum	17.8	0	15 (cylinder)	--
6"-5	Aluminum	22.8	0	15 (cylinder)	--
6"-6	Aluminum	27.8	0	15 (cylinder)	--
6"-7	Aluminum	32.8	0	15 (cylinder)	--
6"-8	Aluminum	37.8	0	15 (cylinder)	--
6"-9	Aluminum	42.8	0	15 (cylinder)	--
6"-10	Aluminum	47.8	0	15 (cylinder)	--
6"-11	Aluminum	52.8	0	15 (cylinder)	--
4"-1	Aluminum	34.9	15 (right side)	10 (cylinder)	--
4"-2	Aluminum	34.9	10 (right side)	10 (cylinder)	--
4"-3	Aluminum	34.9	5 (right side)	10 (cylinder)	--
4"-4	Aluminum	34.9	5 (right side)	10 (cylinder)	--
4"-5	Aluminum	34.9	10 (left side)	10 (cylinder)	--
4"-6	Aluminum	34.9	15 (left side)	10 (cylinder)	--

Table 11. Shallow Underground Tunnel/Chamber Explosion Test
Tunnel/Chamber Internal Airblast Measurements

Station No.	Centerline* Distance (m)	Arrival Time (msec)	Peak Positive Pressure		
			First Peak (MPa)	Second Peak (MPa)	Third Peak (MPa)
C.1	-41.0	7.9	Gage Failed on Shock Arrival		
C.2	-40.9	7.9	Gage Failed on Shock Arrival		
C.3	-29.0	2.1	13.0	44.0	73.0
C.4	-28.9	2.05	11.0	43.0	71.0
C.5	-25.3	3.1	8.6	45.0	--
C.6	-23.7	3.7	2.2	30.0	--
C.7	-22.6	4.8	17.0	25.0	2.7
C.8	-13.7	8.1	7.0	7.6	10.2
C.9	-12.5	8.5	10.0	10.5	10.0
C.10	-4.7	12.0	4.0	7.0	6.5
C.11	-3.2	12.4	1.3	1.9	1.7
C.12	-2.2	12.8	4.5	5.0	4.0
C.13†	-1.7	8.5	9.7	11.0	--
C.14†	0.3	8.5	5.3	--	--

* All distances measured from the tunnel portal minus distances indicate internal gage locations; positive distances indicate external gages.

† Developmental self recording gage package.

Table 12. Shallow Underground Tunnel/Chamber Explosion Test:
External Airblast Measurements

Station No.	Horizontal* Range (m)	Azimuth (deg)	Arrival Time (msec)	Peak Positive	
				Pressure (kPa)	Impulse (KPa-S)
A.1	5	0	15.8	3650.0	34.3
A.2**	5	0	16.3	27000.0	104.0
A.3	10	0	22.0	1600.0	4.5
A.4	25	0	31.5	710.0	--
A.5	75	0	115.0	100.0	1.9
A.6	150	0	286.0	32.0	0.9
A.7	300	0	680.0	14.0	0.45
A.8	600	0	1520.0	5.7	0.21
A.9	900	0	Gage Failed Preshot		
A.10	75	30	120.0	85.0	1.5
A.11	150	30	30.0	25.0	0.72
A.12	300	30	702.0	9.0	0.35
A.13	600	30	Gage Failed Preshot		
A.14	900	30	2360.0	3.4	0.11
A.15	150	45	315.0	17.5	0.48
A.16	300	45	725.0	10.0	0.35
A.17	600	45	Gage Failed Preshot		
A.18	900	45	Gage Failed Preshot		
A.19	25	60	42.8	225.0	1.7
A.20	75	60	135.0	45.5	0.96
A.21	150	60	330.0	17.0	0.48
A.22	300	60	720.0	8.5	0.29
A.23	600	60	Gage Failed Preshot		
A.24	25	90	54.1	78.0	0.90
A.25	75	90	170.0	30.0	0.60
A.26	150	90	Gage Failed Preshot		
A.27	300	90	775.0	6.0	0.19
A.28	600	90	1625.0	2.0	0.09
A.29	50	180	165.0	13.0	0.47
A.30	100	180	295.0	7.0	0.18
A.31	200	180	605.0	3.7	0.21
A.32	400	180	1150.0	0.7	0.072

* All gage ranges are measured from the tunnel portal.

** Stagnation pressure.

Table 13. Shallow Underground Tunnel/Chamber Explosion Test:
Ground Motion Measurements

Station No.	Horizontal Range* (m)	Azimuth (deg)	Arrival Time (msec)	Measured Peak		
				Acceleration (g's)	Particle Velocity (cm/sec)	Displacement (cm)
G.1V	9.0	0	9.52	300.0	510.0	9.4
G.1H	9.0	0	9.52	80.0	1000.0	--
G.2V	100.0	0	40.1	22.5	116.0	--
G.2H	100.0	0	40.1	40.0	29.6	1.72
G.3V	400.0	0	190.0	--	12.0	0.03
G.3H	400.0	0	190.0	--	3.0	0.091
G.4V	100.0	90	77.4	2.23	10.9	0.33
G.4H	100.0	90	77.4	1.17	15.7	0.83
G.5V	200.0	90		No Data; Very Noisy Gage		
G.5H	200.0	90	100.0	0.59	2.7	0.077
G.6V	300.0	90	130.0	--	1.67	0.038
G.6H	300.0	90	130.0	--	1.48	0.048
G.7V	400.0	90	190.0	--	1.56	0.045
G.7H	400.0	90	190.0	--	1.57	0.057
G.8CV	0.0	180		Gage Failed Preshot		
G.9V	0.0	180	10.5	825.0	1940.0	--
G.9H	0.0	180	10.5	949.0	1500.0	--
G.10V	66.0	180	36.2	3.77	14.5	--
G.10H	66.0	180	36.2	1.0	27.9	--
G.11V	166.0	180		No Data; Very Noisy Gage		
G.11H	166.0	180		No Data; Very Noisy Gage		
G.12V	266.0	180	172.0	--	2.86	0.16
G.12H	266.0	180	172.0	--	4.0	0.20
G.13V	366.0	180	206.0	--	2.35	0.039
G.13H	366.0	180	206.0	--	3.37	0.20
G.14V**	6.5	0		No Data; Gage Failure		

* NOTE: All distances for motion gages were measured from center of the chamber.

** TID instrument package, cast into concrete in bucket (artificial missile).

Table 14. Shallow Underground Tunnel/Chamber Explosion Tests:
Sound Pressure Level Measurements

Station No.	Range (km)	<u>Peak Pressure</u>		Measurement Location
		(dB)	(Pa)	
S.1	0.80	143.0*	276.5	Visitor Parking Area (Flag Poles)
S.2	1.21	151.0*	689.5	Beside Access Road, West of Site
S.3	1.61	155.5	1552.0	Beside Access Road, West of Site
S.4	2.41	144.0	310.0	Beside Access Road, West of Site
S.5	3.22	135.5	117.4	Beside Access Road, West of Site
S.6	4.83	121.5	23.7	Cinder Road at Site Gate
S.7	9.66	124.0	31.6	Observation Point (Coso Rest Area)

* Reading presumed invalid due to low battery in recorder package at shot time.

Table 15. Shallow Underground Tunnel/Chamber Explosion
Test: Dynamic Pressure Measurements

Sta. No.	Horizontal Range (m)	Azimuth (deg)	<u>Peak Positive</u>		Over- density (g/mm ³)	Type of Pressure Measurement
			<u>Pressure</u> (kPa)	<u>Impulse</u> (kPa-sec)		
1	75	7.5	93.0	2.000	0	Side-on
2	75	15.0	92.0	1.920	0	Side-on
3	75	15.0	113.0	2.150	0	Stagnation
4	75	15.0	28.8	0.536	0	Dynamic
5	75	15.0	0	0	0.71	Overdensity
6	75	30.0	88.0	1.520	0	Side-on
7	75	30.0	113.0	1.920	0	Stagnation
8	75	30.0	28.0	0.406	0	Dynamic
9	75	30.0	0	0	0.71	Overdensity
10	100	30.0	54.0	1.200	0	Side-on
11	75	60.0	51.2	0.997	0	Side-on
12	75	60.0	54.6	1.100	0	Stagnation
13	75	60.0	6.9	0.107	0	Dynamic
14	75	60.0	0	0	0.41	Overdensity

Table 16. Blast Cubes: Post-Test Measurements and Calculated Data for 75-m Arc (Ethridge, 1989)

Pos. on Arc	No.	Cube Type*	Mass	Azimuth (degree)	Deviation Angle (degree)	Total Displacement (e)	Initial Velocity (m/s)	Dynamic Impulse (kPa-s)	Remarks
0	055	S	27.700	355.70	----	1.60*	----	----	----
1	029	B	0.647	356.24	-9.65	96.98	35.40	0.822	Damaged, Reusable
2	012	P	1.956	356.85	4.76	88.57	32.00	2.250	Few Small Dents
3	070	O	0.352	347.14	6.05	13.74	11.50	1.310	Spattered, Small Dent
4	002	O	2.631	357.44	10.99	56.41	24.80	2.340	Split - Discarded
5	030	B	0.645	358.08	-7.02	120.35	39.70	0.919	Split, Scorched, Dented
6	010	P	1.950	358.71	4.33	76.40	29.70	2.080	Corner Chipped, Edge Dented, Small Impacts
7	042	A	0.348	359.00	1.80	20.47	13.90	1.560	Dented, Paint Badly Spattered
8	026	O	2.617	259.29	1.66	53.37	24.10	2.270	Multiple Dents
9	006	B	0.634	1.81	-0.22	136.88	42.50	0.970	Scorched, Sooted
10	001	P	1.924	2.46	-2.84	80.77	30.50	2.110	Small Dents
11	039	A	0.350	2.76	-3.98	16.26	12.50	1.410	Dent, Spattered
12	010	O	2.615	3.07	-9.77	63.70	26.40	2.480	Top Split Off, Dents, Small Impacts
13	019	B	0.636	3.66	12.28	96.14	35.20	0.800	Scorched, Sooted, Chipped
14	008	P	1.924	4.26	1.56	75.34	29.50	2.030	Small Dents
15	046	A	0.350	4.57	-11.86	33.58	17.70	2.000	12 mm Dent in Corner, Impacts
16	017	O	2.612	4.89	0.44	81.48	30.00	2.810	Small Dents on Two Edges, Small Impacts
17	015	B	0.650	5.42	40.53	69.67	29.60	0.689	Evidence of Sooting
18	018	P	1.797	6.05	2.69	106.78	35.30	2.260	Edge Chipped, Several Dents
19	005	O	2.376	6.68	-4.21	96.90	32.90	2.810	Dented on Edge, Other Small Dents
20	031	S	27.700	7.25	----	0.48	----	----	----
21	028	B	0.691	8.67	15.17	79.81	31.80	0.790	Okay
22	016	P	1.998	9.17	4.89	57.58	25.60	1.840	Few Small Impacts
23	006	O	2.488	9.75	2.59	55.27	24.50	2.190	Small Impacts
24	024	B	0.634	10.32	12.79	71.09	29.90	0.680	Damaged, May be Reusable
25	024	P	1.927	10.94	-3.33	66.14	27.50	1.900	Few Small Impacts
26	048	A	0.351	11.23	-1.31	7.59	8.60	0.975	Paint Spattered
27	022	O	2.592	11.53	5.30	43.71	21.70	2.020	Small Impacts
28	010	B	0.615	12.14	-4.53	75.34	30.90	0.682	Corner Chippec
29	015	P	1.920	12.69	2.52	33.48	19.30	1.330	Dented, Reusable

* Cube materials: S - steel, A - aluminum, P - poplar, O - oak, B - balsa wood

* Estimated value

Table 16. (Continued)

Pos. on Arc	No.	Cube		Azimuth (degree)	Deviation Angle (degree)	Total Displace- ment (e)	Initial Velocity (m/s)	Dynamic Impulse (kPa-s)	Remarks
		Type*	Mass						
30	052	A	0.350	12.98	11.30	3.99	6.29	0.711	Paint spattered and Missing
31	016	O	2.586	13.27	-3.97	33.07	18.70	1.74	Small Impacts
32	007	B	0.611	15.27	25.27	67.06	29.00	0.635	Damaged, Reusable
33	014	P	1.912	15.86	-----	11.23	11.00	0.754	Small Impacts
34	058	A	0.351	16.15	7.29	4.24	6.48	0.733	Paint Spattered, Missing
35	018	O	2.579	16.43	-5.31	7.77	8.74	0.808	Dent, Small Impacts
36	014	B	0.608	17.04	14.25	42.98	22.90	0.499	Small Dents, Impacts
37	013	P	1.893	17.63	0.74	6.76	8.44	0.574	Small Impacts
38	063	A	0.354	17.93	-6.43	1.30	3.65	0.417	Paint Spattered
39	008	O	2.571	18.25	3.77	4.34	6.43	0.592	Small Impacts
40	011	B	0.653	18.88	15.07	41.94	22.50	0.528	Edge Dented, Multiple Small Dents, Impacts
41	025	P	1.789	19.51	-5.25	8.94	8.94	9.76	Small Impacts
42	024	O	2.764	20.11	34.26	11.51	10.74	1.066	Small Impacts
43	020	B	0.622	20.77	15.27	21.56	15.80	0.577	Small Dents
44	004	P	2.012	21.37	-7.28	6.60	8.34	0.602	Small Impacts
45	027	O	2.448	21.99	-2.92	4.48	6.84	0.600	Small Impacts
46	002	B	0.651	22.62	10.81	29.46	18.60	0.434	Small Dents, Impacts
47	030	P	2.017	23.28	3.74	25.87	17.30	1.25	Edge Dent, Small Impact
48	021	O	2.268	23.90	-5.79	5.82	7.51	0.610	Small Impacts
49	022	B	0.500	24.52	15.90	23.70	16.60	0.298	Split - Several Pieces
50	006	P	1.962	25.13	0.46	4.27	6.66	0.469	Damaged, Several Large Dents
51	003	O	2.724	25.78	7.78	2.79	5.10	0.499	Small Impacts
52	025	B	0.603	26.53	13.06	29.41	18.60	0.402	Dents, Small Impacts
53	021	P	1.888	27.16	3.65	5.41	7.52	0.510	Small Dents, Impacts
54	067	A	0.311	-----	-----	Missing	-----	-----	-----
55	004	O	2.565	27.79	-0.68	3.63	5.86	0.539	Split, Small Impacts
56	005	B	0.597	28.35	12.64	27.43	17.90	0.384	Several Dents, Small Impacts
57	007	P	1.880	29.00	-20.79	9.68	10.17	0.686	Dented on One Side

* Cube materials: S - steel, A - aluminum, P - poplar, O - oak, B - balsa wood

Table 16. (Continued)

Pos. on Arc	No.	Cube		Azimuth (degree)	Deviation Angle (degree)	Total Displace- ment (e)	Initial Velocity (m/s)	Dynamic Impulse (kPa-s)	Remarks
		Type†	Mass						
58	043	A	0.354	29.32	-19.61	1.93	4.42	0.504	Dent at Edge, Impact
59	029	O	2.564	29.63	-4.03	2.87	5.18	0.477	Small Dents, Impacts
60	021	B	0.596	32.17	3.45	17.65	14.15	0.303	Split, Dented
61	002	P	1.885	32.74	-0.93	4.17	6.57	0.445	Several Dents, Small Impacts
62	069	A	0.352	33.05	-13.04	1.22	3.54	0.402	Small Dents, Paint Spattered
63	001	O	2.560	33.36	-6.63	3.00	5.30	0.488	Small Dents, Impacts
64	006	B	0.594	34.00	9.23	22.89	16.30	0.348	Multiple Dents
65	020	P	1.883	34.59	-0.09	5.31	7.45	0.503	Small Impacts
66	049	A	0.351	34.89	-29.96	1.30	3.65	0.413	Glancing Dent
67	025	O	2.559	35.19	-10.46	6.10	7.69	0.707	Corner Chipped off by Strike
68	003	B	0.648	35.80	-10.70	25.60	17.30	0.402	Large Dent at Corner, Other Dents, Impacts
69	011	P	1.790	36.40	-18.47	4.78	7.06	0.453	Small Dents
70	011	O	2.748	37.04	-16.64	2.62	4.93	0.484	Dented, Reusable
71	008	B	0.658	37.68	-3.91	18.15	14.40	0.340	Dents, One Large; Small Impacts
72	027	P	1.993	38.28	-25.67	7.58	8.96	0.641	Dented, Reusable
73	007	O	2.416	38.89	-25.50	4.67	6.69	0.582	Dented, Small Impacts
74	027	B	0.535	39.52	13.97	16.43	13.60	0.261	Several Large Dents
75	017	P	1.809	40.09	-2.83	4.70	7.00	0.454	Split, Dented, Not Reusable
76	030	O	2.742	40.52	-5.46	2.49	4.80	0.474	Edge Chipped Off, Small Impacts
77	013	B	0.591	41.03	17.54	15.80	13.30	0.282	Dents, Small Impacts
78	028	P	1.876	41.63	-3.63	6.32	8.16	0.549	Split
79	040	A	0.349	41.91	-16.00	1.83	4.31	0.485	Some Impacts
80	028	O	2.547	42.21	-24.63	8.05	8.90	0.815	Edge Chipped, Corner Missing, Other Dents
81	012	B	0.589	42.84	11.21	15.83	13.35	0.282	Shattered
82	026	P	1.871	43.46	2.51	4.85	7.11	0.477	Shattered
83	054	A	0.347	43.74	-25.43	2.49	5.01	0.562	12 mm Dent in Edge, Spattered
84	012	O	2.542	44.03	-14.51	4.88	6.84	0.625	Corner Chipped Off, Some Impacts

† Cube materials: S - steel, A - aluminum, P - poplar, O - oak, B - balsa wood

Table 16. (Concluded)

Pos. on Arc	No.	Cube		Azimuth (degree)	Deviation Angle (degree)	Total Displace- ment (e)	Initial Velocity (m/s)	Dynamic Impulse (kPa-s)	Remarks
		Type	Mass						
85	016	B	0.588	45.97	15.13	16.33	13.60	0.287	Damaged, Dents
86	006	P	1.962	46.59	27.63	5.89	7.86	0.554	Chipped, Reusable
87	053	A	0.354	46.91	-7.58	2.54	5.05	0.578	Impacts, Dents
88	014	O	2.502	47.22	11.98	2.97	5.27	0.474	Piece Chipped Off Side, Small Dent on top
89	023	B	0.594	47.84	21.98	18.24	14.40	0.302	Large Dent, Small Impacts
90	019	P	1.854	48.42	7.86	7.67	9.02	0.600	Multiple Dents
91	045	A	0.350	47.73			Missing		
92	023	O	2.494	49.03	-5.73	5.38	7.20	0.645	Corner strike, Chipped Off
93	009	B	0.581	53.27	28.98	10.39	10.60	0.221	Small Impacts, Dents
94	023	P	1.842	53.88	-1.69	1.31	3.61	0.238	Dented, Split
95	051	A	0.352	54.18	32.37	0.65	2.61	0.267	Okay
96	009	O	2.746	54.48	29.79	0.66	2.39	0.236	Very Few Small Impacts
97	001	B	0.580	55.05	15.59	11.28	11.10	0.231	Large Dent, Several Small
98	003	P	1.829	55.64	0.47	2.59	5.14	0.339	Impact With Dent, Rock Imbedment, Edge Chipped Off, Small Impacts
99	041	A	0.350	55.96	-7.60	0.46	2.20	0.249	Okay
100	020	O	2.486	56.28	2.10	0.85	2.73	0.244	Small Impacts
101	018	B	0.627	58.82	-4.35	5.84	7.81	0.176	Small Impacts, Dents
102	005	P	1.826	59.40	7.63	1.50	3.87	0.254	Small Impacts
103	044	A	0.353	59.72	6.49	0.22	1.54	0.174	Okay
104	013	O	2.483	60.03	3.86	0.69	2.45	0.218	Small Impacts
105	017	B	0.570	60.65	-0.7	12.42	11.70	0.239	Split, Damaged
106	029	P	1.829	61.25	-28.64	2.76	5.31	0.348	One Edge Chipped Off, Other Dents
107	047	A	0.350	61.56	4.68	0.22	1.54	0.174	Okay
108	015	O	2.453	61.85	-32.49	0.74	2.54	0.244	Small Dent in Corner, Small Impacts

+ Cube materials: S - steel, A - aluminum, P - poplar, O - oak, B - balsa wood

Table 17. Blast Cubes: Post-Test Measurements and Calculated Data for
5-m Arc (Uthridge, 1989)

Position on Arc	Cube No.	Azimuth (deg)	Postshot Azimuth (deg)	Postshot Distance from Portal (m)	Deviation Angle (deg)	Total Displacement (m)	Remarks
1	010	320	331.919	90.44	12.610	85.56	
2	051	330	337.200	125.00	7.499	120.04	
3	079	340	336.844	535.55	-2.931	530.56	
4	008	350	346.842	617.22	-3.184	612.23	Number Partially Scratched
5	085	10	12.139	668.12	2.630	663.13	
6	028	20	23.668	551.23	4.342	546.24	
7	044	30	-----	-----	-----	-----	Not Found
8	025	40	-----	-----	-----	-----	Not Found
9	020	50	-----	-----	-----	-----	Not Found

Cube Parameters: Dimension, 152 mm
Material, steel
Mass, 27.7 kg

Table 18. Blast Cubes: Post-Test Measurements and Calculated Data for 10-m Arc (Ethridge 1989)

Position on Arc	Cube No.	Azimuth (deg)	Postshot Azimuth (deg)	Postshot Distance from Portal (m)	Deviation Angle (deg)	Total Displacement (m)	Remarks
1	009	335	-----	-----	-----	-----	Not Found
2	011	340	-----	-----	-----	-----	Not Found
3	003	345	-----	-----	-----	-----	Not Found
4	039	350	1.978	67.670	14.016	57.92	
5	089	355	-----	-----	-----	-----	Not Found
6	066	5	2.572	206.450	-2.549	196.46	
7	029	10	6.079	97.134	-4.370	87.15	
8	030	15	-----	-----	-----	-----	Not Found
9	035	20	21.600	146.390	1.559	136.39	
10	056	25	-----	-----	-----	-----	Not Found
11	040	30	-----	-----	-----	-----	Not Found
12	081	35	24.470	105.860	-11.614	95.75	

Cube Parameters: Dimension, 152 mm
Material, steel
Mass, 27.7 kg

Table 19. Blast Cubes: Post-Test Measurements and Calculated Data for Cubes in Tunnel
(Ethridge, 1989)

Cube No.	Preshot Distance from Portal (m)	Near Wall*	Postshot Azimuth (deg)	Postshot Distance from Portal (m)	Deviation Angle (deg)	Total Displacement (m)	Remarks
002	2	Right	--	--	--	--	Not found
007	2	Left	353.083	1669.8	-0.17	1673	--
091	12	Right	359.843	2351.9	-0.16	2364	ID number missing; assumed in tunnel because of distance moved and condition
048	12	Left	5.225	1714.2	+5.22	1726	--

18
5 ★ When looking toward the tunnel portal from the chamber.

Cube Parameters: Dimension, 152 mm
Material, steel
Mass, 27.7 kg

Table 20. Wire Drag Gage Results

Gage No.	Azimuth (deg)	Radial Distance (m)	Wire		20-ton Charge		Alternate Method	
			Deflection Angle (deg)	Bend Angle (deg)	Dynamic Radial Distance (m)	Pressure Impulse (kPa-s)	Dynamic Equivalent Charge (tons)	pressure Impulse (kPa-s)
3	60	75	+4	44	132	1.176	25	0.800
8	15	75	+18	--	--	-----	--	-----
9	15	100	+2	60	125	1.328	56	1.144
11	0	75	+15	--	--	-----	--	-----

NOTE: Radial distance measured from tunnel portal. Wire bend angle is the mean angle of wires from vertical. Deflection angle is the mean azimuthal deflection from the original radial alignment, with clockwise being positive.

Table 21. Calculated Values for Minimum Lethal Ejecta
Missile Impact Velocities

Maximum Missile Dimension (m)	Calculated Mass (kg)	Calculated Impact Velocity (m/s)
0.25	2.34	8.2
0.3	4.05	6.2
0.4	9.60	4.1
0.5	18.8	2.9
0.6	32.4	2.2
0.7	51.5	1.8
0.8	76.8	1.4
0.9	109.0	1.2
1.0	150.0	1.0

NOTE: Missile shapes are assumed to be rectangular
parallelepipeds with maximum dimension 4 times
the other two sides. Missiles were assumed to
have density of concrete.

Table 22. Comparison of Airblast Inhabited Building Distances for 22,000 kg NEW; Current Standards versus Measured Distances (in metres).

Source	Hazard Zone					Percent of Current Standard	Hazard Area (m ²)	Percent of Current Standard
	D5 00-300	D4 300-600	D3 600-900	D2 900-1200	D1 1200-1800			
<u>FOR 5.0 kPa (0.73 psi):</u>								
Current Standards (DOD 6055.9-STD) for UNDERGROUND storage	845	756	557	366		100		
Measured Distances, Shallow Underground Tunnel/Chamber Test	632	438	394			75		
Measured Distamces, Alvdalen Test (Vretblad, 1988) Scaled to 22,000 kg NEW	471	444	229			56		
<u>FOR 6.2 kPa (0.9 psi):</u>								
Current Standards, (DOD 6055.9-STD) for ABOVE-GROUND storage	540	540	540			100		
Measured Distances, Shallow Underground Tunnel/Chamber Test	539	369	336			100		
Measured Distances, Alvdalen Test (Vretblad, 1988) Scaled to 22,000 kg NEW	388	358	159			72		

Note: ¹ See Figure 98.